Micro scale reactor system development with integrated advanced sensor technology: A modular approach to the development of microfluidic screening platforms

Oliveira Fernandes, Ana Carolina

Publication date:
2017

Document Version
Publisher's PDF, also known as Version of record

Micro scale reactor system development with integrated advanced sensor technology

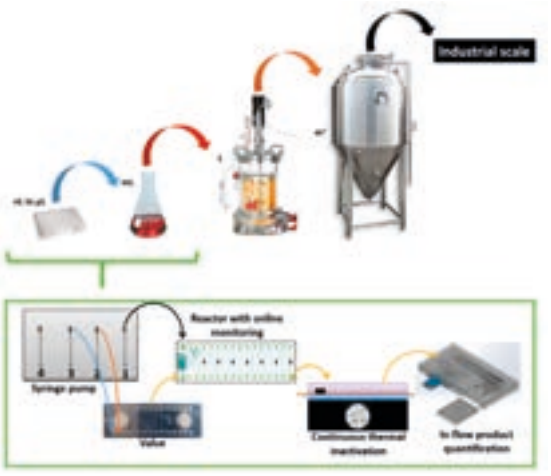

Ana Carolina Oliveira Fernandes

PhD Thesis

August 2017

DTU Chemical Engineering
Department of Chemical and Biochemical Engineering

Danmarks Tekniske Universitet DTU

Micro scale reactor system development with integrated advanced sensor technology

A modular approach to the development of microfluidic screening platforms

PhD thesis

Ana Carolina Oliveira Fernandes

Process and Systems Engineering Centre (PROSYS)
Department of Chemical and Biochemical Engineering
Technical University of Denmark (DTU)

August 2017

Address: Process and Systems Engineering Center (PROSYS)

Department of Chemical and Biochemical Engineering

Technical University of Denmark

Building 229

Dk-2800 Kgs. Lyngby

Denmark

Phone: +45 4525 2800

Web: www.kt.dtu.dk/forskning/prosys

Print: STEP

DTU Chemical Engineering
Department of Chemical and Biochemical Engineering

I am among those who think that science has great beauty. A scientist in his laboratory is not only a technician: he is also a child placed before natural phenomena which impress him like a fairy tale.

– Maria Skłodowska-Curie (1867 – 1934)

Preface

This thesis is submitted in partial fulfilment of the requirements for acquiring a PhD degree at the Technical University of Denmark (DTU). The research has been accomplished from July 2014 to August 2017 and was financed by the People Programme (Marie Curie Actions, Multi-ITN) of the European Union's Seventh Framework Programme for research, technological development and demonstration under grant agreement no. 608104 (EuroMBR). The work presented here was carried out at the Process and Systems Engineering Center (PROSYS) at the Department of Chemical and Biochemical Engineering (KT Kemitkenik) under the supervision of Associate Professor Ulrich Krühne and co-supervision of Professor Krist V. Gernaey and Project Manager Adama M. Sesay (Measurement Technology Unit (MITY), Oulu University, Oulu, Finland).

I would like to thank my supervisors for the opportunity to perform the work presented in this thesis, but especially for the support throughout the project, freedom to pursue side projects and ideas, for the challenges proposed and the fruitful discussions. I have grown considerably, both personally and professionally, thanks to them.

I would also like to express my gratitude to Professor Bernhard Hauer and PhD student Julia Halder (Biocatalysis Group, Institut für Technische Biochemie, Universität Stuttgart) for the collaboration and the opportunity to carry part of my project at their institute during an external stay. A huge thank you to Associate Professor Torsten Mayr and PhD student Shiwen Sun (Institute of Analytical Chemistry and Food Chemistry, Graz University of Technology, Graz, Austria), as well as to Dr. Juan M. Bolivar and PhD student Donya Valikhani (Institute of Biotechnology and Biochemical engineering, Graz University of Technology, Graz, Austria) for the support and discussions, as well as an incredible experience, during my external stay at their respective institutes. Thank you also to my co-supervisor, Adama M. Sesay and PhD student Peter Panjan for their help and knowledge on electrochemical sensors during my external stay at Measurement Technology Unit (MITY), Oulu University, Oulu, Finland and the opportunity to see the midnight sun.

I would also like to thank the KT workshop, especially Ivan, Michael, Benjamin and Lars for their help in assembling and fabricating some of the parts of the devices presented here.

My greatest gratitude to all my colleagues and friends at PROSYS and in Denmark for the amazing support, laughter, cookie breaks and being a family away from home. I would especially like to thank Dasha for being not only a colleague and project partner, but especially an incredible friend throughout everything. Also, to Hilde, Inês and Tannaz a huge thank you for the help and tips with CFD, you are my CFD superheroes! A heartfelt thank you also to

Carina, Francesco, Cigdem, Katrin, Carolina, Catarina, Soheil, Edu, Marie, Gisela and Andrijana for always listening and for great scientific and life discussions.

A big hug and thank you to the extraordinary Peam!

To my family and friends (Inês, Celso, João, Pedro, Inês, Mera, Tavinho, Marta, Raquel, Joana and my amazing "sisters" Ju, Teresa and Mariana) in Portugal, you have always been there for me and are simply amazing …thank you! Obrigada!

To my parents…you are my heart and soul! Thank you…always!

Finally, I would like to thank Tiago for all his love and caring support this past three years, for being my greatest love and for always being able to make me laugh.

Ana Carolina Oliveira Fernandes
Lyngby, August 2017

Summary

Biotechnology is an increasingly relevant field, at a time when most industries strive for the development of greener processes by reducing and/or eliminating the environmental impact of industrial processes, often by limiting the use of certain compounds (e.g. harsh solvents, metal-based catalysts), but also by reducing the number of reaction steps and the quantity of generated waste. The use of biological systems, such as biocatalysts and cells, enables operation at milder conditions, creating new synthetic routes, improving regio- and stereoselectivity, and avoiding (de)protection steps requiring harsh solvents or compounds, among other advantages. However, due to the complexity of biological systems, the development of fermentation or biocatalyst based processes is not straightforward. Similar enzymes may act on similar substrates but operate at different temperatures. Combinations of enzymes in cascade systems may require the spatial separation of the involved enzymes due to incompatible side-products or inhibitions from the reaction components. Certain cells present a faster growth rate at high densities, or different production titres depending on the formation of aggregates or cell adherence. The broad range of biological molecules and cells available for bioprocesses thus require the optimization of specific substrates or operation conditions, which as illustrated, can vary widely between them. Furthermore, the discovery and tailoring of new biocatalysts or cells involves environmental sampling and the generation of new variants, resulting in thousands of biological systems whose industrial or clinical potential needs to be evaluated, often in a relatively short timeframe.

High-throughput analytical systems are the main tool applied to biocatalyst screening. They enable the parallel operation of different reactions and/or fermentations at different conditions (e.g. substrate concentrations, different substrates, enzymes, medium, oxygen availability, etc.). Thus, high-throughput systems allow to cover the possible variations and narrow the feasible operation conditions, substrates and biocatalysts or cells for application at industrial scale. The need for fast and comprehensive characterization of biocatalysts has also pushed the development of new screening platforms, based on microfluidics. Microfluidic systems involve the manipulation of small sample volumes (μL to nL) in miniaturized vessels and structures. Through miniaturization, mass and heat transfer becomes significantly faster, but surface and mass transfer limitations due to diffusion are also increased. Furthermore, microfluidics allows the use of different strategies for each of the unit operations involved in such optimization and screening studies, as well as new sensing and monitoring approaches.

Within microfluidics there are several approaches regarding the integration of the required unit operations, ranging from integration on a single chip to a fully modular approach, where the different units correspond to a single chip but are interconnected through fluidic devices. The latter approach offers more flexibility at a lower cost in terms of the achievable studies with the same unit operations, since these can be placed in a different order depending on the purpose or sample being characterized.

The main goal of this dissertation was to develop a biocatalyst screening platform based on modular microfluidics. With this purpose in mind, three microfluidic modules are presented that can be integrated and used in such modular platform: a microreactor module with integrated oxygen sensors, a microfluidic dilution and quantification module compatible with electrochemical sensors and a module for continuous thermal inactivation of enzymes. The last two modules were developed specifically for applications in online screening. The focus during development was on achieving user-friendly and simple to use platforms that were furthermore easy to connect with other existing platforms and compatible with a wide range of biocatalytic reactions.

The microreactor module enables the continuous monitoring of oxygen levels and was characterized with a biocatalytic oxidation reaction in order to highlight the operational limitations of the system in terms of oxygen depletion at certain enzyme and substrate concentrations. Strategies for *in situ* oxygen generation involving addition of catalase and hydrogen peroxide were applied as solutions to overcoming the identified oxygen depletion limitations. Furthermore, the reactions carried out in the microfluidic system were modelled using computational fluid dynamics, with a good fit between the experimental and simulated data, and the results provided extra insight into the reaction dynamics. The same microreactor was applied to the screening of whole cell variants of a dioxygenase capable of converting alkene substrates. It was used as a complement to the screening of genetically modified biocatalysts using end-point product quantification. The oxygen consumption rate of each variant in the presence of a standard substrate was used as the screening parameter to select the variant with the faster oxidation reaction rate as the best variant for a possible industrial application.

The second module was developed for integration of different types of sensors to achieve online quantification. The module presents a standardized fitting enabling the connection to either other microfluidic platforms or laboratory scale equipment. Screen-printed electrochemical sensors were integrated through pockets that allowed their easy replacement and thus the re-use of the microfluidics' platform. Also, the developed platform included a mixing/dilution channel enclosed by a two-sensor system, which allowed expanding the sensors' detection range by controlling the sample dilution at which the measurements were performed. The dilution unit was optimized with computational fluid dynamic methods that enabled testing several geometries before fabrication, thus accelerating the platform development.

The third microfluidic module was developed to allow unspecific inactivation of biocatalysts (especially enzymes), and thus precisely control the reaction (residence) time at the point of product quantification in the second module. Such control is important when different modules – reactors and/ or sensing units – are used and frequently changed. It can furthermore help to regulate the state of the biocatalyst, since it is depending on the temperature and exposure time. In this way, reversible or irreversible denaturation of the enzymes can be achieved.

The different modules presented in the dissertation are useful additions to a modular microfluidic toolbox for biocatalyst screening. They provide online monitoring of biocatalytic reactions or biotransformations, quantification of reaction products and controlled reaction end-points due to the potential to achieve precise temperature control. Furthermore, the developed computational fluid dynamic models allow for a better understanding of the reaction performed

in the microsystem. The model can be further improved to achieve online data acquisition of reaction kinetics by coupling with a mechanistic model. In the case of the developed mixing/dilution channel, the developed model enabled a fast optimization of the unit operation, thereby decreasing the cost and time spent on such endeavour.

The potential of modular microsystems in biotechnological applications was the main driver for the work performed and presented in this dissertation. The objective of this dissertation was to provide, beside three interesting microfluidic systems, a better understanding of the potential that microfluidics, especially in a modular approach and tightly connected to mathematical modelling, can offer to biotechnology and society.

Resumé

Interessen for bioteknologi har vokset støt, i en tid hvor de fleste industrier i stigende grad fokuserer på grøn omstilling og udvikling. Der er generelt stor fokus på at reducere og/eller eliminere mange af de miljøbelastende effekter fra industrielle processer. Dette afspejles i industrielle processers udviklingen, som går i retning mod at finde alternativer til anvendelsen barske opløsningsmidler og metalbaserede katalysatorer, samt at reducere antallet af reaktionstrin og mængden af genereret affald.

Dette har betydet store fremskridt i udviklingen og anvendelsen af biologiske systemer, såsom biokatalysatorer og celler. Sådanne biologiske systemer giver mange procesmæssige fordele, såsom; 1) muligheden om at køre kemiske reaktioner ved mildere reaktionsforhold; 2) nye syntese reaktioner; 3) forbedret regio- og stereoselektivitet.; 4) overflødiggørelse af kemiske beskyttelses og af-beskyttelses reaktioner der er afhængige af brug af barske opløsningsmidler/kemikalier.

Det er dog ret krævende at udvikle biologiske systemer til industrielle processer, idet udviklingen af fermenteringsprocesser og/eller biokatalysatorbaserede processer er komplekst. F.eks. ensartede enzymer kan håndtere ensartede substrater, men have meget stor variation i performance ved forskellige temperaturer. Derudover kan kombinationen af flere enzymer i kaskade reaktionssystemer kræve en fysisk adskillelse af enzymerne i processen, grundet påvirkningen af biprodukter og/eller inhibering fra forskellige reaktionskomponenter. Yderligere kan det tilføjes at visse celler har en hurtigere vækshastighed ved høje tætheder eller forskellige produkt koncentrationer afhængig af dannelsen af aggregater eller sammenhængende celler. Den brede vifte af biologiske molekyler og celler, der kan fremstilles vha bioprocesser, kræver således optimering af specifikke substrater eller driftsbetingelser der, som ovenfor illustreret, kan variere meget mellem dem. Dertil skal tilføjes at opdagelsen og tilpasningen af nye biokatalysatorer og/eller celler kræver omfattende udtagelse af miljøprøver og dannelsen af nye varianter, hvilket nemt kan resultere i tusindvis af biologiske systemer, der potentielt kan være af stor industriel og/eller klinisk interesse, som skal analyseres og evalueres på relativt kort tid.

Analysesystemer der er i stand til at screene disse mange varianter af biokatalysatorer er derfor et meget vigtigt værktøj. Sådanne analysesystemer gør det muligt at analysere forskellige reaktioner og/eller fermenteringer i parallel ved forskellige reaktionsbetingelser. F.eks. varierende substratkoncentrationer, sammensætning af medier, etc. Dette gør det muligt at identificere mulige variationer, procesbetingelser, substrater og biokatalysatorer eller celler der har potentiale til industrielle applikationer.

Dette behov for hurtig og omfattende karakterisering af biokatalysatorer har skubbet udviklingen af nye screeningsplatforme baseret på mikrofluidsystemer. Mikrofluidsystemer indebærer manipulation af små væskevolumener (µL til nL) i miniaturiserede beholder, kanaler og/eller strukturer. Fordelen ved miniaturisering er at masse og varmeoverførsel bliver markant hurtigere. Dog bliver overflade- og masseoverførselsbegrænsninger på grund af

diffusion også øget. Mikrofluidsystemer gør det muligt at bruge forskellige strategier for forskellige enhedsoperationer, der er involveret i sådanne optimerings- og screeningsundersøgelser, samt nye målings- og monitoreringsmetoder.

Der er flere tilgange til at kombinere og/eller integrere enhedsoperationer i mikrofluidsystemer. Disse tilgange strækker sig fra integration på en enkelt chip til fuldt ud modulære elementer der er linket sammen med rør og slanger. Sidstnævnte mulighed giver stor fleksibilitet idet det er muligt at kombinere modulerne i den rækkefølge der er krævet, afhængig af hvad der ønskes testet.

Hovedformålet med denne afhandling var at udvikle en screeningsplatform baseret på modulære mikrofluidsystemer, til at "screene" biokatalysatorer. I denne afhandling præsenteres tre mikrofluidmoduler, der kan integreres og anvendes som en modulær undersøgelseplatform. Det ene modul er et mikroreaktormodul med integrerede oxygen-sensorer, samt et fortyndings og kvantificeringsmodul. Dette modul er kompatibelt med elektrokemiske sensorer og kontinuerlig termisk inaktivering af enzymer. De to sidste moduler blev udviklet specielt til applikationer i online screening. Fokus under udviklingen af disse moduler var på at opnå simpel og brugervenlig betjening af platformene, samt at de var nemme at forbinde med andre eksisterende platforme og kompatible med en lang række biokatalytiske reaktioner.

Mikroreaktormodulet gjorde kontinuerlig monitorering af iltniveauer mulig og blev karakteriseret med en biokatalytisk oxideringsreaktion. Formålet med karakteriseringen var at identificere operationelle begrænsninger af systemet i form af iltudtømning ved visse enzym- og substratkoncentrationer. I samme system blev strategier for *in-situ* oxygen regenerering også testet, ved tilsætning af katalase og hydrogenperoxid, for at overvinde de operationelle iltbegrænsninger i systemet. Derudover blev reaktionerne i mikroreaktormodulet modelleret ved hjælp af strømnings beregninger, hvor der blev vist en god sammenhæng mellem modellen og de eksperimentelle data. Detter resulterede i ekstra indsigt i reaktionsdynamikken. Den samme mikroreaktor blev brugt til at screene variationer af en dioxygenase enzym i hele celler for deres potentiale til at omdanne alkensubstrater. Dette supplerede til screeningen af genetisk modificerede biokatalysatorer ved anvendelse af produktkvantificering ved reaktionens slutpunkt. Oxygenomdannelsesraten blev bestemt for hver variant, hvor et standard substrat blev brugt som screeningsparameter, for at bestemme varianten med hurtigst oxygen omdannelse som den bedste kandidat til fremtidig industribrug.

Det andet modul blev udviklet for at kunne integrere forskellige typer af sensorer til at sikre online kvantificering. Modulet har en standardiseret samlingsopkobling, hvilket gør det muligt at forbinde andre mikrofluidmoduler eller standard laboratorie udstyr. Trykte elektrokemiske sensorer blev integreret gennem åbninger i modulet, der tillod nem udskiftning og dermed genbrug af modulet. Det udviklede modul omfattede også en blandings- / fortyndingskanal, der var vedlagt et to-sensorsystem, hvilket tillod at udvide sensorernes detekteringsområde ved at kontrollere fortyndingsfaktoren som målingen blev foretaget ved. Fortyndingsenheden blev optimeret vha fluid dynamiske beregningsmetoder, der gjorde det

muligt at teste flere geometrier inden fremstillingen og derved bidrog til at accelerere modul udviklingen.

Det tredje mikrofluidmodul blev udviklet for at sikre uspecifik inaktivering af biokatalysatorer (især enzymer) og derved sikre præcis kontrol af reaktiontidspunktet (opholdstiden) ved produktkvantificering i det samme modul. Denne kontrol er vigtig når forskellige reaktormoduler og/eller sensorer anvendes og ofte udskiftes. Det kan endvidere bidrage til at regulere biokatalysatorens tilstand, da det afhænger af temperatur og eksponeringstid. Dermed kan reversibel eller irreversibel denaturering af enzymerne opnås.

De forskellige præsenterede moduler er nyttige tilføjelser til etableringen af en modulær mikrofluid værktøjskasse til biokatalysator screening. Modulerne tillader online overvågning af biokatalytiske reaktioner eller biotransformationer, kvantificering af reaktionsprodukter og kontrollerede reaktionsendepunkter på grund af præcis temperaturkontrol. Desuden giver de udviklede fluid dynamiske modeller mulighed for en bedre forståelse af den reaktion, der udføres i mikrosystemet. Modellen kan forbedres yderligere for at opnå online dataindsamling af reaktionskinetik ved kobling med en mekanistisk model. I tilfælde af den udviklede blandings- / fortyndingskanal muliggjorde den udviklede model en hurtig optimering af enhedsoperationen, hvilket reducerede omkostningerne og den tid, der blev brugt til en sådan indsats.

Demonstration af potentialet for modulære mikrosystemer i bioteknologiske anvendelser var hovedformålet med det udførte arbejde præsenteret i denne afhandling. Formålet med denne afhandling var at, udover etablering ad de tre mikrofluidsystemer, give en bedre forståelse for potentialet i brugen af mikrofluidsystemer til procesudvikling i bioteknologi, hvor specielt den modulære tilgang i kombination med fluiddynamisk modellering byder på spændende muligheder til fremtidig procesudvikling.

List of Publications

T. Tajsoleiman, D. Semenova, A.C. Fernandes, J. K. Huusom, K. V. Gernaey and U. Krühne, "An Efficient Experimental Design Strategy for Modelling and Characterization of Processes", Conference proceedings, 27th European Symposium on Computer Aided Process Engineering, Volume 40, 2017, Pages 2827-2832 (Published)

A.C. Fernandes, D. Semenova, P. Panjan, A. M. Sesay, K. V. Gernaey and U. Krühne, "Multi-function microfluidic platform for sensor integration", full length paper, New Biotechnology IMTB 2017 special issue (Submitted August 2017)

A.C. Fernandes, B. Petersen, L. Møller, K. V. Gernaey and U. Krühne, "Caught in-between: System for in-flow inactivation of enzymes as an intermediary step in "plug-and-play" microfluidic platforms", full length paper, New Biotechnology IMTB 2017 special issue (Submitted August 2017)

A.C. Fernandes, K. V. Gernaey and U. Krühne, "Connecting worlds – a view on microfluidics for a wider application", review paper, Sensors and Actuators B: Chemical (Submitted August 2017)

Conference contributions

A.C. Fernandes, D. Semenova, T. Mayr, D. Bouwes, A. M. Sesay, K. V. Gernaey and U. Krühne, "Oxygen sensor integration in microbioreactor systems for biocatalytic reactions", 3rd International Conference IMPLEMENTATION OF MICROREACTOR TECHNOLOGY IN BIOTECHNOLOGY – IMTB 2015, Opatjia, Croatia, May 2015, poster presentation.

A.C. Fernandes, D. Semenova, J. Ehrgartner, T. Mayr, A. M. Sesay, K. V. Gernaey and U. Krühne, "Sensor Integration in Microbioreactor Systems for High-throughput Bioprocesses", 3rd European Congress of Applied Biotechnology (ECAB), Nice, France, September 2017, poster presentation.

A.C. Fernandes, D. Semenova, J. Ehrgartner, T. Mayr, A. M. Sesay, K. V. Gernaey and U. Krühne, "Sensor integration in microbioreactor systems for high performance processes", EUROPT(R)ODE XIII - Conference on Optical Chemical Sensors and Biosensors, Graz, Austria, March 2016, poster presentation.

A.C. Fernandes, D. Semenova, J. Ehrgartner, T. Mayr, A. M. Sesay, K. V. Gernaey and U. Krühne, "Sensor Integration in Microbioreactor Systems for High-throughput Bioprocesses", 14th International Conference on MicroREaction Technology (IMRET14), Beijing, China, September 2016, oral presentation.

A.C. Fernandes, D. Semenova, J. Ehrgartner, T. Mayr, A. M. Sesay, K. V. Gernaey and U. Krühne, “Sensor Integration in Microbioreactor Systems for High-throughput Bioprocesses”, 4th International Conference IMPLEMENTATION OF MICROREACTOR TECHNOLOGY IN BIOTECHNOLOGY – IMTB 2017, Bled, Slovenia, oral presentation.

List of Figures

List of Tables

Table of contents

Chapter 1

Introduction

Microfluidics was defined by Whitesides in 2006 as the science and technology involving the study, manipulation and control of small volumes of fluids and particles in channels with dimensions of tens to hundreds of micrometers [1].

From its birth, microfluidics has been referenced as the "promised land" of technology. Microfluidics has for example been envisioned as: (1) capable of miniaturizing industrial plants, thereby increasing their automation and operational safety at low cost; (2) being able to identify rare diseases by running bioanalytics directly on the patient's skin; (3) allowing health diagnostics in point-of-care sites through cheap lab-on-a-chip devices. However, the current state of microfluidics, although technologically advanced, has struggled to reach the originally promised widespread use.

In this chapter, some of the key aspects that have prevented microfluidics from reaching its full potential are identified and discussed, addressing mainly the specialization on a single target of most microfluidic devices. The alternate, multi-use, "plug and play" approach is offered as a possible solution. An overview of the current possibilities for modular unit operations for use in such approach is presented, as well as a brief review of the main materials and fabrication strategies applied in microfluidics. Furthermore, a step-wise guide towards the development of microfluidic platforms is introduced with special focus on the integration of sensors in microfluidics. Finally, the potential of microfluidics in biotechnology is described as the motivation for the work presented in this dissertation. A thesis outline stating the main goals of the presented work, and a brief description of the thesis's different chapters, concludes this introductory chapter.

1.1 Introducing microfluidics

Nowadays, the use of micro- or nanofluidics is moderately wide-spread across several academic fields, from proteomics and drug discovery to waste management and point-of-care (POC) diagnostics [2],[3]. Since the first proof-of-concept [4], the rapidly increasing interest on the micro- or nanofluidics technology can be associated with its advantages, such as the low manufacturing costs, reduced usage of reagents and the possibility for parallelization and automation [5]. These characteristics along with a highly automated control of the fluidic flow, an easy tuning of temperature and concentration diffusion gradients, as well as the available semiconductor technology, have pushed the interest towards miniaturization of unit operations, together with the development of suitable analytical devices and techniques. This subsequently led to an effort towards the integration of these miniaturized units in a single device.

1.1.1 Physics in microfluidics

The main advantages associated with microfluidics are related with the decreased scale of the vessels, such as a lower reagent consumption, smaller sample volumes and faster heat and mass transfer rates. Furthermore, at microscale, certain boundary effects (e.g. surface tension) and physical phenomena that increase inversely with scale (e.g. pressure drop), become more relevant. To fully understand the impact and potential of the strategies employed in microfluidics, it is therefore important to know not only the more relevant phenomena occurring at microscale, but also the mathematical description behind them. This mathematical description is used both in the design of new microfluidic platforms and in the fluidic and mathematical models developed for studying and predicting reactions and molecular interactions in microstructures.

Most microfluidic systems currently used are pressure-driven [6]. In this case, the flow (velocity) of fluids that can be considered as incompressible and uniform-viscous Newtonian (e.g. aqueous solutions) can be described using the Navier-Stokes equation (Equation 1), where $\vec{u}$ is the velocity field, dependent on spatial position and time (m s^{-1}), ρ is the fluid density (kg m^{-3}), η is the viscosity (Pa s) and p is the pressure (Pa) [6].

Equation 1

$$rate\ of\ momentum\ change = convective\ force + pressure\ force + viscous\ force$$

$$\rho\frac{\partial\vec{u}}{\partial t} = -\rho\vec{u}\nabla\vec{u} - \nabla p + \eta\nabla^2\vec{u}$$

The velocity field of fully developed laminar flow in steady-state is unidirectional and can in turn be described by Equation 2, where the frictional forces the liquid is subjected to at the channel walls due to its viscosity are considered. In the case of circular channels of radius R (m), this is termed Poiseuille flow (Equation 3) and results in a parabolic velocity profile (velocity at the center is higher than close to the walls, as observed in Figure 1) [6]. This assumes a no-slip boundary condition for the velocity field at the interface between liquid flow and the channel walls. The no-slip assumption at a solid-liquid interface results from the assumption of complete momentum relaxation of the molecules at the interface in a length scale in the order of the molecular mean free path in the fluid [7]. This assumption may not always be valid in microchannels, especially in the case of non-wetted hydrophobic surfaces with polar fluids [8].

Equation 2

$$\nabla p = \eta\nabla^2\vec{u}$$

Equation 3

$$u = \frac{R^2 - r^2}{4\eta}\left(-\frac{dp}{dx}\right)$$

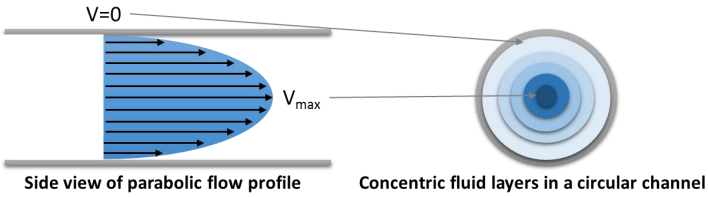

Figure 1 – Schematic representation of parabolic velocity profile in circular channels.

From the Poiseuille flow, assuming a straight and infinitely long channel, Hagen-Poiseuille's law (Equation 4) can be obtained for a straight channel of length L (m) with a uniform pressure gradient and L/R>>1 and L/R>>Re (fully developed flow). The Hagen-Poiseuille law is applied to most pressure-driven microfluidic channels, as a simple (approximate) way of calculating the pressure drop between the inlet and the outlet [6].

Equation 4

$$Q = \frac{\pi R^4}{8\eta}\frac{\Delta p}{L}$$

From the previous equation, it is possible to define the hydraulic resistance (R_H) (Pa s^3 m^{-1}) for circular channels (Equation 5), where r_H (m) is the hydraulic radius (a geometric constant defined as twice the cross-sectional area over the wetted perimeter). This equation can also be applied to rectangular channels with a low aspect ratio, however with around 20% of error in the obtained value. Other expressions have been derived for rectangular channels that result in a lower error [7]. For H(height)/W(width)<<1 aspect ratio channels, Equation 6 can be used [6].

Equation 5

$$R_H = \frac{8\eta L}{\pi {r_H}^4}$$

Equation 6

$$R_H = \frac{12\eta L}{W H^3}$$

The type of flow (laminar, transient or turbulent) can be characterized through the Reynolds (Re) number (Equation 7), which is defined as the ratio between inertial and viscous forces. In Equation 7, V (m s^{-1}) is the characteristic velocity, U (m s^{-1}) is the area-averaged velocity, D (m) is the characteristic length and D_H (m) is the hydraulic diameter. Surface roughness in microchannels can significantly affect flow behaviour, surface functionalization and molecular adsorption dynamics, however at the Re numbers found in microchannels, the friction factor (Equation 8, where C_f is channel friction factor coefficient in fully developed flow) follows the Hagen-Poiseuille theory, being equal to 64/Re [9].

Equation 7

$$Re = \frac{\rho V D}{\eta} \approx \frac{\rho U D_H}{\eta}$$

Equation 8

$$\lambda = \frac{C_f}{Re}$$

In microfluidic channels flow is laminar (Re<2100) and usually in the Stokes regime (Re<1), and so inertial effects are usually negligible [6]. However, for flows with 1<Re<100,

inertial forces become relevant and can be used to achieve facilitated separation, focusing and concentration of cells and particles with inertial microfluidics [10]. In the inertial microfluidics regime two phenomena occur: inertial migration and secondary flow. Inertial migration involves the migration of particles randomly dispersed in the fluid to equilibrium positions next to the channel walls, after a certain distance from the inlet. This occurs due to two counteracting effects resulting from the interaction of the fluid either with the particles (the shear gradient lift force, directing particles towards the channel walls) or the channel walls (the wall lift force, directing particles away from the channel walls) [10]. Secondary flow usually occurs in curved channels or straight channels with obstacles. In curved channels it results from a pressure gradient in the radial direction due to higher momentum of the fluid in the centerline relative to the walls, which leads it to flow outwards, pushing the stagnant flow inwards and creating counter-rotating streams (Dean vortices), illustrated in Figure 2 [10].

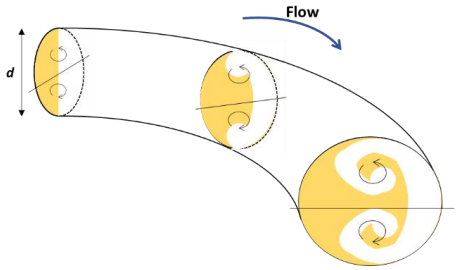

Figure 2 – Schematics of Dean flow effects in a curved circular microchannel, where the arrows indicate the counter-rotating streams.

An extremely relevant phenomenon at microscale is diffusion. Diffusion is the permeation of molecules or particles in a fluid across an interface due to the random Brownian motion resulting from the frequent collisions with atoms or molecules in the liquid or gas [11]. The diffusion coefficient increases with the temperature and depends on the material diffusing and the fluid where diffusion is occurring [11]. The minimum length L_D (m) required for the complete diffusion of a certain molecule or compound in a channel can be calculated by Equation 9, knowing U (m s^{-1}) the area-averaged velocity, D_D (m^2 s^{-1}) the diffusion coefficient of the molecules or compounds diffusing, d (m) the distance it travels in a time t (s) (Equation 10) and the approximate diffusion time, t_D it takes to cross the width of the channel (Equation 11) [6]. However, due to the parabolic velocity profile, since the fluid near the walls moves slower than in the centerline, the growth of the interdiffusion zone varies from $l^{1/3}$ near the top and bottom walls to $l^{1/2}$ in the center of the channel, where l (m) is the distance traveled along the channel [8].

Equation 9

$$L_D = Ut_D \approx U\frac{W^2}{D_D}$$

Equation 10

$$d \approx \sqrt{2D_D t}$$

Equation 11

$$t_D \approx \frac{W^2}{D_D}$$

A measure of whether mixing between two fluids occurs through diffusion or convection is given by the Péclet (*Pe*) number (

Equation **12**), where V (m s^{-1}) is the characteristic velocity transverse to the diffusion, U (m s^{-1}) is the area-averaged velocity, D (m) is the characteristic length, D_H (m) is the hydraulic diameter and D_D (m^2 s^{-1}) is the diffusion coefficient [6]. *Pe* gives an idea of the number of channel widths required for complete diffusional mixing to occur [8]. The larger *Pe*, the more relevant convection is in the transport of particles or fluid mixing [11].

Equation 12

$$Pe = \frac{VD}{D_D} \approx \frac{UD_H}{D_D}$$

Another relevant effect in microchannels is the effect that the channel walls surface has on the flow, such as adhesion (in the case of cells and biomolecules), adsorption, and shear stress. At microscale, these effects are not negligible. Adhesion and adsorption may be tailored by changing the material forming the channel or by surface functionalization. Surface functionalization (e.g. with hydrophobic stripes created through selectively coating portions of the channel bottom wall) can even be used to achieve wall-less channels [8]. However, shear stress is mainly dependent on the geometry and type of flow. Shear stress is the ratio between a force applied on the fluid in motion, which has the opposite direction of the velocity applied, and the area of the surface of the wall in contact with the fluid in motion. When motion begins, it starts from a position away from the wall, being then transmitted linearly, at steady state, to the other "layers" of liquid until the layer next to the wall. This transmission of motion depends on the liquid properties, namely the liquid viscosity. The shear stress at the wall can thus be described by Newton's law of viscosity (Equation 13), where τ_W (Pa) is the shear stress at the wall, η (Pa s) is the viscocity, u (m s^{-1}) is the flow velocity and h (m) is the position along the height of the channel [6]. For aspect ratio (H/W<<1) channels with parabolic flow, the expression for shear stress can be approximated by Equation 14 [6].

Equation 13

$$\tau_W = -\eta \left(\frac{du}{dt}\right)_{at\ wall}$$

Equation 14

$$\tau_W \approx \frac{h\Delta p}{2L} = \frac{6\eta Q}{Wh^2}$$

Another interesting phenomenon at microscale involves the competition between surface tension to reduce the interfacial area of an immiscible fluid and the viscous stresses, which extend the interface in the direction of flow. This can be described by the Capillary number (*Ca*) (Equation 15), where γ (N m^{-1}) is the surface tension [8]. The manipulation of surface tension at microscale gave rise to droplet microfluidics [12], a growing area in microfluidics with wide applicability [13]. Capillary forces have also been used to drive and manipulate flow in microfluidics, using thermal, electric or wettability gradients for example, as an alternative to external pumping devices [8].

Equation 15

$$Ca = \frac{\eta U_0}{\gamma}$$

The presented physical description of flow in microchannels is a summary of the main phenomena involved in flow at the microscale and a simplification of the principal equations describing these phenomena. Other important phenomena, used in more specific applications, that were not mentioned involve polymer deformability and elastic behavior (used in rheology and the study of polymers), properties of buoyancy-driven flows (influence of gravity on solution density gradients that are described by the Rayleigh and Grashof numbers and are highly relevant for protein crystallization in microfluidics), effects of charge accumulation on the surface and formation of the Debye layer (frequently applied in electrokinetics to drive flow [14] and separate molecules) [8].

The particularity of the phenomena presented, and the possibilities they offer in terms of device geometry, flow and material manipulation, and types of study, are one of the main characteristics driving the interest and investment in microfluidic-based devices. Microfluidics is thus a powerful tool to perform both fundamental studies in diverse areas of physics, chemistry and biology [15], as well as a powerful technology to improve industrial processes, clinical diagnostics and applied research.

1.1.2 Microfluidics and the technological market

Initially, microfluidics' research and development activities focused on areas where the highest potential for short-term commercial success was expected [5]. For example, pharmaceutical companies started performing initial screening tests in lab-on-a-chip devices since these presented less false positives and thus higher quality results [16]. Despite the obvious potential, microfluidics has still a very small impact in the technological/analytical market today [2],[3]. Current fields of application of microfluidics are confined to *in vitro* diagnostics (e.g. DNA/RNA hybridization and PCR) [17], [18], [19] pharmaceutical applications (such as drug discovery and screening, as well as drug delivery) [20], [21], biotechnology (e.g. on and in-line process monitoring of fermentations and biocatalytic reactions at small scale) [22], [23], and ecology (e.g. water quality assessment and biological threat detection) [24], [25]. Even though a few microfluidic-based technologies or solutions that include microfluidic parts are available in the market [26], they are mainly used in research laboratories [3]. It is therefore important to reflect on the reason for this relatively low impact, which stands in sharp contrast with the original sky-high ambitions for this field. A more thorough analysis reveals a relatively low impact of microfluidics due to the systems complexity, frequently observed repeatability issues of the existing platforms and the low application flexibility of the majority of the developed microfluidic systems. The difference in physical phenomena occurring at microscale relative to larger scale (e.g. laboratory and large scale fermenters), can lead to the selection of sub-optimal parameters, resulting in process failures, and consequently in a lower trust on data obtained with these platforms. Also, the manufacturing costs and the required initial investment, which translate into high costs of the final devices, lead to a specific and closed company-customer based business model, instead of a general model relying on publicly available and well described systems that can be combined in order to address a wide range of specific customer needs [2]. In this respect, the solution to the low market spread might be found in the development of simpler devices which are easier to (inter)connect, whether in "plug and play" approaches or to already existing external analytical equipment. Changing the focus from

finding the "killer application" [27], [28], to designing and manufacturing generic platforms, more flexible in terms of connectivity and application [16], [2], [29], which are capable of facilitating the integration of multiple unit operations and their associated fluid handling, would undoubtedly boost the microfluidic field's influence in the global market [2], [30]. Multi-purpose devices, especially reusable ones, enable to: (i) lower the cost of the method(s) used; (ii) increase the diversity of tests that can be performed, as well as the diversity of samples that can be handled; and, (iii) probably allow for a higher degree of comparison between samples, since the same devices can be used even if assembled differently. It is important to note here that the wide-spread application of microfluidics is bound by the costs of the final device, the complexity of operation and the dependency on external equipment [31].

Some companies, focused on the development of microfluidic systems have already shifted towards more flexible chips. Nanogen's (Nanogen, Inc., San Diego, US) electronic addressing technology (NanoChip® Electronic Microarray) allows capturing DNA probes in specific locations towards detection of single-base-pair differences, in a "blank slate" platform where the users can define their own assay [32]. This system however, as other similar devices, requires a bulky benchtop workstation for microfluidic device operation, such as the use of robotic liquid handling instruments for liquid handling automation in microfluidic systems [16]. Epigem (Redcar, United Kingdom) designs and fabricates devices for specific applications, while also providing their own strategy for fluidic connection and gaskets for reversible encapsulation, as well as embedded circuit layers. However, there is no standardization, since the systems are either application or client specific. Other commercial producers, such as Micronit Microtechnologies (Enschede, the Netherlands), Microfluidic ChipShop (Jena, Germany) and ThinXXS Microtechnology (Zweibrücken, Germany) also strive towards multiple application systems by having developed standard chips for certain unit operations (capillary electrophoresis, reactors, mixers, etc.) [27]. They also manufacture chips with standardized sizes (for instance microscopy slides and microtiter plates) and microfluidic connections, providing even stages for easy fluidic connection. Connectivity between their own chips is facilitated, while the connectivity with chips from other manufacturers or developed in house by the end user is not easily achieved. Some academic groups have also tackled this issue with interesting approaches based on the LEGO® (Billund, Denmark) "plug and play" concept [33], [34], [35], [36], [37], or even using LEGO® components [30], [38], [39]. There exists also a commercial prototyping system called The LabMatrix™ that provides a set of standard modular chips for molecular studies that can be assembled on a microfluidic breadboard. The set includes microvalves, syringe pumps, a stereomicroscope, UV detection and NanoFlow flow cells [40].

An extremely relevant market for modular microfluidics has been synthetic chemistry and the production of valuable chemicals [41], such as positron emission tomography (PET) tracers, active pharmaceutical ingredients (API) [3], natural products [42], fine and bulk chemicals, particle synthesis, pigments [43], among others. Microfluidics provides valuable advantages in chemistry such as improved selectivity and process safety, smaller footprint, acceleration of mass-transfer limited reactions, faster kinetic information, increase in production rates through a scale-out approach and the intrinsic continuous, rather than batch, production [3]. Hartman *et al.* (2011) provided a good analysis of flow chemistry vs. batch reactors [44], illustrating the advantageous vessel dimensions and mixing properties of microfluidics for flash-chemistry and

fast and/or exothermic reactions. Microfluidics, especially based on droplet generation, is enabling the production of new microparticles and nanomaterials [3], but there are already examples of modular-based flow chemistry being applied to industrial or industrial sized production [43]. For example, Adamo *et al.* (2016) presented a module-based continuous manufacturing platform capable of combining both synthesis and formulation of several pharmaceutical compounds. As proof-of-principle, they produced four different compounds in a gram-per-hour scale. The use of such flexible, reliable and compact manufacturing platforms could simplify formulation of compounds with short shelf-life as well as lower the price of pharmaceuticals for small patient populations [45].

Another relevant example of the potential of modular platforms is biotechnology, by taking advantage of novel approaches to synthesis developed in flow chemistry [46], [47] .

1.1.3 Microfluidics and Biotechnology

Enzyme and strain screening, as well as optimization of bioprocess operation conditions are key steps in the development of a biotechnological process (Figure 3). They involve a reliable and scalable study of all process parameters, along with mapping their influence and interactions for each of the potential biocatalysts/strains [48]. The final process target determines the different requirements and conditions which are in focus during design development, thus further increasing the number of variables to consider during optimization, as well as the variability of the process development as a whole. The high number and variety of enzyme/strain candidates [49] and corresponding optimal conditions, thus result in an expensive and time-consuming development process. Often it is not possible to test all the desired options. Therefore, dependent on the application, high throughput methods [50],[51], mainly performed on microtiter plates and shake flasks are the preferred experimental test platforms. These allow a high throughput due to the use of easily programmed and flexible automatic fluid handling systems [2]. Despite the level of obtained parallelization, these systems offer a reduced amount of available analytics, as well as low process controllability, which results in low quality of information retrieved. Thus the knowledge gained about the process and enzyme/strains is strongly limited [52]. Additionally, the differences in scale between the vessels used for optimization and for the final bioprocess, can lead to the selection of a set of parameters or conditions during the process screening stage which are sub-optimal for the larger scale. This will often result in a less effective industrial process that requires further optimization at the final stage, or even lead to scale-up failure with large economic impact [53]. An increase of monitoring and control of reaction parameters in the screening stage potentially contributes to improve the scale-up of bioprocesses. When developing or choosing a high throughput platform (HTP), it is very important to consider the maximum variation between reactors in the platform (in terms of reproducibility of reaction kinetics, product formation, cell growth, metabolic activities and productivity), which should be less than the detectable level of change in the parameters under investigation. Also, the type of reaction, biocatalyst or cell, the fermentation and minimum culture/reaction volume, as well as, the sampling volume for process characterization (including product titre and quality analysis), the sampling frequency and the required oxygen transfer rate should be taken into account. The

capability for online monitoring towards high information on process conditions plus actuation on these conditions for a more tightly controlled process is highly desirable [54], [55], [51].

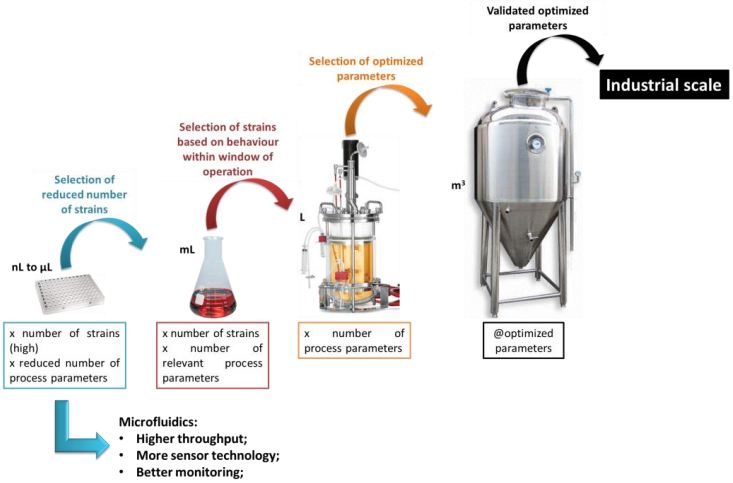

Figure 3 - Schematics of scale-up in bioprocesses and possible role of microfluidics.

Microfluidics and miniaturized analytics can greatly contribute to accelerate the first stage of process development, where the selection of appropriate biocatalyst/strain and start of process parameter optimization are primarily achieved [56]. They can also decrease the error obtained during the first stage of process development by providing platforms capable of parallelization in high numbers and with a variety of integrated sensors, providing both reliable data and substantial process control. The application of microfluidics to biocatalysis, for example, has been considered a key step towards greener processes and process development, by enabling safer handling and point-of-use generation of hazardous compounds [57], as well as production of a lower amount of waste [47]. Microreactors can also increase the process window of a given bioprocess by allowing the performance at wider ranges of temperature, pressure, reaction rate and compound concentrations [47], [57]. Furthermore, due to the different phenomena occurring at small scale (higher influence of surface tension, diffusion control of mass and heat transfer, capillary forces) they can more easily mimic and study the influence of phenomena such as adsorption of biomolecules, cell-cell interaction, formation of biofilms, substrate depletion or excess, etc. These characteristics also allow the use of microdevices for process intensification, especially for multiphase processes [46]. Since a lower consumption of sample and reagents is used, and smaller laboratory space is required, even for the parallelized platforms, a reduction in cost of this development stage is also generally achieved. Microsystems can also contribute to quality-by-design (QbD) by enabling continuous production in the same microreactors used for reaction screening and optimization, through a scale-out approach [46], [47]. The miniaturized platforms and corresponding scale-up strategies towards an industrial process will however vary from field to field. Therefore, the development of single-unit microfluidic platforms, with the above-mentioned characteristics, which can also be easily inter-combined according to the needs of each process, would greatly decrease the equipment cost of this developmental stage. Microfluidics has been applied to cell cultures and fermentations in

the form of microbioreactors, with interesting results and challenges, as can be observed in the reviews written by Schäpper *et al.* in 2009 [52] and Lattermann and Büchs in 2015 [58], but also to biocatalysis enabling improving yield and/or biocatalyst activity and stability, as presented in Asanomi *et al.* (2011) [59], Wohlgemuth *et al.* (2015) [47] and Gruber *et al.* (2017) [60].

Microfluidic systems can accelerate first stage parameter optimization besides biocatalyst/ cell strain characterization and screening. It is however important to take into consideration that there are still differences in phenomena which must be considered when scaling up the optimized parameters. Furthermore, current microfluidic devices, except droplet microfluidic systems [61], still cannot rival with the screening capacity of most microtiter plate systems, especially when supported with robotic fluid handling equipment [46]. Also, due to the decreased dimensions, the available liquid volume for sampling is limited and thus the integration of sensors previously validated using standard analytical equipment is of upmost importance in these systems. Mathematical and fluid dynamic simulation tools could ease the scaling-up from microfluidic systems, by providing a good understanding of the phenomena occurring at both scales and allowing a faster testing and validation of the key operating parameters to consider when scaling.

On the other hand, the small sampling volume required for the integrated sensors can also be used for on-line sensing of processes in larger vessels [62], [63], [64], [65]. However, the type of sample that needs to be handled might require pre-processing due to the presence of contaminants or particles that lead to channel clogging. When pre-treatment is not possible, both the integrated sensor and microchannel need to be resistant to biofouling. Biofouling can be decreased by varying the surface charge or by covering the channel surface with excess of a molecule that does not participate in the process (e.g. proteins like Bovine serum albumin (BSA)). Another issue with detection systems that require biomolecules or dry reagents to achieve target detection is shelf-life of the molecules and reagents in immobilized form before denaturation or degradation occurs, which will, in turn, limit the life-time of the final device. The use of materials with low vapour transition rates for dry reagents, and the encapsulation of the biomolecules within biocompatible polymers can increase these platforms shelf life. A review by Gernaey *et al.* (2012) [56] offers further points to consider as well as improvements to introduce into microfluidic platforms towards a better fit in the biotechnological field (especially fermentation and cell culture). Some of the key points involve: (i) standardization of world-to-chip and chip-to-chip connections, (ii) improved connectivity to benchtop analytics, as well as (iii) the need for improved integrated online sensors and process control software, which is tested and validated in the target industrial environment, and (iv) devices capable of coping with rapidly changing environments in order to better mimic processes at larger scales [56].

1.1.4 Past ideas and current state of microfluidics

Most of the major developments in the microfluidics field foreseen in 2004 by Erickson and Li [5], such as decreased dependence on external equipment towards higher portability, and an increased use of simulation and modelling for device design optimization in the initial stages of device development, still remain to be achieved. Even though a decreased reliance on external equipment was obtained for some applications, most systems still rely on external pumps,

potentiostats, manual/automatic external sample pre-treatment, microscopes, power sources, etc. A higher number of fabricated microfluidic devices are currently being studied by means of mathematical and numerical tools, such as Matlab® and computational fluid dynamics (CFD) [66], with the aim of reducing development time. CFD allows the visualization of spatial distribution of flow velocity, the generation of substrate gradients, as well as the simulation of dynamic flow [6]. These software tools have contributed to a considerable progress in recent years in accommodating the challenges faced when modelling at this scale. However, the lack of standard analytical tools at microscale often hampers the experimental validation of the numerically predicted phenomena. Thus, without proper experimental validation, it is often difficult to convince the user of microfluidic devices of the legitimacy of simulation results.

1.2 The challenge of integration

The integration of several unit operations at microscale was initiated together with the microfluidic fabrication field at the end of the 1980's (e.g. fluid displacement [67], sensing and separation [68], [69], [2]). The semiconductor industry investigated the development of monolithic miniaturized components called micro-electro-mechanical systems (MEMS), such as sensors, valves, separators and mixers, due to the discovery of a suitable material, silicon [70]. The development of MEMS systems was further enabled by the outsourcing of the semiconductor production to the upcoming Asian countries, which allowed to free the existing semiconductor production capacities for research purposes [71]. Miniaturized components based on polymeric materials were also developed, with the appearance of soft-lithography methods [72], [73]. The coupling of several of these components proved however to be technically complicated. The main reason behind this was the choice in fabrication technologies of the individual components, which were usually incompatible [2], as well as the design of both the channels with different dimensions (leading for example to disparate required flow rates for different components) and connections between platforms (mostly un-standardized). Therefore, simpler approaches, applying bench scale equipment (external pumps, microscopes, etc.) were pursued to facilitate the development of individual unit operations [74]. Consequently, in order to reduce the dependency on external devices, the effort towards the development of stand-alone microfabricated devices has recently increased.

A microfluidic platform consists of a set of microfluidic elements, each previously and individually validated, capable of performing a given fluid handling or sample treatment/measuring step (unit operation). Ideally, these unit operations should be capable of being combined and assembled differently depending on the final application [2]. The integration of various unit operations on a single chip requires a holistic understanding of the characteristics of the substrate materials, the available or possible fabrication technologies, the characteristics of the target sample, the chip's final application and the environment in which it will be applied.

The material(s) composition of a microfluidic system is chosen according to the platform's required function, degree of integration and application [75]. Characteristics such as air permeability, biocompatibility, nonspecific adsorption, surface functionalization, optical

transparency, flexibility, solvent compatibility, electrical compatibility, and opportunity for sterilization are considered when choosing a material for a specific application. Material properties also influence the fabrication process and the minimum attainable feature dimension [76]. The robust and leakage free integration of different materials in the same platform is a further challenge [77]. The most frequently used materials can be divided in three categories: inorganic, polymeric, and paper, and a summary of their characteristics is presented in Table 1.

The selection of the fabrication technique is dependent on the choice of materials, the final application of the device, how robust it needs to be and whether or not reusability is required. The choice is also dependent on the type of end user (experienced or not), location of use (point-of-care vs. research laboratory, for example), and the time between fabrication and use (is storage required?). These characteristics will guide the choice of the fabrication methods, from a wide variety available for the production of microfluidic devices. These include prototyping techniques (such as hot embossing, injection molding and soft lithography) and direct fabrication techniques (such as thin film deposition, laser photoablation, photolithography/optical lithography and etching). Furthermore, the choice of a fabrication method takes into account the desired minimum feature dimensions, surface roughness and aspect ratio of the channels, as well as the tolerances and reproducibility of the method, the selected chip material and the final application. For more complex applications, compatibility between different fabrication methods should also be considered during the selection. Heckele *et al* (2003) [78], Ziaie *et al* (2004) [79], Becker and Gärtner (2008) [80], Wu and Gu (2011) [29], Iliescu *et al* (2012) [81], Cheng *et al* (2012) [82], Li *et al.* (2012) [83], Ho *et al* (2015) [84] and Au *et al* (2016) [28] present a good overview of past and current fabrication techniques, and also discuss the main considerations related to the selection of the different methods. A summary of fabrication techniques applied to polymeric substrates is presented in Table 2.

Table 1 –Materials used for microfluidic platforms and their main characteristics [2],[29],[75],[81],[83],[85],[86],[87],[88],[89],[90].

	Inorganic	Polymer	Paper
Material	e.g. Silicon, glass, low-temperature co-fired ceramics (LTCC)	e.g. Polydimethylsiloxane (PDMS), Polyfluoropolyethers, Poly(methyl methacrylate) (PMMA), Polystyrene (PS), Cyclic-olefin copolymer (COC), SU-8	e.g. Whatman no. 1
Fabrication strategies	Batch	Batch or continuous	Batch
Fabrication techniques	Semiconductor industry techniques (etching, lithography, bonding, powder blasting and chemical or physical vapor deposition)	Hot embossing, injection molding, soft lithography, thermoforming, laser ablation, micromachining and photolithography	Inkjet and solid wax printing obtaining hydrophilic channels bound by hydrophobic barriers and either sealed with thin polymer sheets or left open
Smallest dimension	< 100 nm	< 1 µm	~200 µm
Material cost	High	Low	Low
Fabrication cost	High (during development) Low (during mass production)	Low (except for prototyping in the case of injection molding and thermoforming)	Low
Channel characteristics	Hydrophilic, charge stable, defined walls, limited 3D capability	Generally hydrophobic, channel definition dependent on polymer and fabrication strategy, moderate to high 3D capability	Amphiphilic, not very defined channels, moderate 3D capability
Surface functionalization	Yes	Yes	Yes
Integration	With electronic systems (e.g. for data acquisition) or electrodes (for detection)	With electrodes (by deposition onto polymer)	With electronic and magnetic systems, and electrodes (by containing electrical conducting inks)
Combination with other materials	Glass and polymers (transparent materials)	Glass, silicon, other polymers	Electrical conducting inks, carbon or metals (silver, gold, etc.)
Functional elements (e.g. valves and pumps)	Yes (complex fabrication)	Yes (simple to complex fabrication depending on technique)	Yes (simple fabrication)
Advantages	High chemical stability, known surface and insulating properties, high thermoconductivity, high aspect ratio channels	More resistant to mechanical shock, high to low oxygen permeability, easy bonding strategies, less stringent cleaning techniques, disposability, biocompatibility, transparency to most wavelengths	Highly porous matrix, fluid flow through wicking, low cost, easy reagent storage on channel (by dried spots), easy assembly of multiple operation units (e.g. sample metering, filtering and separation), disposability, visual readout
Limitations	High cost of development and fabrication, fragile, low oxygen permeability, requires annealing at high temperatures	Low to high resistance to organic solvents, water evaporation	Challenging precise liquid handling, sample retention during transport, relatively high limit of detection (LOD), limited detection techniques
Commercial availability	Yes	Yes (genetic and molecular biology analysis, protein crystallization, immunoassays)	Yes (mostly qualitative output)

Table 2 - Summary table of the characteristics of the main fabrication strategies used for polymeric microfluidic devices [78], [79], [80], [84], [91], [92], [93], [94].

Fabrication process	Description	Throughput	Surface roughness	Material choice	Cost	Replication	Characteristics
Photolithography	Exposition of a polymeric surface using a laser or UV light	limited	Low	High	Low to high	Medium to high	-
Stereolithography	Exposition and polymerization of a liquid resin, forming 3D structures		High	Limited	Medium to high	Medium to high	3D fabrication with no additional mechanical process steps
Laser ablation	Removal of a defined amount of material (depending on material type, laser wavelength and intensity/ tool size and velocity	Good (fast techniques)	Medium to High	High	Low to medium	High	Surface chemistry and charge are changed in the process
Micromachining				High	Low to medium	High	-
Hot embossing	Application of a pattern (via a stamp) onto a polymer heated just above its glass transition temperature	Good (fast techniques)	Low	High	Low	High	Low stress replication of nanometer structures
Injection molding	Injection of a heated polymer in a mould with the desired microfluidic structure			High	Low	High	3D objects fabrication with no additional mechanical process steps
Casting	Pouring of a heated polymer into a mould with the desired microfluidic structure	Limited	Low	High	Low	Medium	Allows manufacturing highly complex structures (e.g. pumps and valves), using thermoset resins containing metal powder is possible to fabricate embedded electronic components by casting
3D printing	*In situ* polymerization by layer-by-layer focusing if a laser on a photopolymeric liquid or powder resin or bonding of multiple polymer, metal or ceramic laser cutted layers	Limited	Medium to high	High	Low to High	Low to High	Requires expensive equipment; thickness of each layer during fabrication depends on resolution of the stage; allows re-use of left-over polymer

Along with the choice of the material and the fabrication technique, the type of microfluidic platform needs to be considered in advance, such as: (i) single or multiple unit operations on the same chip; (ii) single platform or part of a platform; (iii) integrated quantification and fluidic handling or connection with external equipment; and, (iv) how to perform data and signal acquisition and treatment.

When considering connectivity of the microfluidic chip, several other aspects should also be taken into account: (i) disposability of the device; (ii) to which devices it will connect; (iii) inlets positioned in-plane or perpendicular to the chip; (iv) should it be application-specific; (v) area occupied by connections; (vi) fabrication process; (vii) pressure and temperature tolerance; (viii) compatibility between materials used (e.g. solvents as target detection solutions); (ix) dead volume generated in the connections; (x) sterility; (xi) permeability; (xii) type of sample; and, (xiii) price [81]. Microfluidic interconnections need to provide a low pressure drop and dead volume and hermetic seal, coupled with a reliable performance under multiple uses [95]. Manually fabricated connections may not be built reproducibly, and are thus adding variability to the flow or the operation of the system. The adoption of a standard size inlet diameter, that allows the use of finger tight fittings and standard tubing, facilitates interconnection with other platforms using the same type of connectors, as well as connectivity to most external equipment (HPLC devices and mass spectrometers [96] or Raman spectrophotometers [97] as well as syringe pumps).

1.2.1 Available unit operations in microfluidic chips

To guarantee a wide applicability of modular microfluidic platforms it is essential that the relevant unit operations to most applications are available, and exist or can rapidly be made in such a format. In general, a "plug-and-play" system should contain the following elements:

- **Fluid handling unit**: Such a unit could function as a pump, allowing appropriate flow of the sample in the system, with good control of flowrate and type of flow, ideally allowing a range of possible flow velocities. Another important fluid handling function is a valve system, especially a multi-port valve that enables the control of fluid introduction and followed path inside the system. Sabourin *et al* (2013) [30] developed a very interesting system where liquid handling is automatically achieved with miniaturized and integrated pumps. Other groups decided on a simpler approach such as a magnetically actuated stirrer-based micropump [98], valves actuated by tightening a screw [99], using a Braille display [100], or even capillary forces [101]. Oh *et al.* (2012) presented an interesting guide on design of microfluidic networks to ease fluid handling [6]. Electroosmotic flow (EOF) offers an interesting alternative to pressure driven flow, where the flow front has a flat profile, being capable of generating high flowrates without moving parts [102], [14]. It has been widely applied in bioassays, drug delivery, fuel cells, sludge treatment and microelectronic chip cooling [14], [103].
- **Mixing/dilution unit**: Mixing is an extremely important function when performing reactions or studying the influence of certain compounds, since it needs to occur faster than the reaction effect being studied in order not to influence the outcome [104]. At microscale, mixing occurs mainly through diffusion, but certain strategies can be adopted to improve mixing efficiency. Significant mixing strategies involve passive approaches

which are based on the generation of chaotic mixing with channel bends or topology in the channel [104], or in increasing the contact area between samples via lamination or intersecting channels [105]. Diverse active mixing strategies, such as acoustically-induced microstreams, dielectrophoretic micromixers, electrokinetic actuation [14], velocity pulsing and magneto-hydrodynamic flow have also been thoroughly developed and applied [105].

Mixing can also be performed in order to achieve gradients of certain components through dilution. Niu *et al.* (2011) developed a droplet-based platform capable of performing dilutions within a range of four orders of magnitude by splitting and (re)merging droplets to create reagent gradients [106]. Rho *et al.* (2016) used peristaltic mixing in controlled volume microreactors to generate stepwise concentration gradients of two reagents [107].

- **Sample concentration unit**: This is especially critical for applications that involve extremely diluted samples [77], from water quality testing to detection of cancer cells or viruses in blood. Also, in the human body the physiological concentration of considerable compounds is in the order of nM or lower, thus requiring pre-concentration units for detection. Several strategies involve adhesion of the molecules or cells to the channel walls, which can be functionalized [108] or not [109], using chaotic flow induction to increase enrichment performance. Recently, Pereiro *et al.* (2017) developed a fluidized bed microreactor capable of capturing bacteria from liquid raw samples (e.g. milk) using functionalized magnetic beads [110].
- **Filtration/ purification unit**: Units capable of removing contaminants, or separating cell debris or types of cells from the sample are highly valuable as sample treatment units. Strategies applied to sample filtration/ purification use differences in (i) size (e.g. using capillary forces in a microchannel integrated micropillars (MIMPs) chip to separate plasma from blood [101] or simultaneous isolation of multiple antibodies from serum and multiple cell types from blood using microbeads [111]), (ii) functionalization of channel surface (e.g. with avidin and treated with antibodies conjugated with biotinylated photocleavable crosslinkers with a specific 19-mer DNA sequence to capture cancer biomarkers directly from whole blood [112]), (iii) immunomagnetic separation (e.g. immunomagnetic beads and a micro-aperture chip to separate circulating tumour cells (CTC) from whole blood samples [113]), (iv) adhesion to silica (e.g. extraction of RNA from prepared rat tissue samples using a porous silica monolith column [114]), and (v) solid-phase extraction (e.g. using cation exchange resins [115]).

Concentration and filtration/purification units often function as the same unit, since by isolating or separating a target cell/particle/molecule, its concentration from the initial sample is achieved.

- **Sorting unit**: Besides the ability to isolate a target molecule or cell from a complex sample, it might also be required to differentiate among the purified molecules or cells for a certain characteristic, for which sorters can be used. This is especially relevant when establishing protein or genetic libraries or developing mutants. Sorting of molecules, cells, particles or droplets can be performed using electrostatic actuation (such as, dielectrophoresis [116], [117], [118] or electrostatic charging [119]), optical approaches

(such as optical tweezers or traps [120] or fluorescent activated cell sorting (FACS)), mechanical approaches (e.g. with membrane valves [121]), acoustic approaches (e.g. surface acoustic waves [122]), magnetic approaches (e.g. magnetophoresis or magnetic activated cell sorting (MACS)), channel topography [123], inertial or hydrodynamic focusing or affinity approaches [124].

- **Sample amplification**: Such a unit may enable working around the issue of highly diluted samples, allowing to replicate the target molecules (e.g. DNA or mRNA) [77]. However, the issue of retaining or capturing such molecules remains. Most amplification units perform polymerase chain reaction (PCR) either in chambers (e.g. reverse transcription PCR (RT-PCR) using a thermoelectric Peltier element for temperature control during amplification [114]) or continuously in channels (e.g. real-time PCR of single-DNA per droplet in a circular channel design with zones at different temperatures [125]). Other amplification techniques such as multiple annealing and looping-based amplification cycles (MALBAC) [126] and nucleic acid sequence-based amplification (NASBA) [127] have also been miniaturized in microfluidic devices.
- **Incubation unit**: Such a unit can either work as a reactor, allowing a certain reaction to occur for a defined residence time, a labelling unit, or even as an incubation chamber, allowing growth of organisms. This type of unit requires an excellent control of volume and residence time, and has been extensively used together with droplet microfluidics or single-cell platforms. Several droplet microfluidic platforms present incubation units, which are chambers where the cells or droplets are stored [128], [129] or long channels that allow for a tight control of incubation (residence) time [117].

Strategies for other sample pre-treatment units are presented by de Mello and Beard (2003) [130], Chen and Cui (2009) [131] and Huang *et al.* (2002) [132].

- **Detection unit**: Quantitation of target compounds is one of the major functions and advantages of microfluidics, due to the variety of available sensors, which offer a possibility for real-time and continuous monitoring and proximity to the samples. An overview of the different types of available sensors for microfluidic applications is presented later in the text, but the variety of available sensors ranges from dielectric (e.g. determination of size, shape and composition of droplets at high speed [116]) to optical (e.g. recent application of stroboscopic epifluorescence imaging to hundreds of droplets simultaneously [133] or surface-enhanced Raman scattering (SERS) detection of hazardous materials [134]) and even nano-wires (e.g. nanoribbons capable of performing the detection of multiple biomarkers simultaneously [112]).

The presented list of existing microfluidic chips capable of performing the most relevant and essential unit operations in any screening, optimization or development study is not exhaustive. There is a multitude of approaches for solving pre-treatment and sample concentration issues for example, that with little or no modification could be coupled and/or integrated in a modular platform. By combining the different presented microfluidic systems, most processes in the biotechnological and health fields could be studied on-chip in a flexible "plug-and-play" approach.

A wide application of microfluidics can be achieved if not only modularization, but also standardization of connectors is achieved. Connectivity between the above units could be attained with some of the connectors and interconnectivity ports presented in Pepper *et al.* (2007) [33], where "click on" connectors to standard tubing sizes were developed, and Sabourin *et al.* (2013), which developed multi-connector ports. Connectivity to electrical interfaces could be carried out as presented in Yuen *et al.* (2008) [34], who based their design of fluidic and electrical connections on an electrical breadboard. Adaptation of the above units to the building block concept introduced by Rhee and Burns (2008) [35], Langelier *et al.* (2011) [38] and Vittayarukskul and Lee (2017) [39] would further increase the flexibility and potential of the modules as part of a multi-use "plug-and-play" platform. A set of building blocks that can be arranged in a multitude of different channels and even 3D shapes could be acquired by every research institute, company or diagnostics center, for easy assembly towards their target research. The building blocks could be available together with a simple set of miniaturized electronic components (e.g. pump, charge-coupled device (CCD) imaging technology, potentiostat) that function both as part of the fluidic and detection units, but also as user-friendly validation units for the assembly. For applications that require a higher degree of validation, such as biomedical applications, more complete individual unit blocks could be used.

A concern in the use of a modular approach is the accumulation of fluidic resistance with each module, which can affect flow (and thus downstream) performance and lead to the loss of reagents or involved particles/cells [3]. However, there are several strategies available to reduce pressure drop (e.g. division of flow in different channels) and fluidic resistance (e.g. surface modification towards high hydrophilicity). Furthermore, diverse flow generating strategies (e.g. electroosmotic or capillary flow) could be applied in combination with pressure-driven flow. Also, modules to control backpressure in the pumps, or facilitating pressure equalization along the module assembly, can be integrated.

It is also relevant to highlight the importance of applying mathematical modeling and fluid dynamic simulation to the first stage of development of individual fluidic parts [74]. Such tools can help boost the development progress of microfluidic platforms [135], by aiding in geometry optimization, evaluation of transport phenomena, determination and prediction of reaction (kinetic) parameters and mechanisms and in analyzing experimental data [135]. Modelling provides a more targeted and therefore often more efficient strategy of device development and sensor design, which can result in faster, less wasteful, and more economical device development processes [66]. It also provides information for evaluation and choice of materials (either by modeling interaction between materials, absorption of molecules on the surface or elucidating the influence of properties such as, for example, thermal coefficients). The development of numerical simulation tools with a simple user interface might also contribute to spreading the use of microfluidics to other fields (e.g. environmental sampling, resource recovery, structural analysis of soils or buildings, etc.), including transferring their use to non-microfabrication specialists [74]. As suggested by Chiu *et al.* (2017), the assembly of the building blocks of a modular microfluidic system could be guided by software, taking into consideration both the requirements of the specific application along with the characteristics of the available building blocks [3].

Most modelling approaches applied to microfluidics assume a discretization of the continuum approximation of Navier-Stokes equations to describe flow and phenomena at the microscale through finite difference/volume/element or boundary element methods [47]. Computational fluid dynamic software such as COMSOL Multiphysics® (Burlington, MA, USA), or ANSYS CFX (Canonsburg, Pennsylvania, USA) are used for description of fluid flow in micrometer channels [136]. This, however, cannot appropriately describe phenomena occurring at the molecular scale (such as, for example, chemical bond interactions). As the dimensions of the channels decrease from micrometer to nanometer size, the continuum model no longer holds [136]. The use of hierarchical multi-scale modelling might improve modelling of the involved phenomena (mainly, molecular interactions and biochemical processes) in the reactions/processes performed in microfluidic systems [136], [137], [47]. Hierarchical multi-scale modelling involves the association of the mentioned macroscale methods with atom-based models (within which atoms and molecules are interacting points whose position and velocity is described by a vector, such as in the Molecular dynamics simulation model [136]) and particle-based models (that assume clusters of interconnected particles to simulate molecules or fluid according to a distribution function governed in time by discrete Boltzmann equations, such as in the lattice Boltzmann method) [136], [137], [47].

1.2.2 Considerations regarding materials used in microfluidic systems

One of the attractive features of polymeric materials for diagnostic platforms used in biomedical and clinical applications is their disposability due to their low fabrication cost [74]. These attributes decrease the risk of user contamination when handling potentially dangerous samples or of substances being analysed erroneously due to sample carry-over. However, for most applications in other fields, where contamination issues can be easily solved or are less critical, the use of disposable devices will lead to the generation of unnecessary and possibly difficult to handle waste (most materials used in microfluidic platforms and microsensors are not biodegradable [138]). Furthermore, most microfluidic platforms consist of a variety of materials (including e.g. heavy metals and other compounds potentially toxic to the environment) assembled in an irreversible way or that is difficult to separate, thus increasing the difficulty in disposing of such devices in an environmentally sustainable way. The academic and industrial community should seek to develop multiple use platforms in such situations, as well as invest in biodegradable or transformable/reusable materials, especially when many microfluidic platforms may be used (e.g. screening of enzymes or process parameters). Zein (a prolamin protein from corn), poly (lactic acid) (PLA) [139], silk fibroin and gelatin are examples of biodegradable materials that can be used to fabricate microfluidic devices [138]. Zein has great potential as a plastic substitute [138], [140], [141], [142] since it is biodegradable and can be produced from the excess in the corn industry, adding value to a traditional bioethanol production process and also reducing waste in industry [143]. PMMA is another promising material to obtain “green microchips” since it can be reused after decomposition to methyl methacrylate (MMA) at high temperatures [144].

To conclude, besides the effort to use alternative, more environmentally friendly and/or reusable materials, the microfluidic community should strive to build easily disassembled devices. This would facilitate the reuse or disposal of the different parts of microdevices towards

decreasing the possible environmental impact that an intense use of this technology might bring.

1.3 A guide to the development of stand-alone platforms

In order to develop a stand-alone multi-unit operations microfluidic platform, compatible with a wide range of applications, several considerations should be made. To illustrate the complexity of such endeavor, a guide for the development of a single unit operation microfluidic system is presented here.

In this work, the chosen unit operation is sensing, focusing on biomolecules and/or biological components, due to its relevance and variety of detection techniques. If microfluidic platforms are to be used widely, the integration of sensors and their validation as quantitative detection systems is of major importance. There are three main detection methods used in microfluidics: optical methods, electrochemical methods and mass spectrometry methods, of which optical and electrochemical methods are the most applied due to their selectivity and sensitivity. Other methods involve techniques such as nuclear magnetic resonance (NMR) spectroscopy and mechanical detection (e.g. quartz crystal microbalance (QCM) sensors or microcantilevers) [74]. Within each detection method there are several techniques, whose usefulness or applicability is highly dependent on the desired function of the device and where it will be integrated. Table 3 presents a summary of the main characteristics to consider when selecting a detection method for integration in a microfluidic platform.

Recently, even though new sensing technologies are discovered every year, there has been a shift in sensing research towards more efficient and hybrid integration of the sensing approaches by further developing already existing and validated sensors [145]. The combination of different sensing technologies on the same device can widen its application, by increasing the number of targets it is able to monitor and/or quantify simultaneously.

Table 3 – Summary of the leading detection systems available for microfluidic applications. Integration capability is here assumed as the ease of miniaturization of the sensing system itself in order to be integrated inside any or most microfluidic structures. Portability relates to the miniaturization of required auxiliary equipment to perform the measurement (e.g. potentiometer, microscope, etc.).

Detection method	Advantages	Challenges	Integration capability	Portability
Optical	Fast response; High sensitivity; Compact; Usually contactless; can allow for real-time monitoring and spatially resolved imaging;	Usually dependent on microscopy equipment; May require labelling;	High	Usually low, but can be high if CCD cameras or mobile phones are used
Electrochemical	Can allow for real-time monitoring; can be applied to most biological and chemical samples; potentially low costs in terms of fabrication;	Requires the presence or generation of an electroactive species; difficult miniaturization of measurement equipment; short shelf life of most biosensors; requires control of ionic concentrations pre-experiment;	High	Medium, if measurement systems are miniaturized
Mass Spectrometry	High sensitivity and selectivity; very low detection limits; can be label-free; requires low electrical operation power;	Long analysis time; bulky detection equipment; extensive sample preparation;	Low	Very low
Magnetic	Highly specific (reduced sources of magnetic behaviour in nature, for magneto-resistive sensors); allows for studying behaviour of atoms and molecules (in the case of NMR); No need for optical accessibility (in the case of NMR);	Requires labelling of the target samples and/or very strong magnets; requires expensive fabrication methods; limited reaction time scale (for NMR);	High	High, if measurement systems are miniaturized [146]
Mechanical	Usually label-free detection; sensor integration performed during fabrication (monolithic);	Sensitive to damping effects in the presence of liquid; long detection times; Complex fabrication	High	Medium to high, if measurement systems are miniaturized

The scheme in Figure 4 illustrates the major steps to be considered during the development of a new system for sensor integration. This scheme is divided in 3 steps:

- Step I - development of the system's concept: It is addressing a current need (of a potential client, a clinically relevant analytical device or a research project) and involves the preliminary design, literature research for current technology, and preliminary concept tests in the laboratory. The concept of the device should be concurrent with existing regulations in the field of application, especially when food or health related applications are planned (e.g. highly regulated by the Food and Drug Administration [FDA] and European Medicines Agency [EMA]). Further regulatory issues will not be considered here due to the complexity and variety of the subject. It should also take into consideration the end-users and their requirements for the device [147], [148]. The more general the "need" identified, the more challenging the design of the system, but a wider use microfluidic chip might be achieved. In Figure 4 we use two specific hypothetical examples (monitoring of blood glucose levels in real-time and inline monitoring of glucose concentration in a reactor), but a more generic need could be the development of a system that is adaptable for the online monitoring of several components;
- Step II – Sensor choice and fabrication: It includes an iterative choice and test of the sensor approach (and design) that is best matching the need defined in Step I, as well as the selection of chip material and fabrication method. These choices are often limited by the available technology and materials, as well as their cost of operation and use.
- Step III – Sensor integration: It involves the assembly of the final system for integration of the chosen sensors, based on the desired final application and type of device operation.

The type of integration strategy should be defined from the concept step (step I), since it can limit the used materials or fabrication methods. At this point, further improvement or alterations of the components (developed during step II) of the prototype might be required. Since the final goal is the commercialization or wide use of the device, scaling of fabrication towards mass production should also be considered during development of the prototype.

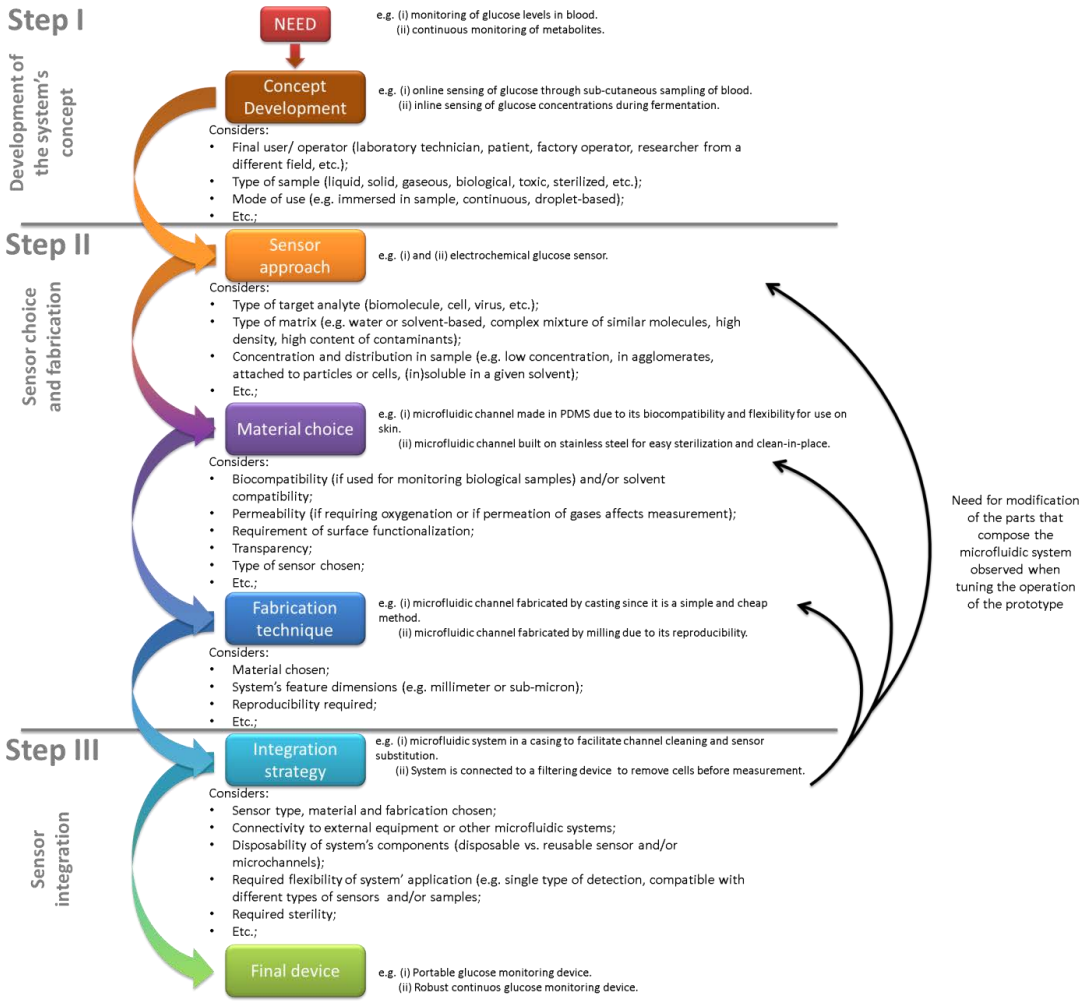

Figure 4 – Decision analysis cycle scheme for developing microfluidic systems for sensor integration, and its application to two hypothetical case studies: (i) a hypothetical portable glucose electrochemical sensing device and (ii) a hypothetical inline glucose monitoring device.

It is important to highlight the need to take a holistic approach to device design, as well as the relevance of thinking about connectivity to other systems during the design phase. When developing a multi-unit operation platform or a system compatible with other multi-unit

operation platforms, these steps should be followed first for each unit operation, and then for their consecutive integration with each other, until the whole-platform integration is achieved. All the time, one should keep all the considerations presented in Figure 4 (e.g. final user, type of sample, location, etc.) in mind.

1.3.1 Guide application to several case-studies:

To illustrate the developed guide, the different steps described in Figure 4 were applied in two hypothetical case studies: (i) a portable glucose electrochemical sensing device; and, (ii) an inline glucose monitoring device. The case studies were included for bringing further clarification of the considerations and decisions involved during the development process of a microfluidic device, and that the decision analysis cycle scheme in Figure 4 intends to facilitate. For each case study, the conclusion of the considerations presented at each step is shown in the figure.

For case study (i), in Step I, the key concept to address is the need for monitoring glucose in blood. This is achieved by defining a device capable of performing measurements in real-time that should be portable and able to draw samples subcutaneously. This concept is achieved by considering the patient as the end user, the importance of constant monitoring of glucose levels in diabetic patients, and therewith of portability, and the best sample format as the blood. In Step II, the development of such a device begins by choosing the best sensing approach, and the appropriate materials and fabrication methods. In the chosen example, an electrochemical sensor is selected due to its ease of miniaturization and the extensive available knowledge on applications of electrochemical sensors for glucose monitoring. Then, considering that the device will be in close and continuous contact with the patient's skin, a biocompatible material was chosen (PDMS). Furthermore, when using some biomolecules, such as the enzyme glucose oxidase, if certain mediators are used, oxygen is required for the reaction and can also be used as a target analyte. Therefore, the use of PDMS is further highlighted due to its permeability to oxygen. The choice of material and the dimensions of the device (also defined in Step I) would then limit the choice of fabrication methods, together with the available methods for the device developer. Finally, in Step III, the combination of the different already described parts (through the use of a casing for easier re-use or substitution of sensors or channels) and the test of the prototype occur.

For case study (ii), the key notion guiding the concept development is the continuous monitoring of glucose in an outlet stream of a lab scale fermenter. Thus, in Step I, the device needs to be robust, withstand relatively high pressures/flowrates, and be easily used by an operator. Furthermore, since the samples contain a complex matrix (media) with organisms, the system needs to be able to withstand sterilization and be connected to a sample pre-treatment device, where biomass is removed to minimize fouling of the sensors. In Step II, an electrochemical sensor is selected due to its price (in case substitution is required due to fouling) and straightforward connectivity and monitoring with electrical interfaces. Then, due to the required robustness of the device and compatibility with cleaning-in-place procedures, stainless steel is chosen as the platform's material. This limits the available fabrication techniques, of which milling offers a relatively lower cost and device completion time. In Step III, the combination of the different components is achieved, with the test on the device's robustness,

the influence of biofouling on sensor performance, as well as the capability of sample pre-treatment to reduce this effect.

1.3.2 Further deliberations

The discussed case studies allow for a clear presentation of the suggested guidelines. However, they are a simplification of real applications of the described devices.

In reality, the extremely strict regulations involving health applications would further limit the types of structures, materials and fabrication methods in the case of case-study (i). A close collaboration between microfluidic developers, physicians and health regulation agencies could be established (such as ISO 13485:2016 for Medical Devices) in order to satisfy demands related to both health safety and patients' quality of life. Regarding case-study (ii), the integration of such a device might be easy to implement into a laboratory scale reactor, as presented, but the final goal would always be its use in pilot or industrial scale reactors. For such larger scale reactors, once again, tighter regulations exist, mainly related with the existing inlets for the reactors and the costs associated with the potentially necessary modifications. These more rigid regulations would very likely add additional iteration steps in the development of the platforms.

Furthermore, simply fabricating more easily connected devices might not be enough to increase their use in the market. As previously mentioned, their validation with currently used analytical methods, which can vary greatly across fields, is of upmost importance to gain trust from the stakeholders (the final customers and/or investors). A wide or multi-use device would have to be validated by all analytical methods commonly used in each specific field, which due to its characteristics, namely dimensions, might be challenging to achieve, and should therefore also be considered as a main objective from Step I. Once validated, such device could in turn become a reference analytical tool of the field, with a simpler application and a lower price. Microfluidics can become an interesting analytical tool, more accessible to the general public, both in terms of cost, portability, and footprint, but also in terms of simplicity of use.

Additionally, it is relevant to highlight that the end-user plays an important role in the development of microfluidic platforms. When the final user of the platform is a patient or someone with little to no-training in the technology or field in question, the device needs to be not only easy to assemble, but "fail-proof". This means it should have a robust operation in order to withstand possible operation errors, such as wrong types of samples, labels or reagent concentrations, and present higher number of redundancies and security protocols, being at a high level of developmental maturity. Such a device should provide limited options in terms of operation and minimize required external input (so to minimize errors from the operator), and provide sufficient and detailed protocols and operation guides. Moreover, if samples from the patient are needed (e.g. in the case of diagnostic devices), the sampling procedure should preferably be non-invasive or at least reduce invasive sample as much as possible, and avoid sample cross-contamination (if measurements of multiple samples are required for monitoring of a disease status for example). Such a platform should also provide already treated data, and if possible guidelines of steps to proceed or suggestions of what the data might signify [149]. On the other hand, if the end-user belongs to a research or medical laboratory, or an industry environment, although the same requirements in terms of validation and safety are expected,

the flexibility in terms of operation modes and assembly structures is higher. Also, additional analytical components and a lower or no data processing effort are expected.

1.4 Motivation and project goals

Synthetic chemistry has had a big impact from microfluidics, in particular modular microfluidics, both at laboratorial and industrial scale. Biotechnology, especially biocatalysis, uses similar approaches to synthetic chemistry in reaction and process development, and can thus have a lot to gain from the adoption of modular microfluidic technology as a standard tool. As mentioned earlier, there is a great need in bioprocess development for high-throughput, low cost and automated screening platforms. Microfluidic systems, with their smaller dimensions, high fluidic and mass/heat transfer control, small footprint and high variety of sensor approaches can offer a solution to this need. Furthermore, the presented concept of modular microfluidics can provide an increased flexibility and applicability to the screening microfluidic systems. A microfluidic system that is compatible with different substrates, reactions and operation conditions, as well as capable of association with other microfluidic systems, can greatly extend its usefulness and field of application. The different existing microfluidic unit operations suitable for a "plug-and-play" platform that were reviewed, along with the presented strategies for their integration and novel connectivity approaches illustrate the potential of modular microfluidics as screening platforms, capable of integrating all the required unit operations (e.g. sample treatment, concentration, detection, purification, etc.).

1.4.1 Project goals

The main goal of this project was thus to develop a microfluidic modular platform for enzyme screening with online reaction monitoring and quantification. The platform was designed considering some of the issues identified in microfluidics, such as the lack of reusability of the materials composing most developed microfluidic platforms, and the difficulty in integration between different developed microfluidic systems due to lack of standardization of channel dimensions and connections.

Following the presented step-wise guide (Figure 4) for the development of stand-alone microfluidic platforms, the modular platform was envisioned for application in an intermediary state of screening, when reaction parameters and kinetic mechanisms of a promising biocatalyst are characterized and/or optimized. This platform is intended for laboratory use by non-microfluidic experts, so each of its modules was designed or chosen to allow easy connection to each other or to benchtop laboratory equipment, and be simple to use. Furthermore, each module enables flexible application, meaning it is compatible with different types of reaction and biocatalyst. The developed modules were also, within available material and fabrication technology limitations, designed to allow easy disassembly of the different components, both to facilitate cleaning and substitution of parts, but also recycling or re-use of the different materials and components. The selected materials were additionally both biocompatible and suitable for most functionalization approaches, to increase compatibility with a wide variety of

biocatalysts. The fabrication methods used were limited to the equipment available in the laboratory (laser ablation and micromilling).

The basic modules identified as useful for such a platform are presented in Figure 5.

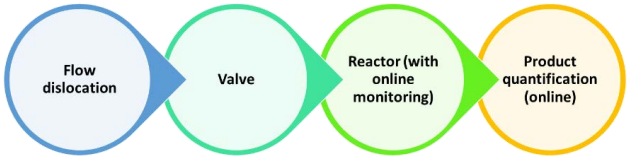

Figure 5 – Schematics of modular platform for enzyme screening.

The final goal was to achieve online monitoring coupled with data analysis for fast comparison between variants or screened reactions, based on data gathered both in the reactor and in the quantification module. Considering the identified basic modules, in such a modular platform, the reactor module should provide insight on the reaction behavior at different residence times (spatial points) in the reactor, while the quantification module was intended for quantification of the target compound and for providing insight on conversion yield and productivity.

A commercial microfluidic system with integrated oxygen sensors was chosen as the reactor module, while the quantification module was developed in-house to allow integration of different types of sensors and sensor geometries and thus be applicable to a wide range of reactions. Between these two modules, a platform for continuous enzyme inactivation, based on temperature, was also developed. This module was designed to guarantee an appropriate quantification and good control of the reaction residence time in between modules, by employing a non-specific method to stop biocatalytic reactions. Additionally, a commercial microfluidic valve was used as a module to enable dynamic measurements or introduction of controlled volumes of compounds. Standardized connectors (HPLC-type connectors and tubing) were used as world-to-chip and chip-to-chip connectivity, hence widening the applicability of the developed modules and the assembled platform. The envisioned platform with the different described modules is shown in Figure 6. Finally, as a step towards online data analysis, all the developed microfluidic platforms and the reactor module were characterized using computational fluid dynamics.

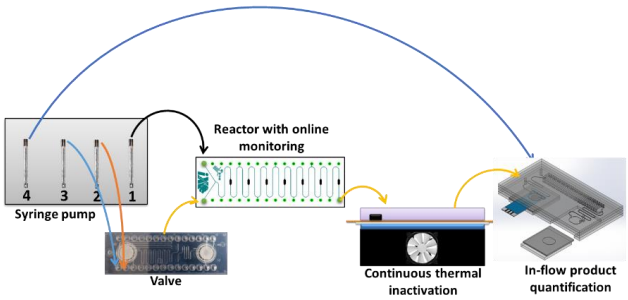

Figure 6 – Schematics of the different microfluidic modules developed for the enzyme screening platform.

1.4.2 Thesis outline

The thesis consists of six chapters, where Chapter 1 includes an overview of microfluidics and the main motivations for the work and Chapter 6 brings the main conclusions of the work achieved and future perspectives for the developed microfluidic modules. Each of the microfluidic modules have a corresponding chapter, each with an introduction more focused on its specific application and state-of-the-art. In each chapter, a materials section is included, and the main obtained results and challenges observed with each module are specified and the main conclusions drawn.

The thesis is thus structured as follows:

- Chapter 1: Introduction to microfluidics, with a particular focus on modular microfluidics. A brief review on physics at microscale, and the main materials and fabrication methods used. A step-wise guide to develop stand-alone microfluidic platforms, which highlights the main considerations to take into account when conceptualizing such a platform, as well as the precautions to take during fabrication.
- Chapter 2: Characterization of the microfluidic reactor module with integrated oxygen sensors using an oxidation reaction with enzymes in solution. The reaction inside the microchannel was also simulated using CFD, which presented a reasonable match with the experimental data.
- Chapter 3: Application of the microfluidic reaction module with integrated oxygen sensors to the screening of dioxygenase variants in whole cell catalysts, as a novel screening tool for an oxidation reaction in whole cell biocatalysts.
- Chapter 4: Development of a microfluidic platform for sensor integration and application with electrochemical sensors to the in-flow quantification and dilution of glucose samples. The dilution channel was optimized based on CFD modelling of different mixing geometries.
- Chapter 5: Development of a microfluidic platform for continuous enzyme thermal inactivation and application to the inactivation of glucose oxidase and catalase solutions. The microfluidic platform's thermal characteristics were simulated using CFD.
- Chapter 6: Summary of the main results obtained from the development and/or characterization of the different microfluidic modules presented. Future perspectives for the further development and potential applications of the developed modules as a screening platform.

Chapter 2

System for monitoring biocatalytic reactions

Biocatalysis is a highly relevant field in biotechnology, with an annual revenue that is expected to reach 400 billion USD by the end of 2017 [49]. Within this field, the enzyme market has grown exponentially from the 1960s and has revolutionized a significant number of products and processes, such as detergents, drug discovery, bioanalytics, organic synthesis and biofuels [150], [22]. To keep up with current market demands new enzymes with higher stability, higher solvent resistance, suitable activity and substrate specificity, and the ability to act on new substrates with high turnover rates are required. Discovery and tailoring of such enzymes involves environmental sampling and generation of variants [49] that results in thousands of enzymes whose industrial or clinical relevance needs to be evaluated. High-throughput techniques are thus highly demanded both for the initial screening of (engineered) variants, as well as for the reaction and process characterization of the most promising biocatalysts. Microfluidics, due to its dimensions and available unit operations, is an increasingly used and valuable screening tool that allows high-throughput and fast screening of the small volume of each generated variant. However, considering the current state of sensor integration and automation in microfluidic-based systems, they are mostly considered for an intermediate stage of biocatalyst screening, when the characterization of more specific parameters is required [46].

In this chapter, a microfluidic system capable, of continuously monitoring oxygen levels, is evaluated as a potential microreactor for application in screening activity and studying reaction kinetics of biocatalysts in solution. Oxidation of glucose by glucose oxidase was performed and allowed to highlight the operational limitations of the system in terms of oxygen depletion at certain enzyme and substrate concentrations. Strategies for *in situ* oxygen generation involving addition of catalase and hydrogen peroxide were likewise applied. Additionally, a calibration curve relating measured oxygen with product concentration at the outlet of the microchannel was performed. The reactions carried out in the microfluidic system were also modelled using computational fluid dynamics, with a good match between the experimental and simulated data, and the results provided extra insight into the reaction dynamics and limitations.

2.1 Introduction

Enzymes are ubiquitous in daily life, from the use in the food (e.g. as food additives) and textile industry (e.g. for bleaching), to the production of bulk chemicals and application in clinical assays [22]. They enable greener and safer production processes (operation at mild conditions of pressure and temperature and with low energy demands), simpler reaction pathways for certain compounds and even production of new molecules, with high turnover rates and substrate selectivity [22]. There is, therefore, a great demand towards finding new biocatalysts. Biocatalysts (and new compounds) can be discovered for instance by terrestrial and

marine microbial sampling, requiring extra steps of isolation, optimization of growth conditions in the laboratory, metagenomics (searching for homology with known enzymes) and activity tests [49], to name a few strategies. New biocatalysts can also be attained through genetic manipulation, constructing functional metagenomic libraries or performing directed evolution, thus generating recombinant biocatalysts that need also to be selected in terms of activity and selectivity towards a target process and/or product [49]. To achieve this, thousands of enzymes and/or cells (in the case of whole cell biocatalysis) need to be screened and new, automated and faster screening procedures are in demand.

2.1.1 Miniaturized systems for biocatalysis and enzyme screening

A strategy to improve the screening efficiency involves miniaturization of the involved technology [22]. Miniaturization has been achieved mainly through two strategies: multi-well plates and microfluidic systems.

2.1.1.1 Multi-well plates

Multi-well plates are polymeric (polypropylene or polystyrene) plates containing usually 6 to 1536 wells with 16 mL down to 10 μL volume, respectively, which are arranged in a 8 cm by 12 cm matrix. They enable screening of up to 10^6 variants on liquid or solid (e.g. agar) media by detection of a chromo- or fluorogenic compound that is produced or consumed in the presence of the target enzyme [22].

It has also been applied to determine kinetic parameters, where substrate concentration, type of substrate, amount of enzyme, etc., can be varied between wells within the same assay [151], [152], [153]. Association with robotic equipment facilitates accurate definition of the concentration range or other varied parameters in each assay [154], [155]. Some adapted trays have been developed that enable single well temperature control and inline monitoring of some parameters through sensor integration in the wells. Individual temperature control, however, is cost-intensive so integrated incubation chambers are usually preferred [58]. The sensors (pH, dissolved oxygen and carbon dioxide concentration [58]) are usually sensor spots based on fluorescent or luminescent detection which are embedded at the bottom of each well [22]. The sensors are evaluated in a matrix by a probe (e.g. optical fiber), and so time-related data obtained depends on the number of samples (wells) being measured and the speed of the scanning probe [156]. Individual well sensor addressing has also been achieved, requiring however more complicated setups [157]. Furthermore, modified microtiter plates, that incorporate a microfluidic network have been developed that enable controlled addition of liquid solutions (e.g. for pH control) through a pneumatic microvalve [157].

In microwell plates, oxygenation and mixing are promoted mostly through shaking, which can lead to mass transfer limitations of oxygen to the reaction taking place. Performed studies have shown that the amplitude and intensity of shaking, the surface (in contact with air) vs. volume ratio and the wells' shape influence the oxygen transfer [22]. Different aeration strategies, such as sparging with air, using square or flower-shaped wells or magnetic micro-stir bars have thus been used [158], [22]. Evaporation is usually minimized in these systems by covering the wells and/or flushing the microwell plate environment with humidified air [159], [157].

Despite the possibility for automation with robotic handling and the variety of strategies employed in microwell plates for improving monitoring and parameter control, the number of parameters that can be monitored continuously is still limited to pH, oxygen, carbon dioxide and optical density. This can limit the scalability of the obtained data due to the lack of proper process overview. The application of mechanistic models can help increasing the level of confidence and applicability of the gathered data [151]. Furthermore, the limitations regarding oxygen mass transfer and evaporation, despite being mitigated with the strategies developed, can limit the application of these systems to certain processes (e.g. using solvents with high evaporation rate, or fast oxidation reactions).

2.1.1.2 Microfluidic systems

Microfluidic systems present a set of characteristics that makes them valuable for high-throughput applications, such as screening of biocatalysts. The reduced dimensions decrease the amount of required reagents and samples, but also increase the surface to volume ratio [160]. This results in increased surface interactions, which are required in many assays (e.g. immunoassays, enzyme immobilization), but also increases contact area between the different solutions, which is highly relevant for example in liquid-liquid extraction and mixing. It also opens the possibility to new assay or reaction geometries and catalyst or reactants positioning inside the channels. Moreover, the small dimensions increase portability of these systems, as well as the ability for parallel operation with a small footprint. Microfluidic systems enable a higher degree of integration (of different components and unit operations on the same chip or of different chips together), which facilitates the development of automated processes [22], [10]. As discussed already in Chapter 1, depending on the material and fabrication method, they can enable a significant cost reduction of the unit operations and the screening platform. Furthermore, the types of available sensors, their integration within the microfluidic system and the type of interactions occurring at this scale can result in a significantly increased sensitivity and a limit of detection hard to rival in macro-devices and microwell plates. Microfluidics also enables studying reactions and/or physical phenomena otherwise impossible, either by allowing a higher control of the environmental conditions (fast mass and heat transport) or by allowing a better control on the phenomena occurring or even eliminating certain effects (e.g. inertial effects) [8]. Another advantage of microfluidics is the freedom and variety of geometries available, which enables taking advantage of the phenomena more relevant at this scale. The main advantages of microfluidics relative to microwell plates are however the possibility for continuous operation [22] and the availability of incorporating a wider range of biosensors.

Microfluidic systems have mostly been applied to enzymes or cell lysates [22]. The simplest approach involves two-inlet microchannels where aqueous solutions of the substrate(s) and enzyme(s) are introduced separately and the reaction occurs along the microchannel [22]. This allows a good control of the reaction residence time (through flowrate selection and length of the channel) and diffusion/mixing of the two solutions (by introducing bends or obstacles in the channel), which can easily be calculated from the equations presented in Chapter 1. In reactions where one of the components has a low solubility in water, two-liquid phase systems can be used by introducing an aqueous and an organic phase or ionic liquid through separate inlets. This approach has also been applied for the enzymatic resolution of chiral compounds [22], or as an

in situ product removal/substrate feeding approach [161]. It is important to consider in this approach how the solvent might affect enzyme activity and stability during operation [60]. Enzymes can also be immobilized (through covalent cross-linking [59], cross-linked enzyme aggregates, (non-)specific adsorption [162], polymer brushes [163]) in the microchannels either by binding to the walls or by immobilization on carriers (e.g. agarose or glass beads), membranes (e.g. nylon, poly(vinylidene)) [59] or monoliths (porous matrices of polymers or silica for example) inside the reactors [22], [150]. Enzyme immobilization improves in general the stability and durability of the biocatalyst [150], but may result in some cases in a loss of activity [60]. Micro-packed-bed reactors have also been developed where the enzymes are immobilized on microparticles and introduced inside a microchamber or a capillary tube, serving as packed-bed reactors [22]. This approach may however lead to increase of backpressure, requiring higher pumping efficiencies.

Multi-enzyme cascade reactions can also be achieved with microsystems by physically separating the reactions in reactors connected in series [60]. This allows a better control of the reaction, especially if the product acts as an inhibitor on the following reaction or promotes undesired side reactions [60]. This spatial separation of the reactions also permits their operation at the optimum conditions for each (temperature, pH, solvent, etc.), thus improving the reaction yield [60]. However, it may be difficult to match the enzyme reaction rates to each other, in order to operate the cascade reaction with the maximum productivity [150]. An enzyme can also be kept in a single reactor, thus avoiding possible side-reactions in the following reactor, either through one of the mentioned immobilization strategies, or by using in-line filtration steps coupled with re-circulation [60]. Enzyme immobilization or retention in a reactor module also facilitates downstream product purification steps, besides enabling a higher degree of control on the reaction space [150]. Furthermore, a simple reversible enzyme immobilization technique would also grant the re-use of the microfluidic reactor and its easy application in a new process [46]. Connection of the reactor modules with chiral columns, solvent extraction modules, filtration and separation systems, allows the exchange of solvents or buffers between reactor modules, as well as removing enzymes and/or products that might affect the next reaction in the sequence, and thus greatly improve the overall yield and productivity [59], [60].

The integration of sensors in microfluidic platforms would facilitate the monitoring and characterization of biocatalytic reactions as well as the optimization of the parameters that fit each and all of the reactions in a cascade system [46]. Of the wide variety of sensing strategies available for microfluidic devices (optical [164], [165], electrochemical [166], mass spectrometry [167], magnetic [168], Raman spectrometry [169], among others [74]), very few have been applied for monitoring and characterization of biocatalytic reactions due to the wide spectrum of generated substrate(s) and product(s) and the need to identify chiral compounds. Quantification is thus usually performed at- or offline with analytical equipment such as high-performance chromatography (HPLC), gas chromatography (GC), mass spectrometry (MS), UV-VIS spectrophotometry and nuclear magnetic resonance (NMR). Even though, miniaturization of some of these techniques (e.g. NMR [146], UV-VIS spectrometry [170], Absorption [171]) or improved world-to-chip connectivity to others (e.g. MS [167], Infrared and UV-VIS spectrometry [170]) have been developed, a simpler approach involves the production of a compound that can easily be detected with existing technology (e.g. optical detection of colorimetric or fluorescent compounds [170]). Another approach, is to monitor the reaction by the change of an operation

parameter which can be directly related to the reaction [46], such as temperature (e.g. exothermic reaction), pH [172], [173] or oxygen [174], [173].

2.1.2 Optical sensing

As highlighted in Chapter 1, and mentioned in the previous section, there are several detection methods that can be applied in microfluidics. Optical detection is one of the most extensively used, especially towards biological applications. Optical-based sensors present several attractive characteristics, such as fast response, compactness, high sensitivity and the possibility of contactless measurement [74]. However, for more complex and dense matrices found in biotechnological or medical applications, and auto-fluorescent or light responsive materials, their application can become difficult or strictly limited. Optical methods can be separated into methods that comprise direct detection by monitoring the light properties, and the detection of modulation of such properties.

Direct detection can be achieved through:

- Fluorescence emission of fluorophores or fluorescent dyes that label the target analyte when excited by a given wavelength is a type of direct detection method. It is a highly sensitive and selective detection method that requires target sample labelling and is the most common method used for biological samples. Fluorescent detection is sensitive to interferences from the sample matrix, thus usually requiring sample pre-treatment [170]. It can also present sensitivity to certain materials (namely polymers) used in microfluidic systems, which present auto-fluorescence;
- Absorbance measurements occur by monitoring the attenuation of a specific wavelength of incident light by absorption by certain functional groups when crossing the sample [170]. It is usually achieved through the use of optical fibers connected to a benchtop absorbance spectroscopic equipment and integrated microlens and slits to extend the optical path. The simplicity of absorbance measurement instrumentation overcomes its lower sensitivity relative to other optical methods (e.g. fluorescence) for application in point-of-care [175], when the range of the target analyte is within the detection limit of the absorbance equipment;
- Luminescence-based methods are characterized by the entrapment of a luminescent probe in a matrix. The analyte permeates through the matrix affecting the emission signal of the probe, which is monitored [176]. A more extensive description of luminescent detection is provided in section 2.1.2.1.

Detection due to modulation of light properties includes:

- Surface plasmon resonance (SPR) detection is based on resonant oscillations of conduction of metallic electrons (e.g. gold or silver) when coupled with photons from polarised light exposed at a particular angle or wavelength. This produces an evanescent wave effect on the metallic sensing surface. Detection occurs through the difference of refractive index between the target sample bound on the surface of the sensor and the dielectric environment [177], [178], [179];
- Evanescent waves are based on a mono-mode optical waveguide, where the field of the guided light decays exponentially with the distance to the core region of the waveguide. When the analyte interacts specifically with the label immobilized on the waveguide, its guiding properties change, consequently changing the evanescent field. Evanescent-based

sensing requires a reduced or no sample pre-treatment since only surface phenomena are detected [180].

- Optical waveguides are based on the formation of a standing wave when an incident light beam fulfils the condition of total reflection. They allow the propagation of light over an increased region that presents a higher refractive index than the surrounding medium. The coupled light intensity used for quantification will vary with the thickness of the adsorbed biomolecules layer (the higher the thickness, the higher the amount of molecules adsorbed at the surface) [177], [181]. These sensors consist of dielectric metal oxides, which can be coated with an indium doped tin oxide (ITO) layer to integrate them with electrochemical sensors [182], [183].
- Interferometry is based on the interference that a light wave that passed through the sample has on another light wave that followed a reference path, considering that both have the same source. When the two light waves are recombined, they produce interference fringes that represent the phase difference between the two light waves. Analyte information is contained in the shifts of the phase and position of the interference fringes [184]. The reference path allows removing the effect of non-specific adsorption and temperature and intensity changes [175]. This type of sensors when combined with waveguides possess a high sensitivity and a broad dynamic range [180].
- Raman spectrometry is based on the detection of Stokes and anti-Stokes shifts of non-zero polarizability molecules. It allows identification of materials through "fingerprinting" with a sub-micron spatial resolution in low concentration samples [185],[169];
- Optical microfibers are micro or nano waveguides with high-contrast index relative to the surrounding material, that enable optical detection with a very low percentage of energy loss of evanescent waves [186];

Optical methods can be coupled with each other to enhance detection or to stimulate a certain specific phenomenon, an example of which is the use of optical fibres and waveguides to increase sensitivity [74]. Table 4 presents a summary of the main characteristics of some of the presented optical detection methods.

Table 4 - Main characteristics of optical detection methods to consider when choosing a sensing approach [74]. In this table disposability refers to the devices ability to be discarded as general waste (once decontaminated).

	Detection method	Type of sample	Analyte concentration	Sample pre-treatment	Limit of detection (LOD)	Compatible materials/ fabrication methods	Reusability	Cost	Disposability	Issues	Examples
Optical	**Fluorescence**	Mainly liquid, but also solid; usually biological	Low to high	Yes, labelling	Down to µM and single biomolecule [74]	Optically clear materials	Medium (risk of cross-contamination or traces of fluorophore)	High	High, but depends on toxicity of device material and fluorophores used	Requires mathematical tools for signal corrections; Depends on available appropriate fluorophores [74]; Usually requires external readout systems (e.g. microscopes)	Temperature and flow velocity determination; cell function monitoring; interaction of biomolecules and protein binding [187]; polymer dynamics [74]
	Absorbance	Gas, liquid	Low to high	Little to none (except maybe dilution)	Down to µM	Optically clear materials, coupled with integrated mirrors and microlenses [175]	High	Medium	High	Requires mathematical tools for signal corrections specially for biological samples due to the presence of water; sensitivity decreases with decreasing path length due to reduced sample volume	Quantitative immunoassays, quantification of biomarkers [188]
	Luminescence	Mainly liquid and gas, especially small molecules,	Low to high	Little to none, but depends on probe sensitivity and matrix chosen	Down to µM	Optically clear materials; mild temperatures or sensor integration post chip fabrication	High (risk of cross-contamination or traces of fluorophore)	Medium to low (depending on probe material and readout system used)	Low, but depends on toxicity of device material and luminophores used	Requires mathematical tools for signal analysis; Care must be taken during fabrication in order not to affect probe; measurement may depend on matrix/probe homogeneity; photobleaching	Determination of process parameters (oxygen and pH), measurement of small molecules (e.g. oxygen, glucose, ethanol) [176];
	SPR	High molecular weight analytes (> 100 Da)	Low to high	Little to none [180]	Down to nanomolar (pM if gold nanoparticles are used [188]) and single biomolecule [74]	Optically clear materials, coupled with nano structures	Medium to low (due to surface functionalization)	Medium to low	Low, but depends on toxicity of device material	Requires a large sensing area, having a low throughput and a small penetration depth; Hard to differentiate specific from non-specific interactions[74], highly dependent on temperature [175]	Material's refractive index, molecular and chemical reactions, binding of biomolecules, polymer dynamics[74], biomolecules and cells [175] detection
	Raman Spectrometry	Liquid	Very low (highly diluted samples)	Yes, but label-free	Down to sub-picomolar and single molecule[74]	Optically clear materials, coupled with nano structures	Medium (risk of cross-contamination or traces of fluorophore)	High	High	May have overlapping peaks; Has a small penetration depth; denaturation of biomolecules may occur due to laser used [74]	Detection of single molecules, study of large biomolecules, analysis of chemical processes [74]

2.1.2.1 Luminescent sensors

Luminescent-based sensing elements can be easily integrated by immobilization of the matrix used for entrapment. The selected matrix should allow diffusion of the target sample through so recognition occurs, but simultaneously prevent leaching of the entrapped sensing element [176]. Luminescent sensors are thus mostly used to monitor small molecules (such as ions and gases) and process parameters (such as temperature and pH) [173]. The choice of matrix, usually polymeric, depends on the sensing probe to be entrapped and target sample, but also on the immobilization surface and/or method. The fabrication method also affects the sensor performance and sensitivity, especially for intensity-based detection approaches where uniformity and homogeneity of the sensing layer impacts accuracy and spatial resolution [176], [164].

A highly relevant factor to consider when integrating this type of sensors is compatibility of the sensor material with the microfluidic chip fabrication steps, especially bonding, when it occurs at high pressure and/or temperature, and plasma treatments [164]. A sensor layer can be integrated in a microdevice through different methods. The most common are spin or blade (or knife) coating, that create films with thicknesses down to hundreds of nanometers, but require patterning after layer deposition with (wet) etching and photolithography techniques [176], [165]. Another commonly used technique is spray-coating, which allows homogenous sensor deposition on different types of surfaces, and where patterning depends on the use of stencils [165]. *In situ* polymerization, for example using sol-gel or photopolymerization of PEG acrylates [176], is also often used, especially for glass or quartz substrates. Photopolymerization results in sensors with highly accurate and small dimensions, through the use of photomasks or moulds [165]. Another approach, involves covalent binding of the probes to the surface (usually glass or modified glass) [189]. Some research groups have opted to use PDMS as the matrix material, thus allowing a simple and direct integration of the sensing probe in the microchannel (also of PDMS or glass) [165]. Another technique, that allows precise definition and positioning of the sensor spots, is inkjet printing [176], [165]. Other research groups have used less standard approaches such as magnetic trapping (embedding magnetic nanoparticles together with the luminescent dye [190]) and optical tweezers (achieving entrapment of functionalized luminescent particles along the channel [191]).

In terms of measurement, sensing can be intensity-based, lifetime-based or based on ratiometric methods [176]. The intensity of the probe's signal can be directly related to the analyte concentration, however it is affected by background fluorescence, inhomogeneities in the dye distribution, excitation intensity, ambient light and photobleaching (especially when long-term and constant excitation of the luminophores is performed) [176], [164]. Both lifetime and ratiometric detection methods are referenced, thus overcoming the influence of external factors in the measurement [164]. Luminescent lifetime methods can be performed based on the frequency-domain, where the excitation light is sinusoidally modulated, resulting in a signal with the same waveform, where the delay (phase shift) of the emission wavelength relative to the excitation is related to the lifetime of the used fluorophore [176]. Lifetime determination in the time domain, on the other hand, can be performed either through single photon counting, where the time between excitation and photon detection is recorded in a decay curve and fitted by an exponential function, or by recording the emission phase in (usually two) time-gates whose

intensity ratio is used for quantification [165]. Fluorescent lifetime imaging microscopy (FLIM), used in cell applications, uses a modulated excitation source and detects the decay in intensity either in the time or frequency domain [192]. In the ratiometric measurements, two compounds (one analyte sensitive and the other a reference dye) which emit at distinct wavelengths are used. The ratio between the two emitted wavelengths is then used for analyte quantification [176], [164].

Readout of luminescent-based systems can be performed with optical fibers, when sensor spots are integrated [174] or if single point measurements are required, resulting in a simple measurement setup. These sensors can also be integrated on the tips of optical fibers, allowing the reuse of the sensors and their application in more cell culturing or biocatalytic reaction formats and scales. However, if a sensing layer is immobilized over the entire surface of the device, spatial imaging of the target analyte can be achieved, enabling the imaging of gradients of the target compound [176]. Furthermore, if multiple fluorophores are immobilized, they can be measured simultaneously allowing measurement of the same analyte or measurement of different analytes in parallel channels [193], [194].

2.1.2.2 Chemical oxygen sensors

Oxygen sensors are among the most well-developed and widely applied sensors, especially within biotechnological and cell applications [176], [164]. There are several types of sensors used for probing oxygen.

The classical oxygen sensor is the Clark electrode, which is composed of a platinum working electrode and a silver chloride reference electrode with potassium chloride as the electrolyte, being all the components covered with a PTFE gas-permeable layer to protect the electrodes from fouling. At a potential of 0.8 V, oxygen is reduced at the working electrode, and an electrical current proportional to the amount of oxygen is produced. These sensors present several disadvantages, such as a low temporal and spatial resolution, the relative size (which complicates their integration in microfluidic systems) and the fact that oxygen consumption is required for its quantification, thus requiring stirring, while producing hydroxide ions which are potentially harmful to cells and biological samples. They are furthermore sensitive to temperature and unreliable for long-term measurements due to depletion of the electrolyte, adsorption of biomolecules to the PTFE layer (which loses permeability) and anode coating with AgCl [192].

On the other hand, optical (chemical) oxygen sensors are usually highly sensitive and fast, inexpensive to produce and easy to integrate in microdevices, even enabling non-invasive monitoring [164]. Furthermore, they do not consume oxygen, thus enabling their application in static environments, and also do not suffer fouling thus being capable of being used for long-term measurements. Optical oxygen sensors are often based on luminophores whose phosphorescent emission is quenched (by collisional quenching [164]) in the presence of oxygen. The decrease in intensity results from an energy transfer from the excited luminophore to the oxygen molecule, generating a singlet (state) oxygen [165]. Singlet oxygen has been observed to interfere with oxygen measurements in microchannels [190]. The quenching mechanism is usually reversible and the degree of quenching depends on the oxygen partial pressure in solution.

The relationship between intensity measured and oxygen partial pressure is described by the Stern-Volmer equation (Equation 16), where I_0 and I correspond to the luminescent intensities without and with the quencher, τ_0 and τ are the corresponding lifetimes, K_{SV} is the Stern-Volmer quenching efficiency constant and pO_2 is the oxygen partial value [164], which is directly related to oxygen concentration by Henry's Law [165]. According to Henry's law, when a liquid and a gas mixture are at equilibrium, the concentrations of the gases in the liquid are proportional to their partial pressures/molar concentrations in the gas mixture.

Equation 16

$$\frac{I_0}{I} = \frac{\tau_0}{\tau} = 1 + K_{SV} pO_2$$

Most dyes are either based on ruthenium or metalloporphyrins (e.g. Pt(II) or Pd(II) complexes), usually trapped in a polymeric layer for easier integration in microfluidic channels or other features [192]. Platinum(II) octaethylporphyrine ketone (PtOEPK), which has a high quantum yield, is one of the most used dyes as sensing element for oxygen studies in cellular applications due to its long lifetime, high photostability, and low photobleaching rate relative to other fluorescent dyes [195]. Furthermore, the excitation (570 nm) and emission (760 nm) wavelengths of this dye induce a large Stokes shift which allows reducing the signal-to-background ratio [196], while reducing influence of background fluorescence or scattering from the polymeric material [164].

Oxygen sensors for microtechnological applications exist in a variety of formats. Soluble, usually water soluble, indicators (oxygen sensitive dyes) are free or entrapped in a polymer that can be mixed with the solution and introduced in the system (a microchannel, for example) [165]. However, they require a high luminophore concentration (turning them sensitive to interferences from the sample) and display a low sensitivity and selectivity, as well as an aggregation tendency, among other disadvantages [164]. An important issue to consider is the need to separate the indicator dye at the outlet, if further analysis are required [165]. The most common sensor format is the sensor layer, a mix of luminescent dye, polymeric matrix and additives dissolved in a solvent which can be deposited through one of the several methods explained in section 2.1.2.1. and then dried, polymerized or cured on a surface. This format allows for higher signal-to-noise ratios and decreasing signal interference by the sample, however they present longer response times (time for sample diffusion through the matrix) and are usually restricted to point measurement or 2D imaging [164]. Another sensor format are sensor particles, obtained either by adsorption of the sensitive dye to the surface of micro or nanoparticles, polymerization or precipitation of the sensor cocktail or by grinding the matrix with embedded dye. This format is the most flexible in terms of integration and application since it can be used either as a dissolved indicator or as a layer. Due to their dimensions, they also present significantly faster response times, a higher dye loading, selectivity and sensitivity, while also featuring three-dimensional imaging [164]. Two- or three-dimensional oxygen imaging provides a better understanding on oxygen distribution and fluidic dynamics in the microfluidic system, as well as on the generation of gradients and other interactions involved in the studied biological systems [164].

2.1.3 Model reaction/ Enzyme models used

Most of the microfluidic platforms presented in this work were characterized with the same model reaction, the oxidation of glucose by glucose oxidase coupled with the decomposition of hydrogen peroxide by catalase, (Chapter 2 and Chapter 4), or using these two enzymes (Chapter 5). Thus, a brief description of these enzymes and their reaction kinetics is presented below. These enzymes were selected as models for the study of the presented platforms due to their commercial availability and extensive accessible literature.

2.1.3.1 Glucose oxidase

Glucose oxidase (GOx, ß-D-Glucose, oxygen 1-oxidoreductase, EC 1.1.3.4) is an 8 nm globular flavo-containing glycoprotein, composed of two identical 80 kDa subunits, that contains two tightly (but not covalently) bound molecules of flavin adenine dinucleotide (FAD), acting as redox carriers [197], [198]. It was first identified in 1928 by Muller in *Aspergillus niger*, but it has since been isolated from a variety of sources over the years (e.g. red algae, citrus fruits, bacteria) [197]. GOx has been widely applied in biosensors and the clinical analytical field for the selective quantification of glucose in biological samples (especially for glucose quantification in the blood of type I diabetes patients), but also in other areas such as food industry (e.g. as a preservative, to improve color and shelf-life of food) and biochemistry (e.g. as a label in immunoassays) [135], [197], [199]. GOx from *Aspergillus niger* is capable of oxidizing glucose, with a preference for ß-glucose, to glucono-δ-lactone, using a variety of oxidizing substrates, such as oxygen, quinones, certain diamines, ferricyanide (widely used in glucose electrochemical sensors) and indophenols [197]. It has been observed that in the absence of an oxidizing substrate (e.g. in anoxic conditions), GOx can become fully reduced, which disturbs the reaction mechanism. In this form, the enzyme is in turn 100 times more sensitive (than the oxidized form of the enzyme) to one of the reaction products from oxidation with oxygen, hydrogen peroxide (at concentrations above 5 mM) [200]. However, the reduced form is also the more stable of the two states [197]. The initial product of glucose oxidation, glucono-δ-lactone is a mild competitive inhibitor of GOx. Glucono-δ-lactone however can hydrolyse spontaneously to gluconic acid, and the higher the pH the more the equilibrium tends to the gluconic acid side [197]. Inhibitors of GOx include micromolar amounts of heavy metals (e.g. mercury and silver), aldohexoses (act as competitors), halide ions at low pH and hydrazines [197].

In terms of reaction kinetics, GOx reacts according with the Ping Pong Bi Bi mechanism (Figure 7,Equation 17) [198]. When ß-D-glucose and oxygen are the substrates, the reaction is nearly irreversible ($\boldsymbol{k_2 \approx k_4 \approx k_6 \approx k_8 \approx 0}$), and can be simplified to a two-substrate substituted-enzyme Michaelis-Menten kinetics (Equation 18) [201], [202] with $\boldsymbol{K_{m\ oxygen}}$ 0.25 mM [197] – 0.82 mM [202] and $\boldsymbol{K_{m\ glucose}}$ around 33 mM [203] – 110 mM [202] for GOx from *Aspergillus niger*. In Equation 18, k_{cat} is the catalytic constant or turnover number (number of molecules of substrate that one molecule of enzyme can convert into product(s) in one unit of time), $[E_0]$ is the total concentration of enzyme at the start of the experiment, and $K_{m\ oxygen}$ and $K_{m\ glucose}$ are the Michaelis constants (concentration at which the reaction rate is half of the limiting rate, where the enzyme is saturated by the substrate) of oxygen and glucose, respectively [204]. The reaction mechanism initiates with the rapid formation of an enzyme-substrate complex, followed by the reduction of FAD. After release of the formed product

(glucono-δ-lactone), the active reduced form of the enzyme ($FADH_2$) is then oxidized by oxygen, generating hydrogen peroxide (and FAD) [197], [198].

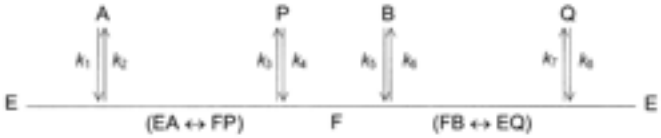

Figure 7 – Scheme (according to the Cleland notation) of the Ping Pong Bi Bi mechanism for GOx, where E is the oxidized form of GOx, F is the reduced form of GOx, A is the ß-D-glucose, P is the glucono-δ-lactone, B is the oxidizing substrate (e.g. oxygen) and Q is the reduced oxidizing substrate (e.g. hydrogen peroxide) (from [198]).

Equation 17

$$\frac{[E_0]}{v_0} = \frac{1}{V_1} + \frac{K_A}{V_1}\frac{1}{[A]} + \frac{K_B}{V_1}\frac{1}{[B]} \Leftrightarrow v_0 = \frac{[E_0]V_1AB}{AB + K_BA + K_AB}$$
$$with\ V_1 = \frac{k_3k_7}{k_3 + k_7}, \frac{V_1}{K_A} = k_1\frac{k_3}{k_2 + k_3}\ and\ \frac{V_1}{K_B} = k_5\frac{k_7}{k_6 + k_7}$$

Equation 18

$$v_{MM} = k_{cat}[E_0] \times \frac{[Glucose][Oxygen]}{K_{m\ oxygen}[Glucose] + K_{m\ glucose}[Oxygen] + [Glucose][Oxygen]}$$

The reaction of GOx using oxygen as the oxidizing agent generates hydrogen peroxide, which is harmful and toxic to most organisms, Thus, in nature, these enzymes are often coupled with peroxidases (enzymes capable of reducing hydrogen peroxide) [205], and especially, catalase.

2.1.3.2 Catalase

Catalase (EC 1.11.1.6), which was identified as a new enzyme and named by Loew in 1902 [206], is mostly an intracellular enzyme found in cells (from plants and bacteria to mammals) that contain a cytochrome system. It is presumed to protect cells exposed to ionizing radiation by decomposing the hydrogen peroxide produced in the process, but other functions are also possible (e.g. oxygen regeneration for re-use by aerobic dehydrogenases) [207]. Catalase is currently used in different applications from assessing the state of wastewater, to fabrication of biofuel cells and cosmetic materials [208].

Catalase is a peroxidase capable of decomposing hydrogen peroxide to oxygen and water, but also of oxidizing H-donors (e.g. ethanol, phenols) [209]. It has four subunits with a hematin (porphyrin heme) prosthetic group each, and an overall molecular weight of 150 kDa [207]. It presents a low stability at low enzyme concentrations, due to a mass action effect that leads to subunit dissociation [208], [210]. At very high concentrations, thermally induced denaturation and aggregation is promoted [208]. It is inhibited by anions such as, acetate, fluoride or cyanide, but also compounds like cyanogen bromide, cyanide, azide, hydroxylamine, mercaptoethanol and aminotriazole [207].

The reaction occurs by formation of an enzyme-H_2O_2 complex through the iron of the prosthetic group (oxidixing the heme to an oxylferryl species), followed by H_2O_2 decomposition where a second H_2O_2 molecule acts as H-donor (and regenerates the resting state of the enzyme) [211]. This reaction is favoured relative to using other H-donors when the substrate

concentration is above 0.1 mM [207]. The decomposition of H_2O_2 does not follow a Michaelis-Menten kinetics, but for hydrogen peroxide concentrations below 200 mM, apparent Michaelis-Menten values can be retrieved [211]. However, it is usually considered to follow a first order reaction (Equation 19), which is proportional to the concentration of H_2O_2 (at least up to 50 mM of hydrogen peroxide) [209]. Turnover numbers of $5.4x10^4$ s^{-1} [211] to $3.5x10^6$ s^{-1} [207] have been reported for catalase.

Equation 19

$$v_{catalase} = k_{catalase}[H_2O_2]$$

The reaction of catalase with hydrogen peroxide is exothermic, like the glucose oxidation reaction by GOx [197]. Hydrogen peroxide seems to have a significant harmful effect on catalase at concentrations above 100 mM [212]. However, addition of hydrogen peroxide and catalase solutions has been applied in bioreactors [213], [208] as an alternative to bubbling the fermentation broth with air.

2.2 Goal

In this chapter, it is intended to provide strategies for the application of a commercially available microfluidic system in the study of enzymatic reactions and biocatalyst screening. This involved the characterization of the system with a specific enzymatic cascade reaction, the oxidation of glucose with glucose oxidase coupled to the decomposition of hydrogen peroxide by catalase. The performed reaction was monitored using integrated luminescent oxygen sensors, coupled with analytical quantification of the main product (gluconic acid) at the outlet by high-performance liquid chromatography (HPLC).

Strategies for *in situ* oxygen generation and validation of the integrated oxygen sensors with external analytical measurements were developed and are also presented. Furthermore, a computational fluid dynamic model including the enzymatic reaction mechanism was developed to gain a more comprehensive understanding of both the chosen reaction and the performance of the used microfluidic system. The model was used to investigate underlying phenomena, such as oxygen limitation, reaction dynamics and the influence of chosen materials, to achieve a better understanding of the obtained experimental data.

2.3 Materials & Methods

2.3.1 Reagents and Materials

Glucose oxidase (EC 1.1.3.4, type VII, from *Aspergillus niger*, ≥100,000 U/g solid), Catalase (EC 232-577-1, from bovine liver, lyophilized powder, 2000-5000 units/mg protein) and Horseradish peroxidase (EC 1.11.1.7, lyophilized, 150 U/mg) were obtained from Sigma (St. Louis, MO, USA). Gluzyme® Mono 10 000 BG (Glucose oxidase from *Aspergillus niger* (23%) with 10000 U/g, wheat solids (39%), Sodium Chloride 32%) and water (6%)) was acquired from Novozymes (Bagsvaerd, Denmark). D- Glucose (anhydrous) was provided by Fluka

(Loughborough, UK). Mono – and di-potassium hydrogen phosphate (anhydrous) were obtained from Merck (Darmstadt, Germany). Poly(ethylene glycol) (PEG) MW 6000 was acquired from Acrōs Organics (Geel, Belgium). Hydrogen peroxide (Perdrogen™, 30% (w/w)), Sodium sulphite, Sodium hydroxide (reagent grade, ≥98%, pellets (anhydrous)), Phosphoric acid (85 wt. % in H_2O, 99.99% trace metals basis), Sodium 3,5-dichloro-2-hydroxy-benzenesulfonate (DCHBS) and 4 Aminoantipyrine (4-AAP, reagent grade) were obtained from Sigma (St. Louis, MO, USA). All solutions were prepared in 50 mM phosphate buffer pH 7.5.

The two 10 mm acryl plates that form the custom-made holder were acquired from Rias A/S (Roskilde, Denmark). The holder was completed with one 5 mm thick SS304 stainless steel plate from Sanistål (Aalborg, Denmark), placed in-between the acryl plates for integration of the microfluidic chip. Flangeless polypropylene (PP) fingertight 1.5875 mm (ID) fittings (XP-201) and flangeless ferrules (P200X) from Upchurch Scientific® (Washington, USA) were used to connect polytetrafluoroethylene (PTFE) 1.5875 mm (OD) x 1 mm (ID) tubing (S 1810-12) or 1.5875 mm (OD) x 0.5 mm (ID) tubing (S 1810-08) from Bohlender (Grünsfeld, Germany). The extrusion poly (methyl methacrylate) (PMMA) sheet with thickness of 2 mm of the second meander channel was acquired from Nordisk Plast (Assentoft, Denmark). The PMMA plate was patterned using laser ablation with a CMA-4030 Laser Engraving machine from GD Han's Yueming Laser Technology co., Ltd (Guangdong, China) and bonded to a 2-mm thick SS304 stainless steel plate from Sanistål (Aalborg, Denmark) with a 142 µm thick double-sided adhesive tape mcs-foil 008 from microfluidic ChipShop (Jena, Germany) also defined with laser abrasion.

2.3.2 Meander microfluidic channel

The used microfluidic channel to perform the oxidation reactions presented in this chapter is a glass and silicon chip developed and batch-produced by iX-factory (now part of Micronit, Enschede, Netherlands) in Dortmund, Germany. The microchannel has two main inlets and one outlet, with 6 side inlets/outlets. It has a serpentine shape with 18.5 turns, 0.504 m length and a total volume of 10.08 µL, while the main inlet branched-channels have a volume of 0.44 µL. The 200 µm deep and 100 µm wide microchannel, as well as the seven chambers with the same geometry of the sensing areas (3.5 mm length and 1 mm width) were defined in a 675 µm silicon wafer by photolithography and deep reactive ion etch. The 1.5-mm inlets for fluidic access were fabricated on a glass wafer through powder blasting. The sensor layer was airbrush spray-dried onto the glass wafer to a thickness of ~2.2 µm using a silicon stencil and then cured for 24h at 60 ^{0}C. The glass and silicon wafers were irreversibly bonded using an anodic bonding process at 180 ^{0}C, 1000 V and 5 kN pressure for 4 h. After bonding, the wafers were diced into chips the size of microscopic slides (75.5 mm x 25.5 mm) [174]. The final meander microchannel with integrated oxygen sensors is presented in Figure 8.

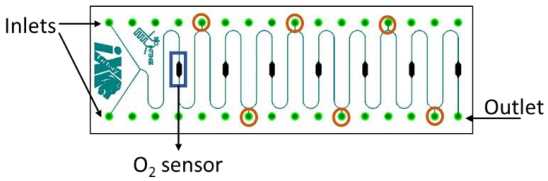

Figure 8 – Schematics of the meander microfluidic channel with the main inlets and outlet emphasized. In orange, the five side inlets are highlighted, and in blue one of the seven oxygen sensors is indicated.

2.3.2.1 Oxygen sensors

The integrated oxygen sensors were developed and fabricated by the group of Ingo Klimant from the Working Group Sensor Materials of the Institute of Analytical Chemistry and Food Chemistry at the Technical University of Graz in Graz, Austria [174]. The sensors are based on the frequency-domain lifetime luminescence measurement of a luminescent platinum(II) meso-tetra(4-fluorophenyl) tetrabenzoporphyrin (PtTPTBPF) sensor dye entrapped in a silicone rubber and polystyrene composite matrix [174]. The PtTPTBPF dye is excitable with red light (620 nm), and emits in the near-infrared (NIR) range (760 nm), which decreases background fluorescence or scattering due to the presence of biological matter. Moreover, the red light used for sensor excitation does not damage biological samples such as cells, enabling its use in a wide variety of biological applications [174]. The sinusoidally modulated red light excites the luminescent dye at a known frequency, which has a phase shift relative to the intensity modulated emitted luminescence [214]. Detection is performed by the measurement of the depth of modulation and phase angle shift of the emitted luminescence as a function of frequency in the presence of oxygen, which quenches the luminescence of the sensor's dye [215]. The quenching behaviour is usually described by a modified Stern-Volmer equation, called the two-site model, where it is considered that the dye can exist in two different environments that are quenchable, but at different rates (Equation 20) [216]. In the equation, I and I_0 are the luminescence intensity of the sensor in the presence and absence of the quencher (oxygen), τ and τ_0 the corresponding luminescence lifetime, f describes the distribution coefficient between the two media, K_{SV} is the quenching efficiency for the first environment, while m is the factor defining the Stern–Volmer constant for the second environment [164], [189].

Equation 20

$$\frac{I_0}{I} = \frac{\tau_0}{\tau} = \left(\frac{f}{1 + K_{SV} \times [O_2]} + \frac{1 - f}{1 + K_{SV} \times m \times [O_2]} \right)^{-1}$$

These oxygen sensors are capable of measuring oxygen concentrations in solution and gas through the measurement of the decrease in luminescent intensity and lifetime as a function of the sensor's oxygen tension [216]. The sensors can be calibrated through a two-point calibration using the two-site model to fit the calibration data and the constants from Table 5. These sensors have a resolution of 0.2-0.6 hPa (2.46×10^{-4} to 7.40×10^{-4} mM of oxygen) at oxygen concentrations below 50 hPa (0.06 mM of oxygen) and 1-2 hPa (0.001 – 0.002 mM of oxygen) at ambient air oxygen concentrations (8.6 mM of oxygen), with a limit of detection of 0.08 hPa (9.85×10^{-5} mM of oxygen) [174].

Table 5 - Constants of two-site model for the sensors used at 25 ^{0}C.

Fixed f	0.83858
Ksv	0.01923
m	0.09793

2.3.2.2 Polymeric valve chip

The used valve microfluidic chip (product code: 19-1850-0155-03) was developed and manufactured by injection molding at Microfluidic ChipShop in Jena, Germany. The chip was made of polycarbonate and contains two different channels, one with 21 µL volume (and 6 possible connections to channels) and another with 7 µL volume (and 4 possible connections to channels), each with their respective manually turned rotary valve. The microfluidic channels defined in the valve chip are 400 x 400 µm [217]. The chip is compatible with 1 mm inner diameter male mini Luer fluid connectors. In order to connect this chip to the meander microreactor, a strategy was devised involving small portions of PTFE tubing with a wider diameter that were used to connect the mini Luer connectors and the 1/16" outer diameter PTFE tubing compatible with the fingertight connectors used in the microreactor and the modular syringe pump system.

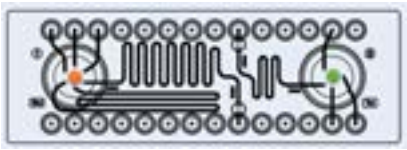

Figure 9 – Schematics of the turning valve system from Microfluidic ChipShop. In orange, the valve corresponding to the 21 µL volume outlet channel and in green the valve corresponding to the 7 µL one.

2.3.2.3 Permeable meander reactor

The used PMMA microchannel was also a meandering microchannel with approximately 100 µm width x 400 µm height and 44 µL volume. The microreactor was defined with one inlet and one outlet, that had the same dimensions as the tube used, i.e. 1.6 mm outer diameter. The channel was fabricated using laser abrasion and bonded to a stainless steel plate with a 142 µm thick double-sided adhesive tape. Plastic o-rings and a small PMMA plate with a hole with 1.6 mm diameter were used as a simple connector to join the outlet of the silicon and glass microreactor to the PMMA microchannel. The o-rings and PMMA plate were kept in place with small office binder clips that provided sufficient pressure to avoid leakage in the inlet during flow conditions.

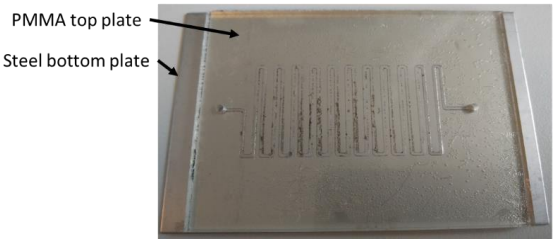

Figure 10 – Photograph of PMMA meander channel.

2.3.3 Enzyme activity measurements

Activity measurements of Glucose oxidase (GOx) and Catalase (Cat) were performed in a UV-1800 UV-Vis spectrophotometer with a CPS 240A cell positioner from Shimadzu (Kyoto, Japan). GOx activity was measured using a protocol adapted from Heuts *et al.* (2007) [218], where the hydrogen peroxide formed in the presence of glucose, is used by horseradish peroxidase (HRP, 4 U/mL) to oxidize 4-AAP (0.1 mM) and DCHBS (1 mM), forming a colorimetric (pink) compound. The formation of this compound can be followed at 515 nm (ε_{515}= 26 mM^{-1} cm^{-1}) and its absorbance can be directly related to the amount of glucose consumed. To measure GOx activity 10 µL of 1:30 diluted GOx solution (~30 U/mL) were added to 990 µL of the reaction mixture. The activity of Cat (~400 U/mL, 0.00241 mM) was measured based on the protocols by Beers and Sizer (1952) [219] and Lück (1965) [220], by following the decrease of hydrogen peroxide concentration at 240 nm (ε_{240}= 43.6 M^{-1} cm^{-1}). To measure Cat activity 30 µL of 1:10 diluted catalase solution was added to 2970 µL of 10 mM hydrogen peroxide. Each spectrophotometric measurement was performed in triplicate for 2 min.

The average kinetic parameters obtained for the two enzymes from the UV spectrophotometer-based assays are presented in Table 6. Table 7 presents the average activity of the GOx solutions used during this work and the corresponding nomenclature used throughout the text.

Table 6 – Kinetic parameters obtained for GOx and catalase from the UV-based activity assays.

Kinetic parameters	Value
$K_{M,\ Glucose}$	26 - 33 mM
V_{max}	1 - 2x10^{-4} mM s^{-1}
$k_{cat,\ Glucose}$	300 -500 s^{-1}
$k_{catalase}$	1.1– 2.6 x10^{-3} s^{-1}

Table 7 – Summary of glucose oxidase enzyme solutions and the corresponding nomenclature used here.

Name	Activity range (U mL^{-1})	Concentration (mol m^{-3})
10xGOx	110 – 170	0.006406
5xGOx	55 – 85 (1:1 dilution of 10xGOx)	0.003023
1xGOx	15 – 30	0.0006406
0.5xGOx	7.5 – 15 (1:1 dilution of GOx)	0.0003023

2.3.4 High-Performance Liquid Chromatography (HPLC) method

All the reaction samples were analysed in an HPLC for quantification of consumed glucose and produced gluconic acid. The measurement was performed with a reversed-phase chromatography on an Ultimate 3000 HPLC (Dionex, Sunnyvale, CA, USA) equipped with a Phenomenex column with 5-µm sized amine particles (Luna 5µm NH2 100Å), operated at 40 ^{0}C and 140 bar. The mobile phase consisted of a 20 mM phosphoric acid (H_3PO_4) solution, flowing at 1 mL/min. The eluted gluconic acid was quantified in the ultraviolet (UV) multiple wavelength detector at 205 nm, while the glucose concentration was determined in the Refract Max 520 refractive index (RI) detector. The amount of each component was obtained by integration of the areas under the corresponding peaks using the HPLC commercial analytical software (Chromeleon 6.8), based on a calibration curve performed for each component. Samples

were measured mixed with 0.5 M sodium hydroxide (NaOH) solution in a proportion 1:2 of solution relative to the sample.

2.3.5 Oxygen concentration measurements

The oxygen measurements inside the silicon meander microchannel were performed using four optical fibres ((Plastic fibre cable, simplex fibre 1 mm, PE-jacket 2.2 mm from Ratioplast-Optoelectronics GmbH, Lübbecke, Germany) connected to a four-channel optical oxygen meter (FireStingO2 from PyroScience, Aachen, Germany). The lifetime luminescent measurement was performed through Pyro Oxygen Logger software provided by PyroScience with the parameters presented in Table 8.

Table 8 – Parameters used for oxygen measurement in the microreactor with FireStingO2 and Pyro Oxygen Logger.

LED intensity	30%
Amplification of signal	400x
Modulation frequency	4000 Hz
Temperature	25 ^{0}C
Sample rate	1 sample per second

Before each set of experiments, the sensors of the microfluidic chip being used were calibrated. Calibration was performed by measuring the dphi values (phase shift of luminescent emission relative to modulated excitation light) for 0 % and 100 % oxygen conditions. In this case, 100 % oxygen condition corresponded to an oxygen saturated buffer solution, which was achieved by shaking the flask containing the solution for several minutes before introducing the solution inside the channel. The 0 % oxygen condition was achieved either by adding an excess of Gluzyme to a glucose solution or using a solution with a sufficient amount of sodium sulphite. In the initial microchannel characterization experiments, this calibration was performed once per day, before initiating the experiments. For most of the data presented in this chapter, however, a simplified calibration was applied. The 2-point calibration was performed before the start of each set of experiments or when some deviation in sensor signal was observed, but not every day. Instead, the same dphi values recorded in the calibration were used and a manual background calibration (to adjust for the light conditions) was performed daily before initiating the experiments.

Monitoring of oxygen during the experiments was performed by measuring partial pressure of oxygen inside the channel with the Pyro Oxygen Logger software. Afterwards, the data was extracted in an Excel file and converted to oxygen concentration using the Henry's law (Equation 21), where p is the partial pressure of the solute in the solution, c is the concentration of the solute in the solution, and k_H is the Henry constant.

Equation 21

$$p = k_H \times c$$

For the calculations, a Henry constant of 811.899 L bar mol^{-1} was considered, which was obtained from an average of Henry constant values presented by Sander (1999) [221]. The oxygen concentration values presented in this work were calculated from an average of three intervals of oxygen partial pressure values measured during each experiment. Each interval

corresponded to the average sampling time at the outlet of one of the three samples measured in the HPLC per initial glucose concentration per experiment.

2.3.6 Oxidation of glucose in the meander microfluidic channel

The performance of the microfluidic channel in terms of quantification was evaluated through the use of an enzymatic cascade reaction, the oxidation of glucose with glucose oxidase coupled with the decomposition of hydrogen peroxide by catalase (Figure 11).

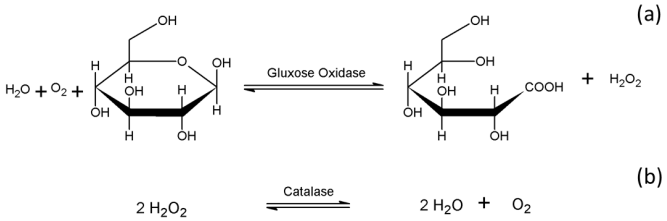

Figure 11 – Glucose oxidation reaction with glucose oxidase (a) and hydrogen peroxide decomposition with catalase (b).

Both enzymes were introduced through inlet 1 (the ratio between the enzymes varied between the different experiments) and the substrates (glucose and oxygen) were introduced through inlet 2, as shown in Figure 12. The glucose solution introduced was always shaken for several minutes before introduction inside the channel, so it would be oxygen saturated. It is thus assumed that the solution in inlet 2 is oxygen saturated, while the concentration of oxygen in the enzyme solution is unknown but lower than in inlet 2. To facilitate the retrieval of the samples a 5-cm long PTFE tube (with 0.5 mm inner diameter) was placed at the outlet. This corresponded to an added 9.82 µL of reaction volume relative to the volume of the meander microchannel. Sampling was performed by submerging the tip of the outlet tube in 100 µL of 0.5 M NaOH solution, used to stop the reaction and move the product towards gluconic acid [222]. The outlet used in the experiments was not the outlet of the reactor due to a limitation of the casing built in-house, so the last side inlet was used as the outlet. The syringe pump system used to introduce the solutions inside the microreactor was a stepper motor-driven modular digital pump Cavro® XP 3000 with two glass syringes with a stroke volume of 250 µL and one glass syringe with 500 µL stroke volume from Cavro Scientific Instruments, Inc. (San Jose, California, USA). The flowrates were defined using LabView™ 2010 (v10.0) from National Instruments (Austin, Texas, USA). The sensors were positioned in accordance with Figure 12 to concede a good overview of the progression of the reaction inside the microreactor.

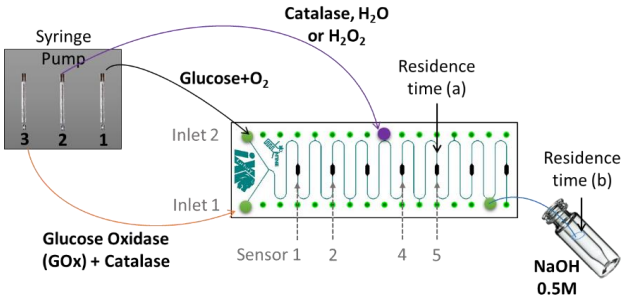

Figure 12 – Schematics of the experimental setup used for monitoring the glucose oxidation reaction coupled with hydrogen peroxide decomposition, calibration curve determination and increase of oxygen concentration inside the channel, with the sampling procedure represented and the position of the four sensors used for measurement highlighted.

2.3.6.1 Characterization of the meander microfluidic channel

The residence time until detection in the different sensors used for monitoring was obtained by introducing water in the channel at a known flowrate (1 μL s^{-1}) and observing when a change in sensor signal was observed for the different sensors. The values used for the calculations, presented in Table 9, are average values of five experiments. Since the values were taken by observation of the raw data, one by one, with an approximate value for the start of flow, they have a wide margin of error associated with them, as can be observed in the table below.

Table 9 – Average values of residence time obtained for the sensors used for reaction monitoring.

Sensor position	Residence time (s)
1	3.55±1.4
2	5.05±1.5
4	7.55±1.6
5	9.25±1.5

For the determination of reaction volume, the whole channel was considered, including a portion between the fifth side inlet and the main outlet, actually not used. The reaction volume considered corresponded to the sum of the volume of the meander microchannel (10.08 μL) and the 5-cm tubing connected to the outlet, thus resulting in a total volume of 19.9 μL for the 0.5 mm ID tubing.

The microfluidic system was also evaluated in terms of enzyme adsorption by comparing a reaction performed with and without polyethylene glycol (PEG). PEG is a hydrophilic molecule that preferably adsorbs to the surface, passivating it and decreasing adsorption by the biomolecules [223]. A solution of Gluzyme (0.2 g L^{-1}) and a solution of glucose (50 mM), both either with or without PEG 6000 (1% w/w) were introduced inside the channel at a flowrate of 0.4 μL s^{-1} and monitored for 4 h. A decrease in oxygen partial pressure would indicate the occurrence of enzyme adsorption in the channel and thus adsorption and accumulation of GOx in the channel. Since no significant decrease of signal was observed during the experiment without PEG (Figure 13), enzyme adsorption was not considered to be a major issue in this system if proper cleaning procedures were implemented. However, the observed variability in

sensor performance between experiments at the same conditions (Figure 13) was thought to derive from inaccurate calibration. Thus, to improve sensor performance and decrease variability between experiments, the final calibration procedure described in section 2.3.5. was adopted.

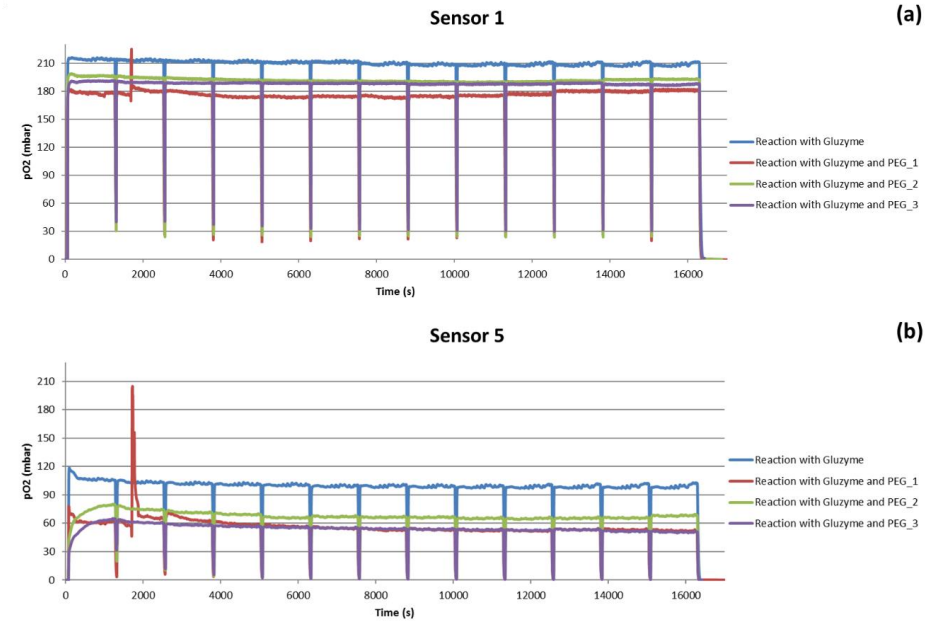

Figure 13 – Oxygen partial pressure measurement of experiments with solution with and without PEG 6000, performed at the same conditions. The peaks observed in the graphs correspond to the passage of an air bubble in the system.

Characterization of the meander microfluidic channel was initially performed using Gluzyme®. However, since the amount and activity of catalase in this enzyme preparation is unknown [224], pure GOx and catalase (commercially available) were used for the quantification experiments.

2.3.6.2 Oxygen quantification calibration curve

In order to achieve a quantitative output of glucose and gluconic acid concentrations from the oxygen sensors, reactions with different residence times were executed. These experiments were performed at different flowrates and structured to be able to match the residence time in oxygen sensor 5, to the residence time at the outlet of the tube, as presented in Table 10. This was performed for only one sensor, since it would be extremely time-consuming to perform the necessary experiments to match the residence time of each sensor with an equivalent residence time at the outlet. Sensor 5 was chosen because it was the last of the monitored oxygen sensors, but not the last of the available oxygen sensors thus allowing a reference point before the reaction was thought to run to an end. This sensor also resulted in a closer match between the flowrate at the outlet and at the sensor between the selected consecutive flowrates. Two

different concentrations of GOx were used (6.046×10^{-4} mol m^{-3} and 3.023×10^{-4} mol m^{-3}) with a high amount of catalase (830 U mL^{-1}), to achieve a higher range of oxygen vs. glucose and gluconic acid concentrations. To achieve the residence times presented in Table 10, experiments were performed at 2, 1, 0.5 and 0.25 µL s^{-1}.

Table 10 – Flowrates and corresponding residence times at sensor 5 and outlet used to achieve the sensors calibration curve (indicated by the green arrows).

Flowrate (µL s^{-1})	Residence time (s)	
	Sensor 5	Outlet
2	4.63	9.95
1	9.25	19.90
0.5	18.50	39.80
0.25	37.00	79.60

2.3.6.3 *Increase of oxygen availability in the meander microfluidic channel*

Two strategies were applied to increase oxygen availability inside the microfluidic channel: addition of catalase and addition of hydrogen peroxide. Both strategies used catalase's ability to decompose hydrogen peroxide in oxygen and water as in Equation 20 (b). Solutions with different amounts of catalase (460 U mL^{-1}, 830 U mL^{-1} and 2950 U mL^{-1}) or various hydrogen peroxide concentrations (0.1 mM, 0.25 mM and 0.5 mM) were introduced at the same flowrate (0.34 µL s^{-1}) through the third side inlet of the microchannel, as presented with a purple arrow in Figure 12. To account for oxygen present in the buffer, water was also introduced in the side inlet, as a third strategy to increase the oxygen concentration in the microchannel. Inlet solutions introduced in the main inlets, also at a flowrate of 0.34 µL s^{-1}, contained 5xGOx with either 94 U mL^{-1} or 830 U mL^{-1} of catalase. The flowrate of 0.34 µL s^{-1} was chosen in order to achieve a total flowrate at the outlet close to 1 µL s^{-1} and allow a better comparison with the experiments performed with only two inlets, with a flowrate of 0.5 µL s^{-1} at each inlet.

2.3.7 *CFD simulations of the oxidation of glucose in the meander microfluidic channel*

The same glucose oxidase and catalase cascade reactions performed inside the microreactor were simulated using a computational fluid dynamic simulation software, ANSYS-CFX Version 16.2 (Canonsburg, Pennsylvania, USA). The three-dimensional designs of the microchannel and tube geometries were designed using a meshing software, ANSYS ICEM CFD® 16.0 (Canonsburg, Pennsylvania, USA), and discretization of the geometry into smaller elements (where the equations for momentum, energy and mass balance are solved by ANSYS-CFX software) was performed (Figure 14). The microchannel geometry contained 478744 elements (61264 elements/ µL). The geometry of the tube used was divided in the fluid region and in the tube region, both defined with o-grids so as to allow a structured circular mesh. The 0.5 mm ID tubing geometry with both the fluid and tube region has 386561 elements (3852 elements/ µL). All designs were simulated with a structured hexahedron mesh.

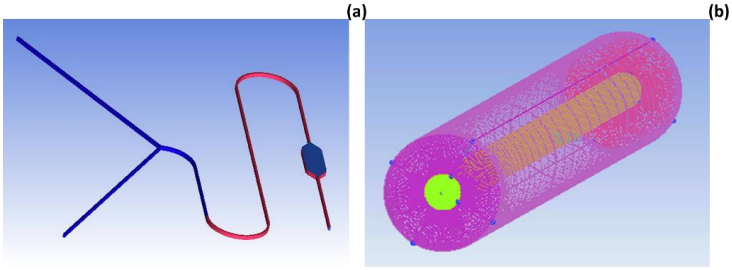

Figure 14 – 3D designs of the silicon and glass meander microchannel (a) and 0.5 mm ID tubing and fluid regions integrated (b) obtained using the meshing software, ANSYS ICEM CFD® 16.0.

The simulations were performed with the same flowrates and substrate concentrations as used in the corresponding experiments, considering laminar flow (as described in Chapter 1) and fluid velocity as the input parameter at the inlets. The outlet was defined as an opening. More details regarding the boundary conditions defined in the simulations can be found in Appendix III. The velocities used in the simulations and corresponding Reynolds numbers are presented in Table 11.

Table 11 – Flowrates used in the experiments and the simulations with the corresponding velocities and Reynolds numbers.

Flowrate ($\mu L\ s^{-1}$)	**$Velocity_{channel}$ ($m\ s^{-1}$)**	**$Re_{channel}$**	**$Velocity_{tube}$ ($m\ s^{-1}$)**	**$Re_{tube\ 0.5\ mm}$**
2	0.05	7.45	0.01	1.49
1	0.025	3.72	0.005	0.74
0.5	0.0125	1.86	0.0025	0.37
0.25	0.0625	0.93	0.00127	0.19

Oxygen concentration was assumed to be at saturation values (0.258 mM is the solubility of oxygen in water at room temperature [225]) in the inlet where glucose was introduced, but at a lower concentration (0.19 mM) in the other(s). The lower value of oxygen was chosen by testing values between 0.15 mM and 0.2 mM of oxygen for one of the simulations. The kinetic parameters were based on the ones obtained in the activity measurements (Table 12), but the catalase reaction rate and the k_{cat} of GOx were altered in order to match the experimental values of oxygen concentration measured by sensor 5 (reference sensor for the calibration curve).

Table 12 – Kinetic parameters used in the CFD simulation of the enzymatic cascade reaction.

Kinetic parameters	**Value**
$K_{M,\ Glucose}$	33 mM
$K_{M,\ Oxygen}$	0.3 mM
$k_{cat,\ Glucose}$	250 - 1200 s^{-1}
$k_{catalase}$	2.586 $x10^{-3}$ – 25.86s^{-1}

The enzymatic cascade reaction was simulated considering the substituted-enzyme mechanism of the Michaelis-Menten equation (Equation 18) [201], while hydrogen peroxide decomposition was assumed to be a first order-reaction (Equation 22) [209] for the experimental conditions tested. The rate constant for catalase was obtained spectrophotometrically for a different catalase concentration, so the ratio between the catalase concentration used in the

experiment and the one used to obtain $\boldsymbol{k_{catalase}}$ was added to the rate expression. The turnover number ($\boldsymbol{k_{cat}}$) was chosen instead of V_{max} so that the amount of GOx added in each experiment (and which was changed between experiments) could be taken into account in the model.

Equation 22

$$v_{catalase} = k_{catalase}[H_2O_2] \times \frac{[catalase]_{experiment}}{[catalase]_{spectrophotometric\ measurement}}$$

In the simulation, it was further assumed that the amount of oxygen obtained from the reaction should be $-v_{MM} + 0.5\, v_{catalase}$, according to the reaction stoichiometry (Figure 11), meaning that the amount of oxygen corresponds to the amount consumed by GOx (equal to the amount of glucose consumed and the hydrogen peroxide and gluconic acid produced) plus the amount produced by catalase (which is half of the amount of hydrogen peroxide consumed).

A diffusivity of 4.95×10^{-11} $m^2 s^{-1}$ was assumed for the enzymes [197], 6.7×10^{-10} $m^2 s^{-1}$ was assumed for glucose and gluconic acid, and a value of 2.1×10^{-9} $m^2 s^{-1}$ assumed for oxygen and hydrogen peroxide [226], [227]. The compound concentrations obtained at the outlet of the microreactor simulation were used as inputs for the corresponding simulation in the tube. The tube material was set to polystyrene with diffusivity for oxygen (the only compound diffusing through the tube material towards the fluid) of 2.8×10^{-7} $cm^2 s^{-1}$ (2.8×10^{-11} $m^2 s^{-1}$, considered the theoretical value) [228]. This value is close to one hundred times slower than oxygen diffusivity in water. PTFE oxygen diffusivity values of 2.8×10^{-6} $cm^2 s^{-1}$ (10 times slower than in water) and 2.8×10^{-5} $cm^2 s^{-1}$ (the same order of magnitude as oxygen diffusivity in water) were also considered in the simulations. Concentration of oxygen on the outside of the tube was assumed to be the atmospheric oxygen concentration, 8.6 mM at 25 °C, calculated from the ideal gas law and assuming a molar fraction of oxygen of 0.21. Further simulations were performed, where oxygen at the interface between the tube and the fluid was fixed at 0.258 mM (oxygen solubility in water), meaning the tube is completely permeable to oxygen. Inside the tube, the same diffusivities and kinetic parameters used in the microreactor simulation were also used for the fluid simulation. All the materials were simulated considering the materials' properties provided by ANSYS-CFX, and the liquid was defined as water.

2.3.7.1 CFD simulation strategy

The objective of the CFD model was to achieve an accurate description of the enzymatic reaction performed in the meander microreactor. To assess the similarity of the simulations to the executed experiments, two parameters were used for comparison: oxygen concentration in sensor 5 (for evaluation of the simulations performed in the microreactor geometry) and measured gluconic acid concentration at the outlet (evaluation of meander and tube simulations by comparison with the HPLC measurements).

In order to mimic the enzymatic reaction in the silicon meander channel, different parameters defined as input in the simulation (kinetic parameters and inlet oxygen concentration) were evaluated. For this purpose, one experiment (*5xGOx* + 94 U/mL catalase at 1 μL s^{-1}) was chosen as the reference for model parameter optimization, since it was the reference to assess the effect of added catalase and hydrogen peroxide in the increase of oxygen availability experiment. For the reference simulation, at the experimentally used enzyme and

substrate amounts, the concentration of oxygen in inlet 2 and GOx turnover number (k_{cat}) were varied between 0.15 and 0.20 mM and between 50 s^{-1} and 4000 s^{-1}, respectively. The different values were simulated only for the meander channel geometry, until an oxygen concentration in sensor 5 was reached that matched the value obtained experimentally was reached.

Then, the oxygen concentration in inlet 2 (0.19 mM) and turnover number (300 s^{-1}) that resulted in the best match with the experimental data were used to simulate all the performed experiments in the meander channel geometry. In addition to the mentioned input parameters, each simulation was defined with the enzyme, glucose and hydrogen peroxide concentrations, as well as the flow velocities used experimentally. In the cases where the oxygen concentration in sensor 5 did not match the experimental values, new values for the kinetic parameters were used. The kinetic parameters (GOx turnover number and catalase reaction rate) were varied within the range presented in Table 12. In the experiments with added hydrogen peroxide and catalase, since catalase should have a prominent role, the reaction rate for catalase ($k_{catalase}$) was varied between 0.002586 s^{-1} and 25.86 s^{-1}. In the experiments for the different residence times, since GOx should have the highest influence, the turnover number was again varied, between 300 s^{-1} and 1200 s^{-1}. Unexpectedly, for some simulations corresponding to experiments performed at similar conditions, different kinetic parameters resulted in the best fit of oxygen values at sensor 5, indicating possible variations in the experimental conditions that were not previously observed. However, in order to allow the comparison of the different simulations, the simulations within a given set of experiments (e.g. calibration curve or amount of GOx) were simulated using the same kinetic parameters, as can be seen in Table 13. The selected parameters corresponded to the values that resulted in the best match with oxygen sensor values for the majority of the simulations within a set of experiments.

The values obtained from the simulations in the meander geometry were afterwards used as inputs in the corresponding simulations in the tube geometry. The same set of parameters was used, and the concentration values of glucose, oxygen, gluconic acid and hydrogen peroxide at the outlet of the meander, were used as inlet concentrations of these compounds in the tube simulations. The effect of oxygen diffusivity in the PTFE outlet tube, as well as catalase's reaction rate in the final gluconic acid production was also assessed in the tube geometry simulations. The value of the catalase reaction rate was varied between 0.002586 and 25.86 s^{-1} only in the tube, to see whether catalase kinetics could change with increased concentration of hydrogen peroxide (in a case were no extra hydrogen peroxide was added). Also, the concentration of oxygen at the interface between the tube and the fluid was either fixed at 0.258 mM (maximum concentration of soluble oxygen) or varied between 2.8×10^{-7} and 2.8×10^{-5} cm^2 s^{-1}, to check how much the amount of oxygen diffusing through the tube can affect the final product concentration obtained.

Table 13 presents a summary of the simulation parameters varied in each simulation, as well as the final value used to obtain the data presented in this chapter. The simulations were performed at different glucose concentrations since not all experiments were performed at the full glucose concentration range (5 to 200 mM). Thus, the simulations corresponding to sets of experiments where lower glucose concentrations were used in some of the experiments, were performed at a lower glucose concentration, as for the experiment set "Amount of GOx" and "Calibration curve".

Table 13 – Summary of the simulations performed and corresponding varied and selected parameters.

Simulation name	Experiment set	[Glucose] (mM)	k_{cat} (s^{-1}) used	k_{cat} (s^{-1}) range	$k_{catalase}$ (s^{-1}) used	$k_{catalase}$ (s^{-1}) range	Oxygen diffusivity in the tube ($cm^2\ s^{-1}$) used	Oxygen diffusivity in the tube ($cm^2\ s^{-1}$) range
10xGOx	Amount of GOx	5	300	250-1000	-	-	$2.8x10^{-6}$	-
5xGOx		5	300	250-1000	-	-	$2.8x10^{-6}$	-
1xGOx		5	300	250-1000	-	-	$2.8x10^{-6}$	-
5xGOx+94 U/mL	Increase of oxygen availability	50	300	50-4000	$2.586x10^{-3}$	-	$2.8x10^{-6}$	-
5xGOx+830 U/mL		50	300	-	$2.586x10^{-3}$	-	$2.8x10^{-6}$	-
5xGOx+94 U/mL+0.25 mM H_2O_2		50	300	-	2.586	$2.586x10^{-3}$-25.86	$2.8x10^{-6}$	-
5xGOx+830 U/mL+0.25 mM H_2O_2		50	300	-	2.586	$2.586x10^{-3}$-25.86	$2.8x10^{-6}$	-
5xGOx+94 U/mL+830 U/mL		50	300	-	0.2586	$2.586x10^{-3}$-25.86	$2.8x10^{-6}$	-
5xGOx+830 U/mL+830 U/mL		50	300	-	0.2586	$2.586x10^{-3}$-25.86	$2.8x10^{-6}$	-
5xGOx+94 U/mL+H_2O		50	300	-	$2.586x10^{-3}$	-	$2.8x10^{-6}$	-
5xGOx+830 U/mL+H_2O		50	300	-	$2.586x10^{-3}$	-	$2.8x10^{-6}$	-
1xGOx+830 U/mL	Calibration curve/ Residence time	50	1000	800-1000	$2.586x10^{-3}$	-	$2.8x10^{-6}$	-
0.5xGOx+830 U/mL		50	1000	800-1200	$2.586x10^{-3}$	-	$2.8x10^{-6}$	-
1xGOx+830U/mL (4.625 s)		10	1000	800-1000	$2.586x10^{-3}$	-	$2.8x10^{-6}$	$2.8x10^{-6}$-0.258 mM
1xGOx+830U/mL (9.25 s)		10	1000	800-1000	$2.586x10^{-3}$	$2.586x10^{-3}$-25.86 (in the tube)	$2.8x10^{-6}$ (but $2.8x10^{-7}$ in the different $k_{catalase}$ in the tube simulations)	-
1xGOx+830U/mL (18.5 s)		10	1000	800-1000	$2.586x10^{-3}$	-	$2.8x10^{-6}$	-
		200	1000	800-3000	$2.586x10^{-3}$	-	$2.8x10^{-6}$	-
1xGOx+830U/mL (37 s)		10	1000	800-1000	$2.586x10^{-3}$	-	$2.8x10^{-6}$	$2.8x10^{-6}$-0.258 mM
0.5xGOx+830U/mL (4.625 s)		10	1000	800-1200	$2.586x10^{-3}$	-	$2.8x10^{-6}$	$2.8x10^{-6}$-0.258 mM
0.5xGOx+830U/mL (9.25 s)		10	1000	800-1200	$2.586x10^{-3}$	-	$2.8x10^{-6}$	-
0.5xGOx+830U/mL (18.5 s)		10	1000	800-1200	$2.586x10^{-3}$	-	$2.8x10^{-6}$	-
		200	1000	800-3000	$2.586x10^{-3}$	-	$2.8x10^{-6}$	-
0.5xGOx+830U/mL (37 s)		10	1000	800-1200	$2.586x10^{-3}$	-	$2.8x10^{-6}$	$2.8x10^{-6}$-0.258 mM

2.4 Results and Discussion

In this chapter, an enzymatic cascade reaction was used to test the applicability of a commercially available meander microchannel with integrated oxygen sensors to the study of enzymatic reactions. The goal was to obtain quantitative data on the reaction progress, as well as to assess the limitations of the channel regarding its intended application. The silicon meander microchannel was thus tested using commercially available purified enzymes, to allow a good degree of control on the proportion of enzymes used in the experiments. This information was then applied, together with the kinetic parameters obtained from the activity measurements performed, as input in the built CFD simulation.

The CFD simulations were executed as a complement of the experimental work, in order to aid in the analysis of the obtained data and provide a higher degree of understanding of the reaction occurring inside the microfluidic channel. This was deemed necessary due to the low concentrations of product measured (<1 mM) and significant degree of variability of the data measured in the HPLC (an average of ±0.35 mM for glucose measurements and ±0.04 mM for gluconic acid measurements). This variability can be caused by the manual sampling method, where the depth of the tubing in the sodium hydroxide (NaOH) solution and the time at which the sampling vial is removed from the outlet may add to the observed variability despite the care taken to avoid its influence on the data measured. Another concern that led to the development of the CFD model was the difference in the mass balance of the HPLC measured samples. An average difference of 1.2 mM±1.6 mM was obtained between the glucose and gluconic acid samples, which is higher than the amount of gluconic acid produced. At first, such a difference was thought to occur due to glucose or gluconic acid decomposition in the presence of sodium hydroxide. Both the concentration and amount of NaOH added solution to the reaction samples was decreased, and despite some decrease in mass balance difference, the difference was maintained to a large extent. Therefore, part of the observed mass balance difference probably corresponds to the amount of hydrogen peroxide produced that is not converted to oxygen by catalase, and which was not quantified in the experiments.

2.4.1 Experimental results

A well-studied reaction (oxidation of glucose by glucose oxidase (GOx)), resulting in a 1:1 stoichiometric consumption of oxygen and formation of product, was chosen to achieve a quantitative understanding of an enzymatic reaction based on the integrated oxygen sensors. Knowing the amount of oxygen present, the amount of oxygen consumed would correspond to the amount of product (gluconic acid) formed. The position of the oxygen sensors along the channel can further enable the knowledge of the concentration of product at different residence times, corresponding to the sensor positions, thus providing additional information on the reaction. However, in a closed system such as the silicon and glass channel, the amount of oxygen available is limited by the amount of oxygen provided, which is the oxygen solubility. Hence, at certain glucose concentrations and GOx amounts, oxygen limitation may be reached.

2.4.1.1 Range of enzyme concentration

Figure 15 presents HPLC results of the amount of gluconic acid measured at the outlet for different initial glucose concentrations and GOx activities. If the outlet tube was impermeable to oxygen, the maximum gluconic concentration obtainable would be limited to the oxygen amount inside the channel, the oxygen solubility (0.258 mM). Since for most of the experiments performed the value obtained was above 0.258 mM, it implies that the PTFE tube used at the outlet is permeable to oxygen and therefore the diffused oxygen was involved in the reaction as well.

As can be observed, a higher concentration of product is obtained with the increase of enzyme activity. However, for the highest activity used (150 U/mL), a very low concentration was measured and results for only two glucose concentrations were possible to obtain. The amount of gluconic acid produced was very similar to the values measured for the lowest GOx activity tested. This could indicate that a very low activity of GOx had actually been used in the experiments. However, in Figure 16 the oxygen measurements for the different GOx activities are shown, and it can be observed that the profile for the highest and lowest GOx activity measurements are quite distinct. At the highest GOx activity, oxygen was consumed very fast inside the channel (Figure 16), since for the first sensor a very small concentration of oxygen was obtained for the lowest glucose concentration. Oxygen limitation was thus probably reached in the first portion of the channel and as a consequence the reaction was unable to proceed. As the value obtained at the outlet was close to the amount of oxygen present inside the channel (0.258 mM), it suggests that the reaction was also not performed in the outlet tube when oxygen was again available, indicating a possible enzyme inactivation.

For the remaining tested GOx amounts a higher concentration of gluconic acid was measured with increasing GOx activity.

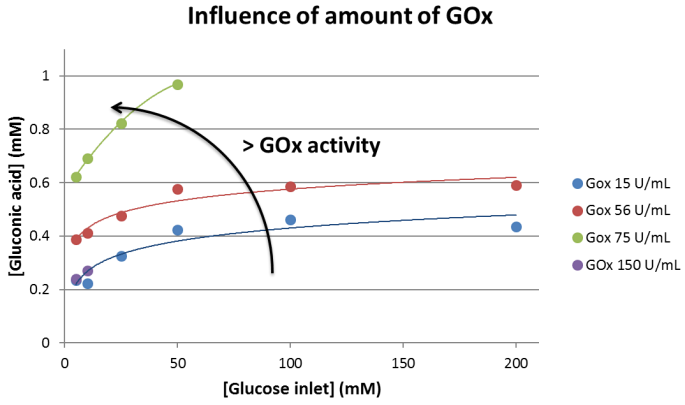

Figure 15 - HPLC measurements at the outlet of the tube for the experiments performed with different amounts of GOx without the presence of catalase.

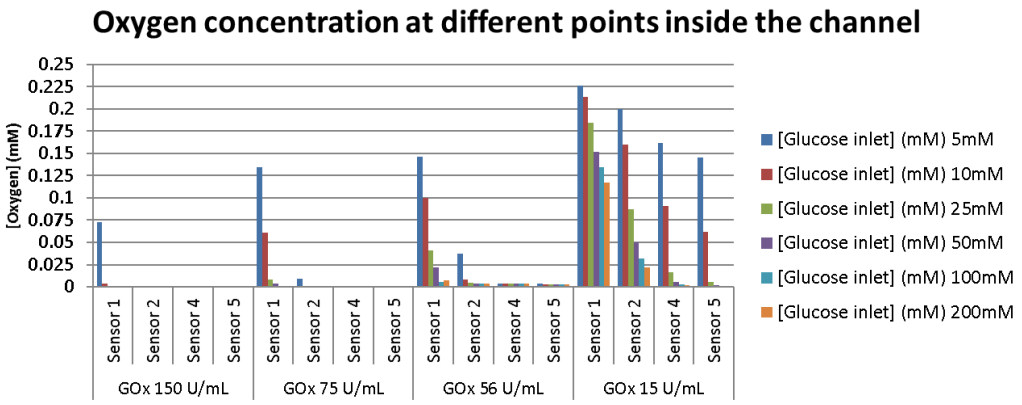

Figure 16 – Oxygen concentration, calculated from oxygen partial pressure values, at the four oxygen sensors for the experiments performed with different amounts of GOx without the presence of catalase.

2.4.1.2 Oxygen sensor calibration curve

Characterization of a new enzyme or comparison of different enzymes, involves the measurement of product formation and/or substrate consumption, so kinetic parameters, substrate specificity, reaction time, etc. can be ascertained. To perform enzyme studies with unknown oxygen-dependent enzymes in the presented meander channel, a correlation between the oxygen values measured in the sensors and the product concentration measured in the HPLC at a given residence time is necessary. Thus, a calibration curve was established where a reference sensor was chosen and its oxygen concentration matched to a gluconic acid concentration measured at the outlet at an equivalent residence time, as presented in Table 10.

To achieve the calibration curve, experiments were performed at four residence times and two enzyme concentrations for six glucose inlet concentrations (Figure 17). The enzyme amounts were selected based on the previous range of enzyme concentration experiments (section 2.4.1.1). The amount of enzyme that allowed performing experiments at longer residence times without achieving oxygen limitation (*1xGOx*) was chosen. Experiments with half that amount (*0.5xGOx*) were also performed in order to have a higher number of experimental points.

As expected, an increase in gluconic acid concentration was obtained with increasing residence time (except for 79.6s, *1xGOx*, 10 mM), and at a higher enzyme concentration. It is also possible to observe a product concentration plateau for the higher glucose concentrations used (50 mM, 100 mM and 200 mM), especially with the increase in residence time. Considering a Michaelis-Menten kinetics, these concentrations could correspond to the substrate saturation of the reaction, meaning that the maximum reaction rate (V_{max}) had been reached. Hence, in this case, with the increase of residence time, a constant increase of product concentration would be expected. However, as can be observed below, gluconic acid concentration at the longest residence time (79.6 s) is the same (for *1xGOx*) or only slightly higher (for *0.5xGOx*) than the product concentration at half that residence time (39.48 s). This again points towards the occurrence of oxygen limitation in the meander channel under the reaction conditions in the meandering channel.

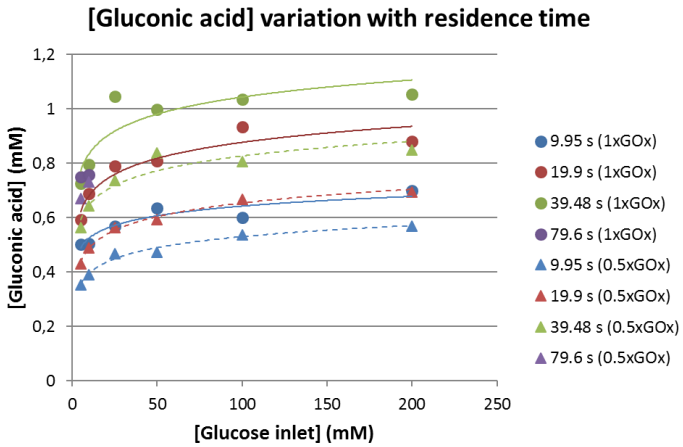

Figure 17 – Gluconic acid concentration for the GOx and catalase reaction performed at different residence times.

The data of the reaction performed at different residence times was used to obtain a calibration curve for oxygen sensor 5, by plotting the gluconic acid values measured in the outlet of the tube against the oxygen concentration values measured at the sensor (Figure 18), as presented in Table 10. The calibration curves for the two tested GOx amounts present similar slopes (1.5 – 1.9 mM of gluconic acid produced per mM of oxygen available). This is in agreement with the assumed enzymatic cascade reaction stoichiometry, since if all the hydrogen peroxide is converted to oxygen, then for each 1 mole of consumed oxygen, half of the produced hydrogen peroxide can be reconverted to oxygen, and 1.5 mM of gluconic acid is produced. However, the previous presented data indicates the occurrence of oxygen limitation, which means that no significant conversion of hydrogen peroxide to oxygen occurs. Thus, the obtained slope should be smaller (between 1 and 1.5 $mM_{product}$ mM_{oxygen}^{-1}). The correlation factor of the obtained slopes was improved when data acquired for the higher glucose concentrations (under oxygen limitation) was disregarded. Simultaneously, the slope of the calibration curves increased to values above the ones expected from the reaction stoichiometry.

The trends obtained for the calibration curves in Figure 18 can thus be an artifact with no real biological meaning, resulting from the high variability of the experimental data and the low oxygen concentration at the reference sensor.

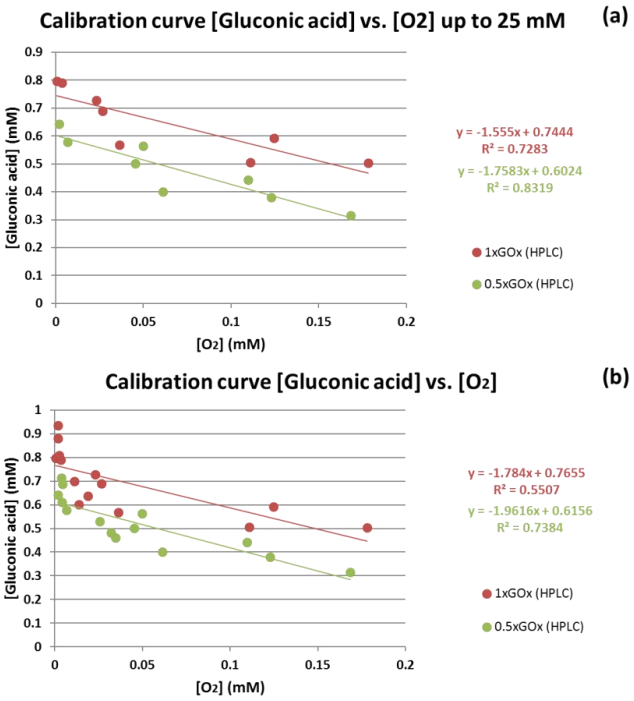

Figure 18 – Calibration curves obtained from experimental data considering experiments up to 25 mM initial glucose concentration (a) or all experiments (b).

2.4.1.3 Increase of oxygen availability inside the channel

As observed in the previous section, oxygen limitation may be easily achieved in this microfluidic system, which can be an issue when performing enzyme screening and reaction characterization. Hence, as a possible solution, different strategies capable of increasing the oxygen concentration inside the system were tested. These strategies involved the introduction of a solution through one of the side inlets (between sensors 2 and 4) available in the silicon meander channel. This side inlet was selected due to its position close to the middle of the microreactor, where a significant decrease of oxygen concentration was expected to occur, and between two of the monitoring points thus allowing a good evaluation of the success of the different applied strategies.

The strategies tested were:

- Increase amount of provided catalase;
- Introduction of oxygen saturated water (through the side inlet);
- Introduction of extra solution of catalase (in different amounts through the side inlet);
- Introduction of hydrogen peroxide (at different concentrations through the side inlet).

Figure 19 presents the summary of the experimental data. As can be observed, a small increase of product concentration was obtained when catalase was added relative to the situation where only GOx is present, but addition of water or extra catalase solutions did not

yield a significant increase of the gluconic acid concentration. If the amount of hydrogen peroxide produced is very small, then addition of increasing amounts of catalase would yield no effect. However, hydrogen peroxide production should be close to the amount of produced gluconic acid, according to the reaction stoichiometry and so sufficient to generate at least 0.10 mM of oxygen. Another explanation is that since the amount of gluconic acid present is approximately the same for the experiments with extra catalase, the catalase reaction rate should be similar between the different experiments, thus resulting in a similar oxygen production from the hydrogen peroxide formed.

The addition of hydrogen peroxide, on the contrary, resulted in an up to 3-fold increase of the amount of gluconic acid produced. Product concentration increased both with concentration of hydrogen peroxide and amount of catalase present. During the experiments with the highest concentration of hydrogen peroxide (0.5 mM), and the highest amount of catalase (830 U/mL), production of oxygen bubbles in the outlet tube was observed, meaning oxygen was being produced in a concentration above the water saturation level (0.258 mM). Since oxygen bubbles can get trapped in the sensors' chambers, this was considered to be the maximum dose of hydrogen peroxide and catalase that could be added in this system for the GOx concentration used. Also, since hydrogen peroxide can lead to enzyme inactivation, higher concentrations or at higher residence times were not considered.

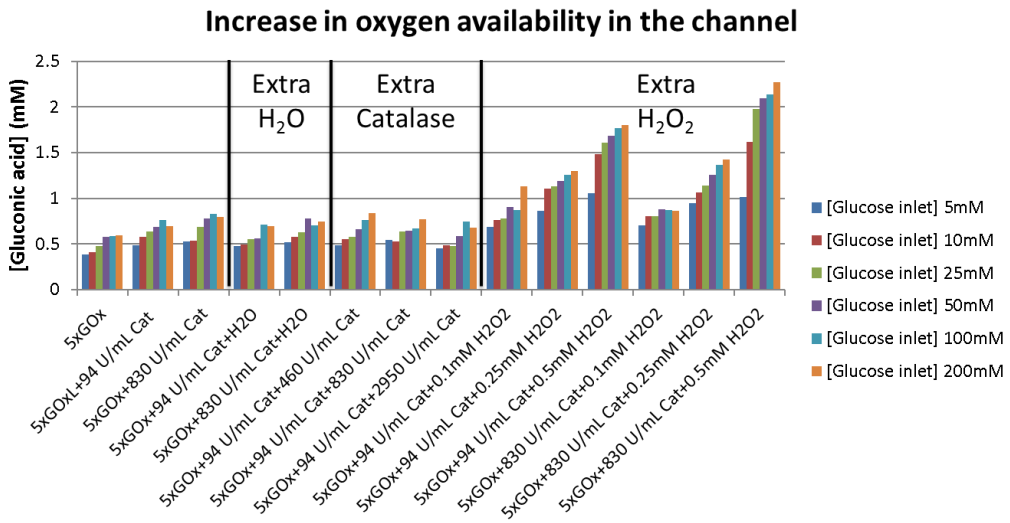

Figure 19 – HPLC measurements at the outlet of the tube for the experiments performed towards increasing oxygen availability in the silicon meander channel.

Even though the oxygen concentration inside the channel can be increased with the presented strategies, when using the silicon meander channel for studying an unknown reaction or cascade reaction, these strategies may not be applicable. There are, however, other strategies for *in situ* oxygen generation, mostly applied in cell culture applications. These strategies can involve:

- a constant flow of air or oxygen gas in the channels or in parallel chambers, which requires the use of bulky pressurized gas cylinders and complex fluidic connections

[229]. This strategy would not be compatible with the presented system, since addition of a flow of oxygen would perturb the oxygen measurements;

- Spatially confined chemical reactions capable of creating (or scavenging) oxygen, such as pyrogallol and sodium hydroxide for scavenging and hydrogen peroxide and sodium hypochlorite for generation. The reactions occur in channels parallel to the cell culture one, taking advantage of the high permeability to oxygen of PDMS. Furthermore, by controlling both reaction rates, different oxygen gradients can be created inside the cell culture chambers [229]. This strategy would also not be compatible with the presented system, since integration of membranes or permeable parallel channels would require a considerable change in design;
- Titanium/ Platinum microelectrodes positioned in channels below the culture chamber, where the amount of oxygen generated is directly proportional to the amount of current running between the anode and the cathode. A special care must be taken in order to quantify and control the amount of reactive oxygen species generated during water electrolysis, which are damaging for biological samples [230]. These electrodes could be integrated in the channel in a similar approach as the oxygen sensors, requiring a membrane to avoid formation of bubbles inside the channel;
- Photocatalytic cells, that mimic a part of the photosynthesis (Photo System II) to generate oxygen from water, are based on the indirect interaction of ultraviolet (UV) light with a semiconducting titanium dioxide (TiO_2) thin film [231], [232], [233]. TiO_2, however, is also used for disinfection of water due to its anti-microbial properties when illuminated and so its application to most cell-based biocatalytic applications can only occur if there is no direct contact between the thin film and the cells, and no accumulation of reactive oxygen and peroxide species [234]. This strategy would also require a change in channel design since silicon is not transparent to UV light and illumination should not be through the top of the channel since UV affects biological materials.

Furthermore, by adding catalase and/or hydrogen peroxide, the values measured by the integrated oxygen sensor cannot be directly used. A well-characterized model of the reaction could be used instead to predict product formation and oxygen levels.

This platform is thus more suitable for studying enzymes with a low activity, a $K_{m\ oxygen}$ lower than oxygen solubility in aqueous solutions or highly diluted samples. However, by greatly decreasing the amount of enzyme used, the concentration of product at the outlet would also be greatly reduced which could lead to issues in the validation of the oxygen measurements. The same issue could be met if a slower reaction would be studied. The balance between enzyme amount, reaction kinetics, residence time, substrate concentration and product concentration are part of the development and optimization of an enzymatic-based system, and the integration of oxygen sensors can facilitate a fast optimization of such parameters by allowing an overview of the (oxidation) reaction proceeding inside the reactor. Moreover, it can allow a fast observation of the effects of other substrates or compounds that can be introduced through one of the 6 side-inlets available.

2.4.2 Simulation data

During the experimental work, as mentioned in the previous section, unexpected phenomena were observed. A very small product concentration was obtained for the highest GOx activity tested. Furthermore, even though the obtained calibration curve presented a slope concurring with the expected cascade reaction stoichiometry, the indication of oxygen limitation in the channel renders it questionable. Finally, when testing different strategies to increase oxygen concentration inside the channel, no significant variation in product at the outlet was observed with the increase of the amount of catalase.

To achieve a better understanding of the observed phenomena and attain a better characterization of the microfluidic system, a computational fluid dynamic model, including the enzymatic cascade reaction, was developed, as explained in section 2.3.7. In the simulation, the experimental conditions and spectrophotometrically measured kinetic parameters were used as initial inputs. By comparing the simulations with the experimental data, an optimization of the input parameters, especially enzyme reaction rate and oxygen diffusivity in the tube, was performed. The final obtained input parameters provide an extra insight into the reaction occurring inside the meander microchannel, as well as a model that more accurately describes it.

2.4.2.1 Mixing and diffusion effects in the CFD simulation

To provide confidence in the developed CFD model, the physical characterization of flow in the microchannel was performed. Hence, some physical phenomena, known to occur in microchannels were evaluated for the developed CFD simulation.

One such phenomena is the "butterfly effect", whereby the components on the top and bottom of the channels have a longer diffusion length (and thus residence time) than in the middle, resulting in a "butterfly" image in the cross section. This effect results from the non-uniform velocity profile in low Reynolds number systems under pressure-driven flows, which generates a difference in residence time of the components in different positions in the channel and consequently a wider diffusion region near the top and bottom of the channel [235]. Such effect was also observed in the simulations and can be observed in Figure 20.

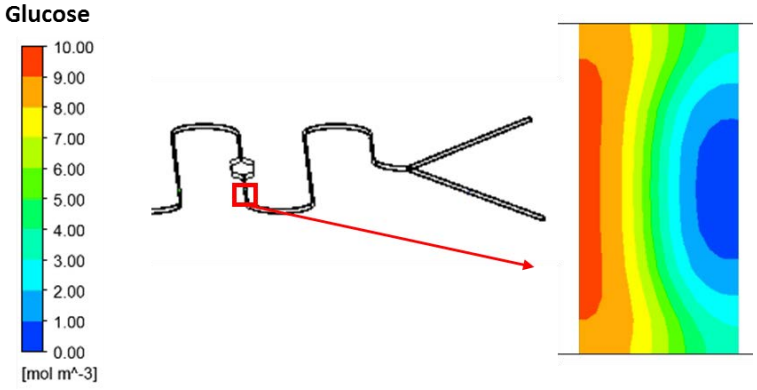

Figure 20 –Cross-section of the simulated silicon meander channel at 1µL s^{-1} 1xGOx+830 U mL^{-1} at 10 mM, highlighting the "butterfly effect".

Lateral diffusion of the different components and corresponding diffusion coefficients used in the CFD simulation were calculated, based on Fick's law as presented in Nock *et al.* (2010) [227] (Equation 23), where D is the diffusion coefficient, x is the diffusion length perpendicular to the flow direction and t is the residence time in the channel.

Equation 23

$$D_{component_{solution}} = \frac{x^2}{4 \times t}$$

As can be observed in Table 14, the diffused distance in a direction perpendicular to the flow by the substances is higher than the width of the channel (> 200 µm) for the diffusion constants considered in the simulation, and so complete diffusion of substrates and products is obtained at both channel locations considered in this work (sensor 5 and tube outlet). However, for the enzymes, these only diffuse between 30 and 125 µm (see Figure 21 for residence time in sensor 5 of 9.25 s corresponding to a diffusion distance of 43 µm). Access of the enzymes to the substrates is then only partial and may result in significant gradient generation across the channel cross-section.

Table 14 – Lateral diffusion of the different components achieved at the position of the reference sensor and the outlet according with Fick's law [227].

Components	D (m^2 s^{-1})	$t_{sensor\ 5}$ (s)	$x_{sensor\ 5}$ (m)	t_{outlet} (s)	x_{outlet} (m)
Oxygen and hydrogen peroxide	$2.1x10^{-9}$	4.625	$1.97x10^{-4}$	9.95	$2.89x10^{-4}$
		9.25	$2.78x10^{-4}$	19.9	$4.10x10^{-4}$
		18.50	$3.94x10^{-4}$	39.8	$5.78x10^{-4}$
		37.00	$5.57x10^{-4}$	79.6	$8.18x10^{-4}$
Glucose and gluconic acid	$6.7x10^{-10}$	4.625	$1.11x10^{-4}$	9.95	$1.63x10^{-4}$
		9.25	$1.57x10^{-4}$	19.9	$2.31x10^{-4}$
		18.50	$2.23x10^{-4}$	39.8	$3.27x10^{-4}$
		37.00	$3.15x10^{-4}$	79.6	$4.62x10^{-4}$
Enzymes	$4.95x10^{-11}$ [197]	4.625	$3.03x10^{-5}$	9.95	$4.44x10^{-5}$
		9.25	$4.28x10^{-5}$	19.9	$6.28x10^{-5}$
		18.50	$6.05x10^{-5}$	39.8	$8.88x10^{-5}$
		37.00	$8.56x10^{-5}$	79.6	$1.26x10^{-4}$

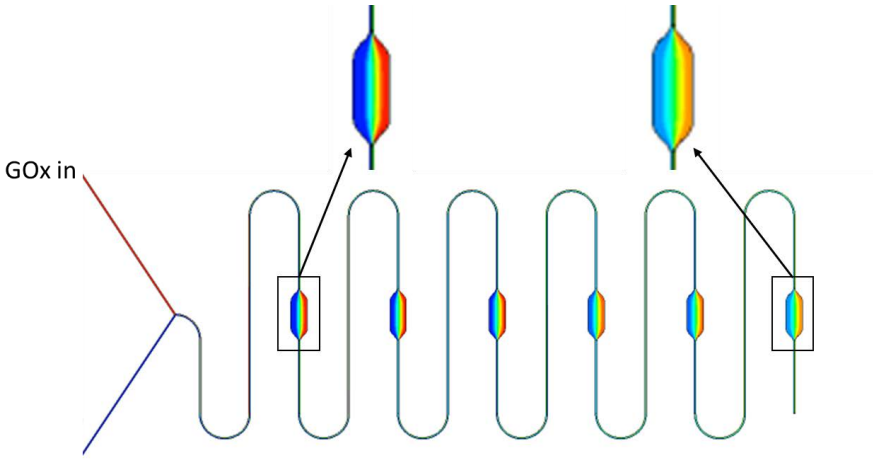

Figure 21 – Simulated *1xGOx* diffusion at 1 µL s^{-1} along the channel considering D=$4.95x10^{-11}$ m^2 s^{-1}.

Simulations were also performed considering the enzyme diffusion as being the same as for the substrates ($6.7x10^{-10}$ m^2 s^{-1}), meaning one order of magnitude faster than the theoretical value. Different experiments and corresponding simulations, at different conditions (e.g. presence or absence of catalase, different residence times, introduction of solutions through a side inlet) are presented in Figure 22. All were simulated considering the two diffusion values, and results are presented side by side (in blue) and compared with the corresponding experimental value (in red).

The use of diffusion values with one order of magnitude difference resulted in a small variation in the oxygen concentration in the sensors, as well as in the concentration of gluconic acid at the outlet at the same k_{cat} (250 s^{-1}). The biggest difference between the compared simulations was observed for *0.5xGOx+830U/mL* (9.25 s), which is highlighted in the figure below. However, as can be observed in the data presented in Appendix I, the observed differences at the different considered diffusion coefficients, were significant enough to consider a different optimal k_{cat} for some of the simulations (300 s^{-1} instead of 250 s^{-1}), while for others a k_{cat} of 1000 s^{-1} was still the value selected. All the values for both simulations are presented in Appendix I.

The small influence of the diffusion coefficient in the data output can be explained if we consider that when the enzymes diffuse completely across the channel width, a dilution of the enzyme occurs. In this case, half the enzyme amount has access to the entire substrate concentration (also half from the inlet concentration). On the other hand, when the enzymes do not diffuse completely across the channel width, the enzymes have access to half of the substrate. However, their faster consumption in half the channel may further promote the substrate diffusion to the portion of the channel containing the enzymes. The resulting substrate consumption and product formation are similar, even though a slightly different reaction rate was obtained for some of the experiments, and thus a similar overall effect is observed.

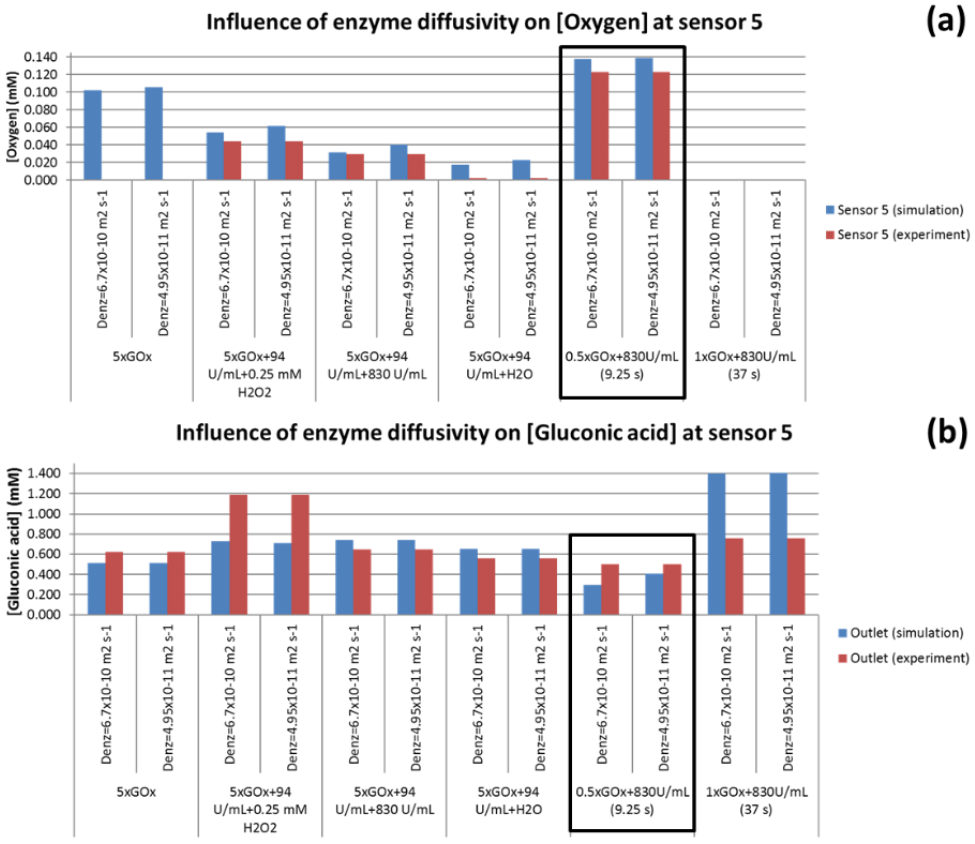

Figure 22 – Influence of the value of diffusivity chosen for the enzymes on the outcome of some of the simulations performed.

Another common effect in microchannels is the development of a parabolic profile (already discussed in Chapter 1). This occurs due to a slower velocity of the flow next to the channel walls, causing an acceleration in the middle of the channel, as can be observed in Figure 23 (a). In Figure 23 (b) it is also possible to observe the effect of the bends of the meander channel and their contribution to mixing. The bends induce a centrifugal force on the fluid, causing an acceleration towards the outside of the channel, exemplified by the deviation from the center of the interface between the two fluids. This rotation is responsible for the asymmetry observed in the "butterfly effect".

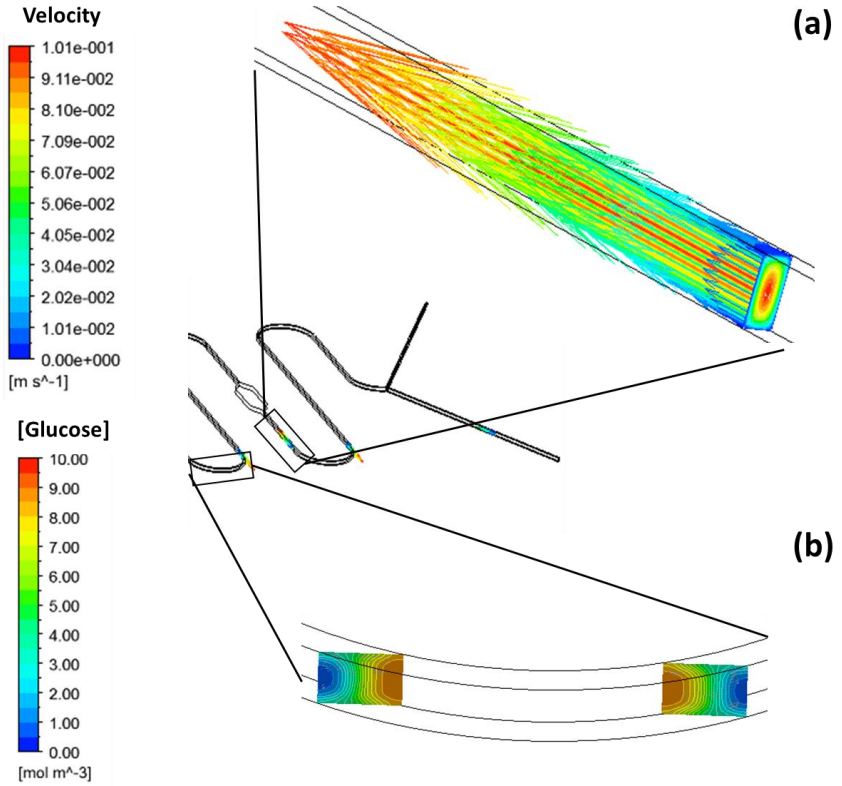

Figure 23 – Axial cross-sections of the simulated silicon meander channel at 1µL s^{-1} 1xGOx+830 U mL^{-1} at 10 mM, highlighting the parabolic profile with velocity vectors (a) and the influence of the channel bends in diffusional mixing (b).

Even though a parabolic profile is observed, no diffusion in the axial direction seems to occur. This is further confirmed, in accordance with the definition presented in Song *et al.* (2012) [235], by the calculation of the Péclet number, *Pe* (Equation 12), for the different velocities used. Axial diffusion can be neglected for *Pe* larger than $\frac{1}{l} = \frac{1}{\frac{L}{W}} = \frac{1}{\frac{Length}{Width}} = 1.98x10^{-4}$. *Pe* was calculated considering the oxygen diffusivity ($2.1x10^{-9}$ m^2 s^{-1}).

Table 15 – Péclet number values for the different velocities used in the silicon meander channel.

$Velocity_{channel}$ ($m\ s^{-1}$)	***Pe***
0.05	2381
0.025	1190
0.0125	595
0.00625	298

According to Figure 24, especially for glucose, it is possible to observe that from the fourth sensor spot onward, a relatively homogenous and well-mixed solution is observed. In terms of the oxygen concentration, and thus of how representative the oxygen measurements obtained

from the integrated sensor spots are, the figure shows a good homogeneity in all the sensor spots except for the first one (sensor 1). The performed measurements at the sensor counted as reference (sensor 5) can thus be considered as representative of the solution at the corresponding residence time.

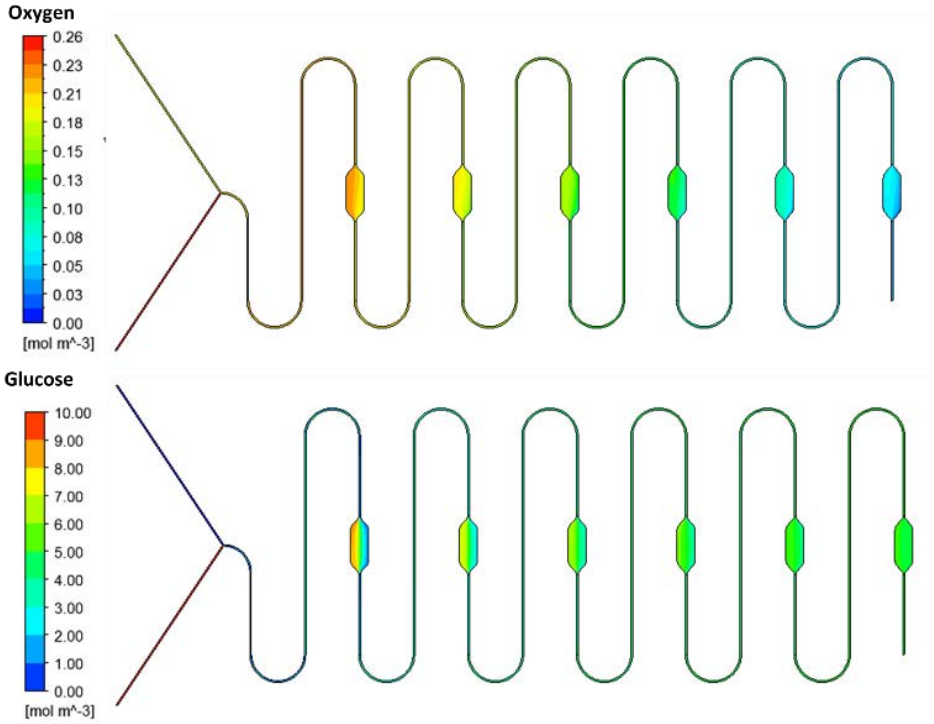

Figure 24 – Oxygen (top) and glucose (bottom) concentrations along the simulated silicon meander channel at 1µL s^{-1} 1xGOx+830 U mL^{-1} at 10 mM.

2.4.2.2 Range of enzyme concentration

Simulations mimicking the reaction with only GOx (section 2.4.1.1) inside the silicon meander channel plus outlet tube system were performed with k_{cat} of 300 s^{-1}, 800 s^{-1} and 1000 s^{-1} (a range which includes the values measured spectrophotometrically (300 to 500 s^{-1}) and is lower than the value found in literature, 1440 s^{-1} [236], [202]) (Figure 25). Similar values of product concentration (Figure 25 (b)) were obtained except for the 150 U/mL experiment, where a much higher concentration of gluconic acid was obtained in the simulation. This clearly indicates the occurrence of an issue in the corresponding experiment (e.g. different enzyme concentration, lower initial oxygen concentration, enzyme inhibition due to low oxygen concentration), while highlighting the usefulness of a reaction model, such as the one presented. Parameters such as enzyme concentration and k_{cat} or oxygen concentration could easily be varied in the model in order to explain which issue occurred experimentally. This was, however, not performed due to time constraints, since the parameters are changed manually in the model.

From Figure 25 (b), it is possible to assume that 300 s^{-1} is the turnover number associated with the glucose oxidase used in the experiments, which is similar to the values obtained experimentally (300 to 500 s^{-1}). This value resulted in the smallest deviation from the experimental product at the outlet. However, if only the oxygen sensor data was available, another turnover number, 800 s^{-1}, would be the selected value, which highlights the need of a comprehensive data set when validating such models.

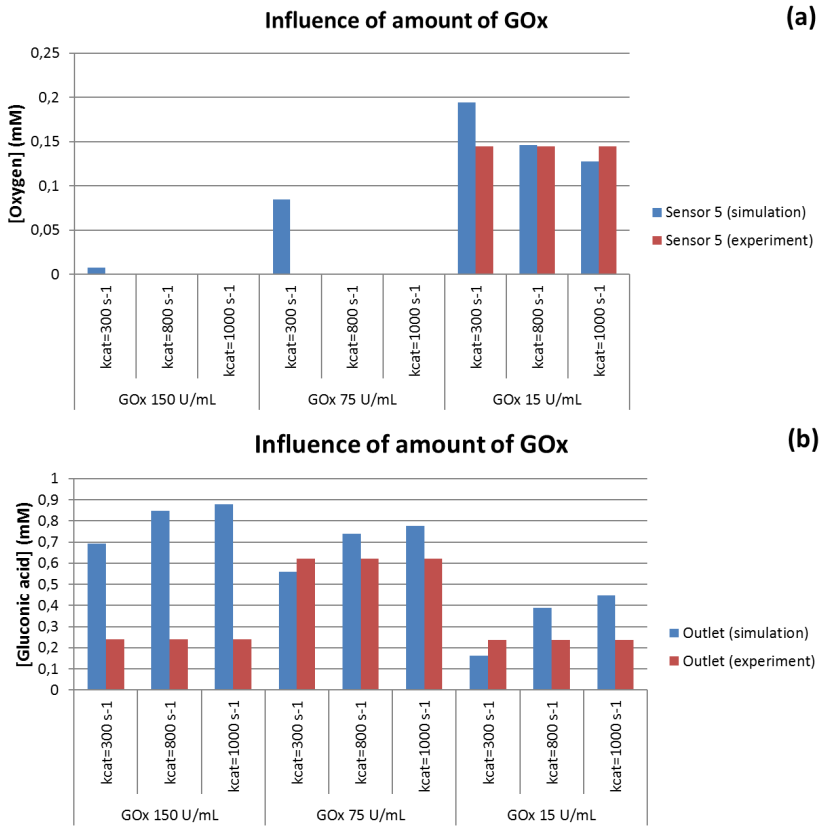

Figure 25 - Comparison between the CFD simulations and experiments performed with different amounts of GOx and 5 mM initial glucose concentration for (a) the oxygen measured in sensor 5 and (b) gluconic acid measured at the outlet of the tube.

2.4.2.3 Oxygen sensor calibration curve

Simulations were also performed for the different residence times and enzyme concentrations at 10 mM inlet glucose concentration (Figure 26). For this set of simulations, a higher k_{cat} of 1000 s^{-1} allowed to better match the measured oxygen values at sensor 5. This value is close to 4-fold the one used in the previous simulations (300 s^{-1}), which indicates that the GOx activity measured experimentally was not correct for this enzyme solutions, thus resulting in a change in the kinetic parameters that best fit the model. This is again a good

example of how models such as the one presented in this work can aid and complement laboratory work.

As expected, from the experimental data presented in section 2.4.1.2 in Figure 17, an increase in gluconic acid concentration is obtained with increasing residence time, and a higher concentration is obtained for the higher enzyme concentration. However, in the simulations a much higher concentration of gluconic acid was obtained for 79.6 s residence time. This can indicate that either the experimental residence time was lower than the one considered in the simulation (and thus the considered flow velocity was higher), or that there is some factor limiting the enzyme performance. A relevant factor could be the concentration of hydrogen peroxide present, whose concentration (and hence inactivating effect) would increase with the residence time. In the presented simulations, inactivation of the enzymes due to the presence of hydrogen peroxide was not considered, since this was not initially assumed to influence the performed reactions for most of the experimental conditions tested.

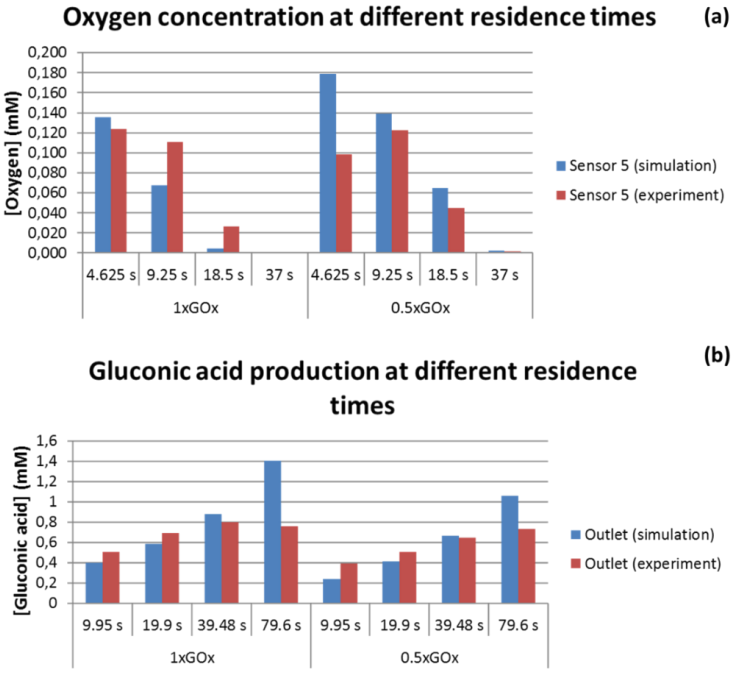

Figure 26 - Comparison between the CFD simulations and experiments performed for different residence times and amount of GOx with 830 U/mL catalase present at 10 mM initial glucose concentration for (a) the oxygen concentration measured in sensor 5; and, (b) the gluconic acid concentration measured at the outlet of the tube.

Simulations were also performed at a higher glucose concentration (200 mM) for *0.5xGOx+830 U/mL Cat* and *1xGOx+830 U/mL Cat* for the residence time at the outlet of 39.48 s. As can be observed in Figure 27, the simulations were capable of predicting values of the obtained gluconic acid concentration that were similar to the ones achieved experimentally, indicating that the observed stabilization of product concentration is most likely due to the enzymatic system at the conditions in the tube. It is relevant to highlight that the experimentally observed gluconic acid, glucose and oxygen concentrations result from a

combination of the flow conditions applied, the channel geometry, the rate of the enzymatic reactions and the diffusion characteristics of the different components involved. In order to fully understand the influence of each of these parameters on the reaction dynamics, models that account for the influence of flow, geometry and diffusion on reaction dynamics, such as the one presented in this chapter, are required.

From what can be observed in Figure 27, hydrogen peroxide does not seem to yield an inactivation effect in the performed experiments, which is expected since according to the simulations, concentrations of up to 1 mM (lower than the inactivating concentration) were obtained. The divergence between the simulation and the experimental data for the 79.6 s residence time is thus most likely due to oxygen limitation conditions, since experiments at glucose concentrations higher than 10 mM could not be performed due to very fast oxygen consumption inside the channel. The model was however not capable of capturing this phenomenon, and hence further optimization of the kinetic parameters used or oxygen diffusivity is required.

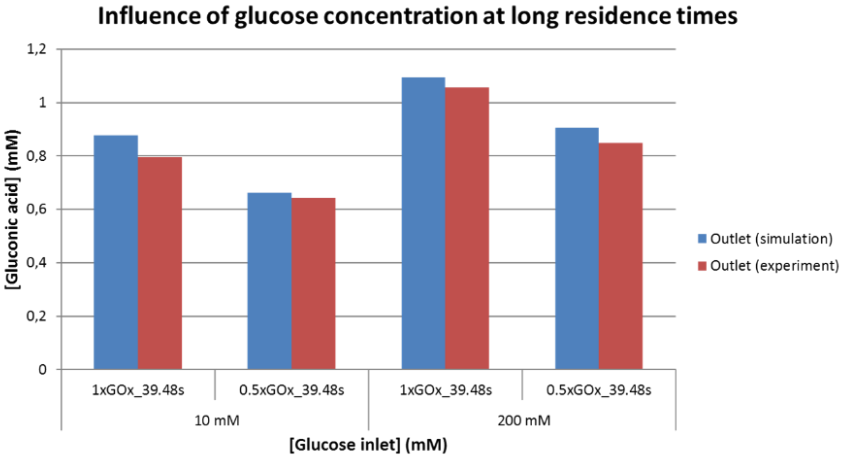

Figure 27 – Comparison between the CFD simulations and experiments performed for different glucose concentration and amount of GOx at 0.5 µL s^{-1} for the gluconic acid measured at the outlet of the tube.

2.4.2.4 Increase of oxygen availability inside the channel

To avoid reaching oxygen limitation inside the channel, a known amount of catalase was added to the GOx reaction. Catalase is capable of decomposing hydrogen peroxide (a side-product of glucose oxidation) to oxygen and water, in a 1:2 stoichiometry of oxygen to hydrogen peroxide. So, for every 0.1 mM of hydrogen peroxide consumed, 0.05 mM of oxygen are expected to be produced, assuming that a sufficient amount of catalase is present, in order to maintain a minimum oxygen concentration inside the channel and a good control on the amount of oxygen provided [210].

Figure 28 presents a comparison between experimental and simulation data for the addition of 830 U/mL of catalase to different concentrations of GOx. It is possible to observe in Figure 28 (b), that approximately the same amount of product was obtained for *5xGOx* and *1xGOx*, while a concentration above half of *1xGOx* was obtained for *0.5xGOx* in the experimental

data. This again indicates that oxygen limitation was reached inside the channel for the highest concentration of GOx, which would explain a similar product concentration as for *1xGOx*. On the other hand, a very small increase in gluconic acid with increase of GOx concentration was obtained for the simulation data, indicating that the influence of GOx concentration on the reaction, at the concentrations used is highly dependent on the amount of oxygen available in the reactor. Once more, it is possible to observe that the differences between experimental and simulated data observed in terms of oxygen values do not always translate into similar differences in the gluconic acid values.

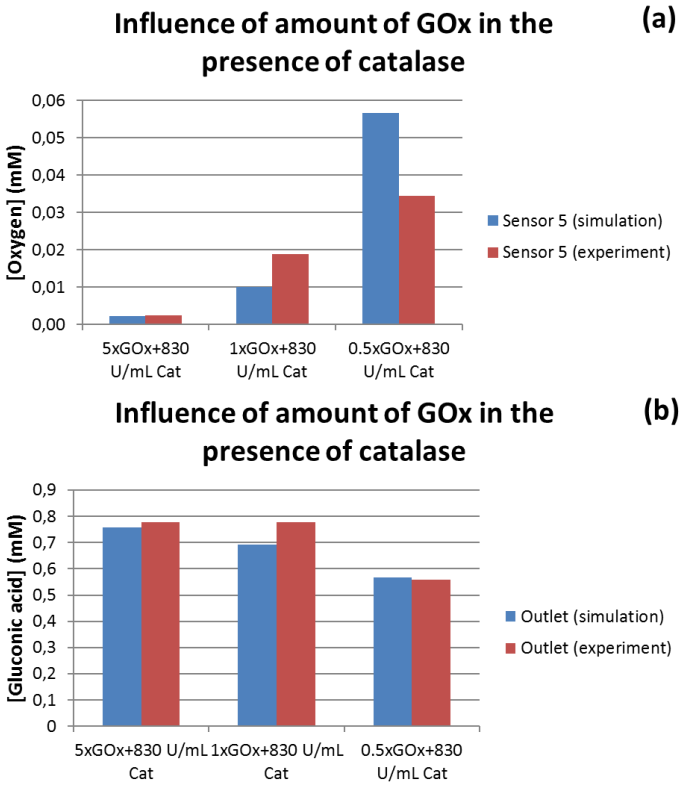

Figure 28 - Comparison between the CFD simulations and experiments performed with different amounts of GOx at the same catalase concentration and 50 mM initial glucose concentration for (a) the oxygen measured in sensor 5 and (b) gluconic acid measured at the outlet of the tube.

The tested strategies to increase oxygen concentration inside the channel (addition of water, extra catalase and extra hydrogen peroxide solutions through a side inlet presented in section 2.4.1.3, Figure 19) were also simulated. Simulations were performed for two catalase amounts at the inlet, and 1 type of side solution (water, catalase 830 U/mL and 0.25 mM). The corresponding simulated experiments (Figure 29) showed a similar trend as observed experimentally. Added water did not yield an increase in product concentration, but addition of extra catalase resulted in a small increase in gluconic acid concentration. In this set of simulations, both the extra catalase and extra hydrogen peroxide simulations were performed

with an increased $k_{catalase}$ of 0.2586 s^{-1} and 2.586 s^{-1}, respectively, compared with 2.586x10^{-3} s^{-1} used for the other simulations. By altering the catalase reaction rate in order to match the measured oxygen values, the amount of obtained gluconic acid was slightly increased. Addition of hydrogen peroxide resulted in the highest increase, but still smaller (less than 2-fold) than the one observed experimentally. Since the difference in oxygen concentration at sensor 5 (Figure 29 (a)) between experimental and simulated points is small, the difference in product concentrations at the outlet (Figure 29 (b)) can be due to a difference in oxygen availability in the outlet tube portion, relative to the one of the experiments. However, as the values are significantly lower than the experimental ones for the hydrogen peroxide simulation, the assumed $k_{catalase}$ value is probably lower than the real one when hydrogen peroxide is present. In Appendix I, Table 2 it is possible to observe that even at the highest tested $k_{catalase}$ (25.86 s^{-1}), the experimental values were not achieved and the oxygen values presented a higher difference than with 0.2586 s^{-1}.

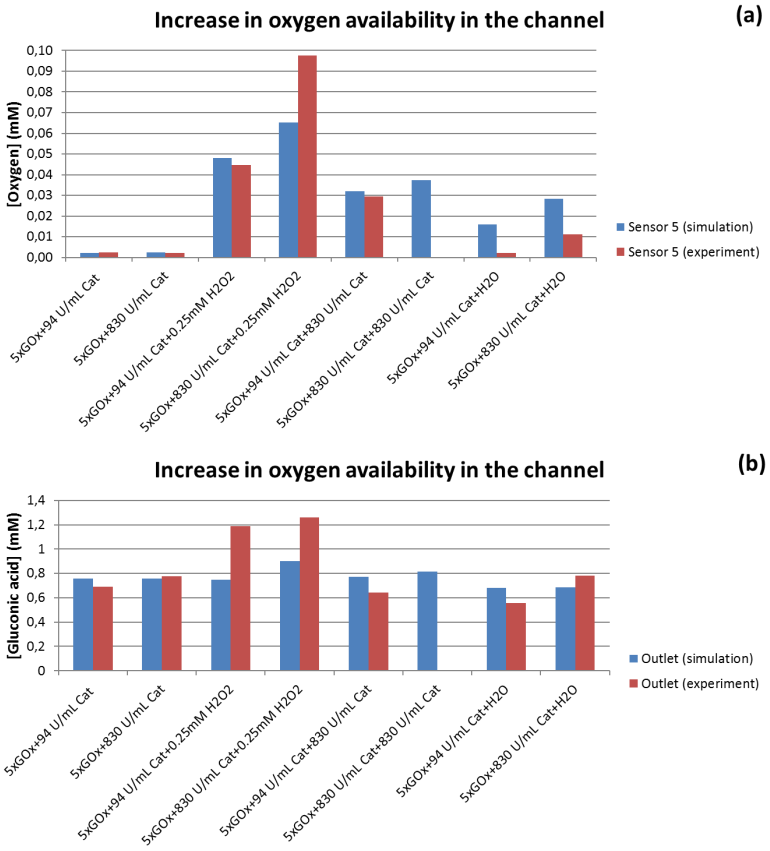

Figure 29 – Comparison between the CFD simulations and experiments performed towards increasing oxygen availability in the silicon meander channel, for (a) the oxygen measured in sensor 5 and (b) gluconic acid measured at the outlet of the tube at 50 mM initial glucose concentration. No experiment was performed corresponding to 5xGOx+830 U/mL Cat+830 U/mL. One of the simulations (5xGOx+830 U/mL Cat+830 U/mL Cat) does not have a corresponding experiment, because it was only deemed interesting to perform an experiment when performing the simulations.

2.4.3 Observations from the CFD simulations

Some parameters in the simulations were altered relative to the ones obtained through spectrophotometric activity measurements. The catalase reaction rate was one of such parameters. As can be seen in Figure 30 (a) it was necessary to significantly increase this parameter in order to more closely match the oxygen concentration values measured experimentally. This may indicate that the addition of hydrogen peroxide to the reaction, led to a change in the catalase reaction rate.

On the other hand, the GOx kinetic parameters obtained from spectrophotometric measurements are apparent kinetic values for the reaction, since they were obtained for a single (and not well controlled) oxygen concentration. Furthermore, along with the catalase reaction rate, they were measured at different conditions (especially in terms of substrate availability) compared to the performed reactions, and thus introduce a deviation from the real case inside the microreactor, that the simulations allow to highlight.

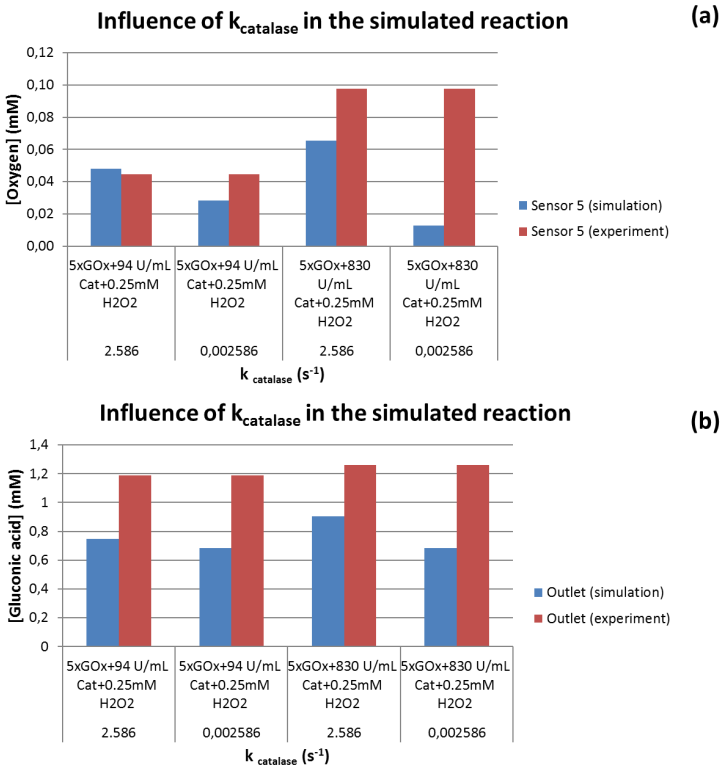

Figure 30 – Effect of the use of different rates of hydrogen peroxide decomposition in the CFD simulations and comparison with experimental data at 50 mM initial glucose concentration for (a) the oxygen concentration measured in sensor 5; and, (b) the gluconic acid concentration measured at the outlet of the tube. These simulations were performed considering diffusivity of oxygen in the tube as 2.8×10^{-6} cm^2 s^{-1}.

The amount of oxygen diffusing through the outlet tube to the enzymatic solution is also an important parameter to consider in the simulations. Thus, simulations were performed where either the oxygen concentration at the interface between the tube and the fluid was fixed

at the maximum possible concentration of soluble oxygen (0.258 mM), or oxygen diffusivity was varied between $2.8x10^{-7}$ and $2.8x10^{-5}$ cm^2 s^{-1}. This variation in oxygen transferred through the tube was performed for two of the residence time experiments, 9.95 s and 79.6 s residence time at the outlet, respectively (Figure 31). When 0.258 mM was considered at the interface, a significant increase of gluconic acid concentration was obtained for the highest residence time (79.6 s). This increase was obtained even though at the fastest residence time the difference between simulated and experimental values is small. The value of gluconic acid concentration, however, was more than 2-fold the experimental one, indicating that the amount of oxygen being transferred is between the theoretical diffusivity value for PTFE and the maximum oxygen concentration (0.258 mM). However, also for the other values of diffusivity simulated (10-fold and 100-fold the theoretical value) the gluconic acid concentration at the outlet was higher than the experimental value for 79.6 s. When all the simulations were performed with both diffusivity values, the 10-fold diffusivity seemed to yield values closer to the experimental data and was thus chosen for data comparison in the previous graphs unless stated otherwise (check Appendix I).

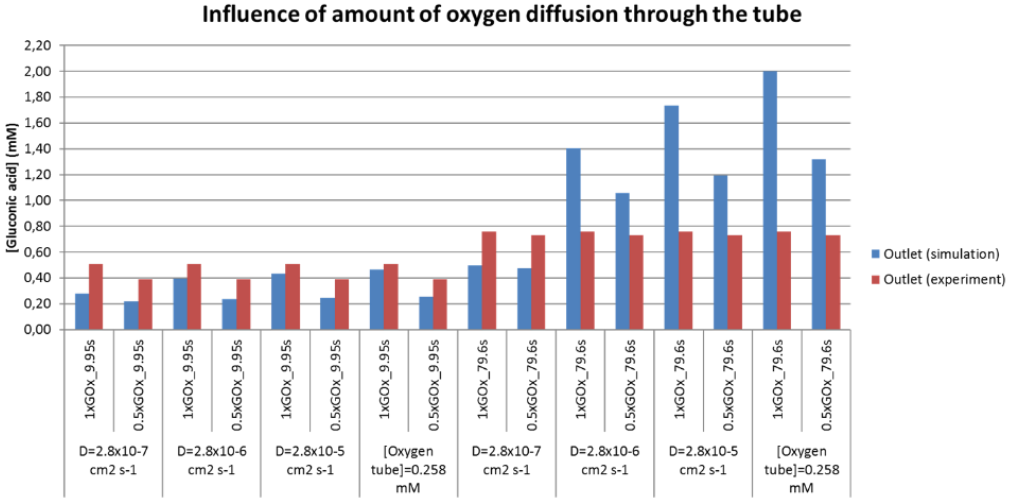

Figure 31 - Comparison between the CFD simulations and experiments performed at 10 mM initial glucose concentration but considering either oxygen diffusivity in the tube or a fixed concentration of oxygen at the interface between the tube and the fluid.

Figure 32 shows the distribution of oxygen concentration inside the tube and inside the fluid for the longer residence time and smaller enzyme concentration. It is possible to observe that for the smaller oxygen diffusivity value (*D theo* in the figure corresponds to $2.8x10^{-7}$ cm^2 s^{-1}) for the tube, no oxygen or a very low concentration seems to be transferred to the fluid (Figure 32 (b)). On the other hand, when the oxygen concentration at the interface is fixed at the maximum oxygen solubility value, a three-fold increase in oxygen concentration is observed in the middle and outlet of the tube, thus explaining the considerably higher product concentration values obtained for this simulation. On the contrary, for the shortest residence time and with a higher enzyme concentration, even though increasing the oxygen concentration at the interface increases the oxygen concentration in the bulk, the difference relative to the lowest diffusivity

case is not as sharp, as observed in Figure 33. There is a higher oxygen availability at the inlet of the tube in this case, which in turn reduces the influence of oxygen diffusing from the tube. The oxygen concentration values obtained at the outlet and in the middle of the tube are very similar in this case.

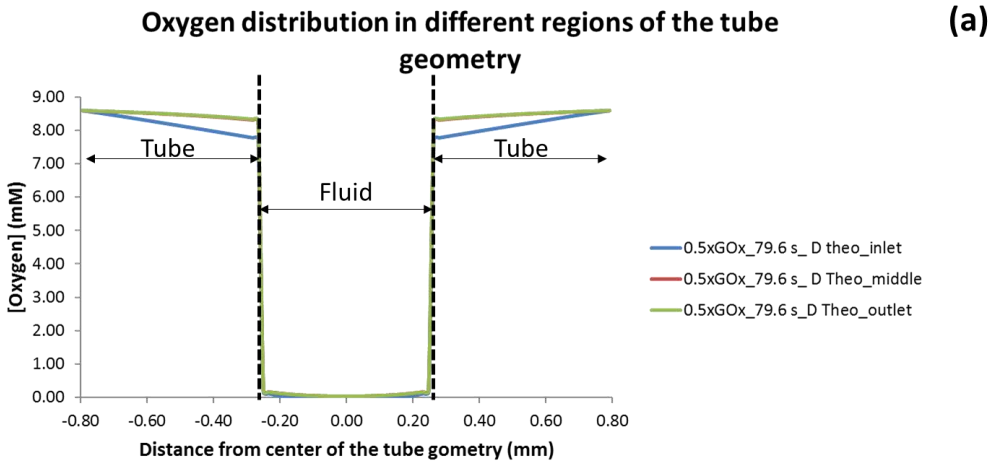

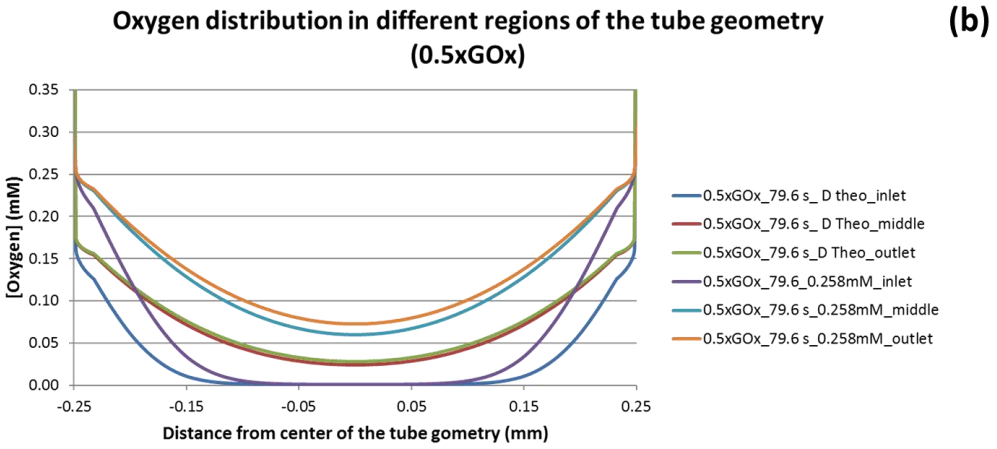

Figure 32 – Oxygen distribution in different regions of the tube and fluid for the longer residence time and 0.5xGOx, considering $D=2.8\times10^{-7}$ cm^2 s^{-1} (a) and oxygen distribution in the fluid considering $D=2.8\times10^{-7}$ cm^2 s^{-1} or oxygen concentration at the interface equal to 0.258 mM (b).

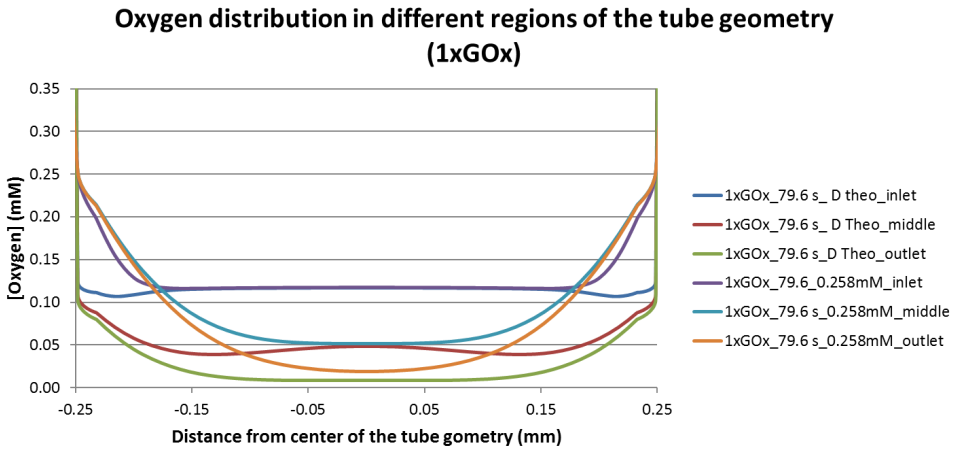

Figure 33 – Oxygen distribution in the fluid considering D=2.8x10^{-7} cm^2 s^{-1} or oxygen concentration at the interface equal to 0.258 mM.

Besides oxygen diffusivity, the influence of $k_{catalase}$ for the reaction occurring only in the tube region was also tested. In this set of simulations, the possible influence of an increased concentration of hydrogen peroxide (relative to the reaction in the meander channel), which would result in a different reaction rate for catalase, was tested. Simulations of *1xGOx* at 1 µL s^{-1} (19.9 s residence time at the outlet) were performed in the tube for $k_{catalase}$ values between 2.586x10^{-3} s^{-1} and 25.86 s^{-1} considering an oxygen diffusivity in the PTFE tube of 2.8x10^{-7} cm^2 s^{-1}. The latter value of diffusivity was used, instead of 2.8x10^{-6} cm^2 s^{-1} used in the other experiments, to discard the effect of increased oxygen diffusivity. As can be observed in Figure 34, only $k_{catalase}$ values above 2.586 s^{-1} seem to significantly affect the obtained gluconic acid concentration. However, even at the highest $k_{catalase}$ value, the experimentally measured values were not achieved, and thus this should not be a significant factor in the reaction occurring in the tube.

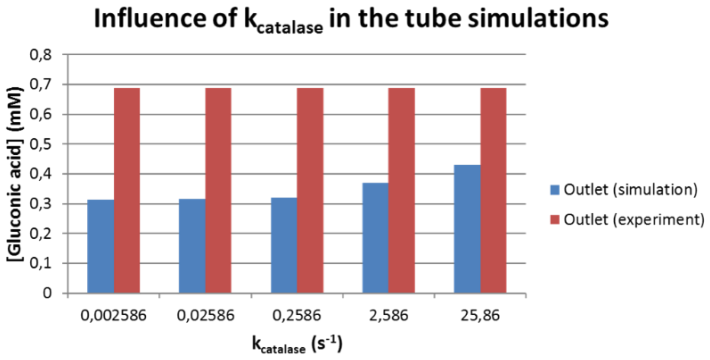

Figure 34 - Comparison between the CFD simulations and experiments performed at 10 mM initial glucose concentration and 1 GOx with 19.9 s residence time but considering different $k_{catalase}$ values in the tube.

A well-characterized model of the reaction could be used to predict product formation and oxygen levels. However, as can be observed from the presented simulations, such model may be complicated and time-consuming to achieve, especially in terms of the selection of appropriate kinetic parameters. The different parameters tested in the simulations were manually changed and are thus most likely not realistic values. Coupling of the above CFD model with a mechanistic kinetic model, capable of performing parameter optimization, would yield a better fit to the data, while simultaneously providing more accurate kinetic parameters. The most relevant parameters requiring optimization in the developed model are GOx turnover number, catalase reaction rate, oxygen concentration at the inlets and oxygen diffusivity through the PTFE tube. Furthermore, even though several mechanistic models, already applied to the study of the coupled GOx and catalase reaction, are based on the two-substrate Michaelis-Menten kinetic mechanism [202], this is a simplification of the actual mechanism of the enzymatic cascade reaction, and may introduce a certain degree of error in the obtained simulation results. For example, one of the assumptions is that the amount of oxygen present is considerably higher than the concentration of GOx [202], which in the case presented is not always true. Thus, the connection to a mechanistic model, where different reaction mechanisms could be rapidly tested, would also greatly improve the applicability of this model to other enzymes and/or cascade reactions.

Such a mechanistic model, validated with oxygen imaging experiments, and its usefulness has already been demonstrated by Ungerböck *et al.* (2013) for a similar microreactor and the glucose oxidation reaction with GOx [135]. They were capable of modeling the Ping Pong Bi-Bi reaction mechanism both for a batch and a microreactor, finding the reaction of the reduced form of the enzyme with oxygen as the rate limiting step. Furthermore, they observed that the Michaelis-Menten kinetics was able to appropriately describe the reaction in the microreactor. They also concluded that for most microfluidic systems, studies can be performed without considering diffusion through convection [135]. Tao *et al.* (2009) developed a mechanistic model for the coupled GOx and catalase reaction, which was also validated with experimental oxygen measurements with and without cell respiration [237]. They also assumed a Ping Pong Bi Bi type mechanism where all the reactions were irreversible for GOx and a first order reaction for catalase. However, they observed that at 25 ^{0}C, the catalase reaction seemed to have a higher order (1.5) than the one assumed and observed at 37 ^{0}C (1), apparently depending on temperature. They proposed another reaction mechanism for the catalase reaction that included the reverse of the first reaction (production of water after reaction with the first hydrogen peroxide molecule) [237].

The use of a mechanistic model coupled with CFD simulation of the reactor and connected online or offline with the oxygen sensors integrated in the silicon meander channel would significantly improve the amount of information collected from the silicon meander channel, since several kinetic mechanisms and parameter values could be compared with the data, both from the sensors and from the quantification of reaction components at the outlet. This would increase the characterization speed of the reaction and/or enzymes being tested, but also the quantification of reaction parameters that are usually difficult to measure experimentally (e.g. certain reaction rates, K_m of the different substrates in a multi-substrate reaction).

2.4.4 Use in a modular platform

Since the focus of this thesis is the development of a modular microfluidic platform for enzyme screening, the silicon meander channel was tested as part of a modular platform by connecting it to other simple microfluidic systems: a commercial polymeric valve chip and a PMMA meander channel fabricated in-house.

2.4.4.1 Connection to a valve chip

The silicon meander channel was connected to a valve microfluidc chip from Microfluidic ChipShop as explained in section 2.2.2.2 and the 21 µL volume outlet channel was used as presented in Figure 35. A solution of Gluzyme (0.2 g L^{-1}) was continuously pumped through the silicon meander channel, while pulses of glucose at different concentrations were introduced using the valve system, and alternated with water.

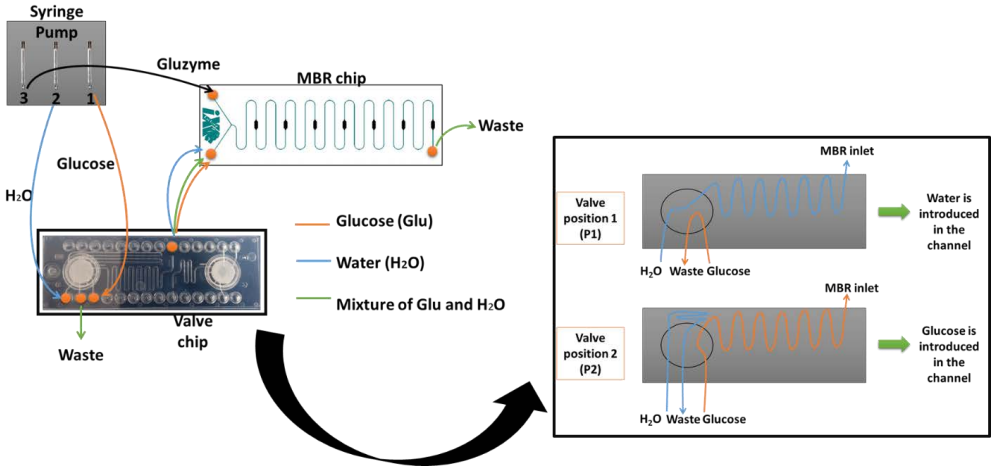

Figure 35 – Schematics of valve chip and silicon meander channel assembly.

As can be observed in Figure 36, for the majority of the glucose concentrations tested a stable value for oxygen partial pressure was obtained when only Gluzyme was present. Introduction of glucose caused a rapid decrease in oxygen values, which tended to be faster the higher the glucose concentration. Also, a lower value of partial pressure was obtained for the slower flowrate used (0.4 µL s^{-1}), since the residence time inside the reactor was increased.

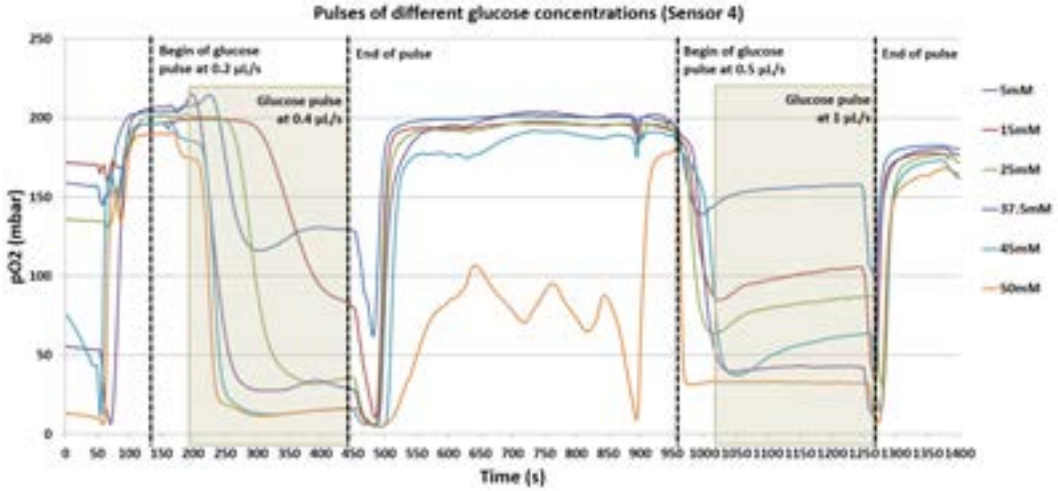

Figure 36 – Variation of oxygen partial pressure in sensor 4 when pulses of glucose at different concentration are introduced in the silicon meander channel at two different flowrates.

The two-chip assembly operated for a minimum of 60 minutes at a time without leakage, and a rapid effect of the introduced solution was observed with the integrated oxygen sensors. Before performing the experiment presented in Figure 36, a test with a food coloring dye (since the valve ship is transparent) was performed. This test intended to more precisely time how long after switching the valve position (for glucose introduction), it would take for the glucose pulse to reach the meander channel (time required to flow through the 21 µL outlet channel plus the outlet tube connecting to the silicon meander channel). This visual test, which main steps are presented in Appendix II, allowed a more detailed and accurate interpretation of the oxygen signal observed during the experiment with Gluzyme and glucose.

2.4.4.2 Connection to a PMMA meander channel

The silicon meander channel was also connected to an in-house developed PMMA meander channel, as presented in Figure 37. This meander channel was the first version of the thermal inactivation platform, whose final version will be discussed in Chapter 5. The enzymatic reaction performed in this reactor was used as reference to evaluate the efficiency of the applied enzyme inactivation strategy. Without the application of temperature, this channel allowed to greatly extend the reaction time to around 132 s (10.08 µL + 79.5 µL of connecting tube + 44 µL of PMMA channel), which resulted in a significantly larger concentration of gluconic acid (Figure 38). However, as observed before, a stabilization of product concentration occurred for the higher initial glucose concentrations. This is an indication that at these concentrations oxygen limitation was again achieved, and that the oxygen diffusing through the PMMA material can still not compensate the amount being consumed in the reaction.

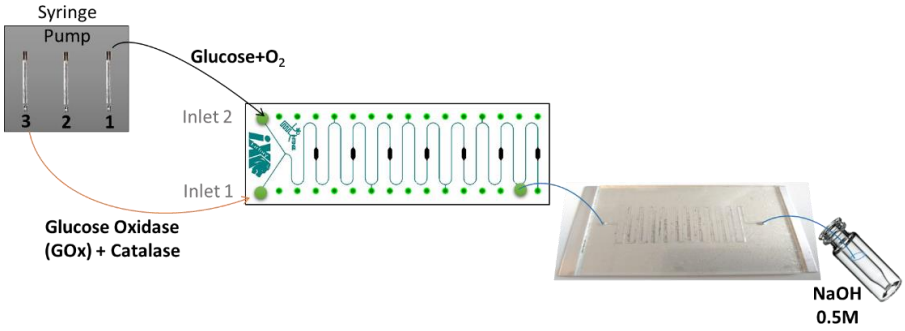

Figure 37 – Schematics of assembly of the silicon meander channel with the PMMA meander channel.

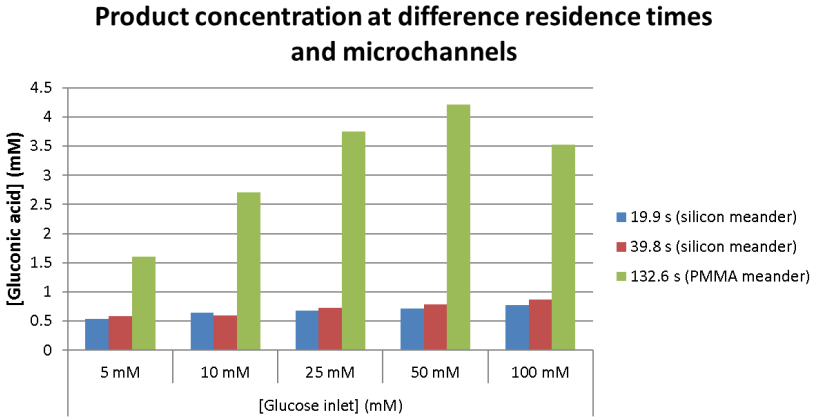

Figure 38 – Concentration of gluconic acid at the outlet of the silicon meander channel and at the outlet of the assembled silicon meander and PMMA meander channel, for the same enzyme concentrations.

2.5 Conclusions

In this chapter, a commercially available silicon and glass meander microchannel with integrated oxygen sensors was investigated as an online monitoring and reactor unit operation in a microfluidic modular platform for screening of oxygen-dependent biocatalysts. The silicon meander channel was used to monitor the oxidation of glucose by glucose oxidase coupled to the decomposition of hydrogen peroxide by catalase. A CFD model of the enzymatic cascade reaction was also developed and its prediction compared with the experimental data.

Oxygen availability was identified as a major issue in the system, since a rapid oxygen consumption occurred with increasing enzyme and substrate concentration, which was closely mimicked in the performed simulations.

To increase the applicability of the meander channel, several strategies for increasing oxygen concentration inside the channel were tested. These involved either introduction of more oxygen, simply by introducing a fresh solution in the middle of the channel, or *in situ* oxygen generation by increasing the amount of catalase present and/or introducing hydrogen peroxide.

Hydrogen peroxide introduction allowed to significantly increase the amount of formed product at the outlet. However, in this case the obtained simulations under-estimated this value, which signifies the kinetic parameter used ($k_{catalase}$) was probably also below the real value.

To validate the information provided by the oxygen sensors, a strategy was developed whereby the oxygen concentration in a reference sensor at a certain residence time was matched to the product concentration quantified in a standard analytical equipment (HPLC) for the same residence time. This strategy allowed a direct connection between the oxygen and product concentrations, if the reaction is not at oxygen limitation in the sensor used for reference. In the presented experiments, this was a significant issue, but calibration curves with similar slopes were obtained, which seems to indicate the feasibility of this strategy. Another approach, would be to integrate sensors for the quantification of the other compounds involved in the reaction (e.g. glucose sensors) in the same microfluidic platform or in a modular unit in sequence (see microfluidic module for sensor integration in Chapter 4). However, to achieve this the reaction would have to have stopped at the point of substrate(s)/product(s) quantification. A simple and unspecific way of attaining this is thermal inactivation, for which another microfluidic platform (presented in Chapter 5) was developed. An alternative to the developed thermal inactivation platform, could be *in situ* heating of the reaction mixture in the tube, immediately at the outlet of the silicon meander channel. This would have the added issues of isolating the silicon chip from the heat source, while complicating the heating setup required. Another alternative could be the introduction of an inactivating compound through one of the last side inlets or in a T-junction place in the outlet tube. The sensors for quantification would, however, have to be immune to the chosen inactivating compound (e.g. sodium hydroxide).

Several parameters in the CFD simulations were also varied for a single experiment to check its possible effect on the obtained simulation output. Even though $k_{catalase}$ increase resulted in an increased gluconic acid concentration at the outlet, its effect is less significant than the amount of oxygen diffusing through the outlet PTFE tube, with which it was possible to match most of the experimental data. A difference of one order of magnitude was found for PTFE oxygen diffusivity relative to the value found in the literature.

The accuracy of the developed model would be significantly increased if it was coupled with a mechanistic model. This would allow a more rapid optimization of the kinetic parameters, that could then be iteratively used in the fluidic model, until a close match to the experimental output would be obtained. A mechanistic model, developed for example in Matlab®, would also increase this fluidic model's applicability, since different and more complex reaction mechanisms could be easily implemented and interfaced with the CFD model, widening its applicability to more reactions.

The microfluidic meander channel was also successfully used as a modular unit with two other microfluidic systems, a commercially available polymeric valve and an in-house developed PMMA meander channel. The connection between the systems was performed through the use of either standardized connectors or in-house built connectors with standard sizes. The operation of the silicon meander channel with both these systems proves its compatibility with operation in a modular format, which together with the presented reaction characterization, makes it a highly useful tool in modular enzymatic screening platforms.

Chapter 3

System for screening whole cell catalysts

All the cell samples and the experiments presented in this chapter were produced in collaboration with Julia Halder and Prof. Bernhard Hauer during an external stay at the Biocatalysis Group, Institut für Technische Biochemie, Universität Stuttgart.

Selective oxidative functionalization of molecules is a highly relevant and often demanding reaction in organic chemistry, requiring the use of complex group-protection schemes and toxic compounds. Certain enzymes, such as oxygenases, are capable of performing selective stereo- and regioselective introduction of oxygen molecules in organic compounds towards the biosynthesis of important precursors or chemicals in the pharmaceutical and chemical industries, and are also capable of bioremediation by degrading insecticides or polyaromatic compounds. Dioxygenases, in particular, are enzymes capable of converting a wide variety of interesting arene as well as alkene substrates, and a considerable effort has been put in their development towards enzymes with better activity and selectivity for certain compounds, This, however, greatly increases the need for screening strategies that allow the identification of the adequate properties for the target reaction and/or substrate.

In this chapter, the meander microchannel with integrated oxygen sensors described in the previous chapter (Chapter 2), was applied to the screening of wild-type and variants of naphthalene dioxygenase (NDO) from *Pseudomonas* sp. NICB 9816-4. These variants were generated through site-directed mutagenesis to obtain enzymes capable of converting alkenes [238]. The oxygen sensors were used to measure the oxygen consumption rate of several variants during the conversion of styrene (substrate) to 1-Phenylethanediol (product). The oxygen consumption rate can be used to compare the different variants in terms of their ability to convert this substrate, and potentially in terms of substrate specificity and reaction rate. It was possible to distinguish endogenous respiration from oxygen consumed in the reaction for the *E. coli* cells tested. Furthermore, it was also possible to identify the higher activity and different reaction rate of two variants, relative to the wild-type NDO. The meander microchannel with integrated oxygen sensors can therefore be used as a simple and fast screening platform for selection of dioxygenase mutants.

3.1 Introduction

The use of biocatalysts has enabled the production of (new) compounds, with high stereo- and/or regioselectivity at milder conditions (lower temperatures, close to neutral pH and atmospheric pressure), in a simpler process (remove the need for protection of functional groups in some reactions) and with less toxic substrates, than the equivalent (when existent) organic chemistry methods [239]. Furthermore, they usually present a several fold increase of reaction rate and may be capable of catalyzing the conversion of non-natural substrates. Also,

biocatalysts: (i) require a lower energy demand that lead to less waste of the catalyst (through recovery and/or immobilization); (ii) allow an increased product titer; and, (iii) demand the use of lower amounts of water [239]. These characteristics can be achieved depending on the biocatalyst and reaction and if adequate process design and intensification methods are used. They can, however, represent a significant fraction of the bioprocess operation cost, due to the cost of development, need of co-factors, loss of productivity (from loss of activity at the reaction conditions), or complex downstream processing emerging from a low enantioselectivity [240]. Nonetheless, by appropriate selection and/or tailoring of the biocatalyst to the desired reaction and/or process, this cost can be decreased and the process made lucrative [240]. In 2014, over 500 industrial products were based on biocatalysis, 150 of which were in the chemical and/or pharmaceutical industry [239].

3.1.1 Whole cell biocatalysts

Whole cell biocatalysis involves the use of a microbial cell (bacteria, fungi or yeast cell) inside which the conversion of (non-)native substrates into a target product occurs [241]. The enzymes involved in the reaction can be from the organism itself but in most cases they are from a heterologous source and are inserted in a microorganism (i.e. named genetically modified expression host); which is easier to grow, better characterized, considered safe and/or already used in industry (e.g. *Escherichia coli*, *Pseudomonas* sp., *Pichia pastoris*, *Saccharomyces cerevisiae*, *Bacillus* spp., *Aspergillus* spp., *Trichoderma reesei*) [239]. The use of whole cell biocatalysts has generally a lower cost than isolated or immobilized enzymes, since there is no need for enzyme purification, or addition of high amounts of co-factors, while simultaneously simplifying the downstream processing [242]. The use of whole cells can additionally increase the stability of the catalysts, by providing a protective casing from the reaction mixture [243]. The use of whole cells further allows a simpler application of enzymes which are membrane-bound, part of a multiprotein complex or co-factor dependent. The encapsulation of an enzyme in a cell enables a faster reaction due to proximity of all the required components for the reaction, such as co-factors, co-substrates or metabolites, besides other enzymes involved in the bioconversion. Regarding co-factor (such as NAD(P)H)) regeneration, the use of whole cells grants the use of regeneration systems of the host organism or its integration into the host organism, hence enabling *in situ* co-factor regeneration without loss of the often expensive compound [240]. The co-factor is regenerated either by using a co-substrate or by enzyme-coupled systems integrated in or part of the microbial host. The coupling of enzymes requires a proper balance between the reaction rates of the different enzymes involved and an efficient drive of the enzymatic route towards the target product. However, co-expression of multiple enzymes can lead to a high metabolic burden and to a lower catalytic performance. An alternative is the expression of each enzyme in a separate organism and combining the different organisms for the bioconversion [244]. Whole cell biocatalysts also shield the enzymes from the environment enabling reactions at harsher or non-natural conditions [244]. Examples of such non-natural conditions are:

- Biphasic systems of water immiscible organic solvents;

- Neat substrate systems (NSSs), where the substrates are usually used as solvents, allowing a monophasic system environment with minimum water addition and high-substrate loads;
- Micro-aqueous solvent systems, where the advantages of NSSs are maintained but the substrates are diluted in another organic solvent;
- Ionic liquids and deep eutectic solvents, which are less toxic and have a lower flammability and vapor pressure than organic solvents.

The use of whole cell biocatalysts as resting cells, besides separating growth phase from catalysis, can moreover decrease the competition of cellular reactions like oxidative phosphorylation with co-factor regeneration. On the other hand, in resting cells, changes in gene regulation can result in protein or membrane instability or a decrease in intracellular enzyme levels, in turn leading to a lower biocatalytic activity [245].

Whole cell biosystems may, furthermore, result in decreased reaction rate due to limitations in substrate mass transport through the cell wall, which can be improved by permeabilization of the wall with chemical (e.g. adding organic solvents, surfactants, chelating agents or altering the cell wall's fatty acid content) or physical (e.g. temperature shock, electroporation) methods [246]. Other approaches involve the expression of membrane transporters, to increase influx of substrate to the cell, or the use of cell surface techniques to display the enzymes on the cell membrane, and even temperature-controlled pore-formation through the use of lytic phage proteins [244].

Whole cell catalysts can also be immobilized during the bioconversion, however there are less immobilization strategies than for purified enzymes. Nevertheless, whole cell catalysts have been immobilized in lentil-like shaped porous polyvinyl alcohol (PVA) carriers from LentiKat's (Prague, Czech Republic), storable for up to 15 months, in ion exchange resins by covering with silicon coating (allowing their application in NSSs), and in polyvinylidene difluoride membranes (with good recyclability in micro-aqueous conditions) in order to ease recovery, increase catalyst load and improve stability and recyclability of these catalysts [244].

In whole cell biotransformations the main parameters to be optimized for process implementation are the oxygen supply, substrate and product toxicity, product stability and co-factor recycling [245]. All the above-mentioned parameters need to be fully characterized and optimized in order to achieve a cost-effective and productive bioprocess.

Engineered enzymes in crude or semi purified form are currently considered more economically viable than whole cell biocatalysts. They present an increased tolerance to harsher conditions (organic solvents, lower or higher pH, high temperature, etc.), can perform the reaction at lower concentrations due to their higher activity and are easier to separate and remove from the reaction media due to immobilization strategies [247]. Nonetheless, around 60% of the industrial biocatalysis is performed using whole cell catalysts [242].

3.1.1.1 *E. coli* as a recombinant whole cell catalyst

E. coli was the first microorganism used as a recombinant host, and has since been used extensively. The preference for *E. coli* is related to its fast growth rates and ability to reach high cell densities (average doubling time is 40 minutes [248]) in simple and low cost media. Also, the ease in genome modification or integration of new DNA through plasmids, as well as the

capability of accumulating heterologous proteins up to 50% of its dry cell weight are relevant factors for its wide use. However, it cannot be applied to the production of more complex proteins (e.g. human protein's requiring post-translational modifications). It may also form inclusion bodies where the target heterologous protein might be aggregated and inactive [239]. Recent research has shown that it is possible to retrieve some proteins by solubilizing the inclusion bodies [249], [250], but it is still preferable to avoid their formation during expression of the target protein.

3.1.2 Dioxygenases

Oxidative biocatalysts can solve some of the issues in conventional chemical oxidative reactions, such as lack of predictability of product structures and cost of oxidizing agents, when trying to obtain relevant hydroxy- and oxo- compounds for the pharmaceutical, agrochemical and food industries. Oxidative enzymes can also be used in other industries, namely for bioremediation, oxidizing insecticides, haloaromatics and polyaromatic hydrocarbons [251].

Oxidases, peroxidases and oxygenases are oxidizing enzymes, which use oxygen as the electron acceptor during the reaction. While oxy- and peroxidases often result in reactive oxygen intermediates, which can react non-specifically, oxygenases are quite stereoselective [251]. Oxygenases can be involved either in the biodegradation/detoxification of carbon sources and toxic compounds, or in the biosynthesis of secondary metabolites (e.g. hormones) [252]. They are usually NAD(P)H dependent and can be further divided into monooxygenases and dioxygenases. Monooxygenases (e.g. cytochrome P450 BM-3) catalyze the introduction of one oxygen atom in the substrate using NAD(P)H as the reducing electron acceptor and are usually dependent on a metal, heme group of a flavin. Dioxygenases (e.g. catechol dioxygenase) are multimeric non-heme iron proteins that can introduce stereo- and regioselectively two oxygen atoms from molecular oxygen in the substrate (e.g. aromatic compounds) [253]. A very important group of dioxygenases are the Rieske non-heme iron-sulfur oxygenases, which have a Rieske group [2Fe-2S] coordinated to the protein by two cysteine and two histidine residues [254]. Rieske non-heme iron-dependent oxygenases (ROs) are best known for the regio- and stereospecific *cis*-hydroxylation of aromatic compounds to produce dihydrodiols, but are also involved in several catabolic and biosynthetic pathways [255]. These enzymes show a great potential for the asymmetric dihydroxylation of alkenes, allowing for a more environmental-friendly process. This reaction in organic synthesis (e.g. Sharpless dihydroxylation) uses toxic metallic compounds (e.g. osmium(VIII) oxide) and often leads to overoxidation and byproduct formation. Furthermore, ROs are capable of catalyzing various oxidation reactions (e.g. monohydroxylations, desaturations, oxidative cyclizations) in a variety of substrates, and the range of substrates can be increased by changes in the topology of the active site, as demonstrated by Gally *et al.* (2015) [256]. The first ROs identified, Naphthalene and Toluene dioxygenases, were discovered in the 1970s and are responsible for the degradation of aromatic compounds by *Pseudomonas putida*. ROs consist of a two- or three-component system that includes (i) a reductase (an electron-transfer protein to obtain the reduction equivalents from NAD(P)H), (ii) a ferredoxin (the protein that shuttles the electrons to the active site (in the three component systems)), and (iii) an oxygenase (the enzyme that performs the conversion) [254]. Naphthalene dioxygenase (NDO), the most studied enzyme in this class, catalyzes the *cis*-1,2-

dihydroxylation of naphthalene using both oxygen atoms from molecular oxygen. The dioxygen reduction occurs by first transferring electrons from the co-substrate (NADH) to a Rieske [2Fe-2S] cluster within the NDO via a flavin-dependent ferredoxin reductase and a separate ferredoxin. The electrons are then donated to the non-heme iron center in the active site and used in the final reduction of dioxygen. A full account of possible catalytic mechanisms for NDO is presented in Barry and Challis (2013) [255], a good characterization of the three-component system can be found in Kauppi *et al.* (1998) [257], and the structural influence on enzyme substrate plasticity of ROs is presented in Ferraro *et al.* (2005) [254]. This enzyme has demonstrated a great degree of customization, allowing to widen the range of obtainable products beyond the ones of the wild-type NDO by site-directed mutagenesis [253].

In terms of application to biotransformations at industrial scale, oxygenases present some limitations due to low stability and dependency on expensive co-factors, as well as the membrane-bound nature of some components of the enzyme system. These factors lead to the application of oxygenases in whole cell systems in order to stabilize the enzyme and achieve *in situ* co-factor regeneration using the metabolism of the host cells [251]. Furthermore, due to the poor water solubility of most oxygenase substrates and products, biotransformations are mostly performed in two-liquid phase systems. Additionally, oxygenases usually present relatively low turnover rates, which coupled with diffusion limitations in the cell membrane, require high expression levels of these enzymes to reach significant whole cell oxygenase activities. Uncoupling effects where reduction of molecular oxygen (and thus oxygen consumption) occurs without substrate oxidation, result in the production of hydrogen peroxide (two-electron reduction) or water (four-electron reduction). This effect can occur in the absence of substrate, when the substrate cannot be oxidized or in the presence of compounds that do not properly fit the active site. Uncoupling effects can in turn lead to an increase in oxygen demand, as well as the production of toxic hydrogen peroxide and a lowered specific activity in the final bioconversion [252]. Overoxidation of the substrate, beyond the desired product, can occur under non-physiological conditions or when the electron transfer components are fused to the oxygenase and may also be an issue with these enzymes [252]. In whole cell systems, the diols produced by dioxygenases are usually further metabolized and so blocked variants are developed for their production [251]. Moreover, insertion of the oxygenase and auxiliary proteins genes in the host's chromosome might decrease instability of the host cell. Another factor to consider in bioconversions with oxygenases is the hydrophobicity of the substrates, which tend to diffuse easily through the cell membrane, and can result in cell wall degradation and cell death. Some of the toxic substrates require counter mechanisms to be implemented in the host cell, the control of substrate concentration (e.g. by substrate addition strategies, using small concentrations), or use of solvent tolerant strains [245].

3.1.2.1 Oxygen influence in cell behavior

Cellular function, especially in tissues, is dependent not only on the oxygen partial pressure but also on the balance between available oxygen and oxygen consumption in the cell microenvironment [192]. For human cells, for example, normoxia (normal level of oxygen) is usually between 2 and 9% and up to 13% in the lungs, which is significantly lower than the level in ambient air (21%). Consumption of oxygen by a static cell culture media is enough to generate

hypoxic environments, and the rate of consumption is dependent on cell density and metabolic rates [192]. Oxygen is used as electron acceptor or oxidizing agent in aerobic metabolic activities, but high concentrations of oxygen can be harmful due to the generation of oxygen radicals [258]. *Escherichia coli* (*E. coli*) is a facultative anaerobe and can switch between aerobic and anaerobic metabolism depending on the nutrients and oxygen concentrations available in the environment. According to Polinkovsky *et al.* (2009) oxygen consumption by *E. coli* increases linearly with the division rate of the cells, being between 20 mmol/h per gram of dry mass at 1 division/h and 6 mmol/h/g at 0.2 divisions/h [259].

Strains that express oxygenases require oxygen not only for the bioconversion but also for endogenous respiration, and so during the biotransformation the oxygen pressure needs to be maintained in order to allow the oxidation reaction to compete with respiration. Maximum whole cell oxygenase activities over 10h to 15h are usually lower than 50 U/g_{cdw}, which can be improved, by focusing on optimizing some of the aspects mentioned in section 3.1.2. above [252].

Microfluidic systems can enable a good control of diffusion and gradient generation, as mentioned in the previous chapters, thus providing the perfect environment for studying the influence of oxygen levels on cells.

3.1.3 Screening of biocatalysts

Biocatalyst screening, especially for new processes or products or when involving non-natural substrates, is a complex task, involving different levels of screening. A general strategy, presented by Ogawa and Shimizu (1999) [260] can be divided in:

(1) A process step, during which the final industrial (potential) process is designed, and the desired type of enzymatic activity defined;
(2) A microorganism step, where a selection of microorganisms to be screened for the enzymatic activity and/or process conditions is performed;
(3) A screening step, where the choice or development of a sensitive assay for screening of the desired biocatalyst's characteristics is achieved.

This strategy does not consider the considerable amount of information obtained by fully sequencing the genome of microorganisms, but provides a classical approach to biocatalyst screening.

Step (1) is extremely dependent on the target reaction or product, on the type of product (whether it is an intermediate compound, a precursor or the final compound), on the industry (inorganic chemistry, agrochemical, pharmaceutical, food), on the required degree of purity or enantioselectivity desired, and type of application (for profit or for bioremediation, for example).

Step (2) can be further divided into three factors [261]:

(a) If a similar reaction to the target reaction has been reported with a similar substrate, the same catalyst or one with the same function should be tested;
(b) If a new reaction is the target, screening of existing libraries is advised, as well as testing of biocatalysts with a broader substrate range;
(c) If library screening has not yielded a good match for the target reaction, wide biocatalyst screening should be performed.

Although, step (2) can be divided in the latter considerations, it usually involves classical techniques such as enrichment-culture (for natural strains), where selection is based on the

ability to assimilate the target substrate, and isolation strategy [260]. Homology search and sequence alignment has enabled the identification of novel biocatalysts and the reconstruction of ancestral biocatalysts with a wider substrate range, as well as the establishment of libraries of biocatalysts with enhanced characteristics by identifying common amino acids, or their substitutions, that yield a certain desired characteristic [247]. This has been especially relevant for identifying enzymes from non-culturable microorganisms, by extracting DNA of samples collected from the environment and comparing with DNA-cosmid libraries. However, the use of gene-libraries tend to disassociate the enzyme from its microbial function [260], which is important to fully understand the potential of the enzyme and the challenges in terms of its applicability. Rapid and high-throughput genome sequencing, as well as high-throughput analysis of mRNA (e.g. hybridizations on microarrays, providing an overview of gene expression and active genes), proteins (e.g. 2D-PAGE) and metabolites (e.g. chromatographic methods coupled with mass spectrometry or nuclear magnetic resonance to provide an overview of active metabolic networks and response to environmental stress) can provide a lot of information regarding enzymes and their possible function in the metabolism of the microorganism [245], [247]. High-throughput genome sequencing provides an overview of the genetic background of both culturable and non-cultivable organisms using platforms such as 454 from Roche, Solexa from Illumina or SoLiD from ABI [239].

Step (3) is often the most difficult of the three steps. The development and characterization of new biocatalysts is frequently hampered by the available screening technologies, often limited to the screening of a single substrate or function for the multiple variants generated.

3.1.3.1 Screening strategies

Methods for biocatalyst screening and variant selection require proper design in order to maintain the association between the phenotype observed and the genotype measured [262]. To perform screening of biocatalysts from wide enzyme or whole cell catalyst collections, not only high-throughput growth systems need to be developed (such as the one developed by Doig *et al.* (2002) using a robotic liquid handling system [154]) but also online quantification and/or monitoring of the reaction is necessary.

The majority of traditional approaches used for screening are performed *in vitro*, thus requiring extraction of the sample from the reaction mixture, or to stop the reaction to perform the quantification of the reaction components. However, *in vivo* screening (when the biotransformation/bioconversion is monitored in the microorganisms) broadens the number of parameters that can be screened and accelerates biocatalyst development and selection. *In vivo* screening strategies present some limitations associated with the host's transformation efficiency and growth rate, but also the expression of the target enzyme, limitations in substrate uptake and intracellular background [263]. Furthermore, the choice of catalyst can be made following a selection or a screening approach. A biocatalyst selection approach excludes the clones without the characteristics of interest (negative clones), while in a screening approach all clones are analyzed and then selected, thus increasing the amount of variants to analyze but also the precision of the activity measurements and screened parameters [263]. Screening of 10^5 to 10^8 variants, where the complement of a key step in the metabolic network is required, has

been achieved with selection methods [264]. In selection approaches, the enzyme activity is usually linked to cell survival and growth in a way that only enzymes with the target activity are able to survive and/or grow under the chosen selective pressure (e.g. enzymes that complement auxotrophy or neutralize lethal conditions). However, this leads to a higher number of false positives than with screening approaches. A selection approach also does not always enable quantification and hence comparison of, for example, conversion rates [263].

Most assays tend to be specific to adequately screen for the intended characteristic, involving standard analytical equipment such as mass spectrometry (MS), gas chromatography (GC), high-performance liquid chromatography (HPLC) or nuclear magnetic resonance (NMR), thus being also quite time-consuming if hundreds or more samples need to be analyzed. Enantioselectivity (measured by enantiomeric excess, *ee*), for example, has been screened using electrospray ionization mass spectrometry (ESI-MS), using isotopical labels, capable of measuring both kinetic resolution of racemates and asymmetric transformation of substrates in up to 1000 samples per day [265]. Derivatization with mass-tagged chiral agents that differ in a substituent remote to the chiral center has also been used for screening enantioselectivity by ESI-MS. This approach does not require chromatographic separation and is tolerant to reactive achiral impurities [266]. MS, GC and HPLC based techniques require however extra steps in sample preparation such as extraction of the compounds, removal of organic phase and separation in a chromatographic separation, which increases the overall analysis time per sample [267].

Faster screening methods often involve the formation or consumption of a colorimetric, luminescent or fluorescent compound and its intensity is related with the substrate's affinity or turnover rate. For example, NADH and NADPH can be measured spectrophotometrically at 340 nm or 260 nm. Consumption of hydrogen peroxide can be followed by measuring samples at 240 nm (usually to measure catalase activity). Horseradish peroxidase catalyzes several reactions (using as substrates, e.g. 2,2'-Azino-bis(3-Ethylbenzthiazoline-6-Sulfonic Acid), 4-aminoantipyrine) that produce colorimetric compounds and can thus be followed spectrophotometrically. The last method involving formation of a colorimetric compound by horseradish peroxidase has also been applied for screening 960 variants from cultures grown on a nylon membrane on top of agar plates. The more intense the color the colony produced, the higher the amount of target product, thus enabling the selection of the higher producing variants for further characterization [268].

Screening in agar plates usually occurs by formation or disappearance of color on the agar surrounding the incubated colonies or by color appearance on the colonies themselves due to bioconversion, providing a straightforward identification of positive colonies. Differences between activity or catalytic rates are, however, not easily achieved with this type of screening and usually only up to 10^5 variants can be analyzed [263]. Coupling of this method with analytical equipment such as HPLC, GC or MS can also be performed. For example, Yan *et al.* (2017) coupled ambient MS with desorption electrospray ionization (DESI) to achieve a label-free platform for real-time screening of biotransformations in bacterial cultures. The DESI system enables sampling from the reaction mixture (ionizing the substrates and products directly from the agar plate) at room temperature in real-time. This is followed by an ion mobility (IM) component that performs the separation of the different ions generated to decrease background noise, and finally by an imaging MS capable of relating the detected chemical

compounds on the surface of the agar plate with their spatial distribution. The measurement of the extracellular product can be performed simultaneously for several substrate libraries, followed by analysis of the DNA of the biocatalysts for genotype/phenotype association [267]. Metagenomic screening allows the selection of genes with the desired function, by direct phenotypical detection, heterologous complementation and induced gene expression, usually through isolation in agar plates supplemented with different substrates (e.g. target substrate, certain antibiotics, co-substrates). In this technique, target activity can be further associated with the expression of a reporter gene (e.g. green fluorescent protein or ß-galactosidase) for easier screening [239].

Microtiter plates are the most frequently used screening devices, due to high-throughput (depending on the number of wells per plate) and compatibility with a wide range of analytical techniques, from colorimetric approaches to GC, NMR or MS. Microtiter plates are, however, usually limited to libraries of up to 10^4 variants [263]. UV-Vis and fluorescent microplate readers and fluorescent digital imaging (in which mutants are passed on to a nitrocellulose membrane from the agar plate where they were cultured) [269] can be used to increase throughput during biocatalyst selection. Schwaneberg *et al.* (1999) developed a high-throughput assay using a robotic workstation and spectral analyzer compatible with 96-well microtiter plates for the analysis of substrate specificity and the activity of mutants of a fatty acid hydroxylating enzyme. This assay was based on detecting the conversion by the mutants of p-Nitrophenoxyhexanoic acid (pNCA)-containing substrates, and showed results for both pure enzymes and cell extracts [270]. This method was then further developed to allow measurements directly from the whole cell biocatalysts, eliminating the cell lysis, resuspensions and centrifugation preparation steps, by permeabilizing the outer cell membrane of *E. coli*. This method used also a replicator tool (developed by Duetz *et al.* (2000) [271]) to transfer cells from agar plates to the 96-wells plate. Despite the increase in the number of samples analyzed in parallel (~3000 clones per day) as well as directly from the cell bioconversion, issues of reproducibility between screens and differences in activity relative to the one measured in shake flasks (due to evaporation, a well-known problem in open microtiter plates) were observed [272]. Samorski *et al.* (2005) developed a system for evaluating induction time and growth differences of whole cell catalysts cultured in 96-well microtiter plates. The system used light scattering, NADH fluorescence and yellow fluorescent protein to monitor the cell culture in all 96 wells through a x-y-stage with an integrated optical fibre bundle. Measurements of optical density (with light scattering and NADH measurements) and amount of expression of an induced fluorescent protein were performed, allowing the optimization of the initial cell density and the time of induction, and the online monitoring of product formation in a microtiter plate [156]. Codexis, a company specialized in enzyme engineering, and other enzyme developing companies (e.g. Ingenza, Nzomics, InnoSyn, Almac), provide systems for enzyme screening based on 96-well microtiter plates for ketoreductases, acylases, ene-reductases, transaminases, lyases, dehydrogenases and halohydrin dehalogenases [261].

Fluorescent microscopy can help locate proteins and measure their activity, as well as protein-protein interactions and protein diffusion coefficients [273]. Infrared multiphoton laser scanning microscopy (NIR-LSM) allows the detection of biomolecules within the cells [273]. Bioluminescence assays can be used to determine coenzymes and to perform detection of reporter genes. However, these methods are not compatible with the long-term measurements

required for metabolic activity assays due to photobleaching of fluorescent compounds or decomposition [273]. Mid-infrared spectroscopy can be used to identify and quantify species present in a bioprocess [273]. Scanning electrochemical microscopy (SECM) can provide information on cell respiratory activity and other redox processes [273].

Spectrophotometric tests are quite desirable due to the possibility of parallelization using microtiter plates, and due to the fact that they are usually quite fast and relatively sensitive (signal amplification methods can also be applied). However, most target compounds are neither colorimetric nor fluorescent and developing an indirect colorimetric detection method can be difficult and time-consuming. The development of surrogate substrates, which are compounds that are added to the culture and generate an optical signal proportional to the target activity, is a good example of the complexity involved in the development of new detection methods [262]. Moreover, these methods, especially colorimetric methods, usually have a high incidence of false positive or negative results which lead to lower precision in the quantification of the target compound [267].

Fluorescence-activated cell sorting (FACS) and Micro Fluorescence-activated cell sorting (μFACS) devices have been used to screen for growth on a new substrate, and to select variants based on enantioselectivity, by linking cell survival with capacity for catalysis of only one enantiomer (selection approach) [274], [264], [247]. Cell survival can also be linked to antibiotic resistance [262]. Flow cytometry also allows assessing whole cell biocatalysts viability and electron transport, besides enzyme activity, achieving a very high throughput (10^8 screened variants per day [262]). FACS on a chip provides a better control on number of cells per droplet (down to single cell), as well as on number of fluorescent reporters per droplet thus presenting highly quantitative results [262].

Recently, some microfluidic approaches to screening of biocatalysts have emerged. Microfluidics can enable a faster measurement and/or monitoring of a higher number of parameters, due to the ease of flow manipulation but also sensor integration. Furthermore, they provide continuous production at lower cost, reagent quantities, higher safety and less waste, while also allowing a better spatial and temporal control of the reactions, and operation at unusual process conditions and catalyst configurations, thus expanding the operation conditions and types of reactions possible [47]. Abate *et al.* (2010) used droplet microfluidics to screen mutants of horseradish peroxidase generated by directed evolution, at rates of thousands per second, being 1000-fold faster than microtiter plate based robotic screening. A stream of yeast cells with mutated enzymes on the surface is co-flown with a fluorogenic substrate and aqueous pL droplets containing a single yeast cell are formed by dispersion in an oil solution. The reaction is initiated by the mix of the two aqueous solutions in each droplet and continues in the incubation section of the first microfluidic device. In the second device, the droplets are dielectrophoretically sorted based on fluorescent intensity using a laser connected to a photomultiplier tube. The microfluidic device was designed in order to allow reinjection of droplets in the systems in order to allow incubation of low activity mutants for later analysis. The detection limit in this case was of ~3500 molecules in 6 pL or <1 turnover per enzyme [117]. Kintses *et al.* (2012) has applied a similar strategy, but performing fluorescent detection of enzyme reactions in lysates of single cells of *E. coli*. Directed evolution of arylsulfatase from *P. aeruginosa* expressed in *E. coli* was performed to explore this enzyme's substrate promiscuity in order to extend its activity towards phosphonate. In the developed microfluidic setup, cell

lysis and reaction are performed simultaneously by fast mixing of substrate and cell lysis agents with the cell solution upon droplet formation. The best variants were selected with laser-induced fluorescence in a second device with a dielectrophoretic sorter, and broken in order to isolate their plasmid content and use it for the next evolution cycle. Droplets generated this way, where the target compound can be optically read, can also be screened using FACS, requiring that the water-in-oil droplets are previously enveloped in water. The second emulsification step however, if performed in bulk, can cause a variation in droplet diameter and hence a lower measurement precision. The whole cycle of variants' screening developed by Kintses *et al.* (2012) was performed in two days with the analysis of 10^7 droplets every 3 hours [61]. Besides water-in-oil droplets, shell-like compartments made with polyelectrolytes can be used to encapsulate cells, which are more stable with detergents used for lysis [262]. This technique also enables the detection of very small improvements of enzymatic activity [263].

In another approach, the cells themselves can be used as femtoliter screening vessels, by only performing the target reactions inside the cells and detecting the resulting fluorescent product also inside the cells by, for example, FACS. In this way, libraries of up to 10^9 variants can be screened [263]. The enzymes can, on the other hand, be displayed on the surface of the cells during the assay by fusion with anchor motifs, being thus more accessible to the substrate (cell surface display technique). In this approach, the product is also displayed on the cell surface and again up to 10^9 variants can be screened. The required fusion however limits the applicability of this approach to libraries of enzyme variants, and needs to be resistant to proteases, have a stable structure and be compatible with the target enzyme. This technique can also be associated with FACS, but the displayed enzymes may lose activity and fluorescent substrate or products need to remain bound to the cell surface during measurement [263].

Droplet-based directed evolution of whole cell catalysts is a very powerful tool to increase screening throughput of engineered biocatalysts, but the use of different sensor technologies (such as NIR [275] or Stroboscopic Epifluorescence Imaging [133], for example) is required to expand its application. Further coupling of such a system with standard analytical equipment such as HPLC, GC or MS would increase its usefulness for biotechnologists and also the range of detected compounds. Packer and Liu (2015) provide a good overview of available screening methods for protein selection, as well as a short guide on how to select which screening method to apply [262].

Another approach to screening allows for an indirect measure of the characteristic targeted, not by the product or substrate of the bioconversion, but by the genetic reporter that encodes that phenotype. This approach is regarded as reaction independent, and the reporter may be colorimetric, fluorescent, bioluminescent or result in conditional survival, cell motility, acidification or cell display. The activity of the reporter measured is connected to the activity of the target enzyme by interference at either the transcription (e.g. activation of a natural or synthetic transcriptional regulator by binding of the product or substrate), translation (e.g. by binding of the product to a ribozyme or reporter inactivation by the enzyme) or post-translational modification level (e.g. direct modification of the reporter by the enzyme), or even enzyme degradation or solubility (e.g. by fusing GFP to the enzyme variant, and thus only soluble GFP variants are positively selected). Reporter-based screening using natural transcriptional regulators are usually extremely selective for the target product, having no false positives. This may increase the applicability as a screening strategy to more types of enzyme

and reactions, but still each case requires the proper choice of reporter and approach [263]. Genetic circuit design, which involves the capacity to design DNA in order to modulate the expression of certain genes or metabolic networks to occur at defined environmental conditions, has also been used to measure the activity of enzyme variants from the expression levels of reporter genes [276], [277].

A simple change in pH due to product formation or substrate consumption has also been traditionally used as an enzymatic screening test (e.g. pantoic acid production by lactonases [260]) for a number of enzymes.

A summary of the commonly used screening approaches is presented in Figure 39.

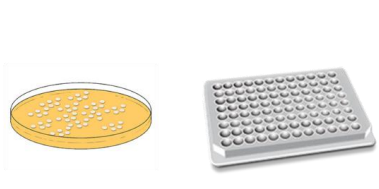

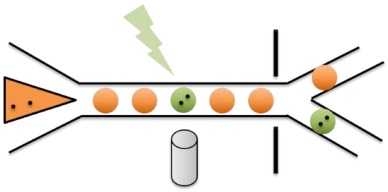

	Agar plate	Microtiter plate	FACS	Droplet microfluidics
Type of sample	Solid; Individual colonies;	Liquid; Sets of cell variants;	Liquid; Sets of cell variants in droplets or Individual cells;	
Library size	10^2 - 10^5	10^4	10^8	10^9
Advantages	Simple; Visual detection by direct phenotypical detection, heterologous complementation and induced gene expression;	Compatible with multiple analytical techniques; High sensitivity; Large dynamic range; Compatible with robotic workstations;	Pico- to femtolitre scale; Low sample and reagent consumption; High-throughput; Continuous operation; Can perform automated sorting;	Compatible with multiple analytical techniques and sensor types; Can perform automated directed evolution;
Disadvantages	Low dynamic range; Labour intensive; Usually requires another method (e.g. microtiter plates) for quantification;	Labour intensive; Works with lysed cells; Small library size; Might require quantification with time-consuming analytics (e.g. GC, MS);	Technnically challenging Limited to fluorescent detection or cell characteristics measured by light scattering;	Requires optimization of emulsions or polyelectrolyte shells used;

Figure 39 – Summary of some of the advantages and disadvantages of the commonly used screening approaches for whole cell biocatalysts.

3.1.3.2 Screening of oxygenases

Screening of oxygenase variants or mutants is specially complicated since the generated products do not cause a change in pH, color or fluorescence, and distinction between regioisomers is often the main objective of the screening program. Screening of these enzymes is thus usually achieved with more time-consuming and sensitive analytical methods, some of them mentioned above, such as GC or liquid-chromatography (LC) often coupled with MS, or

even nuclear magnetic resonance (NMR) [252]. These analytical methods can provide a high degree of throughput. However, this throughput is achieved with a lengthy time period between variant development, reaction performance and analysis of product concentration and range of compounds. High-throughput screening with robotic microtiter-based devices, as mentioned before, enables the analysis of 100 to 1000 samples of cells per day, but tends to provide hits with low activities and regiospecificity, especially in Gram-positive cells and fungi. Screening can also be performed through enrichment cultures, where the organisms grown on the starting material, might be able to degrade the desired substrate. However, oxidation of the substrate might not occur on the target position [252].

Measurement of the initial oxygen consumption rate in the presence of substrate excess has been used for characterization of dioxygenases [278], [279], [280]. A study performed by Parales *et al.* (1999) used oxygen measurements with Clark-type oxygen electrodes to confirm the importance of an aspartate residue for the catalytic activity in NDO enzymes, namely in the electron transfer route. When this residue was modified, no oxygen consumption was observed. Furthermore in this study a stoichiometric consumption of naphthalene and oxygen for wild-type enzymes was observed [281]. Rachinskiy *et al.* (2014) have used monitoring of oxygen levels to detect enzyme deactivation as a parameter in a long-term stability enzyme characterization model. The model integrates the mathematical description of temperature-dependent enzyme (de)activation (considering the enzyme kinetic characteristics) to predict the process properties of an enzyme in order to aid enzyme screening for industrial applications [282]. Despite the availability of oxygen sensor spots, as well as other formats of oxygen sensors, for integration in microtiter plates and shake flasks, the oxygen measurement seems to be used mainly as a monitoring or initial characterization parameter, and not as a screening parameter. As hinted by the use of purified enzyme solutions in the studies where oxygen assays were performed, this could be due to the interference of cell respiration in whole cell solutions (where most of the current screening approaches for this type of enzymes are performed). Moreover, the limited application of oxygen measurement as a screening parameter so far might be related to the lower sensitivity of the traditionally used sensors (Clark-type) or the need of working in closed vessels, when working with highly volatile compounds (and so sensors such as syringe or Clark-type cannot be applied). However, the more recently developed, highly sensitive and fast sensors, with which measurement is performed with optical fibers can contribute to the increase in their usage in this field.

In this work, a microfluidic system with such type of sensors is proposed, where the rate of consumption of oxygen could be used to distinguish variants with high activity from variants with the same activity as the wild-type or even no activity in a fast and parallel way.

3.1.3.3 Biocatalyst tailoring

Biocatalyst selection occurs not only by searching or screening available catalysts that fit or can operate at the desired process conditions, but also through optimization and tailoring of these biocatalysts to perform better at the conditions of the target process [240]. Characteristics that allow the catalyst to better fit the process are, for example, higher pH or temperature range, higher substrate affinity or turnover rate, higher robustness and stability, altered enantioselectivity, conversion of new and/or unnatural substrates, among other characteristics

[240]. Biocatalyst development can also prevent the synthesis of unwanted compounds or even toxic compounds through parallel reactions or other metabolic pathways present [283].

Enzyme tailoring or development of new enzymes can be achieved by natural evolution (enrichment cultures of microorganisms with the target activity, of which metagenomic libraries are made and then from which biocatalysts can be selected), by laboratory evolution (generation of libraries of randomly mutated organisms from which biocatalysts with the target activity can be selected) or by computational design of new catalysts (using computational models or based on existing libraries followed by experimental testing) [263].

This tailoring can be achieved through several techniques, from random or site-directed mutagenesis and directed evolution which act on zones close to the native target sequence, to DNA shuffling and domain swapping which act on areas amid the original sequences [240]. Directed evolution is a highly relevant technique for biocatalyst development, being especially powerful when there is little knowledge regarding the relationship between structure motifs and function [253]. Initially, random mutagenesis and/or recombination of the targeted gene (through error-prone polymerase chain reaction (PCR), repeated oligonucleotide directed mutagenesis, chemical agents, etc.) are performed and mutants selected for the desired property [239]. The genes responsible for the improved enzymes are then targeted in a second round, and so forth, until a library of enzymes with the final improved characteristics is obtained [284]. This approach can result in an increased stability of the enzyme but often a loss of activity is observed. A successful directed evolution requires the occurrence of mutagenesis on the target gene through a practical evolution strategy, as well as the existence of a suitable microbial host for enzyme expression and a suitable screening strategy [246]. Directed evolution can also be performed continuously and *in vivo* using alternating culturing vessels [285]. DNA shuffling can be performed using a computational method (SCHEMA) that estimates the disruption in the enzyme's original structure after DNA recombination is performed. Combinatorial active-site saturation testing (CASTing), which enables the design and screening of the binding to the active site of an enzyme and ProSAR, a program that analyzes the sequence-activity relationship of proteins to perform reagent selection, have both contributed to the generation of enzymes with enhanced catalytic activity and enantioselectivity [277]. Gene synthesis, new bioinformatics tools and protein and mathematical modeling further contribute to the possibilities of tailoring biocatalysts to achieve new functionalities, from higher stability and activity in organic solvents to catalyzing non-natural reactions.

Gene synthesis enables the optimization of certain codons, and introduction of promotors, restriction sites, etc. at more convenient locations in the gene, even having been used to generate complete genomes for metabolic pathway engineering. Another approach employed to achieve non-natural catalytic activities (e.g. involving a different type of chemical bond) is based on an initially promiscuous reaction, meaning an enzyme capable of catalyzing more than one type of reaction, usually with common catalytic steps [247]. Different computational approaches have also been applied to rational design, such as free energy perturbation, substrate docking simulation, molecular, hydrogen bond energy calculation and the Rosetta method [277]. Mechanistic models based on free-energy changes connected to protein unfolding and reaction mechanism can lead to the development of better strategies towards achieving the improved target characteristic [247]. Molecular dynamic techniques are able to predict flexibility of some residues and their association to enzyme function, in order to change enzyme activity or stability

with temperature. The Rosetta method involves quantum mechanics and computational design of enzymes based on existing scaffolds. Currently, most tailoring approaches are a combination of structure-based rational design with computational tools and directed evolution [277]. Cherny *et al.* (2013) coupled predictions from a computational model with results from a screening test of directed evolution variants to improve the catalytic rate of enzymes capable of hydrolyzing nerve agents, as detoxifying enzymes. The initial libraries used for mutant generation were designed using Rosetta, and the obtained data was fed into a transition state model with which new mutants were designed and experimented, until iteratively high activity variants were obtained [286]. Röthlisberger *et al.* (2008) present the combination of enzyme design, modeling and directed evolution to obtain an enzyme capable of performing a reaction that no naturally occurring enzyme catalyzes. Quantum mechanical transition state calculations were performed to design an active site which maximized the stabilization of the transition state of the enzyme for the target catalytic mechanism [287]. Packer and Liu (2015) present a good overview of methods for generation of mutants and screening approaches [262].

The quantification of all or a comprehensive number of the molecules involved in a certain synthetic pathway or reaction can not only accelerate development of biocatalysts, by increasing the available knowledge on that specific reaction, but also provide enough data to develop mathematical models to predict behavior and/or outcome of genetic or process manipulation [245].

3.2 Goal

In Chapter 2, the meander channel with integrated oxygen sensors was used to monitor an oxygen dependent reaction and observe differences in oxygen consumption for different reaction times, enzyme activity and *in situ* oxygen production. This chapter covers an alternate application of such device, extended beyond enzymes in solution to other biocatalyst formats, such as whole cell catalysts. In this case, a system capable of monitoring and measuring oxygen levels and consumption may provide extra input in screening mutants involved in oxygen dependent reactions. Rate of consumption, oxygen availability in the reaction mixture, oxygen and/ or other substrates diffusion limitation, uncoupling effects and cell density effects are some of the possible data that can be obtained with the meander channel with integrated oxygen sensors.

The meander microchannel with integrated oxygen sensors was here used to monitor and quantify oxygen consumption rate during the bioconversion of styrene to 1-phenylethanediol by naphthalene dioxygenase (NDO) variants in *E. coli*. This reaction was chosen as the reference reaction since styrene has a similar molecular structure to both the native substrate of the chosen enzymes (naphthalene) and the target substrates of the modified enzymes (different alkenes). Hence, styrene was used to compare the different variants in terms of ability to convert this family of substrates. The chosen case study involved the screening of two dioxygenase variants and their comparison with the wild-type NDO. The variants were developed by Julia Halder and Prof. Bernhard Hauer at the Biocatalysis Group, Institut für Technische Biochemie (ITB), Universität Stuttgart [238]. The work presented in this chapter was developed in collaboration with the latter researchers, as part of an external stay at ITB.

The main goal for the collaboration with ITB was to test whether such a microfluidic system could be used to accelerate the screening of dioxygenase variants, by identifying the earliest reaction time point where a difference in reaction rate could be observed. These reactions are usually performed for 20 h and the mutants evaluated by quantifying product concentration at the end of the reaction. Thus, the identification of an earlier reaction time where reaction rates are distinct enough to identify a better variant, is highly valuable and would allow a better understanding of the kinetics of the different variants with a potential increase in screening throughput.

3.3 Materials and Methods

The methods for plasmid development, cell culture and induction, as well as, the reaction conditions were developed and optimized by Julia Halder from the Biocatalysis Group, Institut für Technische Biochemie (ITB), Universität Stuttgart. The oxygen measurement setup and approaches presented in this chapter were developed based on previous experience with the meander microchannel with integrated oxygen sensors (presented in Chapter 2).

3.3.1 Materials

All solvents, buffer components and chemicals were obtained from Sigma-Aldrich and Fluka (Steinheim, Germany), Carl Roth GmbH (Karlsruhe, Germany) and Alfa Aesar (Karlsruhe, Germany). *E. coli* JM109 /DE3)_pDTG141 was obtained by Julia Halder and Prof. Bernhard Hauer (Biocatalysis Group, Institut für Technische Biochemie (ITB), Universität Stuttgart) from Prof. Dr. Rebecca Parales (Department of Microbiology and Molecular Genetics, College of Biological Sciences, UC Davis, University of California, California, USA) [288].

3.3.2 Heterologous expression of naphthalene dioxygenase (*in* E.coli)

The general protocol followed to obtain the variants/ mutants was described in Gally *et al.* (2015) [256] and further optimized towards a better reproducibility [238]. For the production of induced biomass *E. coli* JM109 (DE3), cells previously made competent using rubidium chloride were thawed on ice for 5 minutes. Then, 1 µL of plasmid DNA for naphthalene dioxygenase (NDO, *Pseudomonas* sp. NCIB 9816-4, pDTG141) or one of the tested mutants was added to the cells and mixed gently by flicking the base of the eppendorf tube and shortly centrifuging. Cell transformation was performed by heat shock by placing the cells in a waterbath at 42 ^{0}C for 90 s, followed by 2 minutes on ice. The heat shock treatment was followed by addition of 500 µL of LB medium to the cells and incubation for 1h at 37 ^{0}C and 600 rpm. The competent cells were then plated on selective agar plates containing ampicillin (100 µg/mL) and incubated overnight at 37 ^{0}C. In order to generate the induced cells, one colony from the agar plates was used to inoculate a 2 L shaking flask with 500 mL of TB medium and 500 µL of ampicillin. The flask was incubated at 37 ^{0}C and 180 rpm until an optical density (OD_{600nm}) of 0.8 -1 was obtained. The cells were then induced with 0.1 mM of isopropyl ß-D-1-thiogalactopyranoside (IPTG) dissolved in water and incubated at 25 ^{0}C for 16 to 18 h. Indole (Figure 40 (c)) was added to the

induced cells as a simple screening test in the solid phase in order to check if induction was achieved, since cells successfully induced with NDO or variants produce indigo, turning the media blue [289], [283], [290]. A representation of the molecular structure of the different substrates used and/ or mentioned in the text is presented in Figure 40. Influence of indigo (blue color of the cells) was considered negligible since indigo has a wavelength of 420-440 nm while the laser for excitation emits at 620 nm and the detected excitation light from the sensor dye is 760 nm. After induction, the cells were harvested by centrifuging for 20 min at 6000 *g* and 4 ^{0}C in an Avanti J-26XP centrifuge (from Beckman Coulter, California, USA) and resuspended in 0.1 M potassium phosphate buffer (pH 7.2) containing 20 mM glucose.

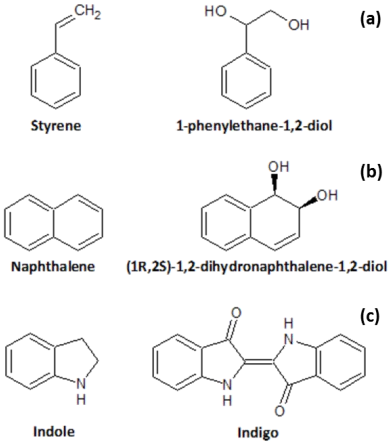

Figure 40 – Substrate (left) and corresponding dihydroxylation product (right) for the biotransformation performed (a), the natural NDO substrate (b) and the substrate for induction screening, indole (c).

3.3.3 Preparation of freeze-dried cells

To obtain freeze-dried cells, the harvested cells were resuspended in 0.9 % sodium chloride (NaCl) solution and centrifuged for 15 min at 4000 *g* and 4 ^{0}C. The cells were then spread uniformly in a petri dish and placed inside a freezer at -80 ^{0}C for up to 2 h. After freezing the cells were placed inside a freeze drier and freeze-dried overnight under vacuum conditions.

3.3.4 Biotransformation

The cells for the reaction for gas chromatography (GC) validation were prepared by dissolving 0.1 g_{cww}/mL and 0.05 g_{cww}/mL (cell wet weight) for the freshly prepared resting cells, or 66 mg_{cdw}/mL and 33 mg_{cdw}/mL (cell dry weight) for the freeze-dried resting cells, in 1 mL of 0.1 M phosphate buffer (pH 7.2) with 20 mM glucose. The cells for the oxygen measurements were also dissolved in 1 mL of 0.1 M phosphate buffer (pH 7.2) with 20 mM glucose, but at lower concentrations (0.005 g_{cww}/mL to 0.05 g_{cww}/mL). Glucose was added for *in situ* co-factor regeneration. Immediately, before starting the reaction, styrene (from a stock solution of 100 mM styrene in pure ethanol) was added to the solution in order to have 1, 1.5 or 2 mM styrene present for the reaction. The reaction was performed in 4 mL vials with a plastic cap (GC and oxygen measurements) or with a plastic cap with a rubber seal (oxygen measurements) in a

tabletop orbital MRH11 Heating ThermoMixer (from HLC BioTech, Bovenden, Germany) at 30 ^{0}C and 400 rpm (with 3 mm shaking diameter). The rotation chosen to perform the bioconversion was optimized by previously measuring oxygen concentration with reaction time using an oxygen sensor integrated in a syringe tip (Fixed Oxygen Minisensor OXF500PT from Pyro Science, Aachen, Germany) connected to an Optical Oxygen Meter - FireStingO2 (from Pyro Science, Aachen, Germany). The rotation which allowed the reaction to be performed with a constant supply of oxygen was the selected one. Two reaction vials were used per residence time, one for GC validation and one for oxygen measurement.

3.3.5 GC analytical measurement

The samples for GC analysis were prepared by centrifuging the cells and extracting the supernatant two times with 500 µL of MTBE. The reaction mixture was analyzed at different reaction times by measuring substrate (styrene) and product (1-phenylethanediol) (Figure 40 (a)) concentration in the GC/FID-2010 (from Shimadzu, Kyōto, Japan). A Zebron ZB-1 column (30 m x 0.25 mm x 0.25 µm, from Phenomenex, California, USA) was used, with hydrogen as carrier gas (constant pressure of 50.2 kPa) and the injector and detector at 250 ^{0}C and 330 ^{0}C, respectively. For the detection, the column oven was set at 70 ^{0}C for 2 min, then raised to 120 ^{0}C at a rate of 15 ^{0}C/min and then raised to 320 ^{0}C at a rate of 50 ^{0}C/min. The GC-FID was operated in split mode, using 1mM of 1-octanol in methyl tert-butyl ether (MTBE) as standard. The retention times of all the substances measured are: 4.016 min for styrene, 6.084 min for 1-octanol and 7.729 min for 1-phenylethanediol.

3.3.6 Oxygen measurement setup

The two setups used for measurement of the oxygen consumption rate in the cell samples are presented in Figure 41. The oxygen measurement was performed using the oxygen platinum(II) meso-tetra(4-fluorophenyl) tetrabenzoporphyrin (PtTPTBPF) sensors integrated in the glass/silicon meander microchannel (from iX-factory, Dortmund, Germany now part of Micronit Microtechnologies B.V., Enschede, Netherlands), previously described in Chapter 2 and in Ehgartner *et al.* (2016) [174]. Both setups include two Cavro® XLP 6000 syringe pumps (from Tecan, Männedorf, Switzerland) with 250 µL syringes controlled with LabVIEW (from National Instruments, Texas, USA). The two syringes were connected to the meander microchannel by polytetrafluoroethylene (PTFE) 1.5875 mm (OD) x 1mm (ID) tubing (S 1810-12) (from Bohlender, Grünsfeld, Germany), using Flangeless polypropylene (PP) fingertight 1.5875 mm (ID) fittings (XP-201) and flangeless ferrules (P200X) (from Upchurch Scientific®, Washington, USA).

In the setup of Figure 41 (a), the sample being measured was first introduced in the syringe and then pushed inside the channel. It required two steps between the sampling and the measurement of the sample, thus also requiring more sample volume than the second approach, which is presented in Figure 41 (b). Furthermore, this approach was used in two formats: multiple sampling from the same reaction mixture at different residence times and single-sampling of the reaction mixture where the reaction for each of the residence times was performed in a different vial. The latter was the one used in the second approach, where the

sample is pulled directly inside the microchannel from the reaction vial, allowing a faster measurement of the oxygen consumption in the sample. Cleaning of the microchannel was performed in between samples with ethanol 5% (v/v) in deionized water and then deionized water. In the first approach, the cleaning solutions were pushed through the channel's second inlet, while in the second approach deionized water was first pulled through the outlet and then the same cleaning procedure as for the first approach was followed.

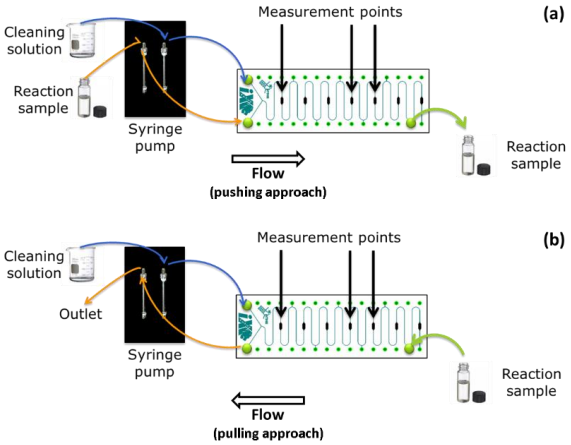

Figure 41 – Oxygen measurement setups used for screening variants for styrene biotransformation: (a) sample pushed through inlet; (b) sample pulled through outlet.

3.4 Results and discussion

The application of the meander channel with integrated oxygen sensors to the measurement of reactions involving whole cells encompassed several challenges. One of the main concerns was the possible clogging of the microchannels due to formation of cell clusters and its effect on fluid flow. *E. coli* cells have dimensions (< 2 µm in length) smaller than the microchannels in the meander chip used, and so no significant obstruction of the channels was expected for relatively diluted solutions used in the experimental work. Another concern involved the cell endogenous respiration rate, which in case of high respiration rates could rapidly consume the oxygen inside the reactor thus preventing measurement of oxygen consumed due to the bioconversion.

In order to address both issues, several dilutions of the wild-type (wt) NDO containing resting cells (*E. coli* JM109 (DE3) cells which were transformed with a pDTG141 plasmid for NDO) without substrate present, were introduced at 1.7 µL s^{-1} (0.085 m s^{-1}, Re 12.7) inside the reactor and the oxygen consumption was measured (Table 16). The flowrate was chosen based on previous experiments with the empty-vector (empty) cells (cells without the enzyme of interest), where the flowrates were varied between 0.21 µL s^{-1} (0.0105 m s^{-1}, Re 1.56) and 4.17 µL s^{-1} (0.2085 m s^{-1}, Re 31.1). At higher flowrates, the cells tended to accumulate faster both at the outlet and inside the channel resulting in a rapid oxygen consumption and leakage issues. Thus, lower flowrates were more appropriate to perform the reaction. However, at very low

flowrates, the oxygen inside the microchannel was completely consumed, leading to the selection of an average flowrate (1.7 µL s^{-1}) as the optimal flowrate for the experiments.

As shown in Table 16, a considerable dilution of the initial sample (1:10) was required in order to achieve a rate of oxygen consumption appropriate for sample comparison. The initial cell concentration was 0.05 g_{cww}/mL, which was half of the cell density usually used for the reaction at lab scale. Since variants with a higher affinity for the substrate or higher reaction rates could result in a faster oxygen consumption, the target oxygen consumption rate of the wt cells (without substrate) had to allow the distinction between faster and slower rates. The value considered as "good" for the purpose of these experiments was 0.02 mM/min, as highlighted in the table below.

Table 16 – Average oxygen consumption rates for different wt cell concentrations calculated for a flowrate of 1.7 µL/s. The cell concentrations used for the experiments are highlighted in red (initially chosen concentration) and orange (concentration used in the final experiments).

Cell concentration (g_{cww}/mL)	Dilution of initial sample	Oxygen consumption rate (mM/min)
0.05	1	-0.061
0.025	1:2	-0.051
0.01	1:5	-0.017
0.005	1:10	-0.019

During the sample dilution/ oxygen consumption rate tuning experiment, a leakage was observed at the outlet after a short period. This occurrence of a leak was more frequent for cell samples that were not properly mixed, and therefore containing previously formed clusters before introduction in the channels. The leakage was probably due to accumulation of cells at the outlet forming a blockage. The following experiments were then performed by placing the meander channel in a vertical position (as in Figure 42) and placing the collection vial below the outlet. This approach was expected to ease the movement of the cells out of the channel, preventing the formation of big clusters of cells that could obstruct the outlet.

The concentration of styrene used for the reaction also required consideration. Since the integrated oxygen sensors are made of polystyrene (polymer chains of styrene monomers), high concentrations of styrene could dissolve the polymeric layer and release the trapped dye, thus causing bleaching of the sensors and loss of sensing ability. Furthermore, a high styrene concentration could also lead to a faster reaction rate and thus faster oxygen consumption, impacting the previously determined optimal flowrate to perform the reaction. In order to test the effect of styrene, droplets of 100 mM styrene solution (50 to 100 times more concentrated than in the experiments), were placed on sensor spots, with no significant changes observed in signal detection. However, since the sensor spots were placed in an open environment, a rapid evaporation of styrene was observed and so the true effect of styrene might not have been measured. The lack of alternative testing devices, besides the meander microchannels used for the experiments, impeded further tests of the styrene effect on the oxygen sensors. The concentrations of styrene chosen to perform the reactions were thus based on the ones used for the lab scale bioconversions, 1 and 2 mM of substrate.

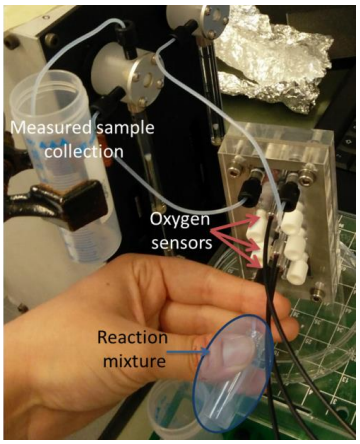

Figure 42 – Picture of the pulling sample setup with the meander microchannel in the vertical position.

Ideally, the meander microchannel with integrated oxygen sensors would function as an online monitoring system. Hence, the experimental setup was assembled in order to allow sampling from the reaction mixture at given reaction times. For this purpose, the reaction vial was closed using a lid with a rubber seal where an orifice allowed access to the reaction volume for the sampling tube connected to the syringe pump. Using the empty cells as the reference sample for quantifying endogenous respiration, the oxygen consumption of wt cells was measured in the presence of styrene. Initially, however, these experiments did not yield the expected difference in oxygen consumption rate between the two cell types measured.

Several factors were considered to identify the reason for the similarity between the two reaction rates:

- The high volatility of the substrate (styrene) could lead to a decrease in concentration over time, since in order to sample the reaction mixture, the vial was not completely sealed and the tubing used might be permeable to styrene.
- The reaction could be faster than expected and have finished at the chosen reaction times monitored.
- The oxygen consumed by the reaction could be meager, resulting in such a slow consumption rate that distinction from cell respiration would be imperceptible or within sensor signal variability.

To avoid some of the possible identified issues, a different sampling strategy was tested. The validation of the oxygen measurements was performed by implementing parallel reactions, instead of quantification of product formation in the outlet of the meander channel, due to the small volumes in the microchannel and in order to keep the standard procedures for product quantification. The reaction was thus performed in two identical vials per residence time placed at the same conditions in the tabletop thermomixer. One of the vials (for oxygen measurement) had a cell concentration with a dilution of 1:10 relative to the other vial. At the different chosen residence times, the vial with the higher cell dilution was opened and then measured in the microreactor, while the other vial was simultaneously prepared for quantification in the GC. By performing the reaction this way, loss of substrate due to evaporation was minimized since the vial was opened immediately before measurement. Furthermore, measurements were

performed at shorter residence times (starting at 5 min instead of 30 min) allowing to detect if the reaction was faster than expected. Additionally, since the cell preparation procedure is considerably longer than the time required for the oxygen measurement, the comparison between freshly prepared cells and freeze-dried cells was also performed. The use of freeze-dried cells would enable to perform tests on the same cells for more than one day while guaranteeing their stability and comparative behavior, as well as analyze older cell samples or samples from different sources (e.g. other laboratory facilities) if required.

Figure 43 presents the results of the experiments described above for freshly prepared and freeze-dried cells at 2 mM styrene concentrations and the corresponding values of product formation measured in the GC. As can be observed, the oxygen consumption rate for wt and empty cells is still very similar for both cell preparations and with quite low rate values. From the parallel GC measurements, it is possible to observe that the bioconversion was much faster than expected, since after 5 min around 50% of the substrate had already been converted. At the end of 30 min 80% of the substrate had been converted, after which the concentration of substrate remained roughly unchanged until the end of the experiment (residence time of 90 min). These concentrations were equivalent to previous lab-scale assays where the reaction had run for 20 h with only end-point GC quantification. The reaction was therefore significantly faster than expected, and could be monitored with sampling points until 30 min of reaction time was reached. This enables a significant increase in the number of variants and reactions that can be screened per day with the standard method. It is also a good example of the valuable input that microfluidic systems can provide in terms of reaction kinetics in this field.

In Figure 43 it is also possible to observe that freshly prepared and freeze-dried cells present a similar behavior in terms of oxygen consumption and reaction output, and so measurements with freeze-dried cells can not only be performed but also compared with the ones made on freshly prepared cells.

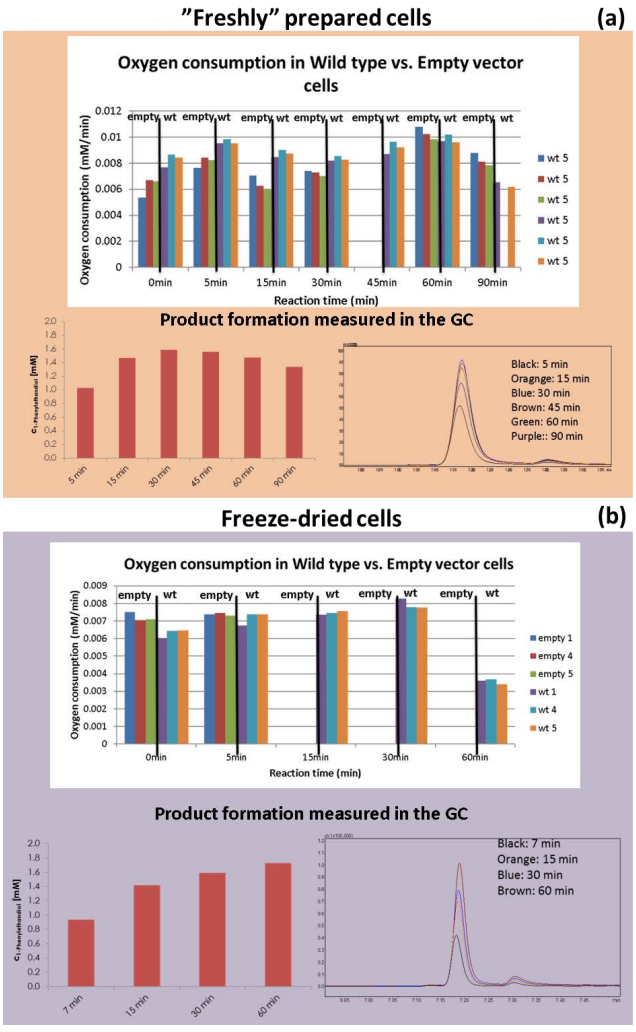

Figure 43 – Summary of oxygen consumption rate and GC measurements of 1-phenylethanediol concentration produced during the reaction for empty-vector (empty) cells and wild-type enzyme containing (wt) cells in (a) fresh and (b) freeze-dried preparations at 2 mM styrene.

Since the oxygen values obtained in these experiments were still equivalent for both cell types, the reaction was performed again but at the same dilution as the one monitored in the meander channel (0.005 g_{cww}/mL), and measured in the GC. No product concentration was detected in these samples, which clarified the similarity in signal for both cell types measured for the 1:10 dilution. Moreover, the time required for the uptake of the sample from the reaction vial to the syringe, followed by introduction of the sample from the syringe into the reactor was higher than 1 min, meaning that the start of the reaction and the probable period for the highest substrate conversion was lost during the sampling step.

To overcome both issues a different approach was implemented. Such approach required the uptake/withdrawal of the sample from the outlet of the meander channel, thereby pulling the sample through the outlet, instead of pushing the sample through the inlet (see Figure 42). Through this process, by having a short tube at the outlet the sampling time was reduced to just a few seconds. This new strategy was further coupled with a lower cell dilution (1:5, in orange in Table 16). Shorter residence times (1 and 3 min) were also implemented in order to check when the start of the reaction occurred. The new sampling strategy associated with a lower cell dilution enabled to measure a difference in oxygen consumption rate between empty and wt cells, as can be observed in Figure 44. Cells containing the wt NDO presented almost 2-fold the oxygen consumption rate of the empty-vector cells. This reaction was also performed at lower styrene concentration (1mM), which resulted in a higher substrate conversion than previously obtained (74 % at 1 min of reaction time). A lower concentration of styrene was used to minimize the impact of substrate concentration on cell behavior, since a decrease in oxygen respiration values, possibly related to substrate concentration, had been observed with longer reaction times. After 15 min of bioconversion the oxygen consumption rate decreased and a stabilization of product concentration is observed, which seems to fit the oxygen consumption rate profile.

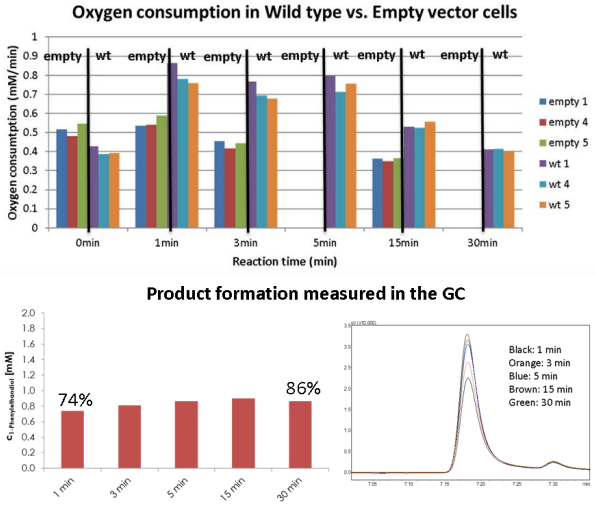

Figure 44 – Oxygen measurements of the reaction of empty and wt cells in the presence of 1 mM styrene concentration, and corresponding GC results for the wt cells of 1-phenylethanediol concentration produced during the reaction and percentage of substrate conversion obtained at 1 and 30 minutes of residence time.

The oxygen consumption rate of two NDO-variant containing cells (V260A and H295A) was also measured in the meander microchannel. As can be observed in Figure 45 (a), a difference between the two variants as well as compared with the wt and the background (empty cells) could be observed. One of the variants (V260A) presented a higher oxygen consumption rate, especially in the first 3 minutes of the reaction, which could indicate a slower initial reaction rate. This would translate in the fact that it should be possible to observe the initial substrate conversion rate, contrary to what was observed with the wt cells. It might also mean

that this variant has a higher reaction rate, leading to a faster oxygen consumption rate. As can be observed in Figure 45 (b), the latter was verified, since a 90% conversion of the substrate was measured in the first minute of the reaction. This variant however, presents a decrease in product concentration at 30 min (Figure 45 (b)) which may indicate further oxidation of the product into another compound or even the production of the other enantiomer of 1-phenylethanediol. The other variant presented an oxygen consumption rate closer to the one of the wt cells, where the rate during the bioconversion is very similar to the endogenous respiration of this variant (value of oxygen consumption rate at 0 min in Figure 45). The observed oxygen consumption rate is also maintained longer above the value for empty cells than for the wt cells. As can be seen in the figure below, this is also the variant (H295A) that presents the lower initial conversion with a steady increase during the 30 min of reaction monitored, while the other two cell types maintain approximately the same value after 3 min. Although H295A has a smaller reaction rate than the other measured enzymes, the increased cell respiration might indicate an interference of the heterologous enzyme with the metabolism of the host organism, which might be interesting to investigate further.

From the presented experiments for empty-vector cells, wt, V260A and H295A, it is possible to conclude that higher consumption rates indicate higher substrate conversion. Moreover, the duration of the oxygen consumption rate above empty-vector cell endogenous respiration levels represents a continuation of substrate conversion, while the decrease in oxygen levels translates in a conservation of product concentration without significant reaction rate.

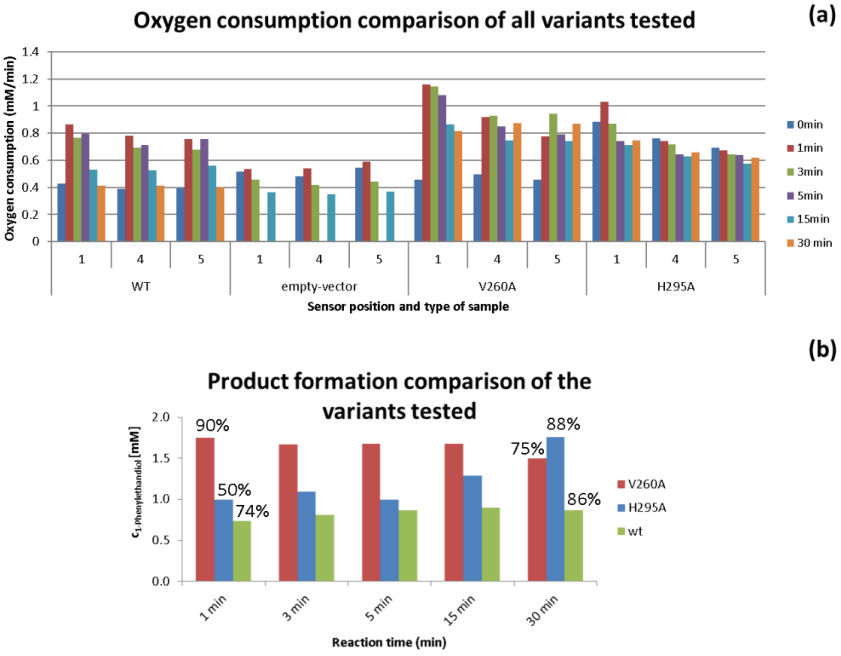

Figure 45 – Oxygen consumption rate values for all the cell types tested with the pulling sample approach and higher cell concentration (a) and GC results for the two variant containing cells (at 2mM styrene) and wt cells (at 1mM) of 1-phenylethanediol concentration produced during the reaction and percentage of substrate conversion obtained at 1 and 30 minutes of residence time (b).

To understand the applicability of the meander channel as a screening platform, and whether it was possible to distinguish oxygen consumption rates due to different substrate concentrations, further experiments were performed. The bioconversion with wt cells was performed at two different concentrations of styrene. As demonstrated in Figure 46 (a), a slightly higher oxygen consumption rate was observed for the higher styrene concentration, but only in the first minute of reaction. The results of substrate conversion obtained from the GC indicate that higher substrate concentration results in a lower initial substrate conversion. This can imply some effect of the substrate on the reaction rate. On the other hand, since the measured product concentrations for the two reactions are quite similar, this might indicate that the reaction rate is limited by substrate diffusion through the cell wall at the concentrations tested.

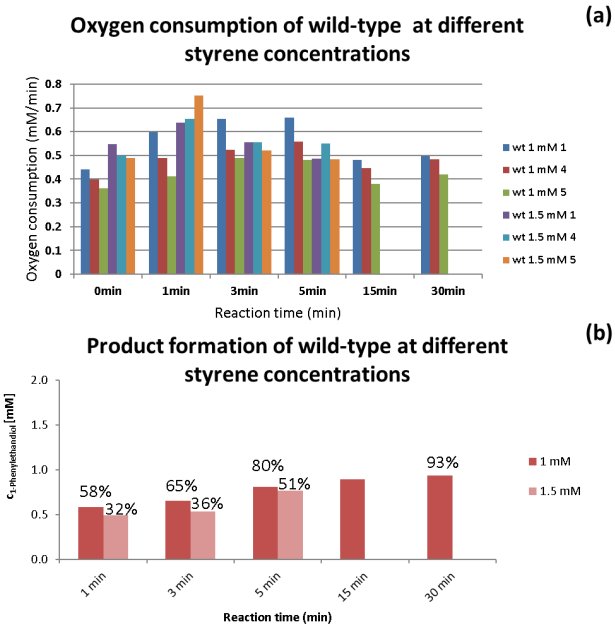

Figure 46 – Oxygen (a) and GC (b) measurements of the reaction wt cells in the presence of two styrene concentrations (1 and 1.5 mM).

It is relevant to mention that the bioconversion at the reaction conditions and cell densities used has a relatively high conversion rate (50 to 70% depending on initial substrate concentration), which greatly contributed to the measurable oxygen consumption difference between the biotransformation and cell respiration. Since higher cell densities might lead to obstruction issues, there is a limitation on the use of this platform in terms of reaction rate to fast reactions only, which generate oxygen consumption rates higher than the host's respiration rate. This limitation can be observed in Figure 45 for the H295A variant. Reactions with slower kinetics, which is usually the case for initial dioxygenase variants, might hence be more difficult to detect with this microfluidic platform. Faster reaction rates, on the other hand, can be more easily screened, by increasing the flowrate used during the detection and/ or by decreasing the cell density used for the biotransformation or for the measurement.

In the extensive literature review, no values of oxygen consumption rate for dioxygenases in whole cells were found. Hence, the attained values during the experiments presented here were compared with values for pure dioxygenases measured with the polarographic method [278]. The comparison between the values is presented below in Table 17. The values from the literature (in blue in Table 17) cited in the table were calculated from the values presented in the articles, considering the enzyme concentration used in the respective assays, so as to have comparable values. The values presented in the table for the NDO and variants tested in this study (in green in Table 17), are an average of the rates obtained in the first three minutes of the reaction (when the highest rates are measured) in sensor 1 (where the more defined oxygen behavior seems to be observed), calculated without the background value of cell respiration.

Table 17 – Comparison of oxygen consumption rate/ oxygen uptake of the whole cell catalyst (in green) with values for pure dioxygenases found in literature (in blue).

Biocatalyst	Substrate	Measurement setup	Oxygen uptake (mM min^{-1})
NDO from *Sphingomonas* CHY-1 [280]	Naphthalene (0.1 mM)	Clark-type oxygen electrode	14.95
NDO from *Pseudomonas* sp. Strain NCIB 9816-4 [279]	Styrene (0.1 mM)		0.0700
NDO (pDTG141) wild-type in *E. coli* JM109 /DE3)	Styrene (1 mM)	Luminescent oxygen sensors	0.3202
NDO variant V260A in *E. coli* JM109 /DE3)	Styrene (2 mM)		0.6553
NDO variant H295A in *E. coli* JM109 /DE3)	Styrene (2 mM)		0.4560

A direct comparison between the values retrieved from the literature (in blue in Table 17) and the ones measured (in green in Table 17) is difficult since different enzymes, substrates, substrate concentrations and oxygen measurement techniques were used. There are one or two orders of magnitude of difference in oxygen uptake between the different catalysts, but it is interesting to notice that the highest uptake rate was obtained for the natural substrate of the enzyme (naphthalene). When comparing biocatalyst performance for the same substrate (styrene), it should be noted that the measurement with whole cells was performed at a substrate concentration that is 10-fold higher relative to the corresponding substrate literature value. If a linear relationship between oxygen concentration rate and substrate concentration is considered, then the rate values obtained for the NDO from *E. coli* JM109/DE3 are half or lower than the one obtained for NDO from *Pseudomonas* sp. NCIB 9816-4. The lower oxygen consumption rate could be related to the already discussed diffusion limitations due to the cell membrane. It should, however, be taken into consideration that the data presented in this chapter indicates that the oxygen consumption rates measured for the NDO from *E. coli* JM109/DE3 are diffusion limited and so a linear relationship between oxygen concentration rate and substrate concentration does not occur.

It is also worth mentioning the degree of variability in the data presented in this chapter, especially in oxygen consumption rate results which was not possible to quantify appropriately throughout the duration of the experiments. This variability can be related to the used sensors, as previously discussed in Chapter 2, especially since there was some degradation of the sensor

signal (due to leaching of the luminescent dye) during this study due to the use of styrene as substrate and ethanol as part of the cleaning procedure. However, variations in the cell concentration used or in the uptake flowrate (in the pulling through outlet strategy) can also have influenced the obtained results. When pulling instead of pushing a liquid solution with pistons pumps there is less control on the actual flowrate being applied, since the resistance to flow is increased by the resistance of the microchannel. If the pressure difference is too high, vapor may be pushed to substitute the space created by the uptake of fluid and bubbles will be observed. Also, if there is no possibility for entrance of air, cavitation may occur, where vapor fills the void left by the uptake of fluid. This is due to vapor formation when the local pressure drops below the liquid vapor pressure, establishing a bubble which collapses when higher pressures are applied. Cavitation is more likely to be observed when low pressures are applied at the outlet or high pump flowrates are used [291], [292]. At the flowrates used to perform the experiments no bubble formation was observed. Furthermore, no sensor signal change was measured that could indicate a sudden change of pressure (e.g. a sudden pressure decrease that could indicate formation of a vapor cavity). Thus, no significant differences were observed during the experiments that could indicate such an effect. Data variability is most likely related to differences in the preparations of the cell solutions due to small variations in the amount of cells weighed, and thus the amount of cells present. The variability in oxygen data obtained can also be inherent to the measurement itself, as also described by Jouanneau *et al.* (2006) with the observed discrepancies in the enzyme activities obtained when the oxygen assay was applied (polarographic assay using Clark-type oxygen sensors) they applied [280].

The microfluidic system presented here cannot compete in terms of throughput with most of the screening systems discussed in section 3.1.3.1. of the Introduction. However, it can provide a different type of input (oxygen consumption rate and maybe other oxidative properties) than the discussed screening platforms. In terms of throughput, the system presented here can perform a single measurement every 10 min (including sample uptake and channel cleaning). This means that in a continuous operation, it would be capable of performing 47 single measurements in an 8h working day and 129 single measurements in a 22h working day (with 2h for thorough cleaning of the microreactor, tubing and system components). Considering the same reactions performed for this work (around 50 min for each to complete), per day we could perform 9 entire reactions in an 8 h working day or 26 entire reactions in a 22h working day. Since each single measurement takes around 10 min, in order to perform measurements every minute of a certain reaction vial, 10 microreactors of this type would have to work in parallel, and such a system is easily achieved with microfluidic units. Furthermore, by working in solution and not in droplet such a system can enable a direct measurement (e.g. side-loop with recirculation) from the reaction vial using a simpler microfluidic arrangement, if a more air-tight setup is assembled. This setup could be achieved by using steel or a less permeable polymer as the tubing material, as well as more appropriate sealed reaction vial caps. The system can also be connected to one of the droplet-based systems discussed in the Introduction so as to achieve a more comprehensive characterization of the mutants during screening.

3.5 Conclusions

The presented results demonstrate the potential of the meander microchannel with integrated oxygen sensors to function as a biocatalyst screening platform for oxygen-dependent whole cell biocatalysts. It was possible to measure the endogenous respiration rate of the *E. coli* cells used, and distinguish respiration rate from oxygen consumption due to styrene oxidation by wild-type NDO. Additionally, the two tested NDO variants showed different oxygen consumption rates from the ones obtained with the wild-type. Variant V260A presented a higher oxygen consumption rate in the first 3 minutes of the reaction, corresponding to a faster styrene conversion (90% after 1 min). On the other hand, variant H295A showed a similar oxygen consumption rate compared to the wild-type NDO, which was equally maintained throughout the monitoring time (30 min), unlike the wild-type NDO, whose consumption rate decreased close to endogenous respiration levels after 15 min. This variant, generated however a smaller conversion rate with a steady increase during the reaction time, indicating a slower reaction rate than the other variants tested. Furthermore, this variant (H295A) allowed to highlight a potential limitation in terms of reaction rates measurable by the microfluidic platform, identifying the reaction rate below which the microfluidic platform is unable to distinguish oxygen consumption due to the biotransformation from the endogenous respiration. The oxygen consumption rates measured with the meander channel with integrated oxygen sensors appear to be concordant with the values found in the literature.

The presented platform shows a great potential as a screening platform for mutants involved in oxidative reactions, especially enzymes with high reaction rates and fast bioconversions. The platform can achieve a relatively high throughput (129 single measurements or 26 reactions per day) which can be further improved by adding more microfluidic systems in parallel and automating sampling. The current throughput of the platform is similar to the one obtained with the GC, where 129 reactions could be measured within 21.5h, without time required for reaction preparation (which would imply a further 6h).

In order to obtain a full characterization of this microfluidic system as a screening platform, it would be interesting to perform experiments with additional variants in order to detect relevant patterns or tendencies observable by using only the oxygen sensors. It would also be interesting to check whether phenomena such as product overoxidation, substrate inhibition or toxicity, or uncoupling effects can be observed or detected through oxygen consumption rate measurements.

Moreover, two different screening approaches can be achieved with this platform: variant comparison or substrate comparison. The first approach, which was the one demonstrated in this chapter, compares the oxygen consumption of different variants relative to the same substrate. A higher rate indicates either higher variant activity or higher substrate specificity for the target substrate. In the second approach, the same cell type can be tested with different substrates. Again, different rates would correlate with differences in specificity and activity. Furthermore, in this case, endogenous cell respiration of the cell without the target enzyme, or of the mutant at different substrate concentrations could further indicate possible toxicity issues from the substrates being screened.

Chapter 4

Multi-purpose platform for sensor integration

The microfluidic platform presented in this chapter was developed in collaboration with Daria Semenova from the PROSYS research group at DTU, Lyngby, Denmark, Peter Panjan and Adama M. Sesay from the Measurement Technology Unit (MITY) at Oulu University, Kajaani, Finland

The limited availability of metabolite-specific sensors for continuous sampling and monitoring is one of the main bottlenecks that may contribute to failures in bioprocess development. Furthermore, only a limited number of approaches exist to connect currently available measurement systems with high throughput reactor units. This is especially relevant in the biocatalyst screening and characterization stage of process development.

In this chapter, a strategy for sensor integration in microfluidic platforms is demonstrated, to address the need for rapid, cost-effective and high-throughput screening in bioprocesses. The developed platform is compatible with different sensor formats by allowing an easy sensor replacement and was built in order to be highly flexible and therefore suitable for a wide range of applications (e.g. enzyme screening, glucose monitoring in fermentations, monitoring biomarkers in biological samples). Moreover, this re-usable platform can be easily connected to analytical equipment, such as HPLC, lab scale reactors or other microfluidic chips through the use of standardized fittings. Also, the developed platform includes a two-sensor system separated with a mixing channel, which allows the detection of samples that might be outside the first sensor's range of detection, by offering the possibility to achieve up to 10 times dilution of the sample solution.

In order to highlight the features of the proposed platform, inline monitoring of glucose levels is presented and discussed as illustrative example. Glucose was chosen due to its importance in biotechnology as a relevant substrate. The platform demonstrated continuous measurement of substrate solutions for up to 12h.

4.1 Introduction

In- or online quantification of reaction products or target compounds in a bioprocess is essential to achieve a high degree of knowledge, and consequently control, regarding reaction (or side-reaction) kinetics, production yield, by-product formation, biomass concentration, process efficiency, etc. [50], [51], [52], [47], [60].

Microfluidic systems show a considerable potential in screening applications and online monitoring. The variety of achievable geometries, high surface to volume ratio and diversity of sensing technologies available at small scale, make them a highly attractive tool for bioprocess development [293]. Moreover, a better control of operating conditions, especially flow, permits a good definition of gradients of substrate or other components involved, which can be further

improved with a higher degree of automation. However, due to the challenges involved in sensor development and integration, microfluidic systems are still application-specific, as they are typically too rigid to address the needs of different bioprocesses [294]. Therefore, a change in the target sample (e.g. type of sample), the used sensor technology or flow conditions, or need for integration with other systems, requires a re-design and the fabrication of a new platform. This greatly reduces the microfluidics range of applications, and therefore also stands in the way for the wide-spread use of microfluidic systems.

One of the main contributors to this microfluidic challenge is sensor integration. Biosensors translate a biological response (from an enzyme or cell) into a quantifiable signal, by connecting the biological element to a transducer, that in turn transforms this signal into an electronic signal that can be amplified and further processed [295]. The use of a biological component allows to greatly increase the specificity of the sensors to a target analyte or a range of target compounds. However, the (bio)sensors in a given microfluidic platform need to be stable under normal operating conditions [295] and are thus optimized for a given set of temperature, sample or flow conditions, consequently being often limited in application. Thus, the applied strategy for sensor integration in a microfluidic platform depends on the detected sample, the type of sensor and the materials that form the sensor and the platform. Furthermore, the main limitation to sensor integration is usually related to the miniaturization of the transducer element [295].

Electrochemical (EC) sensors show great promise in integrated analytical systems due to their robustness, the ease of miniaturization and inexpensive instrumentation [296], [295], [166]. Miniaturization of the instrumentation has been harder to achieve, but relatively portable electrical measurement systems (e.g. potentiostats) have already been developed [297], [298].

4.1.1 Electrochemical sensing

Electrochemistry detects the presence of electroactive species, which can be the target analyte or a product of a redox reaction involving the analyte. Electrochemical (EC) sensors, unlike optical sensors, do not require transparent materials and can therefore be used in a wider range of substrates, from silicon to paper fibers. Additionally, they can be applied to turbid solutions and do not show sensitivity to auto-fluorescence effects from biological samples like optical sensors. On the other hand, EC sensors are affected by differences in pH and ionic strength, and in some situations flow conditions. Also, the sensing area and architecture influence the obtained sensitivity and signal-to-noise ratio [295]. The electrode or required functionalized area to achieve a good sensor performance also limits the miniaturization attainable with electrochemical sensors in order to keep a high sensitivity [299].

EC sensors always involve the interaction between the electrode surface (that can be covered by a layer of the biorecognition element) and the target analyte, yet the electrochemical reaction may occur on (contact EC) or before/outside (contactless EC) the sensor. Electrochemical sensors used for contact detection of biomolecules require functionalization of their surface with molecules (usually enzymes) specific to the target, either by immobilization of the molecules directly on the sensor's surface, immobilization in a membrane placed over the sensor surface, or a combination of both methods. For contactless detection, the electrochemical

reaction might occur either in solution or upstream of the sensor by immobilization of enzymes in monoliths, for example [300].

EC sensors usually present a reference electrode (most often made from Ag/AgCl, that allows maintaining a stable potential during measurement and is placed at a certain distance from the redox reaction), a counter electrode (in contact with the electrolytic solution and providing the connection through which a current is applied to the working electrode) and a working electrode (the sensing or transduction element, made of the same material as the counter electrode, e.g. platinum or graphite), as can be seen in Figure 47 [295], [166].

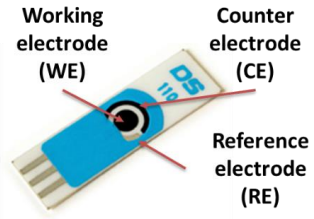

Figure 47 – Highlighted working, reference and counter electrodes in a commercial DS 110 screen-printed carbon electrode from DropSens (Llanera, Spain).

The target analyte can reach the electrode surface through diffusion (due to a concentration gradient between the bulk solution and the inner layer), migration (due to a potential gradient between the bulk solution and the inner layer) or through convection (due to forced movement of the solution) [166]. The inner layer is a charged layer formed over the electrode surface when this has an excess of charge, having the opposite charge of the surface. Above this layer a second layer is also usually formed, called the diffusive layer, that has a gradient of oppositely charged ions relative to the inner layer. Hence, an electric potential is found between these two layers [166].

Detection with EC sensors can be performed through several methods, with conductivity, amperometry and potentiometry being the most common. A visual representation of the main electrochemical methods is presented in Figure 48.

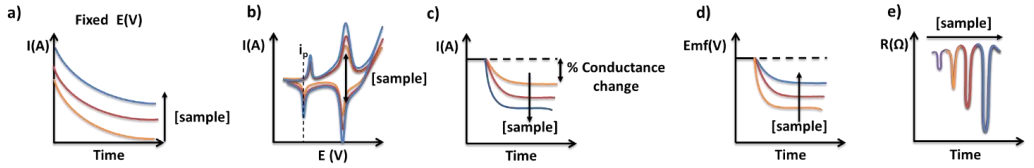

Figure 48 - Schematics of electrochemical detection methods: a) Amperometry (current measured is proportional to the flux of sample to the electrode surface, which depends on the concentration gradient in the bulk solution and thus decreases with time until it stabilizes); b) Voltammetry (e.g. cyclic voltammetry where oxidation/reduction peaks of the target substance or a mediator are measured. The magnitude of the peak corresponding to the monitored reaction (ip) can be qualitatively related to sample concentration); c) Conductometry (measurement of the change in conductivity of the electrode due the presence of charged species); d) Potentiometry (measurement of the change in potential (electromotive force (Emf)) at the ion selective electrode due to accumulation of selective ions at the electrode surface); e) Impedance (measurement of the change in resistance/capacitance of the electrode or the solution in contact with the sensor). Figure adapted from [166].

In amperometric detection (Figure 48 (a) and (b)) an electrical current generated by the oxidation or reduction of the analyte at an applied constant voltammetric potential between the

reference and working electrodes is detected. As can be seen in Figure 48 (a), first a high current is measured, which corresponds to the analyte concentration being depleted in the double-layer formed above the electrode's surface. As the analyte depletion starts occurring in the bulk solution a decrease in current is observed with the decrease of concentration gradient [166]. The potential applied to the working electrode relative to the reference electrode is usually defined at the (mass) diffusion limited current region of the analyte, which results in a linear response with variation of the analyte concentration [102]. Sensitivity of amperometric sensors can be hard to maintain if the sensor surface area is decreased [102]. The most common amperometric measurements are performed either by voltammetry or chronoamperometry. Voltammetry indicates the reversibility of the system by changing the potential in a controlled fashion, but the rate at which the potential is changed affects the obtained results [166]. In chronoamperometry current versus time plots are obtained, where the current is measured at a constant square-wave potential [295]. In chronoamperometry the observed current changes depend on the diffusion layer between the electrode surface and the bulk solution, which controls the transfer of the target analyte to be measured at the electrode's surface [295]. Chronoamperometry can be described by the Cottrell equation (Equation 24), where I is the current, F is the Faraday's constant, n is the number of electrons transferred per detected molecule, A is the electrode surface area, c_0 is the concentration of target analyte, D is the analyte diffusion coefficient and t is time [295].

Equation 24

$$I = nFAc_0\sqrt{\frac{D}{\pi t}}$$

In contact amperometry, care must be taken since many biomolecules such as proteins are not electroactive, thus requiring a label [177]. In the case of detection through enzymatic reactions, a mediator may be required to transport the electrons to the sensor surface. Amperometric sensors can be fabricated together with microchannels by photolithographic processes [75], providing an easy integration with the channel but low target flexibility. Paper or ceramic based amperometric sensors allow high target flexibility by permitting a change of the sensors being used through the use of disposable sensors.

Conductometry (Figure 48 (c)) detects the conductivity responses that differently charged analytes and different analyte concentrations generate between electrodes at a series of frequencies [295], [75]. Hence, they can be applied only to charged species or species that can be charged, lacking however specificity. The low specificity of the technique in turn allows its application to more types of samples with a higher variety of strategies, resulting in an easy miniaturization for application in cell studies (e.g. shape, changes in cell membrane) [102]. In contact conductivity, the electrodes are placed inside the microchannel in direct contact with the sample, while in contactless mode the electrodes are isolated from the sample (for example, by covering them with a photoresist layer), which avoids electrode fouling and bubble formation [75]. Conductometry devices are usually associated with enzymes, used to study enzymatic reactions that create variations in the concentration of charged species [295]. These electrodes can be patterned in silicon wafers or glass through semiconductor technology or on printed circuit boards (PCBs) which are then covered and integrated with a channel. Conductometry

methods are conventional contacted conductivity detection and capacitively coupled contactless conductivity detection (C^4D) methods such as potential gradient detection [75], [301].

In potentiometry (Figure 48 (d)), the measurement is performed through the detection of a generated potential between a reference and an ion-selective working electrode when no current is flown between the two electrodes. This potential is generated due to a built-up of charge separation when ions pass through the selective membrane of the working electrode and a local equilibrium is established at the sensing interface [295]. Potentiometry measures the concentration of ions in a redox reaction up to 10^{-11} M and is mathematically based on the Nernst equation (Equation 25), where E_{cell} and E^0_{cell} are the observed potential at zero current and the constant potential contribution to the electrochemical cell, respectively, R is the universal gas constant, T is the absolute temperature in Kelvin, and Q is the ratio of ion concentration between the anode and the cathode [295]. The fabrication strategies of potentiometric sensors are similar to the ones presented for conductivity and amperometric detection [75], but miniaturization issues are usually involved with the strategy for miniaturization of the reference electrode [102].

Equation 25

$$E_{cell} = E^0_{cell} - \frac{RT}{nF} lnQ$$

Impedance sensors (Figure 48 (e)) measure the change in electrical impedance at a fixed or variable frequency between an electrode and the solution when adsorption of the target molecule to the electrode occurs. Impedance allows studying intrinsic material properties (e.g. polymer degradation, electrolyte degradation, status of car engine oil, cell adherence on sensor structures) that result in a resistivity or capacitivity change [299], [295]. It has also been applied to monitor biorecognition events (e.g. in immunoassays) occurring at the surface of the electrode [295], and presents sensitivity to nonspecific adsorption [166].

Another type of electrochemical sensors is the field effect transistor (FET). FET measures a current resulting from a potentiometric effect at the gate (an electrode where potential is varied relative to two other electrodes, the source and the drain) [295]. An EnFET (enzyme FET) consists of a transistor where the metal gate is replaced with surface functionalization, while an ISFET is an ion-sensitive FET. Target molecule adsorption results therefore in a change in potential at the gate causing a measurable signal between source and drain [295]. These sensors present however some cross-sensitivity and issues with pH change, as well as difficulties in incorporating an appropriate and low-cost reference electrode. The encapsulation of FET greatly influences their stability and reproducibility [299]. Nanowires (e.g. carbon nanotubes (CNTs), conducting polymer nanowires (CPNWs), nanorods, nanosprings) can be used to connect the gates in FET resulting in an increased sensitivity, except for solutions with high ion concentrations [177]. Carbon nanotubes, and other nano-objects (e.g. gold nanowires and nanoparticles) can also be integrated in membranes of amperometric and other types of sensors in order to increase sensitivity and lower the limit of detection [295], [302].

The presented electrochemical methods are often coupled with electrophoresis operations (such as capillary electrophoresis separation) or in electrophoresis systems.

Miniaturization of the electrode area to the micrometer scale, required for integration in microfluidic systems, allows (i) decreasing the measurable currents (down to nanoamperes), (ii)

decreasing required sample volume, (iii) increasing the response time to alterations in the applied potential, (iv) increasing the efficiency of diffusional transport of the target analyte to the electrode's surface, and (v) decreasing the contact resistance [166].

Combination of electrochemical and optical detection can also be performed on the same chip [102], [303]. EC sensors can be combined with other label-free detection methods (e.g. surface plasmon resonance (SPR) [304], quartz crystal microbalance (QCM) [305], optical waveguide lightmode spectroscopy (OWLS) [183]) with the integration of a conductive electrode on the chip [295]. The electrochemical sensors' sensitivity, specificity, precision and operation stability are highly dependent on (i) the used fabrication techniques, (ii) how the miniaturization is performed, (iii) which material deposition methods are used, and (iv) which coatings and immobilization methods of biomaterials and biomolecules are used [306], but also on (v) electrode size, (vi) geometry, (vii) position in the measuring chamber, and (viii) surface structure [166]. So, in other words, the development of EC sensors is a significant and time-consuming optimization problem.

4.1.1.1 Glucose electrochemical sensors

The most successful commercially available and used biosensor is the electrochemical glucose sensor [307], with a worldwide market that is estimated to be close to 10 billion dollars [166]. Its development revolutionized the management of diabetes mellitus in patients, allowing a more accurate and frequent measurement of glucose levels in blood in hospitals, but especially in the patient's home [308]. But the history of glucose and electrochemistry started long before, in 1909 with the electrooxidation of glucose to gluconic acid by Walther Loeb in a sulfuric acid solution using a lead anode [308].

The electrooxidation (non-enzymatic detection) of glucose, performed with different metals (e.g. Pt, Au, Cu, Ni, TiO_2) at alkaline pH shows a high electrocatalytic ability, sensitivity and selectivity towards glucose. Polycrystalline or nanoporous metals or metal nanoparticles supported in carbon nanotubes developed so far show high stability, but with some degradation of the surface due to the alkaline environment which affects the electrode's lifetime [307]. Also, selectivity of electrooxidation of glucose is generally lower than the one obtained with enzymes [307]. Au-nanoparticles prepared by citrate reduction can be an exception, functioning as artificial enzymes capable of oxidizing glucose without requiring electricity [307]. Furthermore, for most of the materials used in glucose electrooxidation, the irreversible adsorption of partial oxidation products or of active species in solution causes the poisoning of the electrocatalysts used for glucose oxidation [307]. This in turn lead to the wide application of enzymes to perform the substrate oxidation [308].

The most used enzymes are glucose oxidases (GOx) and glucose dehydrogenases (GDH). GOx, as mentioned in Chapter 1, has a high selectivity for glucose and oxidation involves the reduction of FAD, followed by its re-oxidation in the presence of molecular oxygen. GOx presents an apparent formal redox potential of -0.048 V vs. SHE (standard hydrogen electrode) at pH 7.2 [308]. GDH has a broader substrate spectrum (e.g. glucose, galactose, xylose), and can have several co-factors depending on the dehydrogenase (NAD, ß-nicotinamide adenine dinucleotide, and PQQ, pyrroloquinoline quinone). NAD-GDH require a source of the co-factor (NAD+) and a redox mediator to lower the voltage required to oxidize NADH [309]. PQQ, unlike FAD, is not

oxidized during the reaction, however presents a lower stability than FAD or NADH-dependent GDH [308], [309]. Glucose oxidation by GDH occurs at a lower potential, 10.5±4 mV at pH 7 and in the presence of an excess of calcium ions [308]. Another relevant enzyme in glucose monitoring is the isoenzyme 2 of hexokinase, that presents a very high specificity. However, its higher price over GOx, dependency on ATP and lower stability prevents its wider application in glucose sensors [307].

Enzyme immobilization on the electrode's surface can be achieved by physical adsorption, however in this case enzyme stability is easily affected by the experimental conditions, such as pH, ionic strength, temperature, charges, etc. Addition of bovine serum albumin (BSA) can improve stability in physically adsorbed enzymes. Covalent attachment is the most effective method for enzyme immobilization, and can be performed with hydroxyl groups of chitosan and 1,4-carbonyldiimidazole, thiolated gold nanoparticles or using the enzyme's amino acid residues. Other immobilization approaches are the physical entrapment or encapsulation of enzyme inside a solid matrix that can be formed of polymers, redox gels, sol-gel or carbon pastes [307].

The first enzymatic glucose sensor was fabricated by Clark and Lyons in 1962, and involved a thin layer of GOx embedded in a semipermeable dialysis membrane placed over a Pt electrode for measuring oxygen depletion (the Clark oxygen sensor mentioned in Chapters 2 and 3) [309]. Oxygen-based glucose measurement can also be achieved with an indium tin oxide (ITO) electrode covered with an oxygen and proton permeable membrane [308]. The first amperometric-based glucose sensor was described in 1973 by Guilbault and Lubrano and was based on monitoring the produced hydrogen peroxide [309].

Glucose sensors that rely on the detection of hydrogen peroxide by GOx oxidation with molecular oxygen (the physiological mediator), are called first generation glucose biosensors (Figure 49) [309].

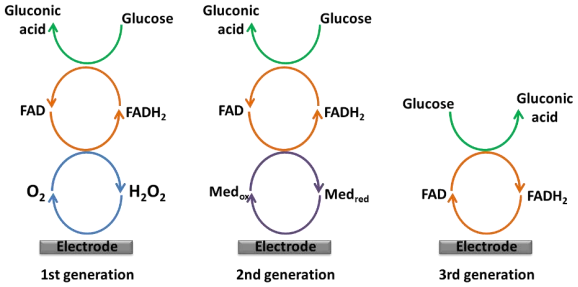

Figure 49 – Schematics of the sequence of redox steps involved in glucose detection with the different generations of glucose biosensors.

In these sensors, amperometric detection of hydrogen peroxide can be performed with (i) anodic oxidation (enables regeneration of oxygen for use in the enzymatic reaction) at +0.3-0.8 V vs. SCE (standard calomel electrode) using Pt on graphite, carbon pastes, carbon nanotubes and conducting polymers; with (ii) cathodic reduction at 0.6 V vs. SCE, using palladium, Pt nanowires and Au nanoparticles in a porous silicate; or by (iii) cathodic detection by co-immobilization of a peroxidase (e.g. horseradish peroxidase), which is oxidized in the process, followed by its mediated or direct electroreduction [308], [307]. Selectivity of first generation biosensors can be increased through tuning of the operating potential to a region where only the

target analyte is oxidized or reduced. The use of metal-hexacyanoferrate-based mediators, such as Prussian blue (ferric-ferrocyanide) or Rhodium and Ruthenium on carbon, allows reducing the overvoltage involved in hydrogen peroxide redox reaction to around -0.1 V vs. Ag/AgCl [309]. In this case, the hydrogen peroxide reduces the metal oxide film on the surface of the electrode to the metal, which can be electrochemically re-oxidized, thus generating the detected anodic current signal [309]. Prussian blue (PB), one of the most used mediators in glucose sensors, acts as a peroxidase [307], and can be co-deposited together with the enzyme or be applied together with carbon ink in screen-printed glucose sensors [309]. More on the specific application of PB in glucose sensors can be found in Karyakin *et al.* (1999) [310], Karyakin *et al.* (2001) [311] and Ricci *et al.* (2003) [312]. Several nanomaterials, such as carbon-nanotube modified electrodes or metallized carbons, have also resulted in a lower anodic potential with a high selectivity in hydrogen peroxide measurement [309], [307]. First generation glucose biosensors are extremely dependent on the oxygen tension and the need for oxygen concentration to be at least one order of magnitude lower than the glucose oxygen concentration (stoichiometric limitation of oxygen), which leads to a reduced upper limit of linearity [309]. Possible solutions to this limitation involve the use of polymer films that enable increasing the oxygen/glucose concentration ratio by tailoring the flux of the substrates to the electrode, or oxygen-rich carbon paste. Using GDH instead of GOx also eliminates the dependence on oxygen [309]. Covering the electrode or enzyme-covered electrode surface with a permselective membrane, also reduces the amount of electroactive species present in the electrode surface that can interfere with the measurement at the used potential in amperometric sensors [309]. This increases significantly the selectivity and sensitivity of a sensor. The membrane can be fabricated with a single polymer, or with mixed layers of different polymers in order to tune its properties in terms of charge, pore size and polarity [309]. Examples of commonly used coatings are cellulose acetate films, negatively charged (sulfonated) Nafion and other ionomers, and electropolymerized films such as polyphenol and polypyrrole [309]. Glucose monitoring in first generation electrochemical sensors depends, not only on glucose and oxygen concentration and pH, as expected, but also on the concentration of redox mediator, the enzyme loading and the current applied to the electrodes [308].

Glucose has also been monitored, although less frequently, through measuring the pH change associated with the production of gluconic acid from glucono-δ-lactone hydrolysis. This is performed by potentiometry using FET, and is more sensitive to other parameters that might affect pH, requiring a well-defined glucose influx and proton out-flux for accurate quantification of glucose [308].

Second generation glucose biosensors (Figure 49) perform the detection through the use of a mediator (Med_{ox}) capable of transporting electrons directly from the FAD redox center of Gox to the electrode's surface [309]. The reduced form of the mediator, obtained during the re-oxidation of the enzyme, is re-oxidized in the electrode, generating a current signal proportional to the concentration of glucose [309]. The need for redox mediators in glucose oxidase based sensors arose from the extremely slow rate at which electron transfer from the reduced FAD ($FADH_2$) to the electrode occurred. This low rate of direct electron tunneling derives from the depth at which FAD is placed inside the GOx conformation, about 13 to 15 Å below the enzyme surface in contact with the electrode [308]. Second generation glucose biosensors can use

diffusional electron mediators (soluble mediating species) such as ferrocene derivatives, conducting salts, quinone compounds (e.g. Methylene blue), transition-metal complexes, and phenothiazine and phenoxazine compounds [309]. These compounds free the reaction from oxygen dependency and lower the potentials used in the measurement thus minimizing interfering reactions on the electrode [309]. Mediators in second generation glucose biosensors must have a low solubility in water, be non-toxic and chemically stable, but most importantly, present a higher rate of electron transfer than the rate of the reaction of the enzyme with oxygen [309]. Another alternative is to use the enzyme embedded in conducting polymers. The polymer provides the connection between the enzyme and the electrode through flexible polymeric chains (e.g. poly(vinylpyridine with tethered complexes of $Os^{2+/3+}$ [308]) and folding around GOx [309]. The use of these polymers results in a fast response with high current density and added stabilization of the enzyme, allowing the fabrication of ultra-small electrodes [309]. The connection of electron relays (e.g. nanocarbon tubes or gold nanoparticles) directly to the enzyme or the FAD center can enable a simpler electrical wiring of the enzyme to the electrode and result in a significantly higher electron transfer rate which can be controlled by e.g. the length of the carbon nanotube used [309].

Since mediated systems tend to lose stability over time under continuous operation, third generation glucose sensors (Figure 49) are currently under development, whereby the enzyme is in direct contact with an electrode capable of operating a low potential (close to the one of the enzyme -0.5 V vs. Ag/AgCl) [309], [307]. To achieve this, the distance between the FAD redox center and the electrode needs to be reduced [309]. A possible solution is the use of conducting organic electrodes based on charge-transfer complexes (e.g. tetrathiafulvalene-tetracyanoquinodimethane (TTF-TCNQ)) [309]. Other approaches involve complex strategies for the reconstitution of the apo-enzyme on co-factor-modified electrodes and the reconstitution on co-factor functionalized nanoparticles that enable the alignment of the enzyme on the electrodes. However, the biggest hope relies on novel nanomaterials such as graphene, polyaniline nanotubes, and ionic liquid functionalized carbon nanotubes with gold nanoparticles [307].

4.1.2 Sensor integration

The degree of complexity of a microfluidic device tends to increase with the number of unit operations and/or mechanical parts that are integrated. However, as stated in Sassa *et al.* (2008) [102], the structure and function of individual components should be simplified to allow the operation of sophisticated microsystems.

When considering a unit of detection, as mentioned previously, the sensor performance depends, among other factors, on its position in the microdevice and of the flow rate applied to the solution measured. Hence, the manner of integration is highly relevant. Furthermore, the integration in microchannels of EC sensors can improve sensitivity due to the closer proximity of the electroactive species to the electrode. It can also improve throughput by integrating different sensors or sensors for different analytes in parallel channels, all the while decreasing analysis time, due to faster diffusion to the electrode's surface and/or by modifying the flowrate used for detection [166].

The simplest strategy for integration of electrochemical sensors involves the fabrication of patterns of electrodes directly on the microchannel substrates and/or using thin- and thick-film methods [299], [102]. The first approach is generally applied on hard and flat substrates (e.g. glass or silicon) [313], [314], [177], [166], where the sensors are deposited onto the channel surface using technologies similar or compatible with the ones used for the microstructures fabrication (semiconductor industry), such that the fabrication of both structures can be performed simultaneously or sequentially [315]. These techniques can also be used in polymeric substrates, however differences between the thermal expansion coefficients of the metals and the polymer where deposition occurs may lead to metal layer stress and sensor cracking. In the thick-film method, a paste containing metal particles or conducting ink (e.g. carbon or graphite ink) is spread on a screen with the geometrical pattern of the contact (electrode). This technique can be used to print sensors onto paper strips, forming screen-printed electrodes (SPEs). The conducting ink or carbon paste can be mixed with biomolecules for direct biosensor printing [86], [80]. Using techniques from the semiconductor industry enables batch fabrication of sensors and/or integrated structures which in turn greatly decreases its cost, however thick-film based sensors allow for overall cheaper fabrication and easier disposability of the sensors [299], [102]. Both individual sensors and sensor arrays (for different target analytes) can easily be obtained with these fabrication methods [299]. The working electrodes are usually made of Pt, Au, C or Ir, while the reference electrode is usually Ag/AgCl [102]. Sensors can be directly integrated in the fluidic channel by patterning on the bottom wall, and exist in a three-electrode configuration or as arrays of working electrodes, each functionalized for a given analyte and with the same working and counter electrodes [102]. The reference and counter electrodes may also be fabricated separately and introduced through the channel inlets. Reference electrodes can also be accomplished using a salt bridge [166]. Sensors fabricated with other technologies (spray-coating [174], coating coupled with embossing [183]) can also be irreversibly encapsulated into a microfluidic channel. Irreversible encapsulation guarantees a leakage and contamination-free operation of the device (after sterilization or when assembled in a clean-room environment), and it is the most frequently used approach.

Another strategy, presented by Frey *et al.* (2010), involves a permanent integration of a thin-film electrode in a flow channel, but the functionalization of the surface can be performed after electrode integration and channel bonding through a capillary-driven deposition channel connected with each electrode [293]. This extends the life-time of the sensing layer since it was not subjected to harsh conditions during channel bonding (e.g. high temperature and/or pressure). A further interesting approach to the integration of electrochemical biosensors in microchannels requires the immobilization of the biorecognition element of the sensor, separately from the electrode, in an area upstream of the electrode position or in the top of the channel directly opposite to the electrode position [316]. This has been shown to increase the sensing performance in some situations [316], by freeing the electrode's surface area for more efficient electron transfer [166]. Embedding of sensors during the 3D printing process is also a possibility, as has already been demonstrated for optical fibers, glass slides and membranes by Yuen (2016) [317]. The advantage of embedding structures during printing is the reduction of post-processing steps, while integration of glass in 3D printing structures increases visual access to the fabricated channels without requiring extra steps of sand blasting and polishing

[317]. Electrodes can also be fabricated separately through conventional techniques and integrated by gluing or bonding in a glass and polymeric channel [318].

Traditional sensor integration thus occurs through fabrication of the sensors with the microstructures and/or irreversible integration/bonding in the channels. However, diverse integration strategies based on either channel or sensor re-usability have recently been developed. A platform design that enables the substitution of the sensors in use and the integration of different types of sensors widens the sensor and platform applicability. Furthermore, devices that require a (re)alignment of the electrodes in the fluidic structure may result in increased variability between experiments, depending on the alignment precision [319], so the use of ports for sensor introduction decreases such variability by allowing a straightforward positioning of the sensors in the platform. This can be achieved using platforms where the channel is not irreversibly bonded and can then be easily and frequently opened [320], [321], [322]. Electrodes, especially disposable or reusable ones, can thus be integrated in the channel through receiving ports [323], [324], [166]. This enables, in the case of re-usable sensors to clean or polish the electrode surface from biofouling [166], but it may also allow the application of a different functionalization for application towards another target analyte. It also permits a re-use of the microfluidic system for different target molecules by allowing the introduction of different sensors.

Erkal *et al.* (2014) developed 3D printed microfluidic structures for integration of electrochemical sensors, where the electrodes were epoxy-embedded on commercial flangeless fitting nuts and integrated through threaded ports [319]. In this case, the ports for electrode integration in the channel had standard dimensions (same outer diameter), allowing electrode interchange, while the inner diameter of the tips of the fitting nuts with embedded electrodes depended on the electrode used [319]. The design files of the 3D printed structures can be easily shared between research laboratories for increased standardization and reliability of tests performed [319]. Screen- or inkjet-printed sensors in paper or polymeric substrates can be used for detection in paper microfluidics or be integrated through ports in microchannels. Reversible encasing of the sensors can be performed through the use of a chip holder (e.g. with mechanical clamping [325], [322]) which applies enough pressure for leakage-free flows. A reversible encapsulation can facilitate sensor or channel surface functionalization and cleaning due to easy access to these surfaces. If the sensor is not irreversibly bonded or encased in the device, it can be further re-used in other microfluidic platforms. The cost of such devices can be consequently reduced, since the sensors can be the most expensive component of a microfluidic platform.

Nevertheless, in all approaches, one of the significant challenges is the integration between the sensor and the channel, which must be performed in order to avoid leakage at the interface [86].

For increased sensitivity along with a longer sensor life-time (especially in cell applications where biofouling can be a significant issue), sensors are usually either covered with a polymeric layer or a membrane is placed between the sensor surface and the biological elements [299].

As mentioned in Chapter 1, chip standardization can also facilitate sensor integration and use by simplifying the connectivity between microsystems. Detection can then be achieved in

different applications with the strategies described above by connecting the microdevice with the sensor to the system where the reaction or fermentation is occurring.

4.1.3 Mixing

Mixing at microscale occurs mainly through diffusion (which depends on the concentration gradient of the species considered) due to the channel and structure dimensions and the consequent laminar characteristic of the flows achieved [11]. However, diffusion is a slow process and so designs capable of rapidly achieving efficient mixing and/or in a short channel, are essential for the development of high-throughput microfluidic systems [160]. Mixing can be increased by raising the chaotic advection effect in order to increase the contact area (and time of contact) between the flows being mixed, occurring mainly in the direction of flow. There are two main types of strategies to achieve mixing in microchannels: active mixing and passive mixing [160].

Active mixing involves the application of an external force on the flown fluid. Fluid perturbation can be caused by acoustic waves (mixing through generation of microstreams with e.g. piezoelectric disks or radio-frequency), dielectrophoresis (mixing induced through particle polarization which drives them towards or away from the electrode), magnetohydrodynamic flow (mixing occurs by generation of Lorentz forces or actuating magnetic particles), electrokinetic pulse (mixing achieved through periodic perturbations of an applied electrokinetic force), perturbation of pressure (mixing achieved by flow velocity pulses or alternate introduction of sample flows) [11], [105].

Passive mixing relies on the modification of the channel shape to induce splitting, folding, stretching or breaking of the flow, usually using only a pressure head to induce a controlled flow [160]. It can be achieved either through lamination-based or advection-based designs. Lamination-based mixing involves splitting and recombination of the flow in order to generate a higher number of interfacial contacts between the flows. This can be performed with T-junctions, split T-junctions, hydrodynamic focusing, channel multi-split followed by recombination, among others [11], [160]. Advection-based mixing, on the other hand, uses structures capable of generating Dean vortices. This can also include intersecting channels (as for lamination-based approaches) or convergent-divergent channels, but with geometries that increase collision and not just recombination of the flows. Furthermore, mixing can be obtained with three-dimensional serpentine channels, where different flows rotate in bends defined in the three dimensions, but can also be split and recombined in the vertical direction. Channels that possess out-of-channel protrusions in diverse angles are also an alternative design. Tesla structures are another advection-based geometry, which involves a combination of thinner channels connected to wider sharp curves, with an increased vulnerability to clogging in a mixed matrix. Advection-based mixing can also occur through introduction of obstacles, called static mixing elements (e.g. staggered herringbone grooves, side-wall protrusions) in one (or more) of the surfaces of the channels. This, together with a serpentine structure (introduction of bends that induce rotation of the flow) is the simplest strategy to increase mixing efficiency. [11], [160]. Mixing in droplets or with slug-flow, is another strategy, resulting in a better control of the residence time (no formation of parabolic velocity profile) with the possibility of generation of

inner flows by using serpentine channels or other strategies that have already been mentioned. Furthermore, the droplets can also be split and coalesced to improved mixing [11].

4.2 Goal

The developed work summarized in this chapter focuses on addressing the current need for adaptable screening platforms with integrated sensors. A flexible multi-function platform is proposed, with disposable and changeable sensors, easily integrated with other microfluidic platforms through a "plug-and-play" approach by using standardized finger tight fittings. The platform can be easily connected to external equipment (e.g. syringe pumps, HPLC), while offering the advantage of in-line use, thus not interfering with the reaction vessel. The choice of material, the thermopolymeric Poly (methyl methacrylate) (or PMMA), and fabrication technology (laser ablation) considered both design flexibility and costs. PMMA and laser ablation allow a fast optimization cycle from design, to fabrication and testing with fluids. Furthermore, since PMMA is a widely available biocompatible and cheap material, it enables a low-cost device fabrication with good reproducibility. Two encapsulation strategies were also tested: chemical bonding and lamination with pressure sensitive adhesive tape.

The classical example of the catalyzed oxidation reaction of glucose by glucose oxidase was chosen as the model reaction to highlight the monitoring capabilities of the developed microfluidic platform. In order to track the changes in inline analyte concentration, first generation amperometric glucose biosensors were chosen for further integration into the developed microfluidic device. Amperometric electrodes were employed due to their wide applicability [326], [327], [328], [329,330], compactness, stability and low price. The selection of first generation EC sensors was guided by its ready availability and knowledge about their fabrication and working principle.

4.3 Materials & Methods

4.3.1 Reagents and materials

Glucose oxidase (EC 1.1.3.4, type VII, from *Aspergillus niger*, ≥100,000 U/g solid) and bovine serum albumin (BSA) were obtained from Sigma (St. Louis, MO, USA). Nafion®117 solution (~5% (v/v) in a mixture of lower aliphatic alcohols and water) and iron (III) chloride (anhydrous, 99.99%) were obtained from Aldrich (Steinheim, Germany). Potassium hexacyanoferrate (III) (ACS reagent, ≥99.0%) and glutaraldehyde solution (25% (v/v)) were obtained from Sigma – Aldrich (St. Louis, MO, USA). D- Glucose (anhydrous) was provided by Fluka (Loughborough, UK). Mono – and di-potassium hydrogen phosphate (anhydrous) were obtained from Merck (Darmstadt, Germany). Isopropanol (2-propanol, anhydrous, 99.5%) used for cleaning was obtained from Sigma (St. Louis, MO, USA).

All the solutions for sensor preparation were prepared with 0.1 M phosphate buffer + 0.1 M KCl, pH 6. Standard solutions were prepared daily in the same buffer. All other solutions were prepared in 0.1 M phosphate.

Customized SPEs on polymeric substrate (DRP-PW-110DGPHOX) were produced by DropSens (Llanera, Spain), while the SPEs on polyester substrate (ItalSens IS-C) were acquired from PalmSens (Utrecht, The Netherlands). The DRP-PW-110DGPHOX SPEs are made of a thicker polymer than the IS-C SPEs. Each sensor is composed of three screen-printed electrodes: (i) the carbon working electrode (with graphene oxide layer in the case of the DRP-PW-110DGPHOX electrodes); (ii) the carbon counter electrode; and, (iii) the silver reference electrode. The diameter of the working electrode in the DRP-PW-110DGPHOX SPE is 0.4 cm, which results in an apparent geometric area of 0.126 cm^2, while in the IS-C SPE the diameter is 0.3 cm with an apparent geometric area of 0.07 cm^2.

The extrusion PMMA sheets with a thickness of 2 mm were acquired from Nordisk Plast (Assentoft, Denmark). The PMMA plates were patterned using laser ablation with a CMA-4030 Laser Engraving machine from GD Han's Yueming Laser Technology co., Ltd (Guangdong, China). Chemical bonding of the PMMA plates was achieved using an anhydrous chloroform solution, ≥99%, 288306 from Sigma-Aldrich (St. Louis, MO, USA). Adhesive assembly and integration of the sensors on the platform were performed with a 142 μm thick mcs-foil 008 from microfluidic ChipShop (Jena, Germany). The PDMS thin sheets used as gaskets were fabricated using the elastomer and curing agent kit of Sylgard® 184 from Dow Corning (Auburn, Michigan). The two 10-mm thick acryl plates that form the custom-made holder were from Rias A/S (Roskilde, Denmark). The holder was completed with two outer 5 mm thick SS304 stainless steel plates from Sanistål (Aalborg, Denmark). Flangeless polypropylene (PP) fingertight 1.5875 mm (ID) fittings (XP-201) and flangeless ferrules (P200X) from Upchurch Scientific® (Washington, USA) were used to connect polytetrafluoroethylene (PTFE) 1.5875 mm (OD) x 1mm (ID) tubing (S 1810-12) from Bohlender (Grünsfeld, Germany).

4.3.2 High-Performance Liquid Chromatography (HPLC) method

All the reaction samples were analysed in HPLC for quantification of consumed glucose and produced gluconic acid. The measurement was performed with reversed-phase chromatography on an Ultimate 3000 HPLC (Dionex, Sunnyvale, CA, USA) equipped with a Phenomenex column with 5-μm sized amine particles (Luna 5u NH2 100A), operated at 40 ^{0}C and 140 bar. The mobile phase consisted of a 20 mM phosphoric acid (H_3PO_4) solution, flowing at 1 mL/min. The eluted gluconic acid was quantified in the ultraviolet (UV) multiple wavelength detector at 205 nm, while the glucose concentration was determined in the Refract Max 520 refractive index (RI) detector. The amount of each component was obtained by integration of the areas under the corresponding peaks using the HPLC commercial analytical software (Chromeleon 6.8), based on a calibration curve performed for each component. Samples were measured mixed with 0.5 M sodium hydroxide (NaOH) solution in a proportion 1:2 of solution relative to the sample.

4.3.3 Microfluidic Platform Fabrication and Sensor Integration

A microfluidic system containing two inlets, two sensing/ measurement chambers, for sensor integration, and one mixing unit was developed and is presented in Figure 50. Figure 50(a) shows a schematic of the microfluidic platform. As illustrated, one of the inlets of the

system is connected to the first chamber, where the reference sensor is located. The second inlet is connected to the mixing chamber, which serves here as a dilution unit but can also be used as a reactor or target labelling unit. The second chamber is positioned after the mixing unit. The sensor integrated in this chamber is the one used for sample quantification and is thus designated detection sensor. Figure 50 (b) and (c) display one more feature of this system. It involves the use of generic rectangular pockets at the bottom plate of the device with direct access to the sensing chambers. The sensor can thus be directly placed in the chamber and covered with a thin polymeric gasket. The system is then closed by placing PMMA inserts in the pockets and sealing the whole platform with help of an outside mechanical holder system. An expanded view of the assembled platform is presented in Figure 51.

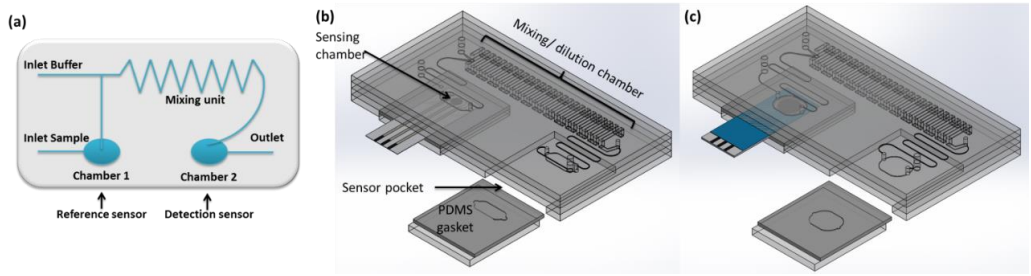

Figure 50 - Schematics of the developed platform, highlighting the different elements and the sensor positions (a) and SolidWorks 3D representation of the assembled microfluidic platform with one integrated IS-C SPE (b), and (c) DRP-PW-110DGPHOX SPE.

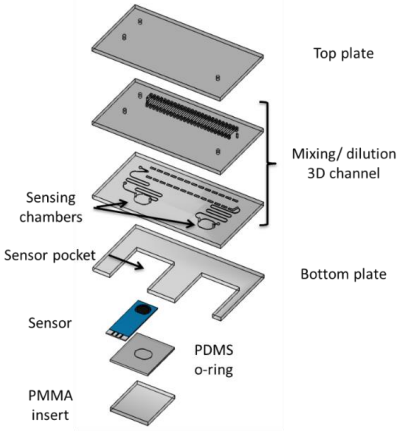

Figure 51 – Schematics of the assembly of the different plates for the three-dimensional mixing geometry and the sensor pockets for the graphene oxide-based sensors.

The design of the device was performed in SolidWorks 2015 (Dassault Systèmes SolidWorks Corporation, Waltham, Massachusetts, USA). This microfluidic platform consists of four PMMA plates ablated by laser ablation, as can be observed in Figure 51.

After ablation, the plates were thoroughly washed with deionized water, dried and then placed in an oven at 80 ^{0}C for 1 hour to release thermal stress before proceeding with the assembling. Two different approaches were used to assemble the PMMA plates: (i) lamination

with double sided pressure sensitive adhesive tape (DAT); and, (ii) chloroform bonding. In the first approach, the cooled plates were glued together and then pressurized with clamps and placed in an oven at 80 ^{0}C for at least 1 hour to remove possible air bubbles disturbing the adhesion. In the chloroform bonding, a procedure adapted from Ogilvie *et al*. (2010) was followed [331]. The dried plates were thoroughly washed with a 99.5% isopropanol solution, dried and then the surfaces to be bound were exposed to chloroform vapours for 2 min before being glued together. The plates were placed at a height of approximately 2 mm from a layer of liquid chloroform inside a closed glass Petri dish. In both approaches, after bonding was completed, the sensors were put in place using thin PDMS gasket sheets, sealing the sensor around the sensing chamber. The PDMS gaskets were fabricated by mixing in a SpeedMixer™ DAC 150.1 FVZ-K from Synergy Devices Limited (High Wycombe, UK). A 1:10 proportion mixture of the curing agent and the Sylgard® elastomer, was poured into a 1 mm PMMA mold with the shape of the sensor pockets followed by curing it in the oven for 1h at 70 ^{0}C.

Once the chip was assembled, the sensors were placed on the sensor pockets, the PDMS gaskets were placed on top and followed by a piece of PMMA. The microfluidic platform with integrated sensors was then positioned in an 'in-house' fabricated casing, which provided the necessary pressure to achieve leakage-free flow. The holder was built by two acrylic plates of 100x100 mm^2 that were micromilled in order to have a cavity with the chip's size and two outer SS304 stainless steel plates with a thickness of 5 mm, to avoid bending of the acryl plates when screwing the assembled holder together. This holder provides enough uniform pressure to avoid leakage of the microfluidic platform.

4.3.4 Mixing unit CFD optimization and characterization

Several passive mixing geometries were designed in SolidWorks 2015 (Dassault Systèmes SolidWorks Corporation, Waltham, Massachusetts, USA). The drawings of these geometries are presented in Figure 52. Each geometry's mixing characteristics were studied with the help of a computational fluid dynamic (CFD) simulation software, ANSYS-CFX Version 16.2 (Canonsburg, Pennsylvania, USA). To this purpose, the three-dimensional designs were imported into a meshing software, ANSYS ICEM CFD® 16.0 (Canonsburg, Pennsylvania, USA), where discretization of the geometries was performed. Discretization divides the geometry in smaller elements, in which the required momentum, energy and mass balance equations were solved by ANSYS-CFX. The number of elements of the 5 simulated structures varied between 845 and 1185 elements/μL, except for design (e) which had 9925 elements/μL. A structured mesh provides a more reliable and accurate output with respect to the results and reduces for many types of problems the simulation time. However, it is more complicated to define and requires longer preparation time. So, as a first approach, all geometries were simulated with unstructured mesh elements using tetrahedral features for the mesh. The best designs (designs (a) and (e)) were then simulated with a structured hexahedron mesh.

At microscale, the flow is laminar and therefore predictable, simply requiring the solution of the Navier-Stokes equation without the use of turbulent models. All geometries were simulated at the target flow conditions (steady state with laminar flow, outlet as an opening and no slip wall conditions) in the integrated microfluidic platform considering a fluid with the

same properties as water (at 25 ^{0}C) where a liquid tracer with diffusivity of $1x10^{-10}$ m^2 s^{-1} was introduced. The average inlet velocity, at the reference sensor, was $1x10^{-3}$ m s^{-1}, while the velocity of the other inlet was varied depending on the simulated degree of dilution. The geometries were evaluated by monitoring the average tracer amount at the outlet, as well as the gradient of its concentration. The best performing geometries were then built using the same procedure as described above for the microfluidic platform. Subsequently they were qualitatively tested using food colour dyes at the simulated flowrates. The geometry that achieved the desired 1:9 dilution with no gradient of tracer at the outlet (design (e)) was then used in the final microfluidic platform design. More details regarding the CFD simulations are presented in Appendix IV.

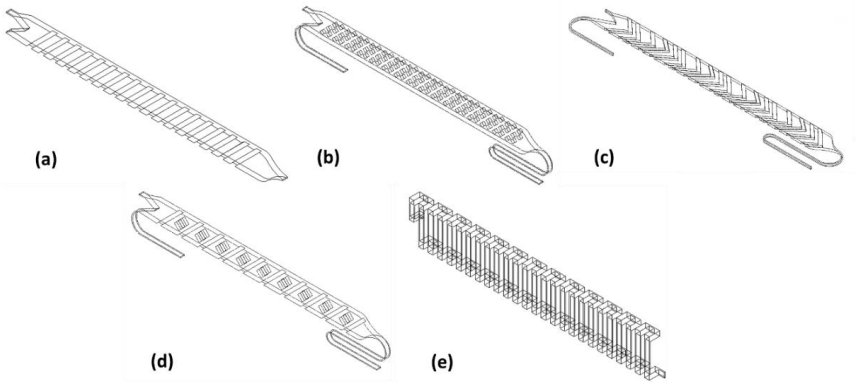

Figure 52 - Mixing chamber designs based on passive mixing structures: slanted grooves (a), squared baffles (b), staggered herringbone (c) combination of herringbone and obstacles (d) and three-dimensional serpentine (e).

4.3.5 Sensor

The sensors presented in this chapter were fabricated at the PROSYS research group together with PhD student Daria Semenova. The presented procedure was based on the methods used at the Measurement Technology Unit (MITY) at Oulu University, which were acquired during a 3-month external stay, of both PhD students at Oulu University. No work related to sensor optimization is presented here, since it is an extensive procedure which has been refined by Daria Semenova.

4.3.5.1 Sensor Preparation

The used biosensors consist of a SPE with immobilized layers of the hydrogen peroxide sensitive catalyst, Prussian Blue (PB) and the biological recognition element, the enzyme glucose oxidase (GOx). The PB modification of SPEs and deposition procedures were adopted from the procedures developed by Ricci *et al* (2003) [312] and Mahosenaho *et al.* (2010) [332]. Freshly prepared precursor solutions of 0.1 M potassium ferricyanide ($K_3Fe(CN)_6$) in 10 mM HCl and 0.1 M ferric chloride in 10 mM HCl were mixed in different proportions. A 1:1 proportion was used in the DRP-PW-110DGPHOX SPEs, while in the IS-C SPEs a 2:1 proportion was used for the detection sensor and a 1:2 proportion for the reference sensor. A

drop of PB (10 µl of total volume) was accurately placed onto the working electrode area, to avoid contact with the counter and reference electrodes. The electrodes were left for 10 min at room temperature and then rinsed with a 10 mM HCl solution and deionized water. The modified electrodes were then left to dry for 1 h in the oven at 100°C for stabilization of the PB layer, and afterwards stored in the dark at room temperature.

Glucose oxidase (GOx) immobilization was performed in a Nafion matrix via a cross-linking method previously described by Ricci *et al* (2003) [312] and Mahosenaho *et al.* (2010) [332]. A drop of 2.5 µl of glutaraldehyde (1 % (v/v) diluted in water) was placed on top of the working electrode area of the PB-modified electrodes and left to dry for 30 min at room temperature. A drop of 3 µl of the enzymatic-Nafion membrane was then applied on the modified working electrode and placed to dry overnight in a climate chamber at 8°C with 40 % of humidity. The enzymatic mixture had the following composition per sensor: GOx (0.074 U in phosphate buffer), BSA (5 vol. % diluted in water) and Nafion (5 vol. % diluted in water). All the components of the enzymatic layer were mixed in a 1:1:1 proportion. The complete glucose biosensors were stored dry at 4°C until use.

4.3.5.2 Sensor Characterization

Cyclic voltammetry (CV) and amperometric measurements (AM) were carried out using a MultiEmStat with a DRP-CAST1X8 interface (DropSens, Llanera, Spain) for 8 independent electrodes under MultiTrace Software 3.4 control (PalmSens, Utrecht, The Netherlands). Fluid flow was maintained by Cavro® XL 3000 syringe pumps from Tecan (Männedorf, Switzerland). The behaviour of the PB layer was studied by cycling in a potential range between - 0.5 and + 1.2 V with a scan rate of 50 mV/s as presented in Figure 53. CV measurements were performed in droplets using phosphate buffer solution (0.1 M phosphate + 0.1 M KCl, pH 6).

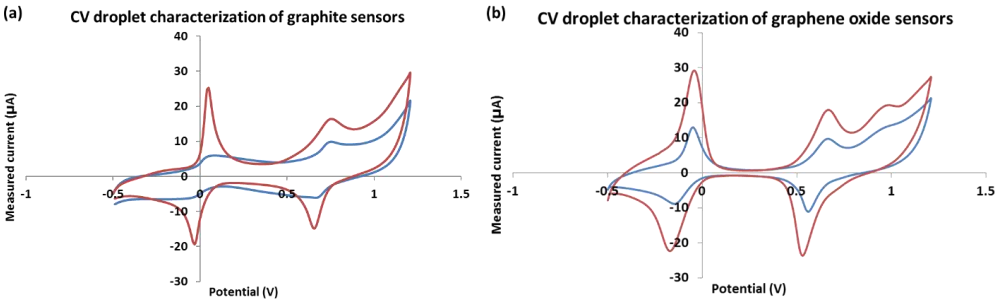

Figure 53 – Cyclic voltammograms of the sensors used for the microfluidic platforms test: (a) for the graphite-based sensors and (b) for the graphene oxide-based sensors. The sensor used in the first chamber is presented in blue, while the sensor used in the second chamber corresponds to the red curve.

The chronoamperometric measurements were performed in a droplet (static condition) at an applied potential of -0.16 V (graphene oxide-based sensors) or -0.04 V (graphite-based sensors) versus a screen printed internal silver reference electrode, as observed for the CVs presented in Figure 53. Static measurements were performed by placing a droplet of 50 µl of different glucose solutions (0.1mM – 8mM) on the electrodes. In-flow (dynamic) measurements were carried out at the flowrates used for the mixing/dilution chamber characterization. The flowrates during characterization varied between 0.25 and 10 µL/s. When a stable baseline

current was reached (30 s and 60 s, for graphene oxide and graphite sensors, respectively) with phosphate buffer solution (0.1 M phosphate + 0.1 M KCl, pH 6), different substrate concentrations were tested and the measurements were recorded. In the static characterization of the glucose biosensors, the drop of 50 µl of known glucose concentration (0.1mM – 8mM) was placed on top of all the electrodes and the current was recorded until it reached a stable value. When the sensors were characterized in flow, a volume corresponding to 3 times the internal volume of the microfluidic platform was first pumped to guarantee that only the target concentration was inside the system. Data was retrieved after stabilization of the signal.

4.3.6 Continuous monitoring of diluted glucose solutions

To perform the dilution inside the microfluidic platform, a 3 mM glucose solution was introduced through the inlet connected to the first sensing chamber (working in this case as a reference sensor – see Figure 50 (a)). A buffer solution (the same as the one used during measurements of the zero point during sensor characterization) was introduced in the second inlet (connected to the mixing/dilution chamber). The flowrate for substrate introduction was kept the same (1 µL/s) while the flowrate of the buffer solution was increased in order to achieve the correct dilution as presented in Table 18. The diluted solution was collected at the outlet of the microfluidic platform and measured in an HPLC for validation of the mixing unit and compared with the data retrieved from the integrated sensors.

Table 18 – Flowrates used to test the mixing/ dilution chamber inside the developed microfluidic platform.

Dilution	Flowrate second inlet (µL/s)	Flowrate in second sensing chamber (µL/s)	Flowrate used for data interpretation (µL/s)
1:1	1	2	2
1:2	2	3	4
1:5	5	6	6
1:9	9	10	10

4.4 Results and Discussion

The microfluidic platform presented in this chapter was built to be suitable in a wide range of applications. To this end, the final design required flexibility in terms of the used sensors and its easy replacement through the use of sensor ports. In this case, the ports were designed as rectangular pockets that allow access of the sensors to a chamber where the sensor can be placed. This approach allows for a wide variety of sensor shapes and widths to be integrated without requiring the modification of the whole platform. Furthermore, it is important to note that the sensor and platform fabrication are independent from each other. In this way, any sensor technology compatible with the platform material can be used, which considerably broadens the future opportunities for the platform's use.

As proof-of-concept, screen-printed electrochemical sensors were chosen due to the cheap fabrication and wide use in microfluidic and health related applications. The possibility of applying these sensors as single-use detection elements is also an appealing concept due to the impending challenges of biofouling that bio-applications can generate during long-term measurements.

Two different types of electrodes were selected for integration in the microfluidic platform, each presenting the same detection principle and target analyte but made of different materials and having different thicknesses. The choice of electrochemical sensors influenced the design of the platform, presented in Figure 50 (b) and (c), due to the required sensing chamber shape. With access to a bigger variety of sensor formats, a more generally applied chamber geometry could be efficiently developed, improving the applicability of the platform. For now, sensors with functional areas within the area of the fabricated chambers can easily be integrated and used. The distance between the measurement chambers (37.2 mm center to center) was defined based on the gap between the inlets of the interface connecting the sensors to the potentiostat used for measurement. In principle, due to the fast fabrication and assembly cycle of the platform (< 2 h), adaptation of the platform to most types of sensors (by adjusting the sensing chamber) can easily be performed. Moreover, sensors that can fit within the fabricated sensing chambers would not require a chamber design, since the PDMS o-rings would provide sufficient coverage to avoid leakages during operation.

The two integrated sensors were subjected to different flowrates during measurement, since one was positioned before the mixing/dilution chamber (first sensing chamber), while the other was positioned after the mixing/dilution unit (second sensing chamber). So, the first sensing chamber was only affected by the flow of one of the inlets (sample inlet). The second sensing chamber, on the other hand, experienced a higher flowrate which was the sum of the flowrate from the two inlets (sample plus buffer for dilution). The overall internal volume of both designs was approximately 500 µl.

4.4.1 Strategy for PMMA assembly

Both bonding strategies allowed for a fast assembly of the different plates that form the platform (less than 15 minutes required), while also achieving a leakage-free flow and enabling the re-use of the platform.

The chemical bonding procedure, however, was not as reproducible as the lamination one, mainly due to the manual control of the exposure time to chloroform vapours. Added variability, which sometimes resulted in deformations of the channel structures, was the manual control of distance between the PMMA plates and the layer of liquid chloroform, as well as the amount of chloroform added to the bonding procedure. Thus, the preferred material for the platform assembly was DAT due to easier and more reproducible alignment of the stack of plates and the avoided use of toxic chemicals.

4.4.2 Mixing and dilution unit

An issue with existing electrochemical sensors is their linear range of measurement, which is often shifted or more reduced than desired [293]. The most used approach to solving this issue involves optimizing the polymeric/diffusing membrane covering the sensor, thus better controlling the analyte diffusion to the electrode's surface. However, tailoring the sample concentration in flow to meet the sensors detection range is also an interesting approach to overcoming this limitation [293]. The presented platform enables the application of the latter method, as a strategy to widen the applicability of the integrated sensors, by integrating a

dilution unit on-chip. The use of the platform can this way be less limited by the available sensors and/or their corresponding detection limit. This is especially relevant in biological and biotechnological applications, where variable substrate (or other components) concentration can occur, often within a wide range (glucose concentrations above 1 mM are usually obtained e.g. in glucose monitoring of diabetes patients [308]). By diluting the fluid matrix that reaches the detection chamber, to the linear range of the sensor, the range of detectable concentrations of the integrated sensor is thus broadened.

The developed dilution platform was based on passive mixing in order to allow dependency on a single piece of external equipment (syringe pump), thus simplifying the equipment required for operation [333]. Several mixing designs (presented in Figure 52) were first simulated using a CFD software (ANSYS-CFX 16.2), before the best design was integrated in the platform and validated. The first designs were based on chaotic mixing generated by obstacles in the channel, since this approach provides fast mixing due to an increased interfacial contact between the mixing phases [333], [105]. The design of obstacles [11] within a chamber was preferred to a zigzag configuration (as presented by Jeon and Shin (2009) [333]) to avoid a high pressure drop [334] due to sharp corners and extended length of the channel. This is relevant when developing a system for use in a series of chips, such as in the case of modular platforms. Also, to reach a design less prone to clogging, more complex mixing structures, such as Tesla structures, were avoided [335].

It is also important to consider when operating a passive mixer, that the mixing capability is highly dependent on the flow velocity. Therefore, the design must be optimized to achieve appropriate mixing at high flowrates. In Figure 54, all designs that include obstacles ((a) to (d)) are presented. It can be observed that the slanted grooves design (Figure 54 (a)) has the best performance, especially at higher flowrates. However, even the structure showing the best performance was not capable of achieving the desired 1:9 dilution. Finally, a 3D serpentine channel was designed and simulated for the same flow conditions as shown in Figure 54 (e), resulting in the best mixing design to achieve a 1:9 dilution at high flowrates.

It is highly relevant to mention that by performing the study of the mixing efficiency of the different geometries presented through CFD, an optimized geometry for the intended purpose was quickly obtained (less than 3 days). This allowed to significantly reduce the development time of the quantification platform. Furthermore, the comparison of different geometries without fabrication and fluidic tests, made it possible that the overall platform development cost was significantly decreased.

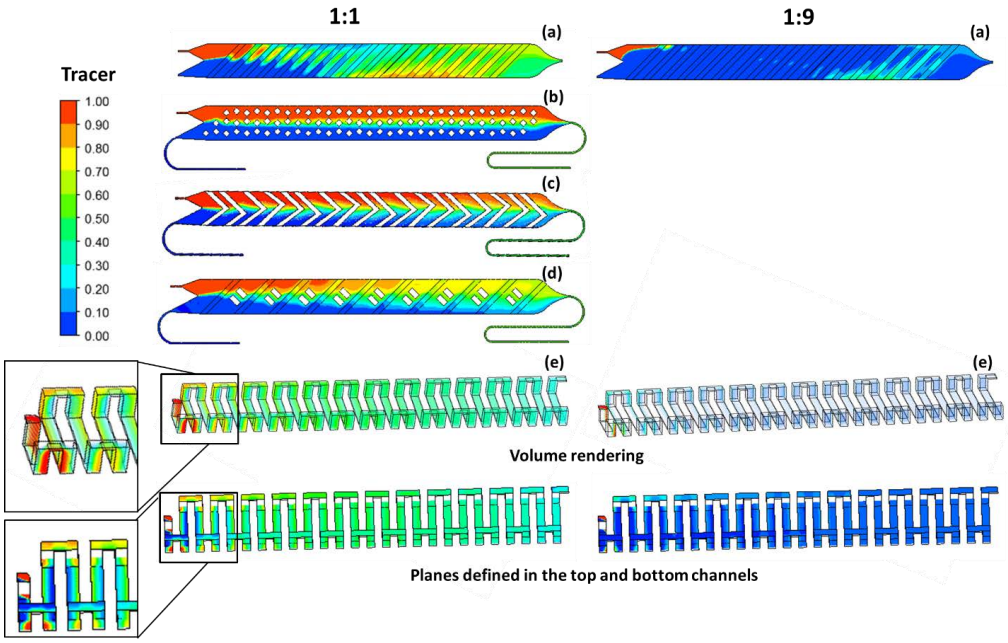

Figure 54 - Comparison of mixing capability between different mixing chamber geometries using CFD simulation for 1:1 dilution at 10^{-3} m/s, and of a 10 times difference between inlet velocities for two geometries (straight diagonal barriers channel and the 3D serpentine channel). In the figure, the different geometries tested for mixing are presented: (a) slanted groves, (b) squared baffles, (c) staggered herringbone, (d) combination of herringbone and obstacles and (e) three-dimensional serpentine channel. For the three-dimensional serpentine channel (e), a view of the entire fluid with volume rendering is presented on the top, with the initial section for 1:1 dilution enlarged, while the bottom images present two planes defined at the top and bottom of the three-dimensional channel.

4.4.3 Sensor characterization

The pairs of EC biosensors integrated in the developed microfluidic platform were characterized both in a static (droplet characterization) and in a dynamic environment (in-flow characterization). Both types of measurements were performed with chronoamperometry for the same substrate concentrations. The magnitude of the measured current, obtained by applying a constant potential between the working and the reference electrodes, is usually proportional to the bulk concentration of the present electroactive species, hence enabling a quantitative output. The static calibration allowed checking performance and sensitivity of each sensor before integration in the developed microfluidic platform. The dynamic measurements were performed at flowrates 0.25 to 10 μL/s. These flowrates were identical to the ones applied during the mixing/dilution experiment, thus enabling to study the influence of flow velocity on the sensor output.

Figure 55 (a) and (b) present the measured calibration curves from the static chronoamperometry measurements. It can be observed that the graphite-based sensors (Figure 55 (a)) show a decreased linear range (only until 1.7 mM of glucose) with a slightly higher apparent sensitivity than the graphene oxide-based sensors (Figure 55 (b)). The latter sensors display a wider range of detection (up to 5 mM of glucose) with a sensitivity lower than 0.2

μA/mM. This difference in the sensor output can potentially be explained by the presence of the graphene oxide layer, which tends to present high chemical stability and improved electrochemical properties. Furthermore, graphene oxide is known to increase the effective surface area of a sensor, thus improving its signal-to-noise ratio, as well as facilitating the functionalization of the surface [336], [337]. Even though more reliable data was thus expected from the graphene oxide-based sensors, both sensor types were tested inside the platform and their dynamic response compared with the static approach.

In Figure 55 (c) and (d) the measured calibration curves for the dynamic method using the microfluidic platform are presented for the different flowrates tested. This characterization was performed by inducing the same flowrate at the two inlets, and as a result the first sensing chamber was subjected to half the flowrate as the second sensing chamber. As illustrated in the figure below, the graphite-based sensors (Figure 55 (c)) present a reduced linear behaviour than previously obtained in the droplet chronoamperometry, while the graphene oxide-based sensors (Figure 55 (d)) show a decrease in the linear range (up to ~4 mM of glucose). Moreover, both sensor types display a variation of the calibration curve with flow. A decrease in the sensitivity (slope), as well as of the detection range, is observed when the applied flowrate increases. The higher difference in static vs. dynamic behaviour observed for the graphite-based sensors can be related to the difference in electrode substrate (graphite is less chemically stable than graphene oxide). Furthermore, the higher surface area of the graphene oxide sensors permits the immobilization of higher amounts of both mediator and glucose oxidase, which along with its intrinsic improved electrochemical properties possibly contributes to the different output observed.

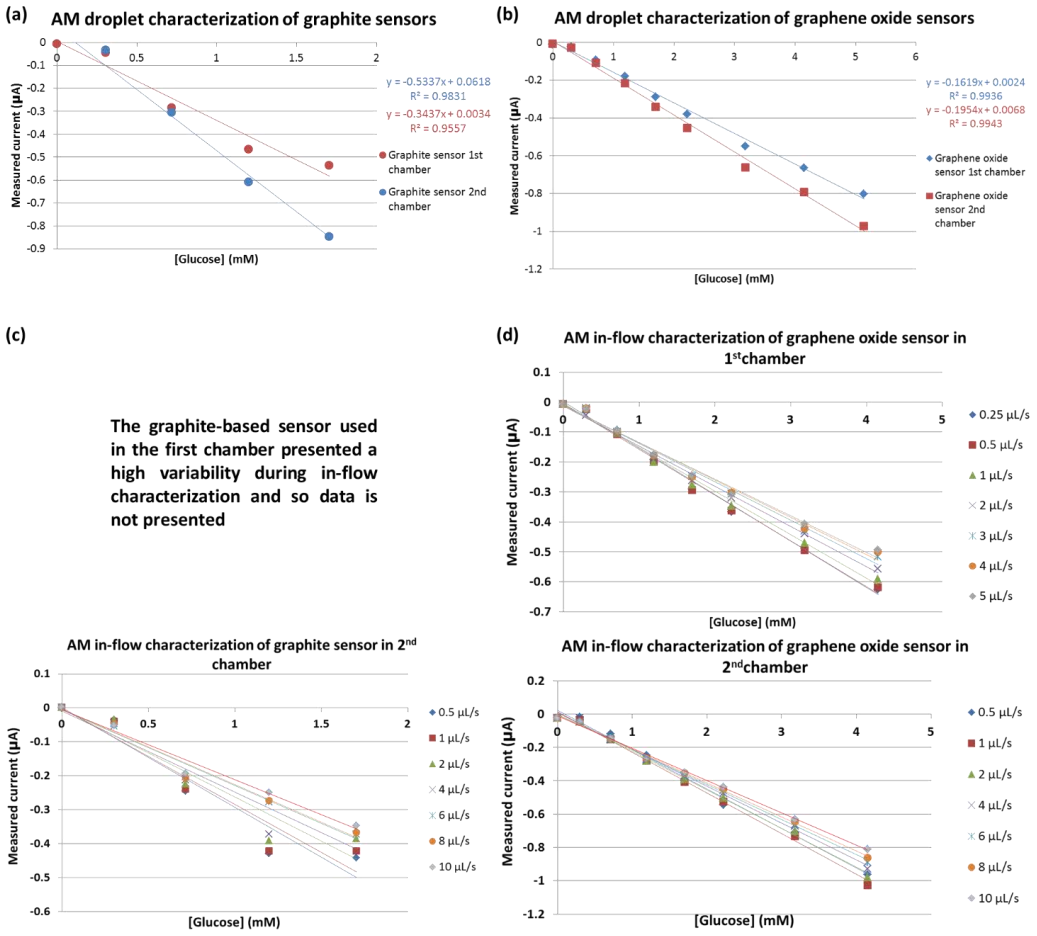

Figure 55 – Droplet amperometric characterization of the biosensors before integration in the microfluidic platform, (a) graphite-based sensors and (b) graphene oxide-based sensors, and in-flow amperometric characterization of the sensors used to test the microfluidic platform, (c) graphite-based sensors and (d) graphene-based sensors.

4.4.4 Influence of flow

The distribution of the measured current relative to the flowrates applied for the integrated graphite and graphene oxide-based sensors was also assessed. A similar trend can be observed for both sensors (Figure 56), being however more pronounced in the graphene oxide-based sensors (Figure 56 (b)). At low substrate concentrations, a slight decrease of the measured current (more negative) is observed with increasing flowrates. For concentrations higher than 1 mM, the opposite trend is observed, where the measured current becomes less negative with increasing flowrates. Both trends are however less prominent for flowrates higher than 5 µL/s.

As mentioned by Sassa *et al.* (2008) [102], the current generated in amperometric sensors depends on the applied flow velocity since the analyte used for detection (that permeates the membrane layer above the sensor) is a small fraction of the bulk concentration. The thickness

of the diffusion barrier formed above the membrane due to flow, together with the concentration gradient formed between the bulk and the diffusion barrier, determine the amount of analyte that reaches the sensor membrane. The amount of analyte that permeates is then defined by the characteristics of the membrane and by the concentration gradient between the diffusion barrier and the electrode's surface (gradient inside the membrane).

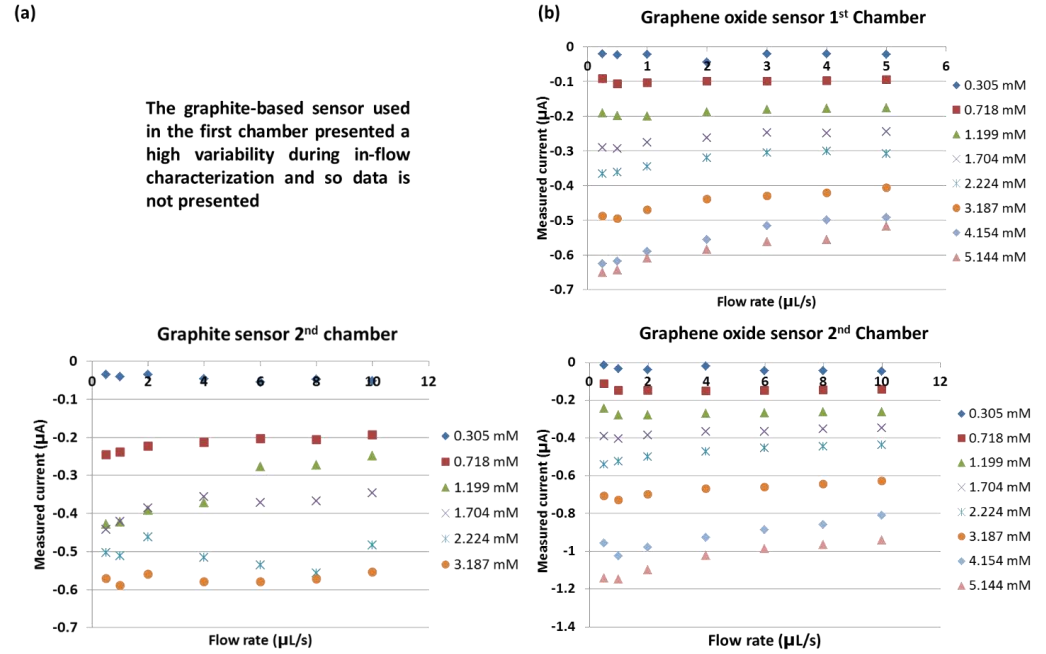

Figure 56 - Influence of flow on the current measured for the range of glucose concentrations tested for both types of sensors used: (a) graphite-based sensors and (b) graphene oxide-based sensors.

In a direct measurement of the analyte, at low flowrates, the analyte measurement process is limited by its mass-diffusion through the stagnant layer of liquid above the membrane, whose thickness decreases with increasing flow rate. Thus, at increased flow velocities, a higher amount of analyte is capable of diffusing and a higher current is obtained. This current increase will reach a plateau when the stagnant layer reaches its minimum thickness and the process is only limited by the analyte diffusion rate through the membrane [318]. However, as it is also verified in this work, the opposite trend is observed with indirect measurement of the analyte, meaning a decrease in current is observed with the increase of the flowrate. In this work, since a higher substrate concentration corresponds to a more negative current, this decrease is translated in a more positive current.

Several papers have reported a decrease of current with the increase of flow velocity in amperometric measurements of sensors where the compound resulting in electric signal is not the analyte (indirect measurement) [316], [318]. Lamberti *et al.* (2012) associated this decrease with a leakage of the generated hydrogen peroxide and consequent wash out from the membrane layer due to the increasing flowrate. This was also confirmed by mathematical and fluidic simulations [318]. This is one of the possible causes for the observed current decrease (in

absolute values) with increasing flowrate. On the other hand, in Figure 56, a slight increase in current was observed with the flowrate in all the used sensors, for a glucose concentration below 1.2 mM, which was not observed by Lamberti *et al.* (2012) where the minimum glucose concentration used in the experimental studies was 1 mM [318]. This effect is however much smaller than the current decrease of flow and might not be significant.

Lamberti *et al.* (2012) also observed that the response time of the electrochemical sensors decreased with increasing flowrate [318]. This was not possible to determine for the electrochemical sensors used, since measurements were performed when the solution was considered at steady state, and thus diffusion of analyte through the membrane had already occurred.

Hashimoto *et al.* (2006) observed that the influence of flow rate on sensor performance decreased with increasing channel heights, which is expected since for the same flowrates, higher velocities are achieved for smaller cross sections [316]. This indicates that the use of deeper channels or, as performed here, wider chambers for sensor integration might aid in decreasing the influence of flow.

Since the applied flowrate and the substrate concentration affect the measured current, a study on the influence of flow on the sensor performance is required and data can only be analyzed by using the calibration curves for each of the applied flowrates.

Lamberti *et al.* (2012) solved the issue of signal dependency on flowrate by decoupling the sampling unit from the quantification unit in two different modules [318]. The same strategy could be applied here, by decoupling the dilution unit (with the first sensor) from the quantification unit (second sensor) through the introduction of a metering channel and a valve. However, if sufficiently sensitive sensors are integrated, no significant decrease in quantification accuracy should be observed. Furthermore, by coupling the sensors with a software capable of estimating the decrease in current with flowrate from a one- or two-point calibration at a given flowrate, the obtained data can be correctly analyzed.

4.4.5 Continuous monitoring of diluted glucose solutions

The successful integration of these sensors and the continuous monitoring of glucose samples in a microfluidic platform were achieved. Figure 57 presents the results of the mixing/dilution chamber test where the integrated sensors were used for continuous monitoring of diluted glucose solutions. The data is plotted relative to an expected glucose concentration, calculated by applying the used dilution to the inlet glucose concentration (3mM). Substrate quantification results of the outlet solutions from the HPLC measurements are also presented in Figure 57. The current measured at the sensors was converted into glucose concentration through the in-flow calibration curve (Figure 55 (c) and (d)) corresponding to the flowrate applied to the sensor (Table 18). As presented, the graphite and graphene oxide-based sensors have a different sensitivity to the substrate, visible by their different response. However, both display a deviation from the HPLC data. The graphite-based sensor under-estimates the glucose concentration and the graphene oxide-based sensor over-estimates it, which can be caused by the influence of the flowrates on the thickness of the diffusion layer above the sensor and thus on the glucose diffusion to the electrode's surface. Additionally, the previously mentioned

leakage of produced hydrogen peroxide might explain the lower substrate concentration measured by the graphite-based sensor. Considering that it presents a lower chemical stability than graphene oxide, a higher amount of hydrogen peroxide could leak without reacting with PB and thus the current measured be lower than expected. The difference between the HPLC and electrochemically measured glucose concentration in the case of the graphene oxide sensor could be due to variability from the HPLC measurement, since only the point at 1.5 mM expected glucose seems to deviate from the overall trend. However, tests at more dilutions and with different initial glucose concentrations should be performed in order to ascertain the cause for the deviations found.

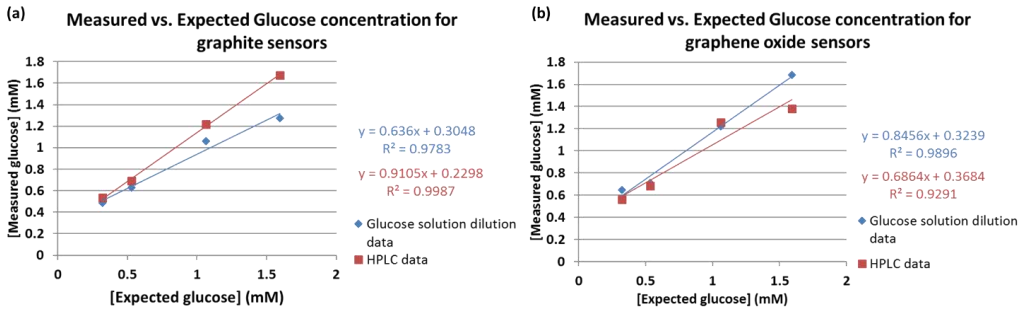

Figure 57 – Comparison of diluted glucose concentration values measured online with the sensors and at the outlet using HPLC, for both types of SPEs used: (a) graphite-based sensors and (b) graphene oxide-based sensors.

In terms of extending the range of application of the electrochemical sensors, other approaches have been more successfully applied. Frey *et al.* (2010) used controlled diffusion of the sample with a buffer solution (flown between the sample (top of channel) and the electrodes (bottom of channel)) to define the thickness of the diffusion layer above the sensor (defined by the thickness of the buffer stream) [293]. With this approach Frey *et al.* (2010) [293] achieved online control of the diffusion layer thickness by controlling the flow rate of the buffer solution. However, since the integration strategy presented in this work is intended for application of different types of sensors (e.g. optical), the focus was on sample dilution to meet the integrated sensors linear range.

Furthermore, it is relevant to highlight that all experiments presented for each set of sensors, were performed continuously for around 12 h. The platform's ability for continuous fluidic operation in a wide range of flowrates and for different sensor substrates and geometries has thus been demonstrated.

4.5 Conclusions

In this work, a microfluidic platform for continuous monitoring of glucose samples for biotechnological applications was developed. This platform involved the successful integration of two electrochemical sensors with different electrode materials and sensor areas, and their validation in continuous monitoring. The comparison between sensor output during static and dynamic measurements allowed the observation of a decrease of detection range for both

sensors, during in-flow measurements relative to the droplet characterization. This change in the sensors' sensitivity derives from the fluid dynamic influence on the diffusion of target analyte to the electrode surface, along with possible leakage of produced hydrogen peroxide. Furthermore, a significant difference in current output was also obtained at low (less than 5 μL/s) and high (above 5 μL/s) flowrates, indicating that the effect of flow velocity is relevant at this scale for the used chamber geometries. Finally, the platform displays the capability of performing sample dilutions of up to 10 times, even at high flowrates, through the use of an integrated mixing unit. This unit allowed tuning the sample concentration according to the sensor's detection limit.

The presented mixing unit can be improved by increasing the number of bends in the meandering channel or by introducing some obstacles within the channel, which is large enough to implement such structures. Thus, higher dilutions of the initial sample could be achieved. Furthermore, since the used sensors present a stabilization in current output at high flowrates, the increase of dilution ratio with increasing flowrates should not affect the performed measurements.

Even though fluidic and analytical simulations of glucose sensors at steady state have been performed [316], [318], the study of the presented platform through fluid dynamic simulation tools (CFD) would significantly increase the understanding on the influence of the observed diffusion effects. Moreover, an optimized chamber geometry, a flowrate range or operation and/or a mathematical relation between static and in-flow calibration curves could be obtained with such a model and thus provide solutions on how to circumvent diffusion effects during data acquisition.

This platform may be further applied to different sensing technologies (e.g. optical, magnetic), due to the presented flexibility in terms of sensor format, as well as ease of assembly and possibility for re-use of both platform and the integrated sensors. Furthermore, a combination of electrochemical and other sensor technologies (especially optical sensing) could be achieved on this platform, by using the predefined pockets for sensor integration. Likewise, the integrated mixing chamber can display a high variety of functions besides the demonstrated dilution ability. It may be further used as a reaction chamber for the screening of biocatalysts, as an inactivation or reaction quenching unit, or even as a labeling unit, by mixing the sample stream with a fluorescent or magnetic marker, depending on the chosen sensing approach.

The described sensor integration method could be further improved if the sensors could be slid into the sensor pockets instead of mounted by disassembling the outer casing. This approach could be achieved by placing a piece of PDMS or other compressible material only in the area directly below the sensing chamber, while having a slit in between the plate with the PDMS and the chamber plate. By introducing the electrode through the slit, the compressible material would apply pressure on the sensor so it closed the sensing chamber to allow leakage free flow. An alternative to this compressible material would be to use a spring or even a threaded nut that could be screwed, depending on the sensor, to push the sensor towards the chamber and thus enable closing the fluidic path.

The developed platform exhibits a multi-function capability using a simple design, standard connectors and low-cost materials. Such a platform can contribute to increasing the number of bioprocess parameters measured online during monitoring, by allowing the

integration of different sensor approaches, as well as their replacement, without the need of changing the platform itself. The overall cost of such platform makes it accessible both to research laboratories and industries. Additionally, the simple design allows for mass production, by changing the fabrication method to e.g. injection moulding, and being consequently feasible for parallelization at a bigger scale.

Chapter 5

Thermal inactivation platform

The need for fast and comprehensive characterization of biocatalysts has pushed the development of new screening platforms, based on microfluidics, which are capable of monitoring several parameters simultaneously with new configurations of liquid handling, sample treatment and sensing. Modular microfluidics allows integrating these newly developed approaches in a more flexible way towards increased applicability of the microfluidic chips to different types of biocatalysts and reactions. A highly relevant operation in such a system is the inactivation of biocatalysts. Such an inactivation module enables the precise control of reaction time at the time of measurement when sensing is performed in another module. This is achieved by avoiding the continuation of the reaction in the following sensing module or connecting tubes. Such control is important when different modules of reactors and/ or sensing units are used and frequently changed. It can furthermore help to regulate the state of the biocatalyst, since dependent on the temperature used and exposure time, reversible or irreversible denaturation can be achieved. In this work, the development, characterization and application of such a module is described for the fast inactivation of two well-known and widely used enzymes, glucose oxidase and catalase. The developed thermal inactivation platform is compared with a standard benchtop orbital shaker with temperature control (ThermoMixer) in terms of inactivation efficiency. Both enzymes were inactivated under flow conditions with 120 s residence time at 338 K (65 ^{0}C) and 20 s residence time at 353 K (80 ^{0}C) in the thermal inactivation module. The performance of the flow system was compared with the ThermoMixer system at 60 s residence time at 353 K (80 ^{0}C). Moreover, partial deactivation of the enzymes was observed for the continuous thermal inactivation module when activity measurements were performed respectively after one and two days after the thermal inactivation. All the inactivated glucose oxidase samples in the microfluidic system presented a significantly decreased activity. Some of the inactivated catalase samples recovered the initial activity, but for the longer exposure time and higher temperatures reduced no activity was measured and aggregate formation was observed. Final enzyme activity obtained for the samples after inactivation conditions with flow in the developed platform was lower than in the ThermoMixer but protein aggregation was observed in both cases. The higher observed loss of activity for the enzymes inactivated under flow conditions may indicate an effective heat transfer to the fluid under dynamic conditions. The presented thermal inactivation unit can easily be integrated in modular microfluidic platforms and be a useful addition for enzyme characterization and screening.

5.1 Introduction

The effect of temperature on biological systems, from enzyme behaviour to cell growth rate and food quality, is an extensively studied effect. Temperature has thus been established as a relevant process parameter and the study of its effect is part of the standard optimization procedure in current processes.

The influence of temperature, like other operation parameters, is studied in order to obtain the threshold value at which a certain enzyme or organism operates at the maximum rate. This value depends on the type of enzyme and its stability, but can be further constrained when other operation variables (e.g. pH, ionic strength, solvent used) are considered. An enzyme temperature range (thermophilic, mesophilic or psychrophilic) is usually a good indication of its structural robustness and how well it will perform under industrial process conditions. Enzyme temperature persistence or resistance to denaturation, for example, has provided good insight into the structural factors leading to increased enzymatic stability. Stable enzymes display a reduced surface area to volume ratio, less cavities, a reduced number of labile amino acids, a more rigid secondary structure, an increased hydrophobic interaction and changes in the solvent-exposed surfaces [338]. Genetic and evolutionary engineering of organisms and enzymes has led to high temperature resistant strains and proteins able to operate at high rates in a wider range of conditions or at previously unfavourable conditions.

Temperature has also extensively been used to inactivate or deactivate enzymes and organisms, either to stop a certain reaction (e.g. avoid enzymatic degradation in cells or tissue samples [339]), perform protein conformational studies, inactivate pathogens in infectious samples (through protein denaturation [339]), or to ensure absence of microbial growth [340] or degradation of food [341].

5.1.1 Mechanisms for enzymatic inactivation

The study of enzyme inactivation is the analysis of enzyme stability at different operation or reaction conditions. Enzyme stability depends, among other factors, on enzyme mobility and folding mechanisms which can vary widely, from natively unfolded proteins that fold upon binding of a ligand, to the existence of several stable and active native conformations for the same enzyme depending on the environment [342]. Enzymes tend to fold in conformations which are the most thermodynamically stable at the environmental conditions. The folding process and the lowest-energy conformation depend on the amino-acid sequence, which in turn encodes for an energy "landscape" where few interactions between residues allow the low energy structure, so folding can be performed rapidly [343]. However, for most enzymes, the native active state is only -5 to -10 kcal/mol more stable than the denatured state, due to the latter higher conformational entropy (conformational freedom) [344]. The denaturing process can occur through the formation of transient intermediate conformations, between the native and the denatured state [344]. In this work, the term enzymatic *inactivation* is used to refer to the reversible or irreversible loss of functional activity of proteins. The term enzymatic *denaturation* will be applied when there is inactivation of an enzyme due to an alteration of its conformation, as stated in Mozhaev and Martinek (1982) [345]. When there is irreversible loss of enzymatic functional activity (meaning irreversible enzyme inactivation), the term enzymatic *deactivation*

will be used. Enzymatic denaturation, or its tendency to reversibly unfold is related to its thermodynamic stability, while deactivation depends on the enzyme's kinetic or long-term stability [346].

Enzyme inactivation can occur through several mechanisms (e.g. protein aggregation, formation/rupture of disulfide bonds, deamidation of asparagine and glutamine residues, disruption of the polypeptide chain, dissociation of a prosthetic group from the active site or subunit dissociation [344], [345]) that result in loss of conformational structure (denaturation) and functional activity (inactivation) [345]. Inactivation due to aggregate formation tends to occur in two steps, where first conformational changes occur that lead to protein denaturation, and then the denatured proteins aggregate through non-covalent interactions, such as hydrogen bonds and hydrophobic interactions. Aggregation decreases with the decrease of available denatured enzyme. Aggregation of enzymes in the native state may also occur, without loss of activity upon dissolution [345]. Aggregation or misfolding upon renaturation (process of regaining enzyme activity following denaturation), generate a high degree of deactivated enzymes and is a common process of denaturation since these conformations are kinetically favoured. Enzymes can also lose activity when intermolecular disulfide bonds are formed (from exposed thiol groups) or destroyed (due to ß-elimination of cysteine residues), phenomena which increase with increasing enzyme concentrations and also result in aggregate formation. Loss of activity through disulfide bond formation or rupture usually occurs in three steps, where thiol-disulfide exchange (formation of intra-molecular bonds) occurs after non-covalent aggregates are formed. Exchange of disulfide bonds is more likely to occur at higher pH, and can also occur, especially the destruction of disulfide bonds, without aggregate formation. Among other covalent processes that contribute to irreversible denaturation are the chemical modification of functional groups (e.g. oxidation of cysteine or methionine residues), deamidation of asparagine and glutamine residues (loss of activity due to extra negative charges in the inner zone of the enzyme) or disruption of the polypeptide chain (which tends to occur on the denatured enzyme only at very harsh conditions or in the presence of proteolytic enzymes) [344], [345].

The denaturing processes described above can be caused or initiated through a variety of process conditions or solvents. Thermal inactivation occurs due to the increase of entropy with temperature (which favours the denatured state) more than the increase of enthalpy (which favours the native state) according to the Gibbs free energy equation [344]. The rate of enzyme inactivation and denaturation is usually higher at higher temperatures, since collision between molecules, as well as surface exposure to interactions, is increased [345]. Guanidinium chloride and urea cause denaturation by increasing the solubility of the hydrophobic lateral chains, increasing the exposition of the hydrophobic groups to the solvent used [344]. These compounds are used in the quantification of the thermodynamic parameters of the denaturing process, since their effect is reversible. Denaturation with pH occurs by titration of the ionizable amino-acids, which might break stabilizing or create destabilizing electrostatic interactions, and so the pH value at which an enzyme denatures is greatly dependent on the enzymatic polypeptide chain. Studies on enzymatic denaturation by pH are usual performed at low pH values (where e.g. carboxylic groups lose their negative charge), since denaturation at higher pH can lead to deactivation (due to the exchange of thiol-sulfide groups described above) [344]. Other denaturing agents, less commonly used in the laboratory, are pressure, surface tension, ultrasound and water removal [344].

Denaturing conditions and/or agents, such as temperature, extreme pH, guanidine hydrochloride (GdnHCl) or urea, can also be used to renature an enzyme by acting on the structure of the non-native conformation. Reactivation of enzymes from aggregates can sometimes be achieved by exposing the enzymes to denaturing agents, since these can break the non-covalent bonds formed during aggregation [345]. Renaturation after exposure to denaturing agents such as guanidine hydrochloride (GdnHCl) or urea can be achieved, even in the presence of high concentrations of these compounds, also due to the persistence of interactions of long-range order in denatured conformations [347], [348]. In case of subunit dissociation, reactivation can also be achieved but is less straightforward [345].

Denaturation is considered irreversible (deactivation) when the protein cannot regain its original functional activity when a sufficiently long period of time has passed since the denaturing effect was removed [345]. In the case of thermal inactivation, deactivation occurs if upon cooling the enzyme does not recover its functional activity [344].

5.1.1.1 Study of enzymatic inactivation

The evaluation and study of enzymatic stability, performed through the analysis of enzymatic denaturing mechanisms, can be achieved with a variety of methods. The most commonly used are UV spectroscopy, fluorescent emission and circular dichroism.

In UV spectroscopy, the absorption of aromatic amino acids such as tyrosine and tryptophan (which are usually placed in an inner zone of the native enzyme) allows following enzyme denaturation. As the aromatic amino acids are more exposed to the water in solution due to denaturation, their polarity changes, causing a decrease in the absorption wavelength [349]. The difference in the absorption spectra of the native and the denatured enzyme presents peaks at 285-288 nm (tyrosine) and/or at 291-294 nm (tryptophan). The low sensitivity of this method can be improved by performing the denaturation above pH 9, where the exposed tyrosine residues are ionized thus causing an increase in absorption at 250 nm that allows the calculation of the degree of residue exposition [344]. UV-VIS spectroscopy can also be used for accurate determination of protein concentration in solution (Mach *et al.*, Chapter 4, pp. 91 to 114 [350]).

Fluorescence spectroscopy presents a high sensitivity for the study of conformational changes of the three-dimensional structure of the enzyme, by following the photo-induced fluorescence emission of aromatic residues such as tryptophan (350 nm) at an excitation wavelength above 295 nm. Again, the denaturation process is followed by a shift in the emission wavelengths to longer wavelengths as the tryptophan residues become exposed to water and change their polarity [344]. This technique can also be applied to the study of enzyme dynamics and function [351], by employing labelled compounds and/ or techniques such as Förster resonance energy transfer (FRET) and single-molecule electron transfer [342].

Circular dichroism (CD) is a highly relevant and widely applied technique in the study of enzyme stability [349], [352], [353], [354]. This technique is based on the differential absorption of left and right circularly polarized radiation in a plane, by optically active chromophores (e.g. disulfide bonds and tryptophan) with chiral center, linked to a chiral center or in an asymmetric environment. CD allows to follow the denaturation of the tertiary enzymatic structure in the near UV (320-260 nm), as well as the enzyme's secondary structure (e.g. α helices and ß sheets)

in the far UV (240 -180 nm), where its intensity is proportional to the content in the secondary structure [344], [355]. CD can also provide information regarding co-factors (e.g. FAD) or metal-centers (e.g. heme moiety), ligand binding and folding intermediate structure, being also used for screening of genetically altered enzymes [355]. CD can also be coupled with stopped-flow [349] to enable studies of the kinetic processes during folding, or with an external magnetic field [354] to achieve more sensitive measurements.

Other techniques used to study enzymatic inactivation are nuclear magnetic resonance (NMR), light scattering, hydrodynamic methods and calorimetric methods. Among the latter, especially differential scanning calorimetry (DSC) measures the apparent molar heat capacity of protein as function of temperature, thus detecting the heat exchange developed during the denaturing process [344], ([350]). It allows the direct calculation of the enthalpy variation occurring during denaturation, as well as the thermodynamic parameters involved in the temperature-dependent conformation change. Such analysis can only be performed to reversible denaturation or molecular transitions [344], ([350]). Estimations of transfer free energy contribution of different bonds (e.g. hydrogen and peptide bonds) can also be obtained from solubility measurements [356]. Infrared spectroscopy (IR) enables conformation analysis of enzymes in water solutions and is based on the characteristic hydrogen bond patterns of carbonyl and amide bonds in the polypeptide chain. It is able of distinguishing α-helixes from ß-sheets and other conformations [349], and chemical entities with covalent bonds can in principle be analysed through the corresponding vibrational absorption bands with IR spectroscopy (Middaugh *et al*., Chapter 6, pp. 137 to 156 [350]). Classical methods of protein folding and structure characterization are extensively described in Shirley *et al*. (1995) [350].

In order to study enzyme deactivation or quantify the amount of irreversibly denatured enzyme, a good approach is to measure its activity, since it is inversely proportional to the number of irreversibly denatured enzymes [344]. Enzyme activity can be measured spectroscopically [353] or with other analytical techniques such as MS or HPLC, by following consumption or production of a compound involved in the reaction, or through a secondary reaction involving a reaction product where a colorimetric or fluorescent compound is generated or consumed [218].

5.1.1.2 Thermal inactivation and deactivation

Traditionally, thermal deactivation is represented as a two-state model, where deactivation occurs when an enzyme denatures irreversibly upon heating. In this classical model an enzyme's temperature-dependent behaviour is determined based on the activation energy of the reaction and the thermal stability of the enzyme [357]. Thus, initially a temperature increase is translated into an increase in enzyme activity until above a certain temperature (enzyme melting temperature), after which further temperature increase results in enzyme denaturation and possible deactivation. However, several researchers have suggested the existence of an inactive intermediate state in rapid equilibrium with the native state, which can simultaneously deactivate through irreversible denaturation at a slower rate than the equilibrium [358], [347], [359], [360], [346].

Mozhaev and Martinek (1982) [345] describe the mechanism for irreversible denaturation of enzymes at high temperatures as occurring by enzyme acquisition of non-native non-covalent

bonds that lead to a new conformation. The new state, although thermodynamically unstable, is kept when the temperature is reduced (e.g. to room temperature) due to conformation kinetics and a decreased molecular mobility of the polypeptide chains, thus preventing native state recovery by the enzyme. Deactivation is often represented as a first-order exponential decay but due to the diversity of mechanisms that can lead to deactivation [361], its mathematical representation can be more complex [359], [346]. Ahern and Klibanov (1988) [362] have described denaturation as the loss of secondary and tertiary structural order towards increased entropy due to random and fast cooperative intramolecular movements that occur above a certain temperature (which depends on the environmental conditions). Denaturation is usually mathematically represented as a reversible equilibrium reaction, since if no chemical modifications of the chain occur after unfolding, renaturation and regain of enzyme activity should occur once the temperature is lowered.

Daniel *et al.* (2010) [357] proposed a model (Equilibrium model) describing this new mechanism, which was developed based on enzyme activity measurements. In this model, it appears that differences in the active site generate the differences between active and inactive states, and that the thermodynamic equilibrium model parameters do not depend on enzyme stability. The shift between active and reversible inactive state, seemed to involve little unfolding of the enzyme conformation. This is compatible to previous observations that loss of activity preceded loss of native conformation in thermal and chemical inactivation [347]. The unfolding in the active site, at higher temperatures than the equilibrium and depending on enzyme stability, could eventually lead to the unfolding of the overall enzyme structure and thus to enzymatic denaturation or even deactivation at a much slower rate. Furthermore, it seems that the thermodynamic parameters (equilibrium temperature and enthalpy change) considered in the model vary with the substrate and co-factor used for the same enzyme. [363]. Chen *et al.* (2011) have shortly afterwards suggested a transient model, where the enzyme under thermal inactivation can exist in three states: an active state in rapid equilibrium with a reversible inactive state and another reversible inactive state reached through the other inactive state and with a lower enthalpy [364].

5.1.2 Thermal inactivation strategies

Thermal inactivation with the intent of denaturing or even deactivating proteins is widely used. Even though the food industry is the main user of temperature as sample stabilizer and inactivating technique, other fields, where the use of chemicals leads to changes in the sample further complicating its processing, are starting to apply it as well [365], [339]. Elevated temperature results in a fast and unspecific inactivation of different types of samples, and can be useful in view of safe handling of bio-samples, food and beverages quality control, proper sample analysis, treatment of waste, etc.

Several technologies, besides conventional heating (e.g. water bath, convection oven), can be applied depending on type (e.g. food or waste), state (e.g. liquid or solid) or thickness of sample, but also operational conditions (continuous or batch).

Conductive heating (CH) includes heating strategies, such as temperature applied through heat plates or the use of thermocyclers. CH is the standard method applied in laboratories for the study of enzyme conformation and kinetics, but it can also be accurately

applied to excised tissue samples with up to 7 mm thickness [366], [339]. Other strategies usually involve heat transfer through absorption of irradiated electromagnetic wavelengths, which is in general more energy efficient and faster than conventional heating. These strategies usually require less than 1 minute of irradiation at the same temperature used in conventional heating to reach an equal or higher inactivation.

Microwave (MW) irradiation or dieletric heating enables non-contact heating of a sample through conversion of microwave energy (1 mm^{-1} wavelengths at frequencies between 300 MHz and 3000 GHz) absorbed by water and/or polarizable organic molecules (whose dipoles continuously (re)align with the applied electromagnetic field) [365]. It presents a rapid volumetric heating and better on/off control than conventional heating, with a characteristic increased temperature in the bulk relative to the sample surface. MW also presents non-thermal effects due to molecule polarization which might result in added breakage of hydrogen bonds and/or changes in the secondary and tertiary structures of proteins [365]. MW irradiation has been applied for inactivation of tissue samples *in situ* (e.g. in brain tissue) [339], sludge treatment [365], and sterilization (e.g. virus [367], spores [368]). Coupling of MW with other processing techniques has also increased its application in the food industry, thus overcoming some of its issues like non-uniform temperature and moisture distribution [369].

Radio frequency-heating (RF) or capacitative dielectric heating generates heat by increasing molecular friction and space charge displacement when an alternating electric field of frequency between 1 and 300 MHz is applied [340]. RF has been investigated as a substitute of conventional heating strategies for solid or powdered foods for blanching and sterilization. The sterilization ability of RF-heating depends on several factors, such as moisture and salt content of the samples, as well as material density and dielectric properties [340], [370]. RF permits a faster heating than conductive approaches and MW of the samples with a more uniform temperature distribution and a higher temperature in the bulk [340]. It may also present similar non-thermal effects as MW heating [370]. RF is also applied in the polymer industry [371]. Since both MW and RF frequencies are within the communication frequency range, only certain frequencies for both techniques are allowed to be used [370].

In Infrared-heating (IR), temperature is increased by changing the vibrational state of specific molecules or functional groups by absorption of 0.78 to 1000 μm wavelengths (range between visible and microwave radiation). The required radiation time to achieve inactivation can span from a few seconds up to 10 min. IR inactivation efficiency depends on the radiation spectrum that can be divided in near-infrared (NIR), mid-infrared (MIR) and far-infrared (FIR). The used radiation spectrum depends on the type and thickness of the target sample so sterilization can be achieved without alteration of sample quality. FIR is more used as a surface heating method, while NIR can achieve a better sample penetration [372]. Hybrid IR inactivation techniques have also been applied [373].

Ohmic-heating (OH) converts alternating electrical current to internal heat through the resistivity of the samples, and is applied mostly in the food industry, especially to high viscosity samples and solid-liquid mixtures [374], [341]. OH has a high penetration depth limit (up to 25 mm), heating the samples uniformly, unlike the previously explained strategies, but requires contact of the samples with the heating electrodes [341], [371]. The generated heat is thus dependent on the thermal conductivity of the samples and on the applied current [375]. It is

cheap and also compatible with a wide variety of processing formats [374], and possesses a better energy efficiency than other methods [371].

Induction heating (IH) produces heat through generation of eddy currents inside a conductor metal, where resistance to so called Foucault currents creates joule heating (heating due to the passage of electric current that depends on resistance of the material). IH allows targeted heating in a defined area directly opposite to the coil where the current is induced [370]. However when the material is placed inside an electricity conducting container damage due to surface burning may occur [371].

5.1.2.1 Temperature control at the microscale and available strategies for enzyme inactivation

Most research laboratories use conventional convective heating, such as water bath, oil bath or hot plates, for applying heat or as inactivating strategies. However, these methods have several issues, for instance with non-uniform temperature distribution between the heating surface and the bulk of the sample and the time required to reach the target inactivation temperature. Microfluidics can solve these issues simply by decreasing the distance between the bulk of the sample and the heating surface. Thus, at microscale, conductive or contact heating is an attractive method to perform fast inactivation.

Conductive heating at microscale can be achieved with a variety of strategies either by integrating heating elements directly in the platform or using external heating elements. Integrated heating has been achieved through the use of exothermic reactions in parallel microchannels in contact with the main channel [376], but also by on-channel microfabrication of resistors and thin-film resistors [377], [378], [379], [380] or metal wires [376]. External heating elements can be hot plates, readily available in most laboratories, but lately thermoelectric modules (TEM) or Peltier elements have gained relevance since they enable a good control of the applied temperatures and are easily integrated with already existing electronic components. In computers and some electronic equipments, Peltier elements are customarily used as cooling elements to avoid overheating of the electronic parts as alternative or complements to fans. Peltier elements are now relatively ubiquitous in benchtop analytical equipment for temperature control [353] (both heating and cooling functions), but are also increasingly used in microfluidic applications [376], [381]. TEM systems are employed in applications that require a high degree of temperature control with fast switching between temperatures, such as on-chip polymerase chain reaction (PCR) [382], [381]. Fast switching between defined temperatures or creation of temperature gradients can be achieved through pre-heating or cooling of the fluids used in the microfluidic system [383], by placing the microchannel between two different Peltier elements, or using two Peltier elements at different temperatures separated by a defined gap [376].

Other (non-contact) heating strategies have also been applied at the microscale, some of them already mentioned for industrial application. MW dielectric heating allowed higher thermocycling rates in PCR applications [376] as well as accelerated reactions [384] compared to integrated heating. This occurs due to the MW's ability to heat the liquid bulk directly [385], [376], but also of heating only specific regions of the microchannel or even single droplets [386]. IR heating is another example of an industrially-used heating strategy that has also been

applied at microscale [387], [376], with greater emphasis on PCR systems [388]. RF heating for example, which is commonly used at industrial scale in the food industry, has been used at microscale to perform magnetic fluid hyperthermia (MFH) on cells [389]. MFH is a technique that enables cell inactivation (e.g. tumour cells) by targeted delivery of heat to cells. The cells are labelled with magnetic nanoparticles, which increase in temperature when subjected to an alternating current magnetic field (e.g. generated in copper coils integrated in a microchip [389]), thus causing temperature denaturation of the target cells. The generated temperature increase occurs due to thermal losses while the particles align to the alternating magnetic field [390]. MFH has also been applied for inactivation of bacteria [391]. Heat inactivation of enzymes coupled to nanoparticles can also be achieved through the use of gold nanoparticles. These particles can create heat when hit by a laser with a wavelength similar to the particles surface Plasmon resonance frequency. The generated heat is localized and can be used to inactivate a specific enzyme in a mixture of different biomolecules, using gold nanoparticles with different shapes and thus different Plasmon frequency [392]. A summary of the main thermal characteristics of these systems are presented in Table 19.

Table 19 – Summary of main thermal properties and applications of several heating strategies at the microscale.

Heating strategy	Heating/ Cooling rate (^{0}C/s)	Temperature range (^{0}C)	Response time	Application
(Thin-film) resistors	5 - 20	25 - 110	1 s - 3 min	PCR [393], [378], [379], lab-on-a-disc [380], protein synthesis [377]
Thermoelectric modules (TEM)	20 - 100	-3 - 120		PCR [393], [382], [381], thermal management [394]
Microwave (MW) heating	5 - 30000	25 - 95	ms - s	PCR [376], Hydrogel polymerization [386], Flow chemistry/drug discovery [384]
Infrared (IR) heating	10 - 65	25 - 95	ms - s	PCR [387], [393], [388], Enzyme inactivation [392]
Radio-frequency (RF) heating	-	25 - 100	-	MHF [389], inactivation of bacteria [391]

5.1.3 Goal

The microfluidic system presented in this work was developed as an intermediary step in a modular microfluidic platform. This type of platforms, based on the "plug-and-play" approach, enable the connection of independently developed microfluidic units, which can be combined or arranged differently depending on the application, type of sample or reaction [40], [41], [42], [43], [44], [45].

To obtain a reliable result from enzymatic reactions, it is necessary for the samples to be quantified immediately or at a well-defined reaction time point (residence time). The quantification of reaction components under flow conditions (as part of a continuous operation platform) requires a comprehensive characterization of the microreactor so that samples can be compared at different reaction times. However, in a modular platform, where the reactor and operation units can be changed, it is essential that the samples reach the quantitative system or sensor in the same conditions. Enzymatic reactions can be stopped through addition of reagents that inactivate the enzyme or through compounds that block the active site, but this

may interfere with the operation of the sensor used for the quantification (e.g. addition of NaOH, as in Chapter 2, or HCl for pH change and enzyme denaturation can destroy the biosensing layer of electrochemical-based sensors, such as the ones presented in Chapter 4).

The presented microfluidic platform intends to address the latter issue by providing an alternate inactivation strategy: temperature-based inactivation of enzymes. The control of the temperature, as stated above, allows an unspecific inactivation of both enzymes and cells, thus simplifying the inactivation procedure while allowing flexibility in terms of application, as required in modular microfluidic platforms. It also enables achieving reversible or irreversible inactivation of the involved proteins depending on the chosen operation conditions, offering a further degree of control on the enzyme state during operation. The use of temperature further avoids the application of solvents or other inactivating agents, simplifying the procedure. Temperature is also used in different research fields, and so its integration in a modular platform increases the platform's applicability in different technical applications. The developed platform's inactivation ability was compared with the standard laboratory method in order to prove its usefulness as part of an enzymatic screening platform.

This platform was specifically developed to allow enzyme inactivation (hence stopping the reaction) in the reaction mixture coming from the silicon meander channel (presented in Chapter 2), so glucose quantification could be performed in the chip for electrochemical sensor integration (presented in Chapter 4). Due to time constrains, however, the final integration of all the platforms presented was not possible.

5.2 Materials & Methods

In this work, a new microfluidic platform for thermal inactivation of enzymes was fabricated and its inactivation ability compared with the standard laboratory procedure, a table top orbital heating device. The required time to achieve the desired inactivation temperature was also simulated using computational fluid dynamics as a complement in the study of the inactivation ability of the two used strategies. In this section, a description of the different performed studies and materials used during this work is presented.

5.2.1 Reagents and Materials

Glucose oxidase (EC 1.1.3.4, type VII, from *Aspergillus niger*, ≥100,000 U/g solid), catalase (EC 232-577-1, from bovine liver, lyophilized powder, 2000-5000 units/mg protein) and horseradish peroxidase (EC 1.11.1.7, lyophilized, 150 U/mg) were obtained from Sigma (St. Louis, MO, USA). D- Glucose (anhydrous) was provided by Fluka (Loughborough, UK). Mono – and di-potassium hydrogen phosphate (anhydrous) were obtained from Merck (Darmstadt, Germany). Hydrogen peroxide (Perdrogen™, 30% (w/w)), Sodium 3,5-dichloro-2-hydroxy-benzenesulfonate (DCHBS) and 4 Aminoantipyrine (4-AAP, reagent grade) were obtained from Sigma (St. Louis, MO, USA). All the solutions for sensor preparation were prepared with 50 mM phosphate buffer pH 7.5. All solutions were prepared in buffer.

The 10-mm marlon polycarbonate plate that forms the channel was from Brett Martin (Newtownabbey, UK). The 2-mm thick SS304 stainless steel bottom plate of the channel, as well

as the structural components of the platform were from Sanistål (Aalborg, Denmark). The polycarbonate and steel parts were milled using an ecoMill 50 from DMG mori (Bielefeld, Germany). The adhesive assembly of the platform was performed with a 142 µm thick double-sided adhesive tape mcs-foil 008 from microfluidic ChipShop (Jena, Germany), previously patterned using laser ablation with a CMA-4030 Laser Engraving machine from GD Han's Yueming Laser Technology co., Ltd (Guangdong, China). Flangeless polypropylene (PP) fingertight 1.5875 mm (ID) fittings (XP-201) and flangeless ferrules (P200X) from Upchurch Scientific® (Washington, USA) were used to connect polytetrafluoroethylene (PTFE) 1.5875 mm (OD) x 1mm (ID) tubing (S 1810-12) from Bohlender (Grünsfeld, Germany).

5.2.2 Enzyme activity measurements

Activity measurements of Glucose oxidase (GOx) and Catalase (Cat) were performed in a UV-1800 UV-Vis spectrophotometer with a CPS 240A cell positioner from Shimadzu (Kyoto, Japan). GOx activity was measured using a protocol adapted from Heuts *et al.* (2007) [218], where the hydrogen peroxide formed in the presence of glucose, is used by horseradish peroxidase (HRP, 4 U/mL) to oxidize 4-AAP (0.1 mM) and DCHBS (1 mM), forming a colorimetric (pink) compound. The formation of this compound can be followed at 515 nm (ε_{515}= 26 mM^{-1} cm^{-1}) and its absorbance can be directly related to the amount of glucose consumed. To measure GOx activity 10 µL of 1:30 diluted GOx solution (~30 U/mL) were added to 990 µL of the reaction mixture. For the inactivation study, the initial rates of glucose consumption/ colorimetric compound formation were compared for a glucose concentration (400 mM) equal to around 10 times the measured K_M (~30 mM). The influence of temperature on HRP was also attained by performing the previous assay with addition of 20 µL of HRP to 980 µL of a constant concentration of hydrogen peroxide (2 mM), 4-AAP (0.1 mM) and DCHBS (1 mM) at different temperatures (298 K (25 ^{0}C), 310 K (37 ^{0}C), 318 K (45 ^{0}C), 328 K (55 ^{0}C) and 333K (60^{0}C)). An increase in activity of around 8-fold was observed, between the lowest and the highest temperature. Concentration of hydrogen peroxide was chosen based on data presented in BRENDA [395] for HRP from *Armoracia rusticana*. The activity of Cat (~400 U/mL) was measured based on the protocols by Beers and Sizer (1952) [219] and Lück (1965) [220], by following the decrease of hydrogen peroxide concentration at 240 nm (ε_{240}= 43.6 M^{-1} cm^{-1}). To measure Cat activity 30 µL of 1:10 diluted catalase solution was added to 2970 µL of 10 mM hydrogen peroxide. Each spectrophotometric measurement was performed in triplicate for 2 min.

5.2.3 High-Performance Liquid Chromatography (HPLC) method

All the reaction samples were analysed in an HPLC for quantification of glucose consumed and gluconic acid produced. The measurement was performed with a reversed-phase chromatography on an Ultimate 3000 HPLC (Dionex, Sunnyvale, CA, USA) equipped with a Phenomenex column with 5-µm sized amine particles (Luna 5u NH2 100A), operated at 40 ^{0}C and 140 bar. The mobile phase consisted of a 20 mM H3PO4 solution, flowing at 1 mL/min. The eluted gluconic acid was quantified in a ultraviolet (UV) multiple wavelength detector at 205 nm, while the glucose concentration was determined in the Refract Max 520 refractive index (RI) detector. The amount of each component was obtained by integration of the areas under the

corresponding peaks using the HPLC commercial analytical software (Chromeleon 6.8), based on a calibration curve performed for each component.

5.2.4 Thermal inactivation platform

The microfluidic thermal inactivation platform has several components, as shown in Figure 58. The microfluidic channel was micromillled in a polycarbonate plate with a meander shape with 150 µm deep and 790 µm wide, as well as a pocket for a temperature sensor (Figure 59 (a)). The microchannel has two main inlets and two side inlets, which provide a wider range of residence times. The channel formed by the main inlets will be referred as main channel (with a length of 325 mm), while the channel formed by the side inlets will be referred to as secondary channel (with a length of 87 mm). The polycarbonate plate was glued onto a thin stainless-steel plate with a patterned 142 µm thick double sided adhesive type, giving the channel an overall height of 292 µm. A PT 1000 temperature sensor (Platinum Thin Film PTFM102A1A0 from Measurement Specialties (Europe) Ltd., Dortmund, Germany) was placed in contact with the steel plate and connected to a controller (Laird PR-59 Advanced Temperature Controller from Supercool AB, Stromstad, Sweden) which was operated from a personal computer (PC). The controller had a EOS LFWLP350-1005 power supply (from EOS, Andheri, Mumbai, India). The steel plate was fabricated with a bended shape on the sides and a metal separation in the middle in order to allow a good positioning of the thermoelectric modules (Peltier elements from Multicomp by Newark element14, Chicago, Illinois, USA), as can be seen in Figure 58. The Peltier elements have a dimension of 40 mm x 40 mm x 3.45 mm and a maximum of temperature differential of 70 K/ ^{0}C during cooling, and can be controlled with the software (SC_Interface) provided with the controller. Before assembly the Peltier elements were covered with a thin layer of a heat transfer paste (HTS Silicone Heat Transfer compound from Electrolube, Leicestershire, UK). To facilitate the cooling of the cool side of the Peltier elements during operation, a heat-sink and a fan were connected to the microchannel assembly. The assembled Peltier elements were placed on the heat sink structure, which was milled in order to have the shape of the Peltier elements and enable a good fit of the microchannel assembly onto the heat-sink (60mmx40mmx10mm, 153AB from ABL Aluminum Components, Birmingham, UK). The fan (614 NGL DC axial fan from Ebm-papst Inc., Farmington, Connecticut, USA) was assembled underneath the heat-sink and connected to the controller. Four metal pillars attached to the heat-sink provided stability to the assembled platform, while enabling some space between the fan and the support of the platform. The connection of the different electronic components was performed in-house, and installed inside a 30 cmx 30 cm x 10 mm plastic box.

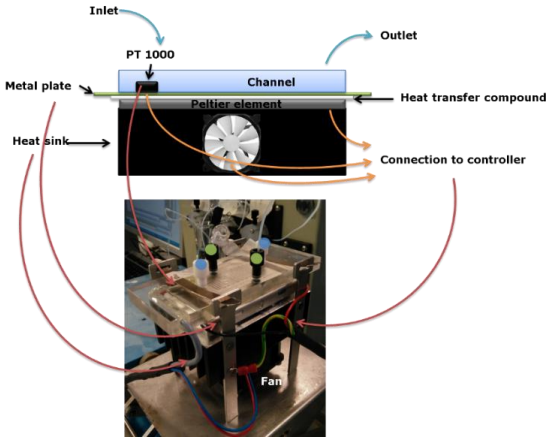

Figure 58 – Schematics and photograph of the assembled microfluidic platform for thermal inactivation of enzymes, with the different components highlighted. In the photograph emphasized with blue dots the inlet and outlet of the main channel, while in green the inlet and outlet of the secondary channel are indicated.

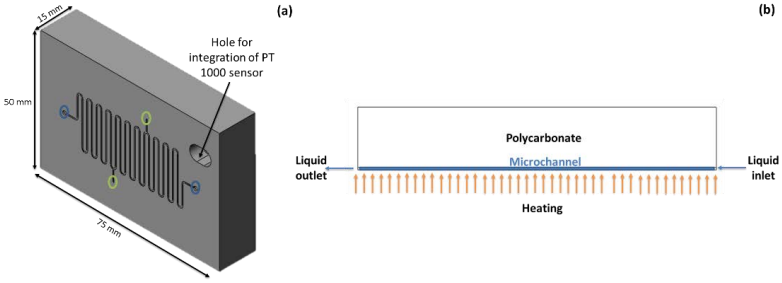

Figure 59 – Schematics of the polycarbonate plate with engraved microfluidic channel (a) where the primary (in blue) and secondary (in green) inlets are highlighted, and schematics of the microfluidic channel used in the CFD simulations (b), where flow direction, position of the microchannel and heating are highlighted.

5.2.4.1 Characterization of thermal performance of the inactivation platform

To understand how the thermal inactivation platform behaved at the different temperatures, the performance of the controller and the temperature sensor were tested.

Different controller parameters were tested in order to minimize temperature overshoot when the heating function was started (with platform at 298 K (25 ^{0}C) to reach the different inactivation temperatures), as well as temperature variability during operation. The best performance was obtained with a proportional-integral (PI) type of control, set with the parameters shown in Table 20. A temperature overshoot of 6 to 16 K/^{0}C was obtained when heating was initiated. The temperature varied between +/- 0.05 K/^{0}C and +/- 2.5 K/^{0}C around the set point temperature during operation. The highest variability was observed for temperatures between 318 K (45 ^{0}C) and 338 K (65 ^{0}C), while the lowest variability and overshoot was observed for 298 K (25 ^{0}C), 310 K (37 ^{0}C) and 353 K (80 ^{0}C). The action of the fan

did not seem to yield a significant effect during operation, so the presented experiments were performed with the fan turned off.

Table 20 – Optimized controller parameters used during the experiments.

Controller parameters	Value
Max power out	30%
Dead-band	3%
Heating Gain	1
Cooling gain	0
Decay when stopped	0.1
KP (proportional constant value)	5
KI (integral constant value)	0.5
Integral value limit	100%
KTr (lowpass filter to limit speed of change of a set point)	2
KTe (lowpass filter of the difference between the temperature sensor and the set point)	3

5.2.5 Thermal inactivation measurements

The study of the enzymatic inactivation ability of the assembled microfluidic platform was performed for each enzyme separately, by pumping the enzyme solution inside the channel at different flowrates to achieve the desired residence times and temperatures, as presented in Figure 60. The used residence times and temperatures are shown in Table 21. Before introduction of the enzyme solution, the channel was heated to the desired inactivation temperature, and flushed with enzyme solution (Reynolds number of 2.05) for a minimum of 6 times the channel volume before sampling was performed. The enzyme solution was then retrieved at the outlet, appropriately diluted (1:30 in the case of GOx and 1:10 in the case of Cat) and measured in the spectrophotometer with the previously described protocol (section 2.2). GOx solutions were also added to a vial with 200 mM glucose solution in a 1:1 proportion, and glucose concentration was measured after 1 day and 2 days respectively in a high-performance liquid chromatograph (HPLC) Dionex UltiMate 3000 UHPLC system with diode array and refractive index detector (from Thermo Fisher Scientific, Waltham, Massachusetts, USA). HPLC data was used to check whether inactivation or denaturation occurred in the platform. In the case of Cat, the same solutions at the outlet of the microchannel were measured after 1 day in the UV/VIS spectrophotometer and hydrogen peroxide consumption compared to the one of freshly inactivated enzyme. The samples of both enzymes were kept at room temperature following inactivation.

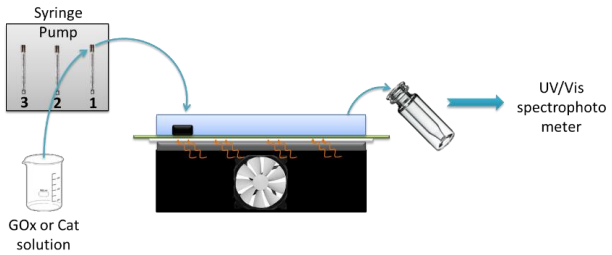

Figure 60 – Schematics of sampling in the microfluidic thermal inactivation platform.

Table 21 – Residence times and temperatures used for the characterization of the microfluidic thermal inactivation platform and comparison with the ThermoMixer.

Channel	Residence time (s)	Flow rate (μL s^{-1})	Flow velocity (m s^{-1})	Temperature (K/^{0}C)
Secondary channel (~87 mm)	10	2	0.0087	298/25
	20	1	0.0043	310/37
	30	0.66	0.0029	318/45
Main channel (~325 mm)	60	1.25	0.0054	328/55
	120	0.625	0.0027	338/65
	180	0.417	0.0018	353/80

The same study of the enzymatic inactivation was performed in a table top orbital MRH11 Heating ThermoMixer (from HLC BioTech, Bovenden, Germany), using similar enzyme solutions and the same temperatures and residence times as for the experiments in the microfluidic system. In this case, 500 μL of the enzyme solution were added to a 4-mL vial already at the target inactivation temperature. The consumption of glucose by the enzyme solutions inactivated in the ThermoMixer was also measured in the HPLC after 2 days. In both sets of experiments GOx solutions were freshly prepared, while Cat solutions were diluted from a stock solution (~1000 U/mL) every day. The activity of Cat in the stock solution was measured daily. The enzymes were kept in ice (around 277 K (4 ^{0}C)) during the experiments and added to the ThermoMixer and to the channel only when these were already heated at the inactivation temperature being tested.

5.2.6 Characterization of thermal inactivation platforms with CFD

Microchannel and 4-mL vial geometries were designed in SolidWorks 2015 (Dassault Systèmes SolidWorks Corporation, Waltham, Massachusetts, USA). The time required to achieve the final inactivation temperature (353 K (80 ^{0}C)) from room temperature (298 K (25 ^{0}C)) was simulated using a computational fluid dynamic simulation software, ANSYS-CFX Version 16.2 (Canonsburg, Pennsylvania, USA). The three-dimensional designs of the microchannel (Figure 59 (a)) and 4-mL vial (Figure 61 (a)) were imported into a meshing software, ANSYS ICEM CFD® 16.0 (Canonsburg, Pennsylvania, USA), and discretization of the geometry into smaller elements (where the equations for momentum, energy and mass balance [396], [397] are solved by ANSYS-CFX software) was performed. The geometry of the 4-mL vial was simplified to a slice of 1.24% of the entire volume, defined based on an axial geometry where the slice corresponds to the volume of 5^0 of the cylinder vial perimeter (Figure 61 (b)). The slice defined contained 11284 elements (107.5 elements/ μL). The microchannel geometry was simplified to a straight rectangular 30 cm long channel with 1/4 of channel width with steel underneath and a 5-mm polycarbonate plate on top (Figure 59 (b)) containing 72144 elements (2312.3 elements/ μL). Both designs were simulated with a structured hexahedron mesh, assuming that the structures and the environment were at 298 K (25 ^{0}C). In order to simulate the whole structure, symmetry was assumed on both sides of both the slice (axial symmetry) and microchannel design. When symmetry is used, the conditions on the areas beyond the simulated volume are a reflection of the simulated conditions. The use of symmetry reduces the computational time required for the simulation [397]. The fluids were simulated according to the Navier-Stokes equation for Newtonian fluids [398] under laminar flow conditions, which

was solved coupled with the energy balance [399] using the Thermal Energy model integrated in ANSYS-CFX.

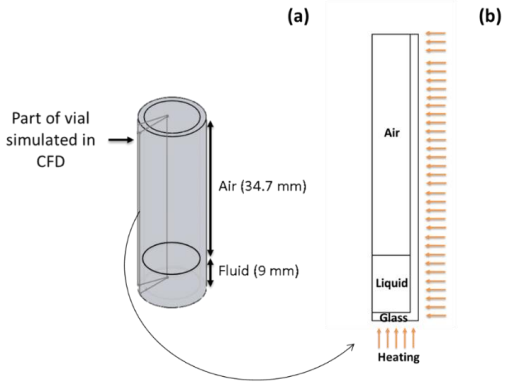

Figure 61 – Schematics of 4-mL vial designed in SolidWorks with the slice used for CFD simulations shown (a) and simulated slice of 4-mL vial with different parts and heating highlighted (b).

The vial was considered to be made of glass flint, with a height of 9 mm corresponding to the liquid (defined as water) and the rest was filled with air. The three phases, solid (glass), liquid (fluid) and gas (air), were defined as separate parts in the geometry with a conservative interface flux condition, where only temperature is conducted into between the solid and the liquid phase. In both the liquid and the air phase, two fluids were defined: water with a density of 997 Kg m^{-3} and air with a density of 1225 Kg m^{-3}. In the air phase, air had an initial volume fraction of 1 and water of 0, while in the liquid phase, the opposite was set. Both fluids were defined as buoyant with 9.81 m s^{-2} as the gravitational acceleration towards the bottom of the vial. The heat was defined as coming only from the glass outer walls (bottom and side of the vial) as presented in Figure 61 (b). The portion of liquid on the bottom was at 277 K (4 ^{0}C) at the start of the simulation, while the air above it was at room temperature (298 K (25 ^{0}C)). A homogeneous Thermal energy model was used to perform the glass vial simulations, in which the volume fractions of the fluids were defined as coupled.

The microchannel (Figure 59 (b)) was filled with liquid under laminar flow with a velocity of 0.025 m s^{-1} (Re 5.60), 0.0025 m s^{-1} (Re 0.56) or 0.0018 m s^{-1} (Re 0.40), and the heat was defined as coming from the bottom of the channel as in Figure 59 (b). All the materials were simulated considering the materials' properties provided by ANSYS-CFX at 298 K (25 ^{0}C), and the liquid was defined as water. The polycarbonate plate was simulated as polystyrene with a specific heat capacity of 1426 J Kg^{-1} K^{-1}. The walls (top and bottom of channel) were defined as having no-slip wall boundary conditions, and the outlet was defined as an opening. The simulations were performed transient in order to obtain the time required for both the liquid and the entire system to reach the target inactivation temperatures.

5.3 Results and Discussion

The thermal inactivation platform was characterized using two well-known and relatively robust commercially available enzymes, Glucose oxidase (GOx) and catalase (Cat), which have been extensively studied and improved. A brief look in BRENDA [400] shows the immense diversity of these enzymes, especially GOx, in terms of origin (from bacteria and fungi to human and other mammals), substrate and catalytic properties. Both enzymes are relatively stable and present enzymatic activity in a wide range of temperatures (293 K (20 ^{0}C) to 333 K (60 ^{0}C) for GOx and 303 K (30 ^{0}C) to 333 K (60 ^{0}C) for Cat), thus providing a good case study to test the efficiency and applicability of the developed inactivation platform.

The platform's performance was compared with the standard laboratory procedure used to achieve thermal enzyme denaturation, a benchtop ThermoMixer. The temperatures and residence times presented in Table 21 were used in both platforms.

5.3.1 Characterization of heating performance with CFD

A simplified geometry of both systems used to achieve enzymatic thermal denaturation of GOx and Cat was characterized in terms of time required to reach the target temperature using computational fluid dynamics. Three of the target inactivation temperatures, 298 K (25 ^{0}C), 318 K (45 ^{0}C) and 353 K (80 ^{0}C), were chosen for comparison of heating performance in the two simulated inactivation systems.

Figure 62 shows the results for the simulated slice of the 4-mL vial, when the glass is pre-heated at 353 K (80 ^{0}C) (Figure 62 (a)) or at room temperature (Figure 62 (b)) at the start of the simulation. As can be observed, the liquid inside the vial reaches 353 K (80 ^{0}C) at a similar time in the simulation at around 160 s for both cases. The liquid reaches the desired temperature at similar times since the temperature gradient driving the heat transfer is the same. After 300 s both the liquid and the air are heated at the desired inactivation temperature, except near the top of the vial where there is heat loss to the environment.

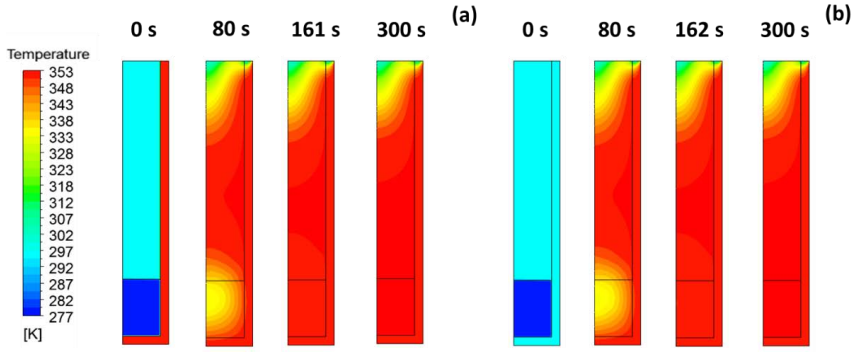

Figure 62 – Results from the CFD simulation of part of the 4-mL vial considering the glass was pre-heated at 353 K (80 ^{0}C) (a) or at 298 K (25 ^{0}C) (b).

For both simulations, uniform heating of the liquid to 353 K (80 ^{0}C) is achieved around 160 s, which is shorter than the longest residence time used for enzyme inactivation in this

study, but longer than most of the inactivation times tested. This indicates that the enzyme solutions inactivated in the ThermoMixer were not uniformly exposed to the same temperature for the shorter inactivation times and so a higher variability might be expected from these samples, since no mixing was used. This is also demonstrated in Figure 63 where the temperature contour plots of the liquid, air and glass at the same residence times used in the experiments is shown. Only part of the liquid is first heated at the target temperature after 120 s of exposure to 353 K (80 ^{0}C) in Figure 63 (a).

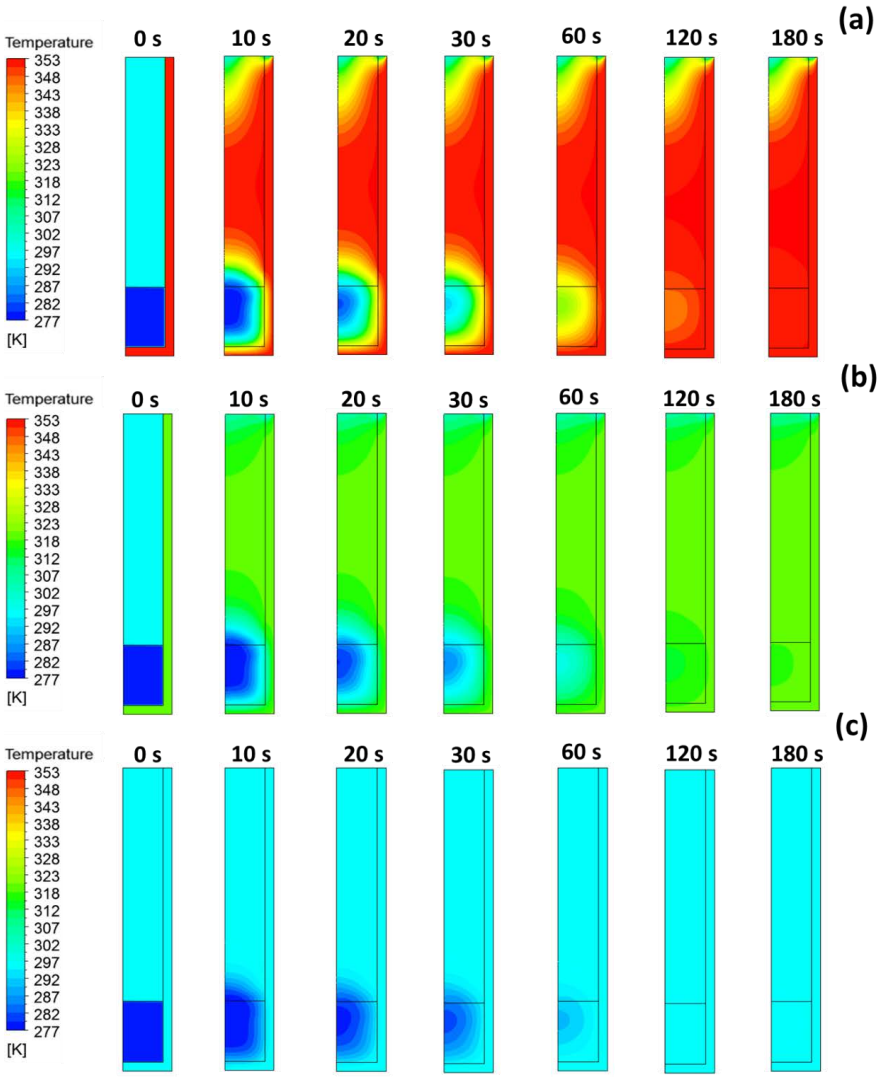

Figure 63 - Results from the CFD simulation of part of the 4-mL vial considering the glass was pre-heated at 353 K (80 ^{0}C) (a), at 318 K (45 ^{0}C) (b) and at 298 K (25 ^{0}C) (c) for the different residence times used.

According to Figure 63 (b) and (c), for 318 K (45 ^{0}C) and 298 K (25 ^{0}C) respectively, the liquid achieves the target temperature earlier than for 353 K (80 ^{0}C). The target temperatures are achieved between 60 s and 120 s after sample heating is initiated and thus variability for the corresponding samples at residence times above 120 s should be very small. Comparing heating times for Figure 63 (a), (b) and (c), the lower the target temperature, the shorter the time required to reach the desired temperature.

Figure 64 and Figure 65 present the temperature distribution for the different inactivation times across an axial and a vertical line, respectively, drawn in the simulated vial geometry. In the figures, the target temperature is reached for all the inactivation temperatures at 180 s. This seems to contradict the previous conclusions that a lower target temperature results in a lower heating time. However, the presented graphs show a one-dimensional representation of the temperature gradient at a defined position in the vial and thus cannot represent the amount of fluid volume at the target temperature, which is better observed in Figure 63.

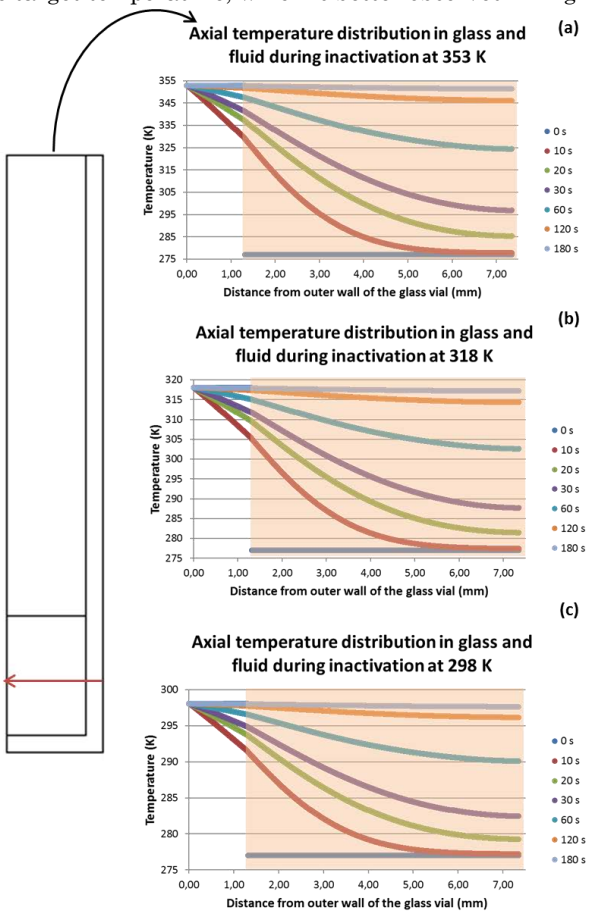

Figure 64 - Results from the temperature distribution along an axial line for the CFD simulation of part of the 4-mL vial considering the glass was pre-heated at 353 K (80 ^{0}C) (a), at 318 K (45 ^{0}C) (b) and at 298 K (25 ^{0}C) (c) for the different residence times used.

In Figure 65 it is also possible to observe that the air close to the fluid reaches the target temperature slower than the air above it, due to the lower temperature of the liquid. Furthermore, the air on the top of the vial, in contact with the environment, presents a constant temperature gradient, resultant from heat loss to the environment, which increases with the inactivation temperature.

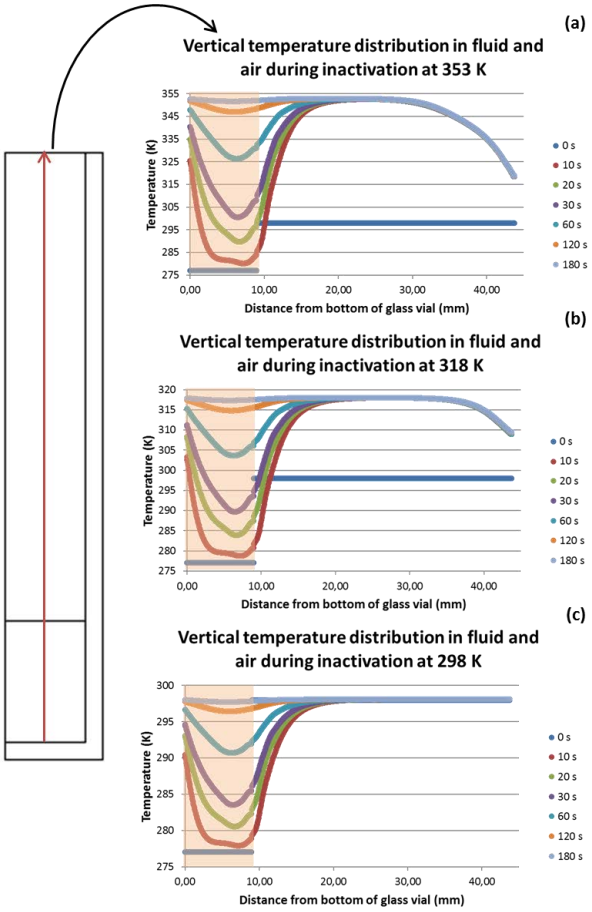

Figure 65 - Results from the temperature distribution along a vertical line for the CFD simulation of part of the 4-mL vial considering the glass was pre-heated at 353 K (80 ^{0}C) (a), at 318 K (45 ^{0}C) (b) and at 298 K (25 ^{0}C) (c) for the different residence times used.

Finally, in all the presented figures, the wider the temperature difference between initial conditions (sample at 277 K (4 ^{0}C) and air at 298 K (25 ^{0}C)) and inactivation temperature (298 K (25 ^{0}C), 318 K (45 ^{0}C) and 353 K (80 ^{0}C)), the faster the heating rate. This is evident in Figure 63 (a), Figure 64 (a) and Figure 65 (a) where a temperature of 318 K (45 ^{0}C) is obtained between 30 s and 60 s, which is consistent with the higher temperature gradient and therewith a higher driving force for the heat transfer to occur in this case (353 K (80 ^{0}C)).

The results from the CFD simulation for the simplified geometry of the microchannel are presented in Figure 66. In this geometry, we considered that the bottom of the microchannel (which corresponds to the steel plate) is at an initial temperature of 353 K (80 ^{0}C), 318 K (45 ^{0}C) or 298 K (25 ^{0}C), respectively, when the enzyme solution at 277 K (4 ^{0}C) is introduced in the microchannel with a linear velocity of 0.0018 m s^{-1} resulting in a Re number of 0.40.

As can be observed for the inactivation temperature of 353 K (80 ^{0}C) (Figure 66 (a)), the liquid flowing inside the channel reaches the desired temperature after 0.6 s. This significantly faster heating of the enzyme solution relative to the 4-mL vial (Figure 63) is expected, considering the microchannel' s small height (292 µm) and reduced volume, which enables a fast heat transfer from the heat steel plate to all transported fluid.

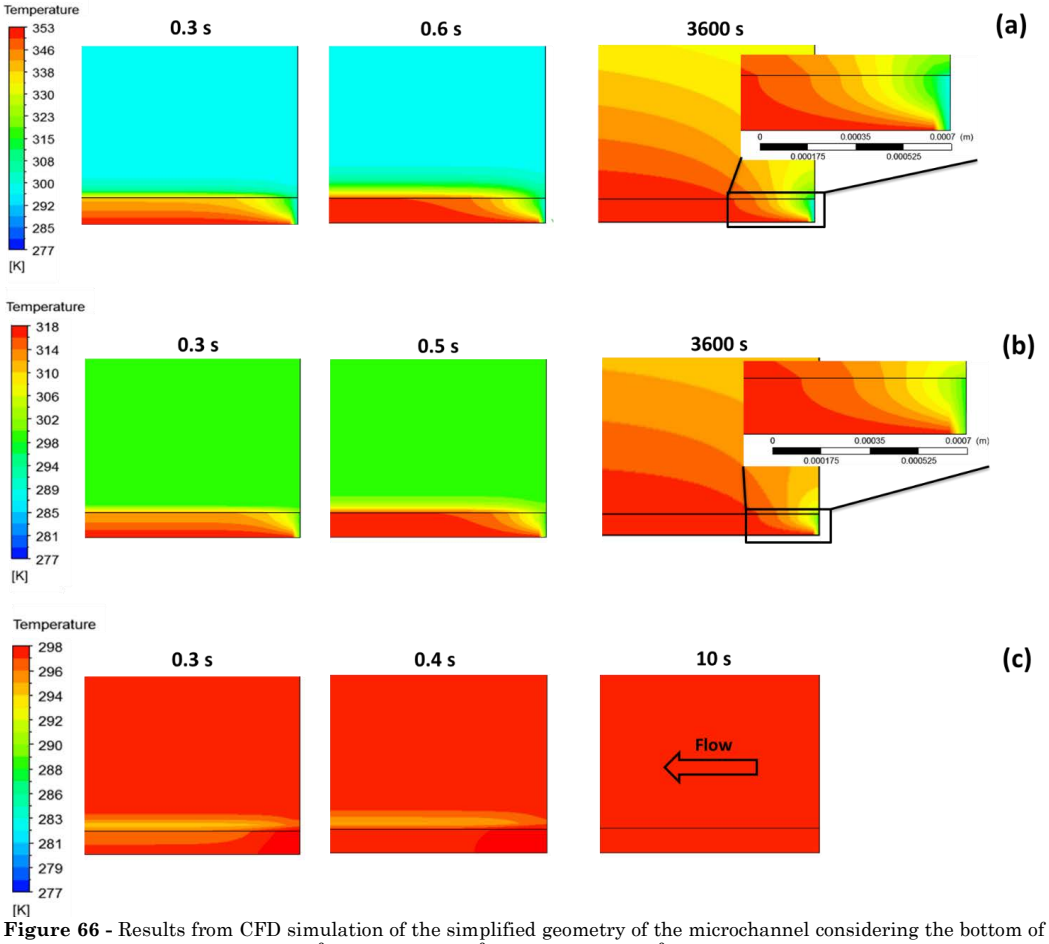

Figure 66 - Results from CFD simulation of the simplified geometry of the microchannel considering the bottom of the channel is heated at 353 K (80 ^{0}C) (a), 318 K (45 ^{0}C) (b) or 298 K (25 ^{0}C) (c), and the average linear flow velocity is 0.0018 m s^{-1}.

The required time for the fluid to reach the chosen inactivation temperature decreases for lower temperatures, as can be observed in Figure 66 (b) and Figure 66 (c). However, as observed above for the 4-mL vial, the same temperatures (318 K (45 ^{0}C) and 298 K (25 ^{0}C)) are reached

earlier in the 353 K (80 ^{0}C) case (at 0.3 s the fluid is already between 338 K (65 ^{0}C) and 353 K (80 ^{0}C)) than for the lower temperatures since the temperature gradient (and thus heat transfer rate) is higher.

It is also relevant to highlight that the inactivation temperature is reached close to the start of the channel, as can be observed in the focused regions in Figure 66. This means that the enzyme solution is exposed to the desired inactivation temperature through the entire length of the microchannel, and thus that the residence times considered during the experiment are close to the real ones. The distance from the inlet at which the entire volume of transported solution reaches the inactivation temperature also decreases with decreasing inactivation temperatures, from 700 μm for the simulation at 353 K (80 ^{0}C) to around 550 μm at 318 K (45 ^{0}C) and 0 μm at 298 K (25 ^{0}C). In all the simulations, at 0.3 s the temperature around the channel (in the polycarbonate plate) is lower than room temperature (298 K (25 ^{0}C)) due to the fluid introduced being at 277 K (4 ^{0}C), but quickly stabilizes to the target temperature. This is more evident in the simulation at 298 K (25 ^{0}C), since the inactivation temperature is equal to room temperature.

To enable the comparison with laboratory enzyme inactivation experiments performed in the microchannel, CFD simulations at 353 K (80 ^{0}C) were performed at different average linear flow velocities varying between 0.0018 m s^{-1} and 0.025 m s^{-1}, to include the range of velocities used in the laboratorial experiments (see Table 21). The temperature of 353 K (80 ^{0}C) resulted previously in the longest distance from the inlet at which the fluid reached the target temperature for the three temperatures simulated. This allows a more comprehensive understanding of the influence of average linear flow velocity on such distance, and thus its influence on residence time. No significant difference was observed in the overall temperature distribution or the times at which the set point temperature was reached between the different velocities. However, the distance from the inlet at which the whole liquid reaches 353 K (80 ^{0}C) increases with an increase in flow velocity, since there is less time due to the fluid's higher velocity for the heat to diffuse across the height of the channel to the solution, as well as some transport of the thermal energy in the direction of the flow (Figure 67). At the lowest simulated velocity this distance is 700 μm, while at the highest simulated velocity the distance is close to 8 mm. For the maximum experimental velocity (0.0087 m s^{-1}) this distance is below 3 mm, which is around 1/30 of the length of channel used (87 mm), and thus its influence in the final used residence time was not considered for the performed experiments.

The presented simulations provide sufficient confidence that the enzyme solution will be uniformly exposed to the inactivation temperature along the entire length of the channel (and close to the assumed residence time).

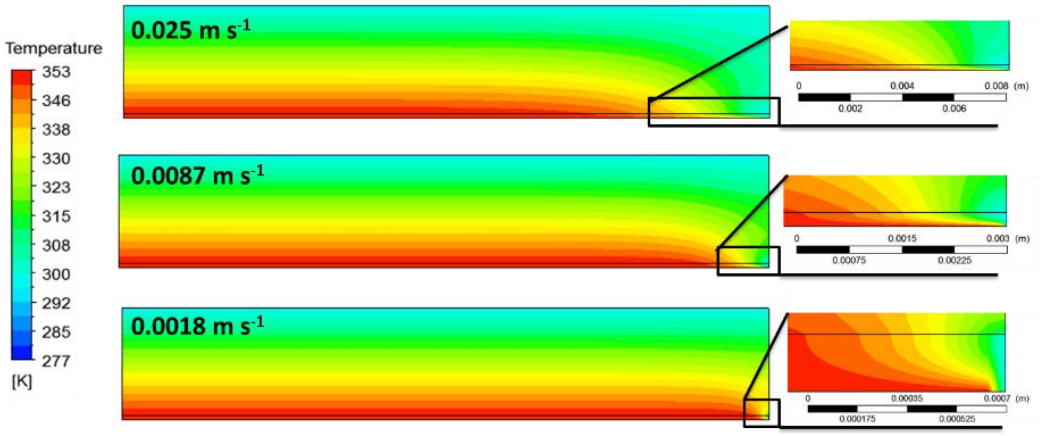

Figure 67 - Results from CFD simulation of the simplified geometry of the microchannel considering the bottom of the channel is heated at 353 K (80 ^{0}C) for different flow velocities.

In all the simulations, after 10 min the distribution of temperature in the microchannel is approximately the same as the one observed after 1 h, with the temperature at the top of the polycarbonate plate at 298 K (25 ^{0}C). During the experiments however, after approximately 10 to 15 min the top of the polycarbonate plate was hot to the touch, indicating a temperature above at least 313 K (40 ^{0}C). This discrepancy could come from the polycarbonate properties (namely the specific heat capacity of 1426 J Kg^{-1} K^{-1}) assumed during the simulation, which could differ from the ones of the polycarbonate used for the microfluidic plate. The temperature during the experiments may also be higher than the simulated ones. However, since the heat provided by the Peltier elements is regulated based on the temperature measured by the PT 1000 sensor, and this sensor is placed close to the channel, this is not expected to be the case. In the simulations, the area surrounding the channel forming most of the platform, as well as the possible influence of the double adhesive tape between the steel and the polycarbonate plate were not considered. These factors might also affect how heat dissipates from the platform, thus influencing the temperature reached on the outside of the platform.

Nonetheless, since the focus of the CFD simulation was to understand the heat transfer to the enzymatic solution flowing inside the channel, which was possible to visualize in the performed simulations, the simulation was considered to have yielded enough understanding of the heating properties of both inactivation strategies to be able to trust in the design of the microfluidic system developed.

5.3.2 Characterization of inactivation performance

The results from the spectrophotometric measurements performed after the enzyme solutions where pumped through the microfluidic channel at various residence times and inactivation temperatures are presented in Figure 68, both for glucose oxidase and catalase. The presented values have a standard deviation between 3.87x10^{-9} M min^{-1} and 8.66x10^{-7} M min^{-1} for GOx and 2.90x10^{-6} M min^{-1} and 1.29x10^{-4} M min^{-1} for Cat. These values were calculated

using the *STDEV.S* function in Microsoft Excel for each set of triplicates measured and then the minimum and maximum standard deviation obtained are the ones presented here.

Both enzymes display a similar inactivation trend. At 338 K (65 ^{0}C) or higher temperatures, a significant decrease in product formation/ hydrogen peroxide consumption is observed in both systems, especially for residence times higher than 60 s. In the ThermoMixer complete inactivation of the enzymes is observed at 353 K (80 ^{0}C) for residence times of 120 and 180 s. This is in agreement with the simulation results reported in Figure 63, where only for these residence times the temperature inside the vial is closer to the desired temperature. In the microchannel, enzyme inactivation occurs at lower temperatures than 353 K (80 ^{0}C). In this system, at 338 K (65 ^{0}C) and residence times of 120 s and 180 s almost no activity is observed. This is a good indication that the whole volume of the enzyme solution has been subjected to the same temperature for the defined residence time in the microchannel, as supported by the simulations.

Both enzymes seem to behave similarly in terms of inactivation at the used temperatures, although a faster inactivation of catalase was to be expected since it is known for being the less stable of the two enzymes [401]. GOx inactivation is known to occur through loss of its co-factor (FAD), which happens around 332 K (59 ^{0}C), followed by loss of conformation above 335 K (62 ^{0}C) (mid-point for loss of secondary and tertiary structure, according to Gouda *et al.* (2003)) [402]. This mid-point of conformation loss may even occur at a lower temperature (328 K (55 ^{0}C)) [403]. The obtained values during the experiments concur with the previous temperatures, since the amount of product at 338 K (65 ^{0}C) is around half of the values obtained at 328 K (55 ^{0}C), and a rapid decrease in activity is observed at 338 K (65 ^{0}C). Catalase, such as GOx, is prone to denaturation for temperatures above 328 K (55 ^{0}C) [404], due to a process of protein denaturation [405], [406] by dissociation of its subunits [401].

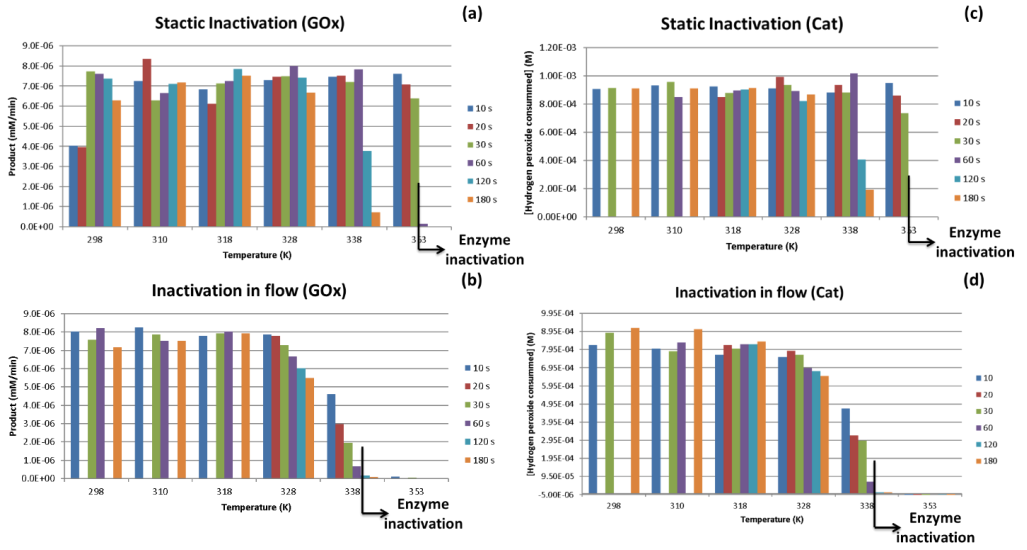

Figure 68- Amount of colorimetric product formation by GOx and hydrogen peroxide consumed by Cat, measured in the spectrophotometer immediately after inactivation in the ThermoMixer ((a) for GOx and (c) for Cat) and microfluidic platform ((b) for GOx and (d) for Cat).

The developed platform is intended for use as an intermediary step between reaction and quantification, and so it should guarantee that the reaction has stopped at the desired residence time before the measurement is performed. Since the measurements executed immediately after inactivation (as it would happen in the modular platform) at 353 K (80 ^{0}C) show no activity for both enzymes, this goal has been achieved.

5.3.3 Characterization of deactivation ability

The developed platform could also be applied as a final step in an enzyme screening platform, depending on enzyme stability, where the inactivated enzyme or reaction mixture could be stored for later use or analysis. To check the stability of the inactivation, whether reversible inactivation or deactivation of the enzymes was achieved in the platform, the activity of the inactivated enzyme solutions was measured after one (Cat) and two days (GOx). The inactivated GOx solutions were added to a 200 mM glucose solution in a 1:1 proportion and the amount of consumed glucose was measured in an HPLC. The measured glucose concentrations in the HPLC for the different samples obtained at the selected temperatures and residence times are presented in Figure 69 (a). Between the measurements at different times in the HPLC, the samples were kept at room temperature (~298 K (25 ^{0}C)) stored inside the device's sampler unit. As can be observed in Figure 69 (a), the samples pumped through the microfluidic system consumed less than 10 mM of glucose after 1 and 2 days, while the samples inactivated in the ThermoMixer, consumed almost all the present glucose. This may indicate that a partial irreversible denaturation of GOx occurs in the microfluidic platform, while in the ThermoMixer the enzyme is able to return to the active state after exposure to the inactivation temperatures and used residence times. It is also possible to notice that the samples inactivated in the ThermoMixer at 298 K (25 ^{0}C) and 310 K (37 ^{0}C), especially at the shorter residence times, present a higher overall variability between them. This might be related to the non-uniform distribution of observed temperature in the simulations performed for the 4-mL vial at the shorter residence times.

In the results presented in Figure 69 (a), significant deactivation of GOx is observed for all the inactivation and residence times tested, even for temperatures below the temperature where FAD dissociation occurs (332 K (59 ^{0}C), according to Gouda *et al.* (2003)) [402]). So, the observed GOx deactivation (at temperatures lower than 332 K (59 ^{0}C)) may indicate that other phenomena, besides temperature, are involved in the loss of conformation (e.g. hydrophobic interactions with channel walls). On the other hand, Zoldák *et al.* (2004) observed that irreversible denaturation of GOx occurred if the enzyme solution was immediately cooled to 293 K (20 ^{0}C) upon inactivation at 328 K (55 ^{0}C). Zoldák *et al.* (2004) also observed that dissociation of the co-factor and of the protein dimer occurred after the inactivation rate limiting step [403]. This may explain in part the observed deactivation for the temperatures below 328 K (55 ^{0}C), but other phenomena might be involved in the extent of detected denaturation, since no significant difference is observed between the different inactivation temperatures tested in terms of glucose consumption.

The inactivated catalase solutions were kept at room temperature overnight and consumption of hydrogen peroxide was measured in the spectrophotometer the following day (Figure 69 (b)). As shown in Figure 69 (b), the samples presented a regain of activity for samples

inactivated at temperatures up to 318 K (45 ^{0}C), and loss or even no activity for samples inactivated at higher temperatures for 180 s.

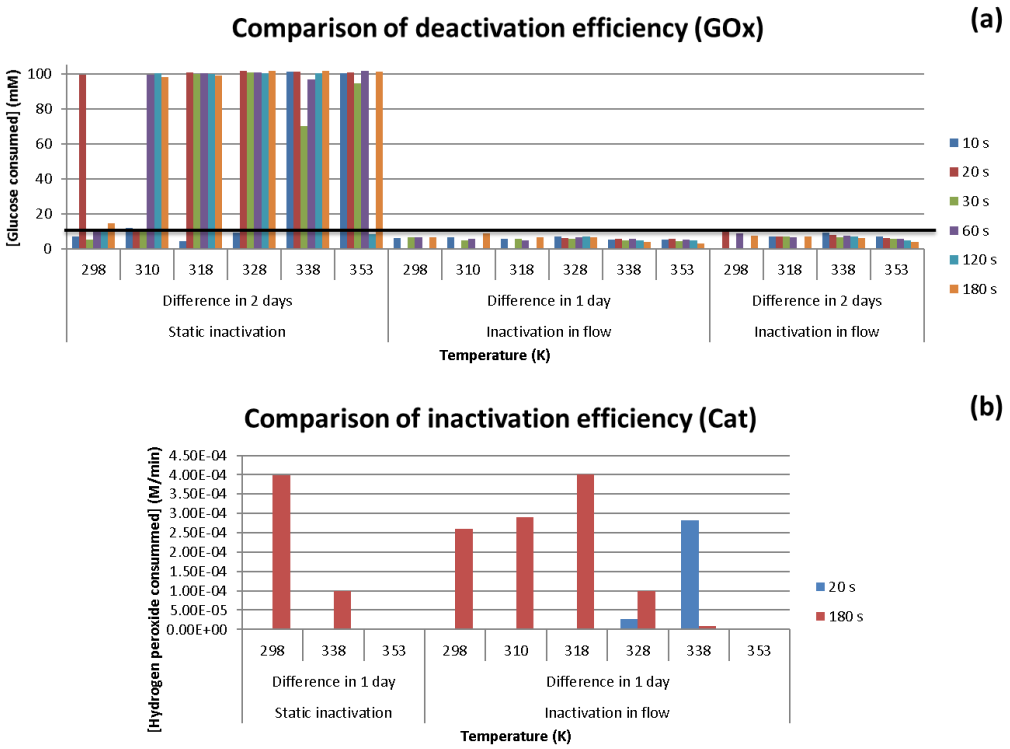

Figure 69 – Substrate consumed by the static and in flow inactivated enzymes (GOx (a) and Cat (b) after 1 and 2 days. The black line represents the maximum value of glucose (a) consumed by the enzyme solutions inactivated in the microfluidic system. Samples of 20 s inactivation times were only measured for the higher temperatures (328 K (55 ^{0}C), 338 K (65 ^{0}C) and 353 K (80 ^{0}C)) used in the microfluidic thermal inactivation platform.

Activity of catalase pumped through the microfluidic system is lower for 338 K (65 ^{0}C) and 353 K (80 ^{0}C) than the one inactivated in the ThermoMixer, since some substrate consumption was measured for the latter samples. The occurrence of deactivation in both systems might be related to the already mentioned lower stability of catalase relative to glucose oxidase, thus translating into a smaller difference in deactivation between the two inactivation strategies. Furthermore, the samples from catalase solutions from both inactivation systems formed agglomerates overnight, especially for the higher residence time (180 s) and inactivation temperatures (338 K (65 ^{0}C) and 353 K (80 ^{0}C)), as presented in Figure 70. Agglomeration of protein indicates loss of conformation due to denaturation of enzymes, and thus enzymatic deactivation, which is consistent with the very low substrate consumption measured for these conditions. Catalase deactivation associated with protein aggregation is a known phenomenon [407].

Nevertheless, for both enzymes, a decrease in enzyme activity is observed with increasing temperature and a significant difference in substrate consumption between the samples

inactivated in the ThermoMixer and in the microfluidic platform was obtained. The observed deactivation phenomenon seems to depend on the type of enzyme, since GOx deactivation occurred mainly in the microchannel at all the used temperatures (possibly due to hydrophobic interactions with the channel), while catalase deactivation occurs mainly due to the effect of temperature. However, for both enzymes, a high degree of deactivation for the duration of the assay was observed.

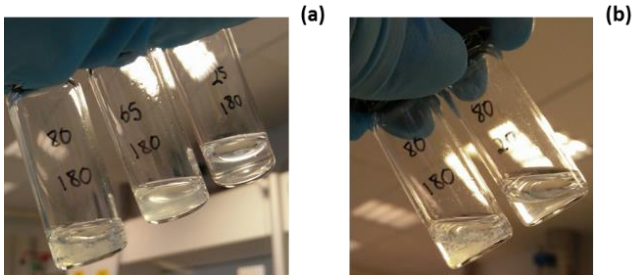

Figure 70 – Photographs showing the formation of agglomerates in inactivated catalase samples after 1 day at room temperature for different inactivation temperatures at the longest residence time (a) and at different residence times at the highest inactivation temperature (b).

The observed (partial) deactivation for both enzymes in the microfluidic system could be influenced by other factors such as the closer proximity of the microfluidic transported enzyme to the heat source (steel plate forming the bottom of the channel) and considerably faster heat transfer to the solution (0.6 s instead of 161 s according to the simulations). The microfluidic system also provides an environment with a more uniform distribution of temperature and time controlled exposure to the desired inactivation temperature, which might contribute to less variability in the measured data and a higher denaturation (resulting in a high degree of aggregation in the case of catalase). Also, the presence of air/vapor bubbles in the fluid, especially at the higher temperatures (338 K (65 ^{0}C) and 353 K (80 ^{0}C)) can contribute to higher denaturation of the enzymes in the microfluidic channel. Proteins are sensitive to the interaction with air/liquid interfaces, which are known as a major cause of enzyme denaturation, due to exposure of hydrophobic regions and increasing protein-protein interactions, as well as adsorption of the proteins to the interface, which in turn may lead to enzyme aggregation [408], [409]. Furthermore, the platform has a layer of double sided adhesive tape between the steel bottom plate and the channel polycarbonate plate, thus forming part of the walls of the channel. During fluid flow the enzyme may have been exposed to residues of adhesive from this tape, which could further contribute to denaturation. However, since the two enzymes performed differently when pumped inside the system (aggregation in the case of catalase but not glucose oxidase, for example), this is probably not a significant factor.

Deactivation at high temperatures occurs through a mix of conformational changes and covalent process [410]. If no covalent bonds are formed or are formed to a small extent, only denaturation occurs and full functional activity could be regained using one of the strategies previously mentioned in the introduction. In this work, no special enzyme treatment was applied to induce reactivation, except placing the enzyme at room temperature after the inactivation, since the goal was to achieve enzyme inactivation. However, the capability to

control both inactivation and reactivation, especially in a continuous format is very interesting in terms of potential applications, and could be tested using the presented platform.

The described system may not allow heating and cooling rates as fast as some other technologies presented in the introduction (e.g. MW heating), but offers a simpler setup and easier integration with other modules. The used Peltier elements can be easily substituted if a wider range of temperatures is required, and together with the integrated PT 1000 sensor, provide a good control of the applied temperature. Integration is facilitated by using standard inlet finger tight connectors, but also by designing the meander channel with dimensions compatible with most commercial microfluidic systems. Furthermore, the inclusion of two channels with different lengths increases the flowrate range and thus the number of different inactivation times possible for the platform, further increasing its flexibility towards different reactor or sensing modules.

5.3.4 Other considerations

The specific application for which the thermal inactivation platform presented here was developed, was to achieve inactivation of the reaction mixture coming from the silicon meander channel so as to perform online quantification of glucose with the glucose electrochemical sensors integrated in the platform presented in Chapter 4. Due to time constraints, however, the final integration of all these platforms was not possible. Nonetheless, it should be highlighted that inactivation of both enzymes (GOx and catalase) could be achieved within the flowrates used in the silicon meander channel (between 0.125 and 2 $\mu L\ s^{-1}$). Furthermore, the solutions should cool rapidly to a temperature close to room temperature, especially if dilution of the inlet solution would be applied, thus not significantly affecting the integrated sensors. However, tests with the integrated platforms would need to be performed in order to validate this hypothesis. In the case when cooling had not proceed at sufficient speed, due to the reaction being already stopped, a longer outlet tubing, connecting the thermal inactivation and the quantification platforms, could be used to guarantee the reaction mixtures are always at similar temperatures during quantification.

5.4 Conclusion

The presented thermal inactivation platform is capable of achieving fast inactivation of mesophilic enzymes, such as glucose oxidase and catalase. Inactivation is achieved in this system at temperatures around the mid-point of inactivation at relatively long exposure time (120 s at 338 K (65 ^{0}C)) or at a higher temperature in a duration compatible with continuous inactivation of enzymes coming from a reactor module (20 s at 353 K (80 ^{0}C)). Furthermore, partial deactivation of both enzymes is achieved in the system, which may enable the control of enzyme inactivation at the outlet of the platform and thus guarantee sample storage with the enzyme(s) without the reaction proceeding significantly. The developed continuous thermal inactivation platform has an improved performance relative to the standard inactivation method at laboratory scale, a benchtop ThermoMixer, since inactivation is achieved faster for both enzymes and with a lower residual activity. The characterization of temperature

distribution and heating efficiency of both inactivation methods by using computational fluid dynamics, also showed a faster heating rate and uniform temperature distribution for the developed microfluidic system. The simulations also demonstrate that the introduced fluid is heated to the inactivation temperature within 3 mm of the channel length for all the experimental flow velocities. The assumed inactivation times can thus be considered as close to the real inactivation exposure times that the enzymes experienced.

Control of the reactivation process could be a further advantage with this system. If a solution with denaturant agents is added to the enzyme upon collection at the outlet or by coupling with another microchannel, formation of covalent bonds and thus irreversible enzyme denaturation, can be avoided. The continuous enzymatic thermal inactivation system could also be used to perform reactions at well-controlled temperatures, allowing introduction or removal of reaction components through the secondary channel. The platform could be further applied for the characterization of enzyme activity at different temperatures, by coupling the system with an online sensor for a reaction product, or even a camera if a colorimetric assay is used, since the system is transparent. By inverting the position of the Peltier elements, in order to achieve temperatures below ambient temperature or even temperatures below 273 K (0 ^{0}C), characterization of psychrophilic enzymes could be performed. On the other hand, by changing the Peltier elements to other thermoelectric modules with a wider temperature difference between the cool and the hot side, characterization of thermophilic enzymes could also be attained, thereby greatly extending the applicability of this module.

Chapter 6

Project outcome and future perspectives

As mentioned in this thesis, there is an increasing need for fast, comprehensive and high-throughput platforms for the screening and characterization of biocatalysts that can provide a high information output. Despite the constantly developed creative and multiplexed microfluidic approaches, the achieved high-throughput capabilities still fall short of the required. Microfluidics can still not compete with the high-throughput requirements provided by microtiter plates and standard analytical equipment, such as HPLC and GC. Nevertheless, microfluidic systems can significantly accelerate the screening phase of process development by simplifying intermediary screening and characterization steps.

This simplification can be achieved through the fabrication of generic microfluidic modules, which can integrate different sensing methods or accommodate a wide range of concentrations of the target analyte. Another approach is the use of a general sensor, e.g. oxygen or pH, to quickly compare different catalysts before proceeding to a more detailed characterization or to be used as a complement to the characterization achieved with benchtop analytical equipment. Furthermore, the automation and parallelization of such systems would allow an operator-free performance of these simplified approaches. Both strategies were investigated in more detail in Chapter 4 and Chapter 3, respectively.

Acceleration of screening could be further increased through the combination of such simple automated quantification and monitoring chips with sorting modules, such as the ones described in Chapter 1. A higher amount of data could thus be gathered from the parallelized online monitoring, but also a collection of optimal biocatalysts would simultaneously be obtained. Interconnectivity between the different systems could even result in an iterative selection of the optimal biocatalyst or operational conditions, by (re)submitting the sorted optimal catalysts to a narrower set of process parameters. An example of such strategy has been applied in droplet-based directed evolution, as mentioned in the introduction of Chapter 3. CFD models, similar to the one presented in Chapter 2, as well as mechanistic models could be linked with sensor data, thus providing in-depth understanding of reaction kinetics and the biocatalysts' window of operation.

However, such endeavor can only be achieved if standardized microfluidic designs and connections are offered and applied. An effort to share designs of microfluidic structures should be made, similar to current attempts at sharing and/or facilitating access to developed mathematical and mechanistic models. For the latter, this has resulted in effortless incorporation and application of different models, even when developed in different computational languages. However, unlike mathematical models, the outcome and combination of microfluidic designs can vary greatly with the fabrication technique, especially its resolution, and/or materials available. Hence, careful selection of the fabrication technology and assembly method has to be made in order to ease device validation and modular application.

In this thesis, a small contribution to such vision is presented in the form of three microfluidic systems with different functions: online reaction monitoring with oxygen sensors in a microreactor, sensor integration with *in situ* sample dilution in a quantification module, and thermal enzyme inactivation module.

The microreactor module was applied to two different types of biocatalysts, an enzyme in solution and a whole cell catalyst, demonstrating the flexibility of this microdevice in terms of sample material. The chosen case-studies also allowed demonstrating this microreactor's applicability to different types of study performed during a bioprocess screening phase: characterization of reaction kinetics and operation window (Chapter 2) and comparison of a desired property, such as oxygen consumption rate (Chapter 3).

The former study (Chapter 2) was performed with the help of a computational fluid dynamic model, demonstrating the usefulness and capabilities provided by the association of data acquisition with a reaction model, in terms of attaining increased knowledge on the reaction. The performance of this model would be significantly improved by combination with a mechanistic model, where different reaction mechanisms, kinetic constants, side or competitive reactions, deactivation models and/or thermodynamic parameters could be defined, enabling an iterative and automated optimization of the reaction parameters. Such a model could thus contribute with added insight into an unknown reaction mechanism besides the empirical knowledge gained from the experimental data. The use of mathematical and fluidic models can considerably improve the accuracy of a mechanistic model as well as enable the prediction of properties of a certain biocatalyst or of its behavior in the presence of a given substrate, based on previous empirical knowledge obtained at a different set of operational conditions and/or with similar biocatalysts.

In the second case-study (Chapter 3), different biocatalysts were screened in terms of oxidation rate (the target property) for the same reference substrate. It would be also possible to apply such strategy in the microreactor system, but to the characterization of a biocatalyst with different and more industrially relevant substrates. This would require the use of a multi-entry valve system (to introduce a metered volume of the different tested substrates) coupled with a mixing system in case the reaction dynamics are slower than the ones measured in the case presented in Chapter 3. Solvent resistant materials would have to be used in the valve system, tubing and mixer used, but the presented designs for the commercial polymeric valve (Chapter 2) and for the mixing/dilution unit (Chapter 4) could still be applied.

The platform for sensor integration with *in situ* sample dilution (Chapter 4) has been successfully used for a long period of time (up to 12 h) with two different screen-printed electrochemical glucose sensors, capable of quantifying diluted glucose solutions. The chosen materials (PMMA and double sided adhesive tape) and fabrication method (laser ablation), enabled a fast prototyping cycle from design to use. New chamber sizes and geometries can thus be easily implemented in the microchip design, if differently sized or shaped sensors are required. However, the improvement of the sensing chamber design towards a slip-in/slip-off type of sensor port would result in a more practical device.

Validation of the mixing/dilution unit was performed by comparing data from the integrated sensors and HPLC measurements at the output. The influence of flow velocity inherent to this type of sensors, due to the laminar flow conditions and membrane over the sensing element, was taken into account considering the previously performed in-flow calibration curves. Quantification by these sensors can be refined by tailoring the chambers' dimensions or even separating the dilution and the quantification units. The platform's performance may be further improved if electrochemical sensors with direct analyte detection are used. In this case, by operating at higher sample dilutions (and thus high flowrates), a minimum diffusion layer, as well as minimal influence of flow velocity, may be achieved. The same can be accomplished by decreasing the height of the chambers resulting in a higher velocity on the sensor surface for the same applied flowrates.

The platform presented in Chapter 4 may also serve as a microreactor module with a two-point monitoring. The two integrated sensors could, in such case, be used to quantify the substrate at the inlet and at the outlet of the microreactor, providing direct product quantification as long as reaction stoichiometry and compound interactions are known. Alternatively, the first sensor could present exact substrate quantification at the inlet, while the second sensor would quantify the product or a side-product at the outlet. The latter strategy would be extremely useful for cascade systems requiring spatial separation of the reactions involved, and in situations where the substrate of the reaction occurring in the module is the product of a previous reaction. Moreover, depending on the integrated sensor and on its functionalization, more than one reaction compound could thus be monitored.

Another possible application for the developed quantification/dilution platform is as an in-flow labeling unit, by enabling a good contact between the two introduced streams, as well as by tailoring the provided amount of each stream. Further tests, possibly aided by the already developed CFD model for this mixing/dilution unit, should be performed to assess the efficiency of the platform as a labeling unit.

The thermal inactivation platform (Chapter 5) allowed to take full advantage of the fast heat transfer occurring at microscale, resulting in the inactivation of two different enzymes in flow within 20 s at a relatively high temperature (80 ºC). Denaturation of part of the enzymes in solution was also achieved within this very short interval, suggesting that control of the type of inactivation, may also be possible with this system by better studying the relationship between exposure time and inactivation temperature, and denaturation, as well as the percentage of irreversibly inactivated enzymes in the process. Furthermore, if upon collection at the outlet or by coupling with another microchannel, a solution with denaturing agents is added to the enzyme, formation of the covalent bonds resulting in enzyme denaturation may be avoided, and a better control of inactivation reversibility be attained.

This system may also be used to perform reactions at well-controlled temperatures, allowing introduction or removal of reaction components through the secondary channel. The platform could then be further applied to the characterization of enzyme activity at different temperatures, by coupling the system with an online sensor for a reaction product, such as the quantification platform described in Chapter 4.

Activity studies of extremophiles at different temperatures may also be possible in the developed platform simply by changing the integrated Peltier elements. The electronic circuit

established can hence be changed in order to allow a fast switch between different thermoelectric modules to increase the applicability of the platform.

Both platforms presented in Chapters 4 and 5 are simple to fabricate, using low cost and accessible materials, have a design and concept compatible with mass production and are re-usable, which further lowers their overall cost. Their characteristics, together with the biocompatibility of the materials selected, wide application channel design and standardized connections make both platforms good additions to any modular microfluidic-based screening platform.

Finally, even though it was not possible to accomplish it during these past three years, it would be exciting to connect the different modules discussed above and monitor the glucose oxidation with the GOx and catalase cascade reaction system, as initially intended. The application of the developed platforms to such a well-studied reaction system, would allow to validate their modular capabilities and ease of operation, as well as to identify possible operational issues. The validation of the different developed modules operating together would then enable its application to relevant case studies towards eventually establishing it as standard biocatalyst screening tool for laboratory facilities.

Appendix

Appendix I

Summary of all the simulations performed in Chapter 2

Table 1 – Summary of simulation performed assuming an enzyme diffusion coefficient of 6.7×10^{-10} $m^2 s^{-1}$.

Name	[glucose in] (mM)	k_{cat} (s^{-1})	$k_{catalase}$ (s^{-1})	D_{oxygen} (cm^2 s^{-1})	[Oxygen] (mM)				[Gluconic acid] (mM)			[H2O2] (mM)	[Glucose] (mM)		
					Sensor 5 (sim)	Outlet (sim)	Sensor 5 (exp)	Outlet (tube)	Outlet (sim)	Outlet (exp)	Outlet (tube)	Outlet (tube)	Outlet (sim)	Outlet (exp)	Outlet (tube)
5xGOx+94 U/mL	50	250	0.002586	0.00000028	0.002199	0.000530	0.002417212	0.00515362	0.224474	0.6895	0.31147	0.294541	24.7623	24.252	24.67530
		250	0.002586	0.0000028	0.002199	0.000530		0.0262652	0.224474		0.726703	0.636911	24.7623		24.2601
		250	0.002586	2.8E-05	0.002199	0.000530		0.0444744	0.224474		1.09712	0.947414	24.7623		23.8897
5xGOx+830 U/mL		250	0.002586	0.00000028	0.00232907	0.000654703	0.002182663	0.00515363	0.225212	0.777	0.311647	0.294368	24.7616	26.6155	24.67510
		250	0.002586	0.0000028	0.00232907	0.000654703		0.0262653	0.225212		0.726765	0.636838	24.7616		24.26
		250	0.002586	2.8E-05	0.00232907	0.000654703		0.0445108	0.225212		1.09876	0.948593	24.7616		23.888
		500	0.002586	0.00000028	8.15E-05	6.86E-05			0.22527				24.7615		
10xGOx	5	1000	0	0.00000028	1.70E-05	1.69E-05	0.000242486	0.00195692	0.225236	0.241	0.321407	0.299731	2.27336	4.245	2.17719
		250	0	0.00000028	0.0147181	0.00190571		0.00419216	0.225747		0.317202	0.295881	2.27285		2.1814
		1000	0	0.0000028	1.70E-05	1.69E-05		0.0158762	0.225236		0.87839	0.750939	2.27336		1.62021
		250	0	0.0000028	0.0147181	0.00190571		0.0318055	0.225747		0.659268	0.584901	2.27285		1.83933
5xGOx		1000	0	0.00000028	3.68E-05	3.40E-05	0.000307	0.00293761	0.225467	0.623	0.319074	0.298218	2.2731	4.202	2.17949
		250	0	0.00000028	0.102187	0.0755216		0.00620117	0.153634		0.311331	0.290175	2.34505		2.18735
		1000	0	0.0000028	3.68E-05	3.40E-05		0.0218548	0.225467		0.776762	0.67478	2.2731		1.7218
		250	0	0.0000028	0.102187	0.0755216		0.0484365	0.153634		0.514591	0.469225	2.34505		1.98409
1xGOx		1000	0	0.00000028	0.125009	0.102487	0.144863	0.00719884	0.125878	0.236	0.305889	0.285745	2.37283	6.111	2.19282
		250	0	0.00000028	0.198304	0.19209		0.115585	0.0330976		0.136845	0.127197	2.46560		2.36185
		1000	0	0.0000028	0.125009	0.102487		0.0571119	0.125878		0.455071	0.419137	2.37283		2.04364
		250	0	0.0000028	0.198304	0.19209		0.149533	0.0330976		0.13842	0.12854	2.46560		2.36028
5xGOx+94 U/mL+0.25 mM H2O2	50	250	0.002586	0.00000028	0.017552	0.00712544	0.044547623		0.206827	1.1885			16.3729	16.83	
		250	0.02586	0.00000028	0.0177466	0.0073167			0.207395				16.3723		
		250	0.2586	0.00000028	0.0196618	0.00920078			0.213091				16.3665		
		250	2.586	0.00000028	0.0359201	0.02513			0.257232				16.3225		
		250	2.586	0.00000028	0.0539291	0.0411364		0.00616504	0.235065		0.386954	0.2792	16.34470		16.19280
		250	2.586	0.0000028	0.0539291	0.0411364		0.0325052	0.235065		0.72934	0.572979	16.34470		15.8504
		250	2.586	2.8E-05	0.0539291	0.0411364		0.0539711	0.235065		0.964063	0.774477	16.34470		15.6157
		250	25.86	0.00000028	0.0816688	0.0630347			0.352193				16.2276		
		250	25.86	0.00000028	0.109029	0.091745			0.297937				16.28180		
		250	0.002586	0.00000028	0.0305797	0.01624		0.00616265	0.198319		0.298135	0.364499	16.38140		16.28160

Name	[glucose in] (mM)	k_{cat} (s^{-1})	$k_{catalase}$ (s^{-1})	D_{oxygen} ($cm^2\ s^{-1}$)	[Oxygen] (mM)				[Gluconic acid] (mM)			[H2O2] (mM)	[Glucose] (mM)		
					Sensor 5 (sim)	Outlet (sim)	Sensor 5 (exp)	Outlet (tube)	Outlet (sim)	Outlet (exp)	Outlet (tube)	Outlet (tube)	Outlet (sim)	Outlet (exp)	Outlet (tube)
5xGOx+830 U/mL+0.25 mM H2O2	50	250	0.002586	0.00000028	0.0177466	0.00731667	0.097672507		0.207426	1.259			16.3723	16.896	
		250	0.02586	0.00000028	0.0196619	0.00920035			0.213151				16.3665		
		250	0.2586	0.00000028	0.03592	0.0251271			0.257197				16.3225		
		250	2.586	0.00000028	0.0816687	0.0630346			0.352193				16.2276		
		250	2.586	0.00000028	0.0720164	0.05344		0.00616887	0.370598		0.542897	0.123515	16.20920		16.03690
		250	2.586	0.0000028	0.0720164	0.05344		0.0325512			0.870866	0.430325	16.20920		15.7089
		250	2.586	2.8E-05	0.0720164	0.05344		0.0540937			1.10544	0.630947	16.20920		15.4744
		250	25.86	0.00000028	0.0913324	0.0678447			0.376219				16.2036		
		250	25.86	0.00000028	0.120446	0.0992354			0.313119				16.26670		
		250	0.002586	0.00000028	0.0143212	0.0052831		0.00616263	0.209289		0.298431	0.363611	16.37050		16.2814
5xGOx+940 U/mL+830 U/mL		250	0.002586	0.00000028	0.0176895	0.00726546	0.029340463		0.207075	0.6445			16.3726	16.1065	
		250	0.02586	0.00000028	0.019103	0.00869773			0.209803				16.3699		
		250	0.2586	0.00000028	0.0314163	0.0210636		0.0052114	0.231868		0.3414	0.243474	16.3478		16.23830
		250	0.2586	0.0000028	0.0314163	0.0210636		0.0273886	0.231868		0.741156	0.574505	16.3478		15.8385
		250	0.2586	2.8E-05	0.0314163	0.0210636		0.0467426	0.231868		1.06195	0.845477	16.3478		15.5177
5xGOx+830 U/mL+830 U/mL		250	0.002586	0.00000028	0.0178313	0.00740237			0.207542				16.3722		
		250	0.02586	0.00000028	0.020451	0.00999427			0.21443				16.3652		
		250	0.2586	0.00000028	0.0391728	0.0279015		0.00521236	0.260736		0.386154	0.19948	16.3189		16.19350
		250	0.2586	0.0000028	0.0391728	0.0279015		0.0273981	0.260736		0.77908	0.535414	16.3189		15.8006
		250	0.2586	2.8E-05	0.0391728	0.0279015		0.0468004	0.260736		1.09988	0.806264	16.3189		15.4798
5xGOx+940 U/mL+H2O				0.00000028	0.0302236	0.0191952	0.00203		0.248468	0.5575			16.3313	14.9535	
		250	0.002586	0.00000028	0.0175462	0.00711969		0.0061626	0.20683		0.297559	0.28131	16.3729		16.28220
		250	0.002586	0.0000028	0.0175462	0.00711969		0.0324827	0.20683		0.651915	0.577096	16.3729		15.9278
		250	0.002586	2.8E-05	0.0175462	0.00711969		0.0539384	0.20683		0.894593	0.784894	16.3729		15.6851
5xGOx+830 U/mL+H2O				0.00000028	0.0544072	0.0394311	0.01114		0.32448	0.779			16.25530	16.586	
		250	0.002586	0.00000028	0.0307588	0.0164246		0.00616267	0.19868		0.29883	0.2805	16.38110		16.2810
		250	0.002586	0.0000028	0.0307588	0.0164246		0.032483	0.19868		0.652285	0.575679	16.38110		15.9275
		250	0.002586	2.8E-05	0.0307588	0.0164246		0.0539963	0.19868		0.89525	0.783658	16.38110		15.6845

Name	[glucose in] (mM)	k_{cat} (s^{-1})	$k_{catalase}$ (s^{-1})	D_{oxygen} ($cm^2\ s^{-1}$)	[Oxygen] (mM)				[Gluconic acid] (mM)			[H2O2] (mM)	[Glucose] (mM)		
					Sensor 5 (sim)	Outlet (sim)	Sensor 5 (exp)	Outlet (tube)	Sensor 5 (sim)	Outlet (sim)	Sensor 5 (exp)	Outlet (tube)	Sensor 5 (sim)	Outlet (sim)	Sensor 5 (exp)
1xGOx+830U/mL	50	250	0.002586	0.00000028	0.123499	0.103842	0.018839168		0.124091	0.8075	0.311031	0.292265	24.8628	23.9285	
		500	0.002586	0.00000028	0.0550014	0.0343572			0.194235				24.7926		
		1000	0.002586	0.00000028	0.0068	0.00226466		0.0058587	0.22412				24.7627		24.67580
		1000	0.002586	0.0000028	0.0068	0.00226466		0.0299016			0.691043	0.607828	24.7627		24.2958
		1000	0.002586	2.8E-05	0.0068	0.00226466		0.0497915			0.993768	0.863798	24.7627		23.9931
0.5xGOx+830U/mL		250	0.002586	0.00000028	0.170349	0.158484	0.034514333		0.0678416	0.594			24.9191	21.2758918 9	
		500	0.002586	0.00000028	0.123513	0.10386			0.124076				24.8628		
		1000	0.002586	0.00000028	0.0550182	0.0343718		0.00914674	0.194226		0.304638	0.28605	24.7927		24.68230
		1000	0.002586	0.0000028	0.0550182	0.0343718		0.0455332			0.567002	0.509069	24.7927		24.4199
		1000	0.002586	2.8E-05	0.0550182	0.0343718		0.0700276			0.708898	0.632692	24.7927		24.278
		2000	0.002586	0.00000028	0.00680491	0.00226666			0.22413				24.7627		
1xGOx+830U/mL (3.083 s)	10	1000	0.002586	0.00000028	0.166405	0.154306	0.151596039	0.00441158	0.0741354	0.542094017	0.319164	0.915701	4.80295	3.99182906	4.55792
1xGOx+830U/mL (4.625 s)		250	0.002586	0.00000028	0.202167	0.197252	0.123739242		0.0283068	0.5055			4.9189	4.125	
		500	0.002586	0.00000028	0.180808	0.171247			0.0557999				4.89139		
		1000	0.002586	0.00000028	0.139851	0.122078		0.00673907	0.107655		0.276018	0.25612	4.8395		4.67114
		1000	0.002586	0.0000028				0.0423075			0.393374	0.354443	4.8395		4.55378
		1000	0.002586	2.8E-05				0.0712063			0.430639	0.387505	4.8395		4.51652
		1000	0.258 mM	0.00000028	0.139851	0.122078		0.116221	0.107655		0.461336	0.415415	4.8395		4.485820
1xGOx+830U/mL (6.17 s)		1000	0.002586	0.00000028	0.113286	0.0902762	0.065687257	0.00439839	0.139854	0.554196581	0.320226	0.291006	4.840310	3.42401709 4	4.65994
1xGOx+830U/mL (9.25 s)		250	0.002586	0.00000028	0.17969	0.169183	0.110886788		0.0568452	0.689			4.94054	4.626	
		500	0.002586	0.00000028	0.137673	0.118163			0.109608				4.88779		
		1000	0.002586	0.00000028	0.0644809	0.036992		0.00640897	0.192573		0.312374	0.291037	4.80481		4.68501
		1000	0.002586	0.0000028				0.0409734	0.192573		0.583367	0.523228	4.80481		4.41402
		1000	0.002586	2.8E-05	0.0644809	0.036992		0.0676724	0.192573		0.687105	0.617952	4.80481		4.31028
		1000	0.02586	0.00000028	0.0644809	0.036992		0.00640844	0.192573		0.313999	0.289341	4.80481		4.68338
		1000	0.2586	0.00000028	0.0644809	0.036992		0.00641387	0.192573		0.331242	0.27178	4.80481		4.66614
		1000	2.586	0.00000028	0.0644809	0.036992		0.00643514	0.192573		0.431203	0.16611	4.80481		4.56618
		1000	25.86	0.00000028	0.0644809	0.036992			0.192573				4.80481		

Name	[glucose in] (mM)	k_{cat} (s^{-1})	$k_{catalase}$ (s^{-1})	D_{oxygen} ($cm^2\ s^{-1}$)	[Oxygen] (mM)				[Gluconic acid] (mM)			[H2O2] (mM)	[Glucose] (mM)		
					Sensor 5 (sim)	Outlet (sim)	Sensor 5 (exp)	Outlet (tube)	Sensor 5 (sim)	Outlet (sim)	Sensor 5 (exp)	Outlet (tube)	Sensor 5 (sim)	Outlet (sim)	Sensor 5 (exp)
1xGOx+830U/mL (18.5 s)	10	250	0.002586	0.00000028	0.135475	0.114933	0.026724109		0.111688	0.7965			4.88893	4.506594595	
		500	0.002586	0.00000028	0.060737	0.032526			0.195268				4.80539		
		1000	0.002586	0.00000028	0.00195548	0.000322005		0.00769506	0.225648		0.3742	0.351152	4.77438		4.62583
		1000	0.002586	0.0000028	0.00195548	0.000322005		0.0440309	0.225648		0.876404	0.80383	4.77438		4.12362
		1000	0.002586	2.8E-05	0.00195548	0.000322005		0.0698596	0.225648		1.07163	0.989242	4.77438		3.9284
	200	1000	0.002586	0.0000028	0.000191937	0.000170382	0.001880697	0.0300138	0.225979	1.055	1.09354	0.9802	99.7747	97.42	98.9071
1xGOx+830U/mL (37 s)	10	250	0.002586	0.00000028	0.0594424	0.0307167	0.000508363		0.196589	0.759			4.80357	3.861108108	
		500	0.002586	0.00000028	0.00173098	0.000435421			0.227052				4.77289		
		1000	0.002586	0.00000028	0.000168555	0.000167702		0.00935793	0.227888		0.49605	0.466228	4.77202		4.503860
		1000	0.002586	0.0000028	0.000168555	0.000167702		0.0484676	0.227888		1.40098	1.32291	4.77202		3.59893
		1000	0.002586	2.8E-05	0.000168555	0.000167702		0.0740795	0.227888		1.73353	1.65069	4.77202		3.26638
		1000	0.002586	0.258mM	0.000168555	0.000167702		0.124152	0.227888		2.001460	1.920720	4.77202		2.998440
0.5xGOx+830U/mL (3.083 s)		1000	0.002586	0.00000028	0.194691	0.188432	0.188467169	0.00924474	0.037854	0.542094017	0.302663	0.276023	4.8391500	3.317615385	4.57434
0.5xGOx+830U/mL (4.625 s)		250	0.002586	0.00000028	0.213033	0.21054	0.098479688		0.0142486	0.39027027			4.93297	4.347918919	
		500	0.002586	0.00000028	0.202167	0.197252			0.0283068				4.9189		
		1000	0.002586	0.00000028	0.180814	0.171255		0.0500766	0.0557913		0.217697	0.199536	4.8914		4.72949
		1000	0.002586	0.0000028	0.180814	0.171255		0.0995402			0.236248	0.215034	4.8914		4.71094
		1000	0.002586	2.8E-05	0.180814	0.171255		0.121197			0.241652	0.219645	4.8914		4.70554
		1000	0.002586	0.258mM	0.180814	0.171255		0.171844			0.251127	0.227841	4.8914		4.696060
		2000	0.002586	0.00000028	0.139864	0.122093			0.107639				4.83952		
0.5xGOx+830U/mL (6.17 s)		1000	0.002586	0.00000028	0.166433	0.153406	0.142687313	0.00785836	0.0740057	0.619752137	0.305976	0.279842	4.906260	3.262145299	4.67429
0.5xGOx+830U/mL (9.25 s)		250	0.002586	0.00000028	0.201595	0.196195	0.122764202		0.0288472	0.501702703			4.96854	4.263189189	
		500	0.002586	0.00000028	0.17969	0.169183			0.0568493				4.94054		
		1000	0.002586	0.00000028	0.137687	0.118182		0.0115505	0.109613		0.294546	0.275839	4.88778		4.70285
		1000	0.002586	0.0000028	0.137687	0.118182		0.0692117			0.407869	0.37578	4.88778		4.58952
		1000	0.002586	2.8E-05	0.137687	0.118182		0.0986961			0.431654	0.397702	4.88778		4.56574
		2000	0.002586	0.00000028	0.0645017	0.0370114			0.19255				4.80483		

Name	[glucose in] (mM)	k_{cat} (s^{-1})	$k_{catalase}$ (s^{-1})	D_{oxygen} ($cm^2\ s^{-1}$)	[Oxygen] (mM)				[Gluconic acid] (mM)			[H2O2] (mM)	[Glucose] (mM)		
					Sensor 5 (sim)	Outlet (sim)	Sensor 5 (exp)	Outlet (tube)	Sensor 5 (sim)	Outlet (sim)	Sensor 5 (exp)	Outlet (tube)	Sensor 5 (sim)	Outlet (sim)	Sensor 5 (exp)
0.5xGOx+830U/mL (18.5 s)	10	250	0.002586	0.00000028	0.178541	0.167447	0.04522381		0.0579554	0.642918919			4.94248	4.506594595	
		500	0.002586	0.00000028	0.135475	0.114932			0.111689				4.88892		
		1000	0.002586	0.00000028	0.0607579	0.0325461		0.0118503	0.195248		0.361745	0.340965	4.80541		4.638910
		1000	0.002586	0.0000028	0.0607579	0.0325461		0.0674234			0.663199	0.620755	4.80541		4.33746
		1000	0.002586	2.8E-05	0.0607579	0.0325461		0.0966097			0.734479	0.690435	4.80541		4.26618
	200	1000	0.002586	0.0000028	0.00302871	0.00106401	0.003765649	0.0440333	0.225085	0.849351351	0.905624	0.824982	99.7757	90.54783784	99.0952
	10	2000	0.002586	0.00000028	0.00195815	0.000322326	0.04522381		0.225656	0.642918919			4.7744	4.506594595	
0.5xGOx+830U/mL (37 s)	10	250	0.002586	0.00000028	0.134761	0.113687	0.001961409		0.112622	0.73227027			4.88752	3.861108108	
		500	0.002586	0.00000028	0.0594427	0.0307087			0.19677				4.80332		
		1000	0.002586	0.00000028	0.00173208	0.000434823		0.0138348	0.227053		0.476935	0.452155	4.77291		4.523030
		1000	0.002586	0.0000028	0.00173208	0.000434823		0.0716926			1.05793	1.01258	4.77291		3.94203
		1000	0.002586	2.8E-05	0.00173208	0.000434823		0.100296			1.19305	1.14744	4.77291		3.80691
		1000	0.002586	0.258 mM	0.00173208	0.000434823		0.164194			1.321810	1.275770	4.77291		3.678150

Table 2 – Summary of simulation performed assuming an enzyme diffusion coefficient 4.95×10^{-11} $m^2 s^{-1}$.

Name	[glucose in] (mM)	k_{cat} (s^{-1})	$k_{catalase}$ (s^{-1})	D_{oxygen} (cm^2 s^{-1})	[Oxygen] (mM)				[Gluconic acid] (mM)			[H2O2] (mM)	[Glucose] (mM)		
					Sensor 5 (sim)	Outlet (sim)	Sensor 5 (exp)	Outlet (tube)	Outlet (sim)	Outlet (exp)	Outlet (tube)	Outlet (tube)	Outlet (sim)	Outlet (exp)	Outlet (tube)
5xGOx+94 U/mL	**50**	250	0.002586	0.0000028	0.004500	0.001562	0.002417212		0.224321	0.6895			24.7626	24.252	
		300	0.002586	0.0000028	0.002182	0.000647		0.0236714	0.224793		0.756334	0.658998	24.7621		24.2306
5xGOx+830 U/mL		250	0.002586	0.0000028	0.00463227	0.00168894	0.002182663		0.225131	0.777			24.7618	26.6155	
		300	0.002586	0.0000028	0.00228897	0.000750682		0.0236463	0.225667		0.757894	0.658319	24.7612		24.229
10xGOx	**5**	1000	0	0.0000028	1.71E-05	1.69E-05	0.000242486	0.0158757	0.2256	0.241	0.878573	0.75078	2.27303	2.37098	1.62006
		800		0.0000028	2.28E-05	2.12E-05		0.0174969	0.225696		0.847286	0.727346	2.27294		1.65135
		300		0.0000028	7.87E-03	1.46E-03		0.0286608	0.226627		0.692374	0.609567	2.27204		1.80629
		250		0.0000028	0.0213497	0.00578261			0.223767				2.27491		
5xGOx		1000		0.0000028	1.93E-04	4.18E-05	0.000307	0.0218578	0.226147	0.623	0.777396	0.674732	2.2725	2.62881	1.72125
		800		0.0000028	0.0010407	0.00013662		0.0244739	0.22657		0.740472	0.646673	2.27208		1.75818
		300		0.0000028	0.0845417	0.0561467		0.043213	0.175127		0.55879	0.503513	2.32356		1.9399
		250		0.0000028	0.105514	0.0797485		0.0484454	0.150798		0.514389	0.467745	2.34790		1.984310
1xGOx		1000		0.0000028	0.127604	0.105779	0.144863	0.0572454	0.123737	0.236	0.448572	0.417418	2.37497	2.77336	2.04427
		800		0.0000028	0.145954	0.127883		0.0720098	0.100671		0.389239	0.359482	2.39804		2.10947
		300		0.0000028	0.193949	0.186726		0.141238	0.0390863		0.164075	0.151945	2.45963		2.33464
		250		0.0000028	0.198897	0.192846			0.0326726				2.46604		
5xGOx+94 U/mL+0.25 mM H2O2	**50**	300	0.002586	0.0000028	0.0281441	0.0134121	0.044547623	0.0291318	0.200284	1.1885	0.682862	0.683173	16.3795	16.83	15.8969
		300	0.02586	0.0000028	0.0283588	0.0136368			0.20075				16.379		
		300	0.2586	0.0000028	0.0304678	0.0158485			0.205267				16.3745		
		250	2.586	0.0000028	0.0612789	0.046877		0.0324984	0.22267		0.709173	0.593863	16.35710		15.87060
		300	2.586	0.0000028	0.0481456	0.0345107		0.0291464	0.238977		0.747022	0.615632	16.34080		15.8328
		300	25.86	0.0000028	0.100148	0.0823456		0,0291743	0.309729		0,867044	0,484823	16.27000		15,7127
5xGOx+830 /mL+0.25 mM H2O2		300	0.002586	0.0000028	0.0127715	0.00389953	0.097672507	0.0292902	0.209951	1.259	0.682934	0.674688	15.7812	16.896	15.3082
		300	0.02586	0.0000028	0.014215	0.0052563			0.216055				16.3637		
		300	0.2586	0.0000028	0.0265273	0.0167552			0.263577				16.3162		
		250	2.586	0.0000028	0.0806781	0.0619495			0.347709				16.23210		
		300	2.586	0.0000028	0.0652629	0.0467368		0.0292062	0.376541		0.902097	0.458561	16.20320		15.6776
		300	25.86	0.0000028	0.0751761	0.0501244		0,0292135	0.408895		0,939785	0,418665	16.1709		15,64

Name	[glucose in] (mM)	k_{cat} (s^{-1})	$k_{catalase}$ (s^{-1})	D_{oxygen} ($cm^2\ s^{-1}$)	[Oxygen] (mM)				[Gluconic acid] (mM)			[H2O2] (mM)	[Glucose] (mM)		
					Sensor 5 (sim)	Outlet (sim)	Sensor 5 (exp)	Outlet (tube)	Outlet (sim)	Outlet (exp)	Outlet (tube)	Outlet (tube)	Outlet (sim)	Outlet (exp)	Outlet (tube)
5xGOx+94 U/mL+830 U/mL	50	300	0.002586	0.0000028	0.0161246	0.00564555	0.02934046		0.208044	0.6445			16.3717	16.1065	
		300	0.02586	0.0000028	0.0178383	0.0072091			0.21153				16.2686		
		250	0.2586	0.0000028	0.0403365	0.026896		0.0273881	0.226056		0.739576	0.574807	16.3537		15.84020
		300	0.2586	0.0000028	0.0319829	0.019979		0.0246496	0.234847		0.772379	0.596387	16.3449		15.8074
		300	2.586	0.0000028	0.0667084	0.0467522			0.297733				16.282		
		300	25.86	0.0000028	0.0603778	0.0401005			0.343885				16.2359		
5xGOx+830 U/mL+830 U/mL		300	0.002586	0.0000028	0.0162418	0.00575519	-		0.208534	-			16.3712	-	
		300	0.02586	0.0000028	0.0189374	0.0082311			0.215791				16.364		
		250	0.2586	0.0000028	0.04722324	0.0332728			0.250999				16.3287		
		300	0.2586	0.0000028	0.0374267	0.0248136		0.0246591	0.263936		0.812538	0.555565	16.3158		15.7672
		300	2.586	0.0000028	0.0560496	0.0377804			0.337725				16.242		
		300	25.86	0.0000028	0.0553405	0.036642			0.353575				16.2262		
5xGOx+8300 U/mL+830 U/mL		300	0.002586	0.0000028	0,0174009	0,00685505	-	0,0273845	0,213343	-	0,708459	0,60744	16,3664	-	15,8713
		300	0.2586	0.0000028	0,0502698	0,0347214		0,0274211	0,332305		0,861518	0,449565	16,2474		15,7182
5xGOx+8300 U/mL+830 U/mL		300	0.002586	0.0000028	0,026681	0,0155768		0,0273949	0,250115		0,757055	0,55729	16,3296		15,8227
		300	0.2586	0.0000028	0,0545465	0,0363486		0,0274379	0,352947		0,890457	0,417805	16,2268		15,6893
5xGOx+94 U/mL+H2O		250	0.002586	0.0000028	0.023049	0.00983621	0.00203	0.032484	0.203674	0.5575	0.651221	0.576887	16.3761	14.9535	15.92860
		300	0.002586	0.0000028	0.0159439	0.00548206		0.0291317	0.207743		0.682962	0.601424	16.3720		15.8968
5xGOx+830 U/mL+H2O		250	0.002586	0.0000028	0.0389812	0.0220088	0.01114		0.192456	0.779			16.38730	16.586	
		300	0.002586	0.0000028	0.0282959	0.0135665		0.0291561	0.200668		0.684142	0.600831	16.37910		15.8956
1xGOx+830U/mL	50	250	0.002586	0.0000028	0.122971	0.104066	0.018839168		0.124927	0.8075			24.8621	23.9285	
		500	0.002586	0.0000028	0.0566694	0.0372226			0.192625				24.7944		
		800	0.002586	0.0000028	0.0199434	0.00978666		0.0341833	0.218571		0.654692	0.578412	24.7684		24.3323
		1000	0.002586	0.0000028	0.010126	0.00427456		0.0299261	0.223228		0.692713	0.608249	24.7637		24.2942
0.5xGOx+830U/mL		250	0.002586	0.0000028	0.16973	0.158153	0.034514333		0.0688226	0.594			24.9181	21.27589	
		500	0.002586	0.0000028	0.122985	0.104082			0.124911				24.8621		
		800	0.002586	0.0000028	0.0786935	0.0575224		0.0524642	0.172425		0.52298	0.471712	24.8146		24.464
		1000	0.002586	0.0000028	0.0566852	0.0372363		0.0455968	0.192612		0.568232	0.508978	24.7944		24.4188
1xGOx+830U/mL (4.625 s)	10	1000	0.002586	0.0000028	0.135628	0.120323	0.123739242	0.0422708	0.112382	0.5055	0.397151	0.355216	4.83477	4.125	4.55
		800	0.002586	0.0000028	0.152378	0.139633		0.0539954	0.0915403		0.358973	0.322868	4.85561		4.58818
		1000	0.002586	2.8E-05				0.0710629			0.434502	0.0710629			4.51265
		1000	0.002586	0.258mM				0.116018			0.465327	0.416466			4.48183
		1000	0.002586	0.00000028				0.00668666			0.279051	0.256318			4.6681

Name	[glucose in] (mM)	k_{cat} (s^{-1})	$k_{catalase}$ (s^{-1})	D_{oxygen} ($cm^2\ s^{-1}$)	[Oxygen] (mM)				[Gluconic acid] (mM)			[H2O2] (mM)	[Glucose] (mM)		
					Sensor 5 (sim)	Outlet (sim)	Sensor 5 (exp)	Outlet (tube)	Outlet (sim)	Outlet (exp)	Outlet (tube)	Outlet (tube)	Outlet (sim)	Outlet (exp)	Outlet (tube)
1xGOx+830U/mL (9.25 s)	10	1000	0.002586	0.0000028	0.0678637	0.0416443	0.110886788	0.0410414	0.189395	0.689	0.58434	0.522747	4.80802	4.626	4.41307
		800	0.002586	0.0000028	0.0939903	0.0683461		0.0474617	0.162318		0.533174	0.481557	4.8351		4.46424
		1000	0.002586	0.00000028				0.00641165			0.313749	0.291094			4.68367
		1000	0.02586	0.00000028				0.00640998			0.314317	0.290503			4.6831
		1000	0.2586	0.00000028				0.00641526			0.31983	0.284815			4.67759
		1000	2.586	0.00000028				0.00642076			0.369469	0.232372			4.62795
		1000	25.86	0.00000028				0.00642071			0.430271	0.170503			4.56714
1xGOx+830U/mL (18.5 s)	10	1000	0.002586	0.0000028	0.00413121	0.00067439	0.026724109	0.0440915	0.225515	0.7965	0.877353	0.804566	4.77467	4.506595	4.12283
		800	0.002586	0.0000028	0.0145544	0.00328086		0.0503952	0.223363		0.810222	0.748203	4.77696		4.19010
	200	1000	0.002586	0.0000028	0.000310214	0.000184037	0.001880697	0.030027	0.226084	1.055	1.09504	0.981439	99.7747	97.42	98.9057
		800	0.002586	0.0000028	0.000713418	0.000292282		0.0339027	0.225949		1.03598	0.932958	99.7749		98.9649
		3000	0.002586	0.0000028	5.62E-05	5.61E-05		0.0166885	0.226353		1.34743	1.18718	99.7744		98.6533
1xGOx+830U/mL (37 s)	10	1000	0.002586	0.00000028			0.000508363	0.00935974		0.759	0.49601	0.467076		3.861108	4.504000
		1000	0.002586	0.0000028	0.000169498	0.000167699		0.048538	0.228017		1.4044	1.32623	4.77199		3.59561
		800	0.002586	0.0000028	0.00022917	0.000210349		0.0547717	0.227811		1.29133	1.22478	4.7722		3.70868
		1000	0.002586	2.8E-05				0.0740795			1.73362	1.65079			3.26639
		1000	0.002586	0.258mM				0.124149			2.001350	1.921910			2.998660
0.5xGOx+830U/mL (4.625 s)	10	1000	0.002586	0.0000028	0.178463	0.170113	0.098479688	0.099315	0.0585338	0.39027027	0.238789	0.21597	4.88864	4.347919	4.70838
		800	0.002586	0.0000028	0.187378	0.180608			0.0471474				4.90003		
		1200	0.002586	0.0000028	0.169658	0.15978		0.0830889	0.0697316		0.278539	0.251676	4.87743		4.66862
		1000	0.002586	0.00000028				0.049558			0.219959	0.200271			4.72721
		1000	0.002586	2.8E-05				0.120905			0.244201	0.220587			4.77030
		1000	0.002586	0.258mM				0.17155			0.2537	0.228839			4.69347
0.5xGOx+830U/mL (9.25 s)	10	1000	0.002586	0.0000028	0.139065	0.120117	0.122764202	0.0696285	0.108703	0.501702703	0.408266	0.375346	4.88872	4.263189	4.58916
		800	0.002586	0.0000028	0.155236	0.139528			0.0884519				4.90897		
		1200	0.002586	0.0000028	0.123413	0.101648		0.0588398	0.127917		0.458765	0.419329	4.86951		4.53866

Name	[glucose in] (mM)	k_{cat} (s^{-1})	$k_{catalase}$ (s^{-1})	D_{oxygen} ($cm^2\ s^{-1}$)	[Oxygen] (mM)				[Gluconic acid] (mM)			[H2O2] (mM)	[Glucose] (mM)		
					Sensor 5 (sim)	Outlet (sim)	Sensor 5 (exp)	Outlet (tube)	Outlet (sim)	Outlet (exp)	Outlet (tube)	Outlet (tube)	Outlet (sim)	Outlet (exp)	Outlet (tube)
0.5xGOx+8 30U/mL (18.5 s)	10	1000	0.002586	0.0000028	0.0651115	0.0365112	0.04522381	0.0675538	0.191463	0.642918919	0.662413	0.619873	4.80895	4.506595	4.338
		800	0.002586	0.0000028	0.0917885	0.06388			0.163925				4.83649		
		1200	0.002586	0.0000028	0.0428222	0.0179671		0.0602235	0.20969		0.721808	0.672119	4.79072		4.2786
	200	1000	0.002586	0.0000028	0.00469412	0.00166786	0.003765649	0.0440701	0.224644	0.849351351	0.90679	0.825898	99.7763	90.54784	99.0942
		800	0.002586	0.0000028	0.0101777	0.00415662			0.222311				99.7787		
		1200	0.002586	0.0000028	0.00231592	0.000782312		0.0397884	0.225471		0.957224	0.867905	99.7754		99.0436
		3000	0.002586	0.0000028	0.000121258	0.000112717		0.0241981	0.226217		1.19621	1.0641	99.7746		98.8046
0.5xGOx+8 30U/mL (37 s)	10	1000	0.002586	0.00000028			0.001961409	0.013842		0.73227027	0.476844	0.453028		3.861108	4.523190
		1000	0.002586	0.0000028	0.00251765	0.000513647		0.0718141	0.227061		1.0587	1.0138	4.77297		3.94134
		800	0.002586	0.0000028	0.0112583	0.00210561			0.225353				4.77474		
		1200	0.002586	0.0000028	0.000697572	0.000300875		0.0645182	0.227454		1.1481	1.09523	4.77256		3.85192
		1000	0.002586	2.8E-05				0.100296			1.19309	1.147752			3.80694
		1000	0.002586	0.258 mM				0.164191			1.321700	1.277060			3.678330

Appendix II

Test of assembled silicon meander channel and polymeric valve chip

The assembly of the silicon meander channel and the polymeric valve chip was also evaluated by continuously introducing glucose, while alternatively introducing pulses of Gluzyme (0.2 g L^{-1}) or water. All the solutions were introduced at 0.05 µL s^{-1} (images 1. 2 and 3), 0.2 µL s^{-1} (images 4 and 5) and 0.4 µL s^{-1} (images 7. 8 and 9). Tests with food coloring dye performed only with the valve chip allowed to precisely time when the pulse of Gluzyme solution was introduced in the silicon meander, and are used in the figures below to illustrate the different points in the experiment. The images are numerated according to the order in which the corresponding moment in the graph presented occurs. The same schematics as presented in Chapter 2, section 2.3.2.1 were used.

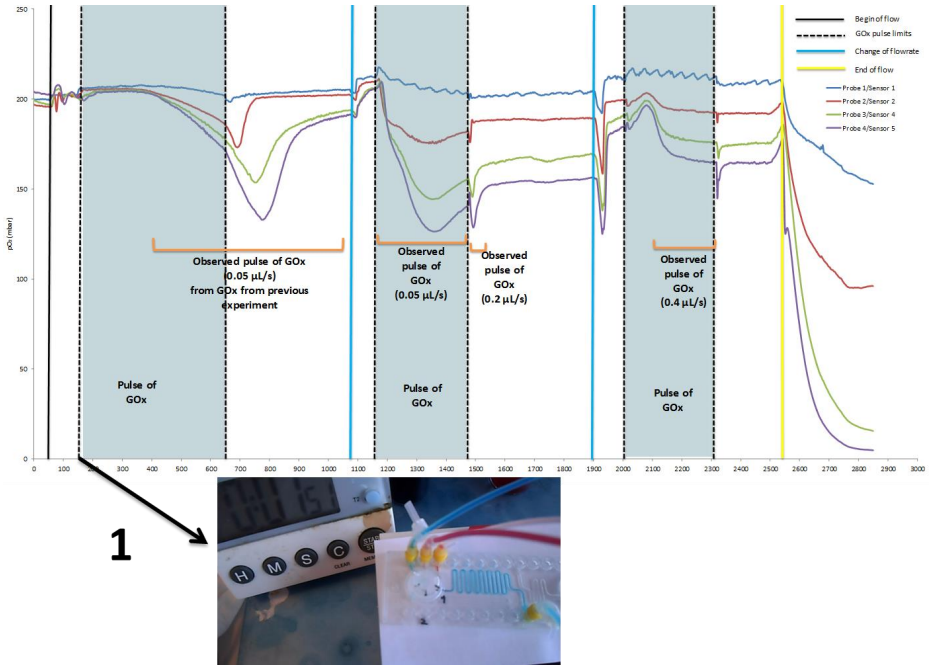

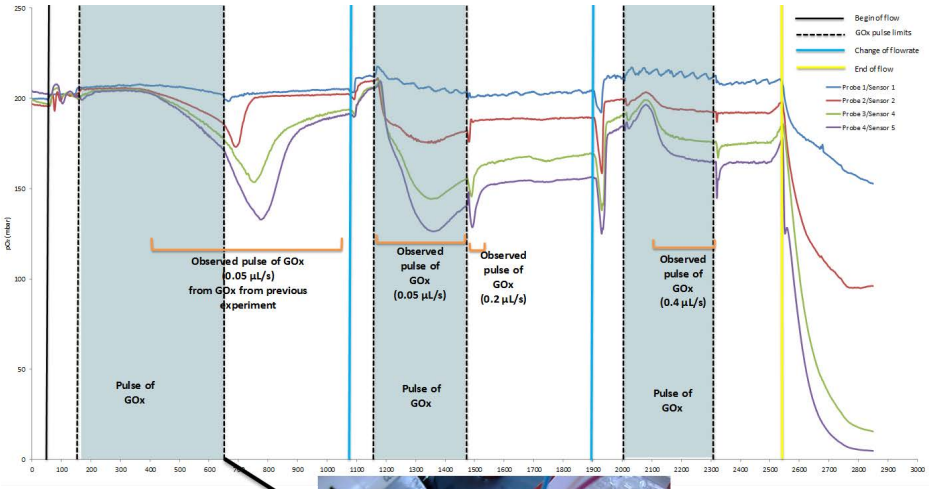

2

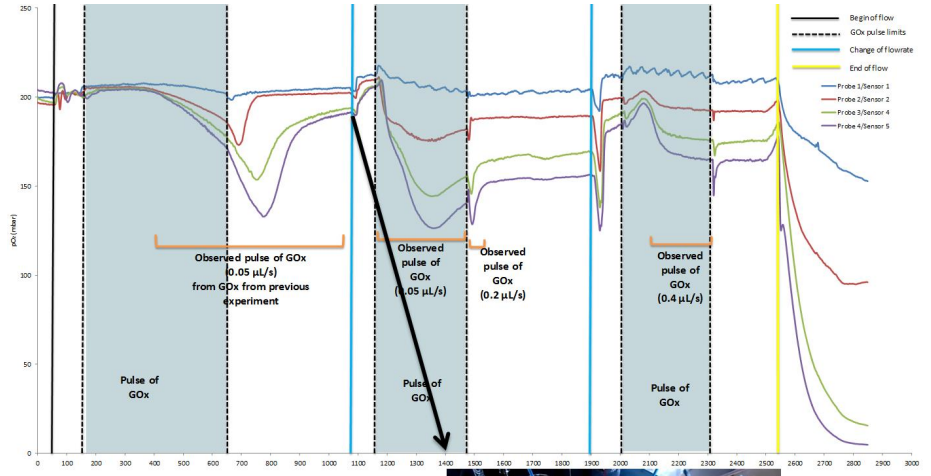

3

Gluzyme in tube connecting to MBR chip has not reached the tube's end and thus, entered MBR chip

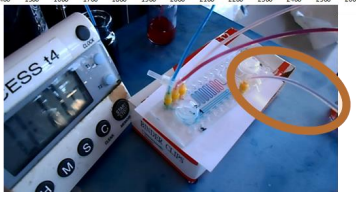

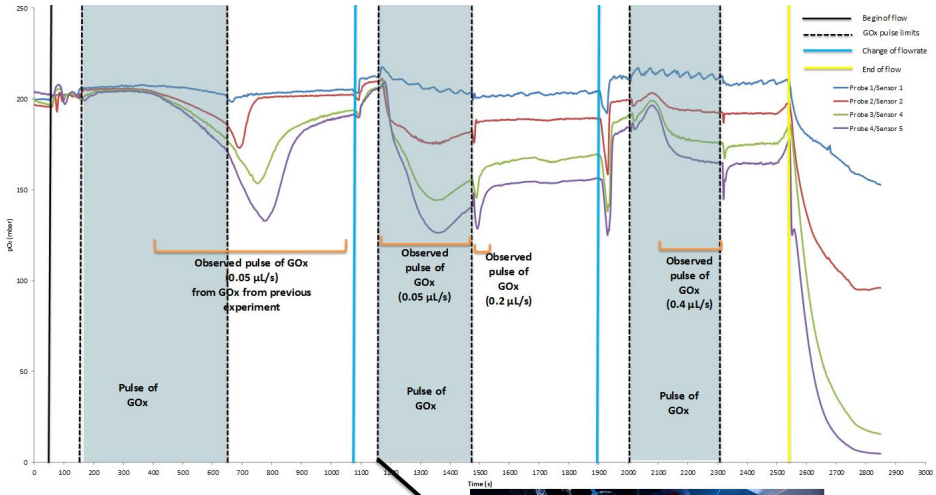

4

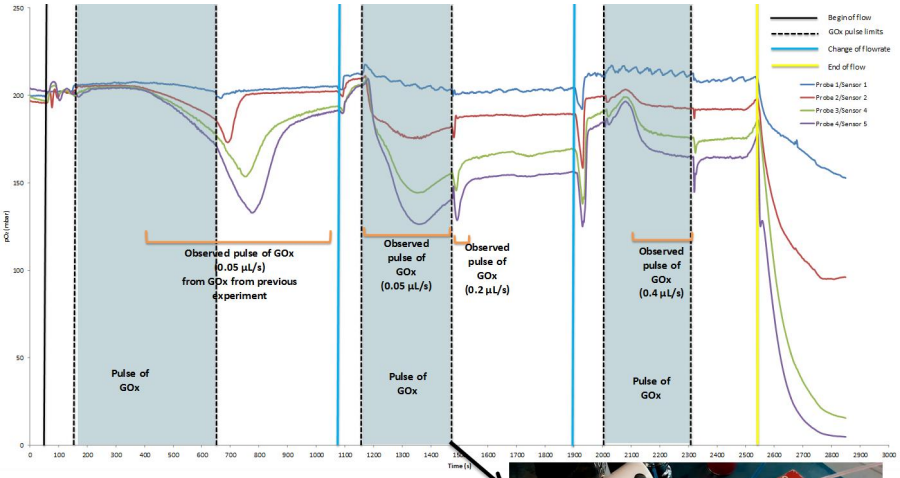

5

Tube connecting to MBR chip is filled with GOx by the end of the pulse

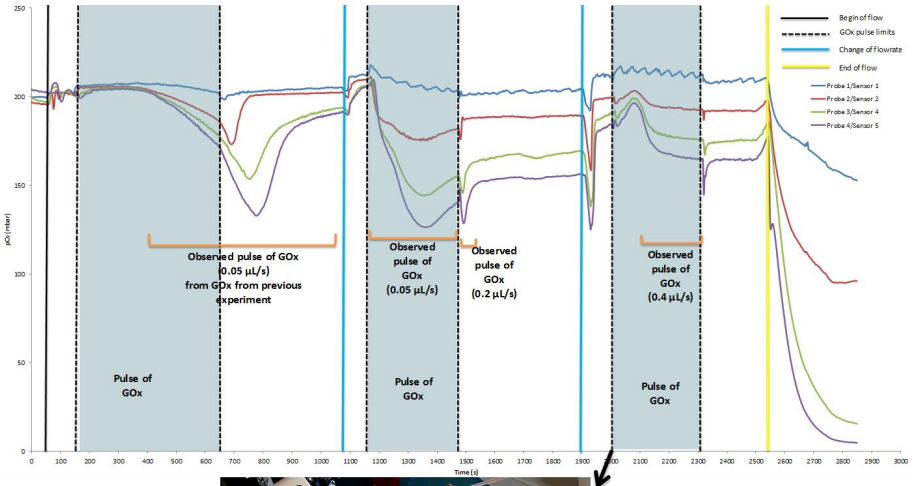
Begin of flow
GOx pulse limits
Change of flowrate
End of flow
Probe 1/Sensor 1
Probe 2/Sensor 2
Probe 3/Sensor 4
Probe 4/Sensor 5
Observed pulse of GOx (0.05 µL/s) from GOx from previous experiment
Observed pulse of GOx (0.05 µL/s)
Observed pulse of GOx (0.2 µL/s)
Observed pulse of GOx (0.4 µL/s)
Pulse of GOx
Pulse of GOx
Pulse of GOx
pO2 (mbar)
Time [s]

6

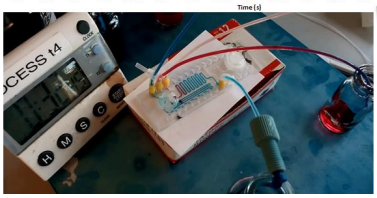

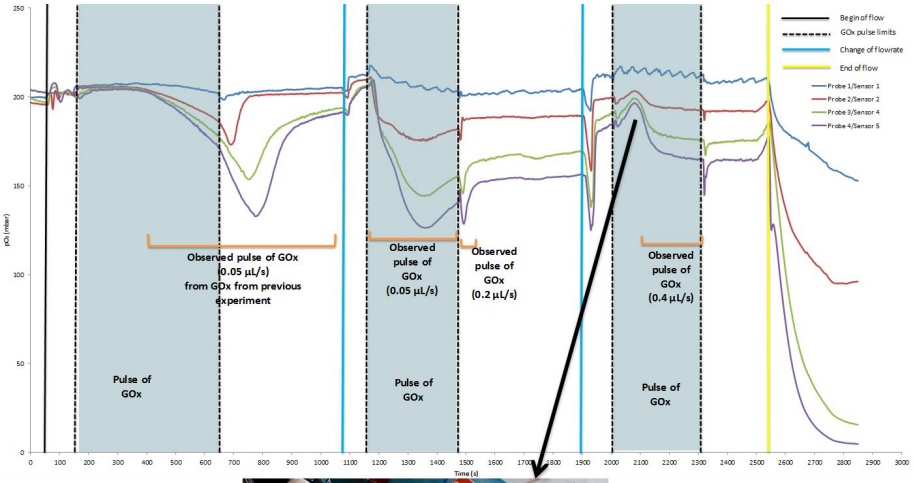
Begin of flow
GOx pulse limits
Change of flowrate
End of flow
Probe 1/Sensor 1
Probe 2/Sensor 2
Probe 3/Sensor 4
Probe 4/Sensor 5
Observed pulse of GOx (0.05 µL/s) from GOx from previous experiment
Observed pulse of GOx (0.05 µL/s)
Observed pulse of GOx (0.2 µL/s)
Observed pulse of GOx (0.4 µL/s)
Pulse of GOx
Pulse of GOx
Pulse of GOx
pO2 (mbar)
Time [s]

7

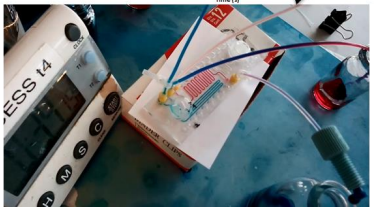

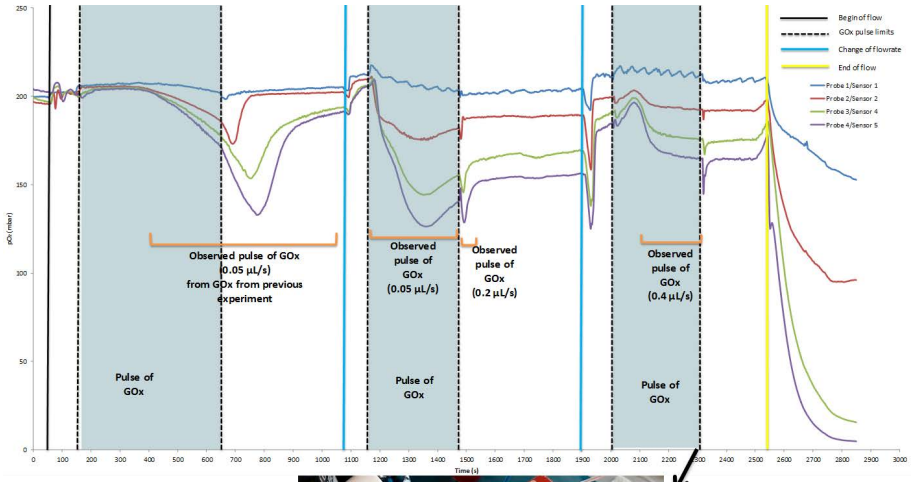

8

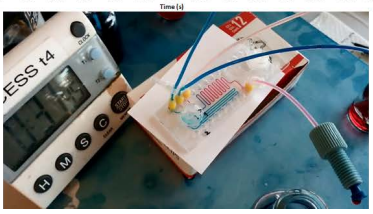

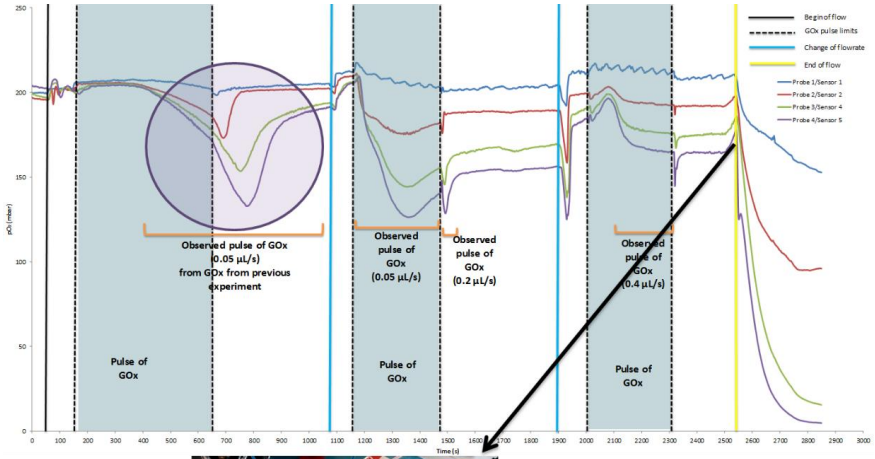

9

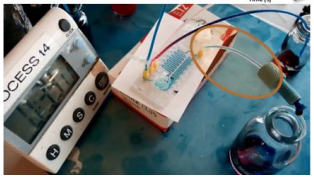

Tube connecting to MBR chip still has GOx (purple at outlet) by the end of the flow

Explains Peak observed in the beggining of flow (is due to Gluzyme from previous experiment)

Appendix III

Table 3 – Domain Physics for meander channel for the simulation *1xGOx+830 U/mL* at 9.95 s.

Domain - Meander	
Type	Fluid
Location	INLET_ASSEMBLY INLET_BLOCKS, PIPE_ASSEMBLY PIPE_BLOCKS, PIPE_ASSEMBLY PIPE_BLOCKS 2, PIPE_ASSEMBLY PIPE_BLOCKS 3, PIPE_ASSEMBLY PIPE_BLOCKS 4, PIPE_ASSEMBLY PIPE_BLOCKS 5, PIPE_ASSEMBLY PIPE_BLOCKS 6
Materials	
Water	
Fluid Definition	Material Library
Morphology	Continuous Fluid
Settings	
Buoyancy Model	Non Buoyant
Domain Motion	Stationary
Reference Pressure	1.0000e+00 [atm]
Additional Variable	Catalase
Kinematic Diffusivity	4.9500e-11 [m^2 s^-1]
Option	Transport Equation
Additional Variable	GOx
Kinematic Diffusivity	4.9500e-11 [m^2 s^-1]
Option	Transport Equation
Additional Variable	Gluconolactone
Kinematic Diffusivity	6.7000e-10 [m^2 s^-1]
Option	Transport Equation
Additional Variable	Glucose
Kinematic Diffusivity	6.7000e-10 [m^2 s^-1]
Option	Transport Equation
Additional Variable	H2O2
Kinematic Diffusivity	2.1000e-09 [m^2 s^-1]
Option	Transport Equation
Additional Variable	Oxygen
Kinematic Diffusivity	2.1000e-09 [m^2 s^-1]
Option	Transport Equation
Turbulence Model	Laminar
Domain Interface - Domain Interface 1	
Boundary List1	Domain Interface 1 Side 1
Boundary List2	Domain Interface 1 Side 2
Interface Type	Fluid Fluid
Settings	
Interface Models	General Connection
Mass And Momentum	Conservative Interface Flux
Mesh Connection	Automatic

Domain Interface - Domain Interface 2	
Boundary List1	Domain Interface 2 Side 1
Boundary List2	Domain Interface 2 Side 2
Interface Type	Fluid Fluid
Settings	
Interface Models	General Connection
Mass And Momentum	Conservative Interface Flux
Mesh Connection	Automatic
Domain Interface - Domain Interface 3	
Boundary List1	Domain Interface 3 Side 1
Boundary List2	Domain Interface 3 Side 2
Interface Type	Fluid Fluid
Settings	
Interface Models	General Connection
Mass And Momentum	Conservative Interface Flux
Mesh Connection	Automatic
Domain Interface - Domain Interface 4	
Boundary List1	Domain Interface 4 Side 1
Boundary List2	Domain Interface 4 Side 2
Interface Type	Fluid Fluid
Settings	
Interface Models	General Connection
Mass And Momentum	Conservative Interface Flux
Mesh Connection	Automatic
Domain Interface - Domain Interface 5	
Boundary List1	Domain Interface 5 Side 1
Boundary List2	Domain Interface 5 Side 2
Interface Type	Fluid Fluid
Settings	
Interface Models	General Connection
Mass And Momentum	Conservative Interface Flux
Mesh Connection	Automatic

Table 4 – Boundary physics for meander channel for the simulation *1xGOx+830 U/mL* at 9.95 s.

Domain	**Boundaries**	
Meander	**Boundary - Inlet GOx**	
	Type	INLET
	Location	INLET_ASSEMBLY INLET1
	Settings	
	Additional Variable	Catalase
	Additional Variable Value	2.8530e-03 [m^-3 mol]
	Option	Value
	Additional Variable	GOx
	Additional Variable Value	6.0470e-04 [m^-3 mol]
	Option	Value
	Additional Variable	Gluconolactone
	Additional Variable Value	0.0000e+00 [m^-3 mol]
	Option	Value
	Additional Variable	Glucose
	Additional Variable Value	0.0000e+00 [m^-3 mol]
	Option	Value
	Additional Variable	H2O2
	Additional Variable Value	0.0000e+00 [m^-3 mol]
	Option	Value
	Additional Variable	Oxygen
	Additional Variable Value	1.9000e-01 [m^-3 mol]
	Option	Value
	Flow Regime	Subsonic
	Mass And Momentum	Normal Speed
	Normal Speed	2.5000e-02 [m s^-1]

	Boundary - Inlet Glucose	
	Type	INLET
	Location	INLET_ASSEMBLY INLET2
	Settings	
	Additional Variable	Catalase
	Additional Variable Value	0.0000e+00 [m^-3 mol]
	Option	Value
	Additional Variable	GOx
	Additional Variable Value	0.0000e+00 [m^-3 mol]
	Option	Value
	Additional Variable	Gluconolactone
	Additional Variable Value	0.0000e+00 [m^-3 mol]
	Option	Value
	Additional Variable	Glucose
	Additional Variable Value	1.0000e+01 [m^-3 mol]
	Option	Value
	Additional Variable	H2O2
	Additional Variable Value	0.0000e+00 [m^-3 mol]
	Option	Value
	Additional Variable	Oxygen
	Additional Variable Value	2.5800e-01 [m^-3 mol]
	Option	Value
	Flow Regime	Subsonic
	Mass And Momentum	Normal Speed
	Normal Speed	2.5000e-02 [m s^-1]
	Boundary - Domain Interface 1 Side 1	
	Type	INTERFACE
	Location	INLET_PIPE_CONNECTOR
	Settings	
	Additional Variable	Catalase
	Option	Conservative Interface Flux
	Additional Variable	GOx
	Option	Conservative Interface Flux
	Additional Variable	Gluconolactone
	Option	Conservative Interface Flux
	Additional Variable	Glucose
	Option	Conservative Interface Flux
	Additional Variable	H2O2
	Option	Conservative Interface Flux
	Additional Variable	Oxygen
	Option	Conservative Interface Flux
	Mass And Momentum	Conservative Interface Flux

	Boundary - Domain Interface 1 Side 2	
	Type	INTERFACE
	Location	PIPE_ASSEMBLY PIPE_OUTLET
	Settings	
	Additional Variable	Catalase
	Option	Conservative Interface Flux
	Additional Variable	GOx
	Option	Conservative Interface Flux
	Additional Variable	Gluconolactone
	Option	Conservative Interface Flux
	Additional Variable	Glucose
	Option	Conservative Interface Flux
	Additional Variable	H2O2
	Option	Conservative Interface Flux
	Additional Variable	Oxygen
	Option	Conservative Interface Flux
	Mass And Momentum	Conservative Interface Flux
	Boundary - Domain Interface 2 Side 1	
	Type	INTERFACE
	Location	INLET_PIPE_CONNECTOR 2
	Settings	
	Additional Variable	Catalase
	Option	Conservative Interface Flux
	Additional Variable	GOx
	Option	Conservative Interface Flux
	Additional Variable	Gluconolactone
	Option	Conservative Interface Flux
	Additional Variable	Glucose
	Option	Conservative Interface Flux
	Additional Variable	H2O2
	Option	Conservative Interface Flux
	Additional Variable	Oxygen
	Option	Conservative Interface Flux
	Mass And Momentum	Conservative Interface Flux

	Boundary - Domain Interface 2 Side 2	
	Type	INTERFACE
	Location	PIPE_ASSEMBLY PIPE_OUTLET 2
	Settings	
	Additional Variable	Catalase
	Option	Conservative Interface Flux
	Additional Variable	GOx
	Option	Conservative Interface Flux
	Additional Variable	Gluconolactone
	Option	Conservative Interface Flux
	Additional Variable	Glucose
	Option	Conservative Interface Flux
	Additional Variable	H2O2
	Option	Conservative Interface Flux
	Additional Variable	Oxygen
	Option	Conservative Interface Flux
	Mass And Momentum	Conservative Interface Flux
	Boundary - Domain Interface 3 Side 1	
	Type	INTERFACE
	Location	INLET_PIPE_CONNECTOR 4
	Settings	
	Additional Variable	Catalase
	Option	Conservative Interface Flux
	Additional Variable	GOx
	Option	Conservative Interface Flux
	Additional Variable	Gluconolactone
	Option	Conservative Interface Flux
	Additional Variable	Glucose
	Option	Conservative Interface Flux
	Additional Variable	H2O2
	Option	Conservative Interface Flux
	Additional Variable	Oxygen
	Option	Conservative Interface Flux
	Mass And Momentum	Conservative Interface Flux

	Boundary - Domain Interface 3 Side 2	
	Type	INTERFACE
	Location	PIPE_ASSEMBLY PIPE_OUTLET 3
	Settings	
	Additional Variable	Catalase
	Option	Conservative Interface Flux
	Additional Variable	GOx
	Option	Conservative Interface Flux
	Additional Variable	Gluconolactone
	Option	Conservative Interface Flux
	Additional Variable	Glucose
	Option	Conservative Interface Flux
	Additional Variable	H2O2
	Option	Conservative Interface Flux
	Additional Variable	Oxygen
	Option	Conservative Interface Flux
	Mass And Momentum	Conservative Interface Flux
	Boundary - Domain Interface 4 Side 1	
	Type	INTERFACE
	Location	INLET_PIPE_CONNECTOR 3
	Settings	
	Additional Variable	Catalase
	Option	Conservative Interface Flux
	Additional Variable	GOx
	Option	Conservative Interface Flux
	Additional Variable	Gluconolactone
	Option	Conservative Interface Flux
	Additional Variable	Glucose
	Option	Conservative Interface Flux
	Additional Variable	H2O2
	Option	Conservative Interface Flux
	Additional Variable	Oxygen
	Option	Conservative Interface Flux
	Mass And Momentum	Conservative Interface Flux

	Boundary - Domain Interface 4 Side 2	
	Type	INTERFACE
	Location	PIPE_ASSEMBLY PIPE_OUTLET 5
	Settings	
	Additional Variable	Catalase
	Option	Conservative Interface Flux
	Additional Variable	GOx
	Option	Conservative Interface Flux
	Additional Variable	Gluconolactone
	Option	Conservative Interface Flux
	Additional Variable	Glucose
	Option	Conservative Interface Flux
	Additional Variable	H2O2
	Option	Conservative Interface Flux
	Additional Variable	Oxygen
	Option	Conservative Interface Flux
	Mass And Momentum	Conservative Interface Flux
	Boundary - Domain Interface 5 Side 1	
	Type	INTERFACE
	Location	INLET_PIPE_CONNECTOR 5
	Settings	
	Additional Variable	Catalase
	Option	Conservative Interface Flux
	Additional Variable	GOx
	Option	Conservative Interface Flux
	Additional Variable	Gluconolactone
	Option	Conservative Interface Flux
	Additional Variable	Glucose
	Option	Conservative Interface Flux
	Additional Variable	H2O2
	Option	Conservative Interface Flux
	Additional Variable	Oxygen
	Option	Conservative Interface Flux
	Mass And Momentum	Conservative Interface Flux

	Boundary - Domain Interface 5 Side 2	
	Type	INTERFACE
	Location	PIPE_ASSEMBLY PIPE_OUTLET 4
	Settings	
	Additional Variable	Catalase
	Option	Conservative Interface Flux
	Additional Variable	GOx
	Option	Conservative Interface Flux
	Additional Variable	Gluconolactone
	Option	Conservative Interface Flux
	Additional Variable	Glucose
	Option	Conservative Interface Flux
	Additional Variable	H2O2
	Option	Conservative Interface Flux
	Additional Variable	Oxygen
	Option	Conservative Interface Flux
	Mass And Momentum	Conservative Interface Flux
	Boundary - Outlet	
	Type	OPENING
	Location	PIPE_ASSEMBLY PIPE_OUTLET 6
	Settings	
	Additional Variable	Catalase
	Additional Variable Value	0.0000e+00 [m^-3 mol]
	Option	Value
	Additional Variable	GOx
	Additional Variable Value	0.0000e+00 [m^-3 mol]
	Option	Value
	Additional Variable	Gluconolactone
	Additional Variable Value	0.0000e+00 [m^-3 mol]
	Option	Value
	Additional Variable	Glucose
	Additional Variable Value	0.0000e+00 [m^-3 mol]
	Option	Value
	Additional Variable	H2O2
	Additional Variable Value	0.0000e+00 [m^-3 mol]
	Option	Value
	Additional Variable	Oxygen
	Additional Variable Value	0.0000e+00 [m^-3 mol]
	Option	Value
	Flow Direction	Normal to Boundary Condition
	Flow Regime	Subsonic
	Mass And Momentum	Opening Pressure and Direction
	Relative Pressure	0.0000e+00 [bar]

	Boundary - Meander Default	
	Type	WALL
	Location	INLET_ASSEMBLY WALL, PIPE_ASSEMBLY MEANDERWALL, PIPE_ASSEMBLY MEANDERWALL 2, PIPE_ASSEMBLY MEANDERWALL 3, PIPE_ASSEMBLY MEANDERWALL 4, PIPE_ASSEMBLY MEANDERWALL 5, PIPE_ASSEMBLY MEANDERWALL 6, PIPE_ASSEMBLY SENSOR, PIPE_ASSEMBLY SENSOR 2, PIPE_ASSEMBLY SENSOR 3, PIPE_ASSEMBLY SENSOR 4, PIPE_ASSEMBLY SENSOR 5, PIPE_ASSEMBLY SENSOR 6, PIPE_ASSEMBLY SIDEINLET, PIPE_ASSEMBLY SIDEINLET 2, PIPE_ASSEMBLY SIDEINLET 3, PIPE_ASSEMBLY SIDEINLET 4, PIPE_ASSEMBLY SIDEINLET 5, PIPE_ASSEMBLY SIDEINLET 6
	Settings	
	Additional Variable	Catalase
	Option	Zero Flux
	Additional Variable	GOx
	Option	Zero Flux
	Additional Variable	Gluconolactone
	Option	Zero Flux
	Additional Variable	Glucose
	Option	Zero Flux
	Additional Variable	H2O2
	Option	Zero Flux
	Additional Variable	Oxygen
	Option	Zero Flux
	Mass And Momentum	No Slip Wall

Table 5 – Domain physics for the tube for the simulation *1xGOx+830 U/mL* at 9.95 s.

Domain - Fluid	
Type	Fluid
Location	LIQUID
Materials	
Air at 25 C	
Fluid Definition	Material Library
Morphology	Continuous Fluid
Settings	
Buoyancy Model	Non Buoyant
Domain Motion	Stationary
Reference Pressure	1.0000e+00 [atm]
Additional Variable	Catalase
Kinematic Diffusivity	4.9500e-11 [m^2 s^-1]
Option	Diffusive Transport Equation
Additional Variable	GOx
Kinematic Diffusivity	4.9500e-11 [m^2 s^-1]
Option	Transport Equation
Additional Variable	Gluconolactone
Kinematic Diffusivity	6.7000e-10 [m^2 s^-1]
Option	Transport Equation
Additional Variable	Glucose
Kinematic Diffusivity	6.7000e-10 [m^2 s^-1]
Option	Transport Equation
Additional Variable	H2O2
Kinematic Diffusivity	2.1000e-09 [m^2 s^-1]
Option	Transport Equation
Additional Variable	Oxygen
Kinematic Diffusivity	2.1000e-09 [m^2 s^-1]
Option	Transport Equation
Heat Transfer Model	Isothermal
Fluid Temperature	2.5000e+01 [C]
Turbulence Model	Laminar
Domain - Tube	
Type	Solid
Location	SOLID
Settings	
Domain Motion	Stationary
Domain Interface - Domain Interface 1	
Boundary List1	Default Fluid Solid Interface Side 2
Boundary List2	Default Fluid Solid Interface Side 1
Interface Type	Fluid Solid
Settings	
Interface Models	General Connection
Mesh Connection	GGI

Table 6 – Boundary physics for the tube for the simulation *1xGOx+830 U/mL* at 9.95 s.

Domain	**Boundaries**	
Fluid	**Boundary - Inlet**	
	Type	INLET
	Location	INLET 2
	Settings	
	Additional Variable	Catalase
	Additional Variable Value	2.8530e-03 [m^-3 mol]
	Option	Value
	Additional Variable	GOx
	Additional Variable Value	6.0500e-04 [m^-3 mol]
	Option	Value
	Additional Variable	Gluconolactone
	Additional Variable Value	1.8940e-01 [m^-3 mol]
	Option	Value
	Additional Variable	Glucose
	Additional Variable Value	4.8080e+00 [m^-3 mol]
	Option	Value
	Additional Variable	H2O2
	Additional Variable Value	1.8178e-01 [m^-3 mol]
	Option	Value
	Additional Variable	Oxygen
	Additional Variable Value	4.1644e-02 [m^-3 mol]
	Option	Value
	Flow Regime	Subsonic
	Mass And Momentum	Normal Speed
	Normal Speed	5.0000e-03 [m s^-1]
	Boundary - Default Fluid Solid Interface Side 1	
	Type	INTERFACE
	Location	INNERTUBE_2
	Settings	
	Additional Variable	Catalase
	Option	Zero Flux
	Additional Variable	GOx
	Option	Zero Flux
	Additional Variable	Gluconolactone
	Option	Zero Flux
	Additional Variable	Glucose
	Option	Zero Flux
	Additional Variable	H2O2
	Option	Zero Flux
	Additional Variable	Oxygen
	Option	Conservative Interface Flux
	Mass And Momentum	No Slip Wall

	Boundary - Outlet	
	Type	OPENING
	Location	OUTLET 2
	Settings	
	Additional Variable	Catalase
	Additional Variable Value	0.0000e+00 [m^-3 mol]
	Option	Value
	Additional Variable	GOx
	Additional Variable Value	0.0000e+00 [m^-3 mol]
	Option	Value
	Additional Variable	Gluconolactone
	Additional Variable Value	0.0000e+00 [m^-3 mol]
	Option	Value
	Additional Variable	Glucose
	Additional Variable Value	0.0000e+00 [m^-3 mol]
	Option	Value
	Additional Variable	H2O2
	Additional Variable Value	0.0000e+00 [m^-3 mol]
	Option	Value
	Additional Variable	Oxygen
	Additional Variable Value	0.0000e+00 [m^-3 mol]
	Option	Value
	Flow Direction	Normal to Boundary Condition
	Flow Regime	Subsonic
	Mass And Momentum	Opening Pressure and Direction
	Relative Pressure	0.0000e+00 [Pa]
Tube	**Boundary - Default Fluid Solid Interface Side 2**	
	Type	INTERFACE
	Location	INNERTUBE_1
	Settings	
	Additional Variable	Oxygen
	Option	Conservative Interface Flux
	Boundary - Toptube	
	Type	WALL
	Location	TOPTUBE
	Settings	
	Additional Variable	Oxygen
	Additional Variable Value	8.6000e+00 [m^-3 mol]
	Option	Value

	Boundary - bottom	
	Type	WALL
	Location	BOTTOMTUBE
	Settings	
	Additional Variable	Oxygen
	Additional Variable Value	0.0000e+00 [m^-3 mol]
	Option	Value
	Boundary - wall out	
	Type	WALL
	Location	OUTWALL 2
	Settings	
	Additional Variable	Oxygen
	Additional Variable Value	8.6000e+00 [m^-3 mol]
	Option	Value

Appendix IV

Table 7 – Domain Physics for meander channel for the slanted grooves geometry (1:1 dilution).

Domain - Fluid	
Type	Fluid
Location	SOLID
Materials	
Water	
Fluid Definition	Material Library
Morphology	Continuous Fluid
Settings	
Buoyancy Model	Non Buoyant
Domain Motion	Stationary
Reference Pressure	1.0000e+00 [atm]
Additional Variable	tracer
Kinematic Diffusivity	1.0000e-10 [m^2 s^-1]
Option	Transport Equation
Turbulence Model	Laminar

Table 8 – Boundary Physics for meander channel for the slanted grooves geometry (1:1 dilution).

Domain	**Boundaries**	
Fluid	**Boundary - inlet1**	
	Type	INLET
	Location	INLET1
	Settings	
	Additional Variable	tracer
	Additional Variable Value	1.0000e+00 [kg m^-3]
	Option	Value
	Flow Regime	Subsonic
	Mass And Momentum	Normal Speed
	Normal Speed	1.0000e-03 [m s^-1]
	Boundary - inlet2	
	Type	INLET
	Location	INLET2
	Settings	
	Additional Variable	tracer
	Additional Variable Value	0.0000e+00 [kg m^-3]
	Option	Value
	Flow Regime	Subsonic
	Mass And Momentum	Normal Speed
	Normal Speed	1.0000e-03 [m s^-1]
	Boundary - outlet	
	Type	OPENING
	Location	OUTLET
	Settings	
	Additional Variable	tracer
	Additional Variable Value	0.0000e+00 [kg m^-3]
	Option	Value
	Flow Direction	Normal to Boundary Condition
	Flow Regime	Subsonic
	Mass And Momentum	Opening Pressure and Direction
	Relative Pressure	0.0000e+00 [Pa]
	Boundary - wall	
	Type	WALL
	Location	WALLS
	Settings	
	Additional Variable	tracer
	Option	Zero Flux
	Mass And Momentum	No Slip Wall

Appendix V

Table 9 – Domain Physics for glass vial geometry at 353 K.

Domain - air	
Type	Fluid
Location	AIR
Materials	
Air Ideal Gas	
Fluid Definition	Material Library
Morphology	Continuous Fluid
Water	
Fluid Definition	Material Library
Morphology	Continuous Fluid
Settings	
Buoyancy Model	Buoyant
Buoyancy Reference Density	1.2250e+03 [kg m^-3]
Gravity X Component	0.0000e+00 [m s^-2]
Gravity Y Component	-9.8100e+00 [m s^-2]
Gravity Z Component	0.0000e+00 [m s^-2]
Buoyancy Reference Location	Automatic
Domain Motion	Stationary
Reference Pressure	1.0000e+00 [atm]
Heat Transfer Model	Thermal Energy
Homogeneous Model	On
Turbulence Model	Laminar
Domain - fluid	
Type	Fluid
Location	WATER
Materials	
Air Ideal Gas	
Fluid Definition	Material Library
Morphology	Continuous Fluid
Water	
Fluid Definition	Material Library
Morphology	Continuous Fluid

Settings	
Buoyancy Model	Buoyant
Buoyancy Reference Density	1.2250e+03 [kg m^-3]
Gravity X Component	0.0000e+00 [m s^-2]
Gravity Y Component	-9.8100e+00 [m s^-2]
Gravity Z Component	0.0000e+00 [m s^-2]
Buoyancy Reference Location	Automatic
Domain Motion	Stationary
Reference Pressure	1.0000e+00 [atm]
Heat Transfer Model	Thermal Energy
Homogeneous Model	On
Turbulence Model	Laminar
Domain - glass	
Type	Solid
Location	GLASS
Settings	
Domain Motion	Stationary
Domain Interface - Default Fluid Fluid Interface	
Boundary List1	Default Fluid Fluid Interface Side 1
Boundary List2	Default Fluid Fluid Interface Side 2
Interface Type	Fluid Fluid
Settings	
Interface Models	General Connection
Mass And Momentum	Conservative Interface Flux
Mesh Connection	GGI
Domain Interface - Default Fluid Solid Interface	
Boundary List1	Default Fluid Solid Interface in air Side 1,Default Fluid Solid Interface in fluid Side 1
Boundary List2	Default Fluid Solid Interface in glass Side 2
Interface Type	Fluid Solid
Settings	
Interface Models	General Connection
Heat Transfer	Conservative Interface Flux
Mesh Connection	GGI

Table 10 – Boundary Physics for glass vial geometry at 353 K.

Domain	Boundaries	
air	**Boundary - Default Fluid Fluid Interface Side 1**	
	Type	INTERFACE
	Location	WATER_2
	Settings	
	Heat Transfer	Conservative Interface Flux
	Mass And Momentum	Conservative Interface Flux
	Boundary - Default Fluid Solid Interface in air Side 1	
	Type	INTERFACE
	Location	Primitive 2D C
	Settings	
	Heat Transfer	Conservative Interface Flux
	Mass And Momentum	No Slip Wall
	Boundary - top	
	Type	OPENING
	Location	TOP
	Settings	
	Flow Direction	Normal to Boundary Condition
	Flow Regime	Subsonic
	Heat Transfer	Opening Temperature
	Opening Temperature	2.5000e+01 [C]
	Mass And Momentum	Opening Pressure and Direction
	Relative Pressure	0.0000e+00 [Pa]
	Fluid	gas
	Volume Fraction	Value
	Volume Fraction	1.0000e+00
	Fluid	water
	Volume Fraction	Value
	Volume Fraction	0.0000e+00
	Boundary - sym1_air	
	Type	SYMMETRY
	Location	SYM1
	Settings	
	Boundary - sym2_air	
	Type	SYMMETRY
	Location	SYM2
fluid	*Settings*	
	Boundary - Default Fluid Fluid Interface Side 2	
	Type	INTERFACE
	Location	WATER_1
	Settings	
	Heat Transfer	Conservative Interface Flux
	Mass And Momentum	Conservative Interface Flux

	Boundary - Default Fluid Solid Interface in fluid Side 1	
	Type	INTERFACE
	Location	Primitive 2D A
	Settings	
	Heat Transfer	Conservative Interface Flux
	Mass And Momentum	No Slip Wall
	Boundary - sym1_water	
	Type	SYMMETRY
	Location	SYM1_WATER
	Settings	
	Boundary - sym2_water	
	Type	SYMMETRY
	Location	SYM2_WATER
	Settings	
glass	**Boundary - Default Fluid Solid Interface in glass Side 2**	
	Type	INTERFACE
	Location	Primitive 2D, Primitive 2D B
	Settings	
	Heat Transfer	Conservative Interface Flux
	Boundary - sym1_glass	
	Type	SYMMETRY
	Location	SYM1_GLASS
	Settings	
	Boundary - sym2_glass	
	Type	SYMMETRY
	Location	SYM2_GLASS
	Settings	
	Boundary - top_wall_glass	
	Type	WALL
	Location	TOP_WALL
	Settings	
	Heat Transfer	Fixed Temperature
	Fixed Temperature	2.5000e+01 [C]
	Boundary - wall	
	Type	WALL
	Location	WALL
	Settings	
	Heat Transfer	Fixed Temperature
	Fixed Temperature	8.0000e+01 [C]

Table 11 – Domain Physics for meander channel for the thermal inactivation platform at 0.0087 m s^{-1} inlet flow.

Domain - fluid	
Type	Fluid
Location	FLUID
Materials	
Water	
Fluid Definition	Material Library
Morphology	Continuous Fluid
Settings	
Buoyancy Model	Non Buoyant
Domain Motion	Stationary
Reference Pressure	1.0000e+00 [atm]
Heat Transfer Model	Thermal Energy
Turbulence Model	Laminar
Domain - pmma	
Type	Solid
Location	PMMA
Settings	
Domain Motion	Stationary
Domain Interface - Default Fluid Solid Interface	
Boundary List1	Default Fluid Solid Interface Side 1
Boundary List2	Default Fluid Solid Interface Side 2
Interface Type	Fluid Solid
Settings	
Interface Models	General Connection
Heat Transfer	Conservative Interface Flux
Mesh Connection	GGI

Table 12 – Boundary Physics for meander channel for the thermal inactivation platform at 0.0087 m s^{-1} inlet flow.

Domain	Boundaries	
fluid	**Boundary - inlet**	
	Type	INLET
	Location	INLET
	Settings	
	Flow Regime	Subsonic
	Heat Transfer	Static Temperature
	Static Temperature	2.5000e+01 [C]
	Mass And Momentum	Normal Speed
	Normal Speed	8.7000e-03 [m s^-1]
	Boundary - Default Fluid Solid Interface Side 1	
	Type	INTERFACE
	Location	TOP_CHANNEL_1
	Settings	
	Heat Transfer	Conservative Interface Flux
	Mass And Momentum	No Slip Wall
	Boundary - outlet	
	Type	OPENING
	Location	OUTLET
	Settings	
	Flow Direction	Normal to Boundary Condition
	Flow Regime	Subsonic
	Heat Transfer	Opening Temperature
	Opening Temperature	2.5000e+01 [C]
	Mass And Momentum	Opening Pressure and Direction
	Relative Pressure	0.0000e+00 [Pa]
	Boundary - sym1_fluid	
	Type	SYMMETRY
	Location	SYM1
	Settings	
	Boundary - sym2_fluid	
	Type	SYMMETRY
	Location	SYM2
	Settings	
	Boundary - heating	
	Type	WALL
	Location	METAL
	Settings	
	Heat Transfer	Fixed Temperature
	Fixed Temperature	8.0000e+01 [C]
	Mass And Momentum	No Slip Wall

pmma	**Boundary - Default Fluid Solid Interface Side 2**	
	Type	INTERFACE
	Location	TOP_CHANNEL_2
	Settings	
	Heat Transfer	Conservative Interface Flux
	Boundary - sym1_pmma	
	Type	SYMMETRY
	Location	SYM1_PMMA
	Settings	
	Boundary - sym2_pmma	
	Type	SYMMETRY
	Location	SYM2_PMMA
	Settings	
	Boundary - endings	
	Type	WALL
	Location	END
	Settings	
	Heat Transfer	Adiabatic
	Boundary - envrionment	
	Type	WALL
	Location	ENVIRONMENT
	Settings	
	Heat Transfer	Fixed Temperature
	Fixed Temperature	2.5000e+01 [C]

Bibliography

[1] G.M. Whitesides, The origins and the future of microfluidics., Nature. 442 (2006) 368–373. doi:10.1038/nature05058.

[2] D. Mark, S. Haeberle, G. Roth, F. von Stetten, R. Zengerle, Microfluidic lab-on-a-chip platforms: requirements, characteristics and applications., Chem. Soc. Rev. 39 (2010) 1153–82. doi:10.1039/b820557b.

[3] D.T. Chiu, A.J. deMello, D. Di Carlo, P.S. Doyle, C. Hansen, R.M. Maceiczyk, R.C.R. Wootton, Small but Perfectly Formed? Successes, Challenges, and Opportunities for Microfluidics in the Chemical and Biological Sciences, Chem. 2 (2017) 201–223. doi:10.1016/j.chempr.2017.01.009.

[4] S.C. Terry, J.H. Jerman, J.B. Angell, A gas chromatographic air analyzer fabricated on a silicon wafer, IEEE Trans. Electron Devices. 26 (1979) 1880–1886. doi:10.1109/T-ED.1979.19791.

[5] D. Erickson, D.Q. Li, Integrated microfluidic devices, Anal. Chim. Acta. 507 (2004) 11–26. doi:10.1016/j.aca.2003.09.019.

[6] K.W. Oh, K. Lee, B. Ahn, E.P. Furlani, Design of pressure-driven microfluidic networks using electric circuit analogy, Lab Chip. 12 (2012) 515–545. doi:10.1039/C2LC20799K.

[7] H. Bruus, Microscale Acoustofluidics, Royal Society of Chemistry, Cambridge, 2014. doi:10.1039/9781849737067.

[8] T.M. Squires, S.R. Quake, Microfluidics: Fluid physics at the nanoliter scale, Rev. Mod. Phys. 77 (2005) 977–1026.

[9] G.P. Celata, M. Cumo, G. Zummo, Thermal-hydraulic characteristics of single-phase flow in capillary pipes, Exp. Therm. Fluid Sci. 28 (2004) 87–95. doi:10.1016/S0894-1777(03)00026-8.

[10] J. Zhang, S. Yan, D. Yuan, G. Alici, N.-T. Nguyen, M. Ebrahimi Warkiani, W. Li, Fundamentals and Applications of Inertial Microfluidics: A Review, Lab Chip. 16 (2016) 10–34. doi:10.1039/C5LC01159K.

[11] Y.K. Suh, S. Kang, A review on mixing in microfluidics, Micromachines. 1 (2010) 82–111. doi:10.3390/mi1030082.

[12] P. Zhu, L. Wang, Passive and active droplet generation with microfluidics: a review, Lab Chip. 17 (2017) 34–75. doi:10.1039/C6LC01018K.

[13] L. Rosenfeld, T. Lin, R. Derda, S.K.Y. Tang, Review and analysis of performance metrics of droplet microfluidics systems, Microfluid. Nanofluidics. 16 (2014) 921–939. doi:10.1007/s10404-013-1310-x.

[14] M. Gao, L. Gui, Electroosmotic Flow Pump, in: K. Pesek (Ed.), Adv. Microfluid. - New Appl. Biol. Energy, Mater. Sci., InTech, 2016. doi:10.5772/64601.

[15] H.A. Stone, A.D. Stroock, A. Ajdari, ENGINEERING FLOWS IN SMALL DEVICESMicrofluidics Toward a Lab-on-a-Chip, Annu. Rev. Fluid Mech. 36 (2004) 381–411. doi:doi:10.1146/annurev.fluid.36.050802.122124.

[16] C. Haber, Microfluidics in commercial applications; an industry perspective., Lab Chip. 6 (2006) 1118–1121. doi:10.1039/b610250f.

[17] C.D. Chin, V. Linder, S.K. Sia, Commercialization of microfluidic point-of-care diagnostic devices, Lab Chip. 12 (2012) 2118. doi:10.1039/c2lc21204h.

[18] L.R. Volpatti, A.K. Yetisen, Commercialization of microfluidic devices, Trends Biotechnol. 32 (2014) 347–350. doi:10.1016/j.tibtech.2014.04.010.

[19] S. Ishii, T. Segawa, S. Okabe, Simultaneous quantification of multiple food- and

waterborne pathogens by use of microfluidic quantitative PCR, Appl. Environ. Microbiol. 79 (2013) 2891–2898. doi:10.1128/AEM.00205-13.
[20] A. Kang, L, Chung, B. G., Langer, R. and Khademhosseini, Microfluidics for drug discovery and development: From target selection to product lifecycle management, Drug Discov. Today. 13 (2008) 1–13. doi:10.1016/j.drudis.2007.10.003.
[21] P. Neuži, S. Giselbrecht, K. Länge, T.J. Huang, A. Manz, Revisiting lab-on-a-chip technology for drug discovery., Nat. Rev. Drug Discov. 11 (2012) 620–32. doi:10.1038/nrd3799.
[22] P. Fernandes, Miniaturization in biocatalysis, Int. J. Mol. Sci. 11 (2010) 858–879. doi:10.3390/ijms11030858.
[23] H.M. Hegab, A. ElMekawy, T. Stakenborg, Review of microfluidic microbioreactor technology for high-throughput submerged microbiological cultivation, Biomicrofluidics. 7 (2013). doi:10.1063/1.4799966.
[24] J. Mairhofer, K. Roppert, P. Ertl, Microfluidic systems for pathogen sensing: A review, Sensors (Switzerland). 9 (2009) 4804–4823. doi:10.3390/s90604804.
[25] H. Bridle, B. Miller, M.P.Y. Desmulliez, Application of microfluidics in waterborne pathogen monitoring: A review, Water Res. 55 (2014) 256–271. doi:10.1016/j.watres.2014.01.061.
[26] S. Sharma, J. Zapatero-Rodríguez, P. Estrela, R. O'Kennedy, Point-of-Care diagnostics in low resource settings: Present status and future role of microfluidics, Biosensors. 5 (2015) 577–601. doi:10.3390/bios5030577.
[27] N. Blow, Microfluidics: in search of a killer application, Nat. Methods. 4 (2007) 665–670. doi:10.1038/nmeth0807-665.
[28] A.K. Au, W. Huynh, L.F. Horowitz, A. Folch, 3D-Printed Microfluidics, Angew. Chemie - Int. Ed. 55 (2016) 3862–3881. doi:10.1002/anie.201504382.
[29] J. Wu, M. Gu, Microfluidic sensing: state of the art fabrication and detection techniques., J. Biomed. Opt. 16 (2011) 80901. doi:10.1117/1.3607430.
[30] D. Sabourin, P. Skafte-Pedersen, M.J. Søe, M. Hemmingsen, M. Alberti, V. Coman, J. Petersen, J. Emnéus, J.P. Kutter, D. Snakenborg, F. Jørgensen, C. Clausen, K. Holmstrøm, M. Dufva, The MainSTREAM component platform: a holistic approach to microfluidic system design., J. Lab. Autom. 18 (2013) 212–228. doi:10.1177/2211068212461445.
[31] S.K. Sia, L.J. Kricka, Microfluidics and point-of-care testing, Lab Chip. 8 (2008) 1982. doi:10.1039/b817915h.
[32] G. Huang, Ying, Hodko, Dalibor, Smolko, Daniel , Lidgard, Electronic Microarray Technology and Applications in Genomics and Proteomics, in: M.M.J.H. Ozkan (Ed.), BioMEMS Biomed. Nanotechnol. Vol. II Micro/ Nano Technol. Genomics Proteomics, Springer New York LLC, 2006: pp. 3–21.
[33] M. Pepper, N.S. Palsandram, P. Zhang, M. Lee, H.J. Cho, Interconnecting fluidic packages and interfaces for micromachined sensors, Sensors Actuators, A Phys. 134 (2007) 278–285. doi:10.1016/j.sna.2006.06.028.
[34] P.K. Yuen, SmartBuild-a truly plug-n-play modular microfluidic system., Lab Chip. 8 (2008) 1374–1378. doi:10.1039/b805086d.
[35] M. Rhee, M. a Burns, Microfluidic assembly blocks., Lab Chip. 8 (2008) 1365–73. doi:10.1039/b805137b.
[36] P.K. Yuen, J.T. Bliss, C.C. Thompson, R.C. Peterson, Multidimensional modular microfluidic system., Lab Chip. 9 (2009) 3303–5. doi:10.1039/b912295h.
[37] J. Lim, F. Maes, V. Taly, J.-C. Baret, The microfluidic puzzle: chip-oriented rapid prototyping, Lab Chip. 14 (2014) 1669. doi:10.1039/c3lc51399h.
[38] S.M. Langelier, E. Livak-Dahl, A.J. Manzo, B.N. Johnson, N.G. Walter, M.A. Burns,

Flexible casting of modular self-aligning microfluidic assembly blocks, Lab Chip. 11 (2011) 1679. doi:10.1039/c0lc00517g.

[39] M. Rahbar, L. Shannon, B.L. Gray, R. Amin, S. Knowlton, A. Hart, K. Vittayarukskul, A.P. Lee, A truly Lego ® -like modular microfluidics platform, J. Micromechanics Microengineering. 27 (2017). doi:10.1088/1361-6439/aa53ed.

[40] P. Zhou, L. Young, K. Lynch, The LabMatrix system, J. Assoc. Lab. Autom. 8 (2003) 5–10. doi:10.1016/S1535-5535(03)00012-1.

[41] V. Hessel, D. Kralisch, N. Kockmann, T. Noël, Q. Wang, Novel process windows for enabling, accelerating, and uplifting flow chemistry, ChemSusChem. 6 (2013) 746–789. doi:10.1002/cssc.201200766.

[42] J.C. Pastre, D.L. Browne, S. V. Ley, Flow chemistry syntheses of natural products, Chem. Soc. Rev. 42 (2013) 8849. doi:10.1039/c3cs60246j.

[43] K.S. Elvira, X.C. i Solvas, R.C.R. Wootton, A.J. deMello, The past, present and potential for microfluidic reactor technology in chemical synthesis, Nat. Chem. 5 (2013) 905–915. doi:10.1038/nchem.1753.

[44] R.L. Hartman, J.P. McMullen, K.F. Jensen, Deciding whether to go with the flow: Evaluating the merits of flow reactors for synthesis, Angew. Chemie - Int. Ed. 50 (2011) 7502–7519. doi:10.1002/anie.201004637.

[45] A. Adamo, R.L. Beingessner, M. Behnam, J. Chen, T.F. Jamison, K.F. Jensen, J.-C.M. Monbaliu, A.S. Myerson, E.M. Revalor, D.R. Snead, T. Stelzer, N. Weeranoppanant, S.Y. Wong, P. Zhang, On-demand continuous-flow production of pharmaceuticals in a compact, reconfigurable system, Science (80-.). 352 (2016) 61–67. doi:10.1126/science.aaf1337.

[46] J.M. Bolivar, J. Wiesbauer, B. Nidetzky, Biotransformations in microstructured reactors: More than flowing with the stream?, Trends Biotechnol. 29 (2011) 333–342. doi:10.1016/j.tibtech.2011.03.005.

[47] R. Wohlgemuth, I. Plazl, P. Žnidaršič-Plazl, K. V. Gernaey, J.M. Woodley, Microscale technology and biocatalytic processes: Opportunities and challenges for synthesis, Trends Biotechnol. 33 (2015) 302–314. doi:10.1016/j.tibtech.2015.02.010.

[48] S. Rameez, S.S. Mostafa, C. Miller, A.A. Shukla, High-Throughput Miniaturized Bioreactors for Cell Culture Process Development: Reproducibility, Scalability, and Control, Am. Inst. Chem. Eng. 30 (2014) 718–727. doi:10.1002/btpr.1874.

[49] C.C.C.R. de Carvalho, Whole cell biocatalysts: essential workers from Nature to the industry, Microb. Biotechnol. 10 (2017) 250–263. doi:10.1111/1751-7915.12363.

[50] P. Rohe, D. Venkanna, B. Kleine, R. Freudl, M. Oldiges, An automated workflow for enhancing microbial bioprocess optimization on a novel microbioreactor platform, Microb. Cell Fact. 11 (2012). doi:10.1186/1475-2859-11-144.

[51] Q. Long, X. Liua, Y. Yanga, L. Lia, L. Harvey, B. McNeilb, Z. Bai, The development and application of high throughput cultivation technology in bioprocess development, J. Biotechnol. (2014). doi:10.1016/j.jbiotec.2014.03.028.

[52] D. Schäpper, M.N.H.Z. Alam, N. Szita, A.E. Lantz, K. V Gernaey, Application of microbioreactors in fermentation process development: a review, Anal Bioanal Chem. 395 (2009) 679–695. doi:10.1007/s00216-009-2955-x.

[53] M. Funke, A. Buchenauer, U. Schnakenberg, W. Mokwa, S. Diederichs, A. Mertens, C. Mu¨ller, F. Kensy, J. Bu¨chs, Microfluidic BioLector—Microfluidic Bioprocess Control in Microtiter Plates, Biotechnol. Bioeng. 107 (2010) 497–505. doi:10.1002/bit.22825.

[54] J.I. Betts, F. Baganz, Miniature bioreactors: current practices and future opportunities, Microb. Cell Fact. 5 (2006). doi:10.1186/1475-2859-5-21.

[55] R. Bareither, D. Pollard, A Review of Advanced Small-Scale Parallel Bioreactor Technology for Accelerated Process Development: Current State and Future Need, Am. Inst. Chem. Eng. 27 (2010) 2–14. doi:10.1002/btpr.522.

[56] K. V. Gernaey, F. Baganz, E. Franco-Lara, F. Kensy, U. Krühne, M. Luebberstedt, U. Marx, E. Palmqvist, A. Schmid, F. Schubert, C.F. Mandenius, Monitoring and control of microbioreactors: An expert opinion on development needs, Biotechnol. J. 7 (2012) 1308–1314. doi:10.1002/biot.201200157.
[57] B. Gutmann, D. Cantillo, C.O. Kappe, Continuous-flow technology - A tool for the safe manufacturing of active pharmaceutical ingredients, Angew. Chemie - Int. Ed. 54 (2015) 6688–6728. doi:10.1002/anie.201409318.
[58] C. Lattermann, J. Büchs, Microscale and miniscale fermentation and screening, Curr. Opin. Biotechnol. 35 (2015) 1–6. doi:10.1016/j.copbio.2014.12.005.
[59] Y. Asanomi, H. Yamaguchi, M. Miyazaki, H. Maeda, Enzyme-immobilized microfluidic process reactors, Molecules. 16 (2011) 6041–6059. doi:10.3390/molecules16076041.
[60] P. Gruber, M.P.C. Marques, B. O'Sullivan, F. Baganz, R. Wohlgemuth, N. Szita, Conscious coupling: The challenges and opportunities of cascading enzymatic microreactors, Biotechnol. J. (2017) 1–13. doi:10.1002/biot.201700030.
[61] B. Kintses, C. Hein, M.F. Mohamed, M. Fischlechner, F. Courtois, C. Lainé, F. Hollfelder, Picoliter cell lysate assays in microfluidic droplet compartments for directed enzyme evolution, Chem. Biol. 19 (2012) 1001–1009. doi:10.1016/j.chembiol.2012.06.009.
[62] E.E. Krommenhoek, M. van Leeuwen, H. Gardeniers, W.M. van Gulik, A. van den Berg, X. Li, M. Ottens, L.A.M. van der Wielen, J.J. Heijnen, Lab-Scale Fermentation Tests of Microchip With Integrated Electrochemical Sensors for pH, Temperature, Dissolved Oxygen and Viable Biomass Concentration, Biotechnol. Bioeng. 99 (2007) 884–892. doi:10.1002/bit.21661.
[63] C.H. Wu, L. Scampavia, J. Ruzicka, B. Zamost, Micro sequential injection: fermentation monitoring of ammonia, glycerol, glucose, and free iron using the novel lab-on-valve system, Analyst. 126 (2001) 291–297. doi:10.1039/b009167g.
[64] Y.H. Kim, J.S. Park, H. Il Jung, An impedimetric biosensor for real-time monitoring of bacterial growth in a microbial fermentor, Sensors Actuators, B Chem. 138 (2009) 270–277. doi:10.1016/j.snb.2009.01.034.
[65] A. Calvo-López, O. Ymbern, D. Izquierdo, J. Alonso-Chamarro, Low cost and compact analytical microsystem for carbon dioxide determination in production processes of wine and beer, Anal. Chim. Acta. 931 (2016) 64–69. doi:10.1016/j.aca.2016.05.010.
[66] I.P. Rosinha Grundtvig, A.E. Daugaard, J.M. Woodley, K. V. Gernaey, U. Krühne, Shape optimization as a tool to design biocatalytic microreactors, Chem. Eng. J. 322 (2017) 215–223. doi:10.1016/j.cej.2017.03.045.
[67] H.T.G. van Lintel, F.C.M. van De Pol, S. Bouwstra, A piezoelectric micropump based on micromachining of silicon, Sensors and Actuators. 15 (1988) 153–167. doi:10.1016/0250-6874(88)87005-7.
[68] A. Manz, Y. Miyahara, J. Miura, Y. Watanabe, H. Miyagi, K. Sato, Design of an open-tubular column liquid chromatograph using silicon chip technology, Sensors Actuators B. Chem. 1 (1990) 249–255. doi:10.1016/0925-4005(90)80210-Q.
[69] A. Manz, D.J. Harrison, E.M.J. Verpoorte, J.C. Fettinger, A. Paulus, H. Lüdi, H.M. Widmer, Planar chips technology for miniaturization and integration of separation techniques into monitoring systems. Capillary electrophoresis on a chip, J. Chromatogr. A. 593 (1992) 253–258. doi:10.1016/0021-9673(92)80293-4.
[70] K.E. Petersen, Silicon as a Mechanical Material, Proc. IEEE. 70 (1982) 420–457.
[71] J. Bryzek, Impact of MEMS technology on society, Sensors Actuators A Phys. 56 (1996) 1–9. doi:10.1016/0924-4247(96)01284-8.
[72] D.C. Duffy, J.C. McDonald, O.J.A. Schueller, G.M. Whitesides, Rapid prototyping of microfluidic systems in poly(dimethylsiloxane), Anal. Chem. 70 (1998) 4974–4984. doi:10.1021/ac980656z.

[73] S.T.B. and David C. Duffy, Olivier J. A. Schueller, G.M. Whitesides, Rapid prototyping of microfluidic switches in poly (dimethyl siloxane) and their actuation by electro-osmotic flow, J. Micromech. Microeng. 9 (1999) 211–217.
[74] J. Wu, M. Gu, Microfluidic sensing: state of the art fabrication and detection techniques, J. Biomed. Opt. 16 (2011) 80901. doi:10.1117/1.3607430.
[75] P.N. Nge, C.I. Rogers, A.T. Woolley, Advances in Microfluidic Materials, Functions, Integration, and Applications, Chem. Rev. 113 (2013) 2550–2583. doi:dx.doi.org/10.1021/cr300337x.
[76] C. Becker, H., Beckert, E., Gärtner, Microfluidic Manifolds with High Dynamic Range in Structural Dimensions Replicated in Thermoplastic Materials., Appl. Opt. 2009 MRS Spring Meet. (2009).
[77] R. Mariella, Sample preparation: The weak link in microfluidics-based biodetection, Biomed. Microdevices. 10 (2008) 777–784. doi:10.1007/s10544-008-9190-7.
[78] M. Heckele, W.K. Schomburg, Review on micro molding of thermoplastic polymers, J. Micromechanics Microengineering. 14 (2003) R1–R14. doi:10.1088/0960-1317/14/3/R01.
[79] B. Ziaie, A. Baldi, M. Lei, Y. Gu, R.A. Siegel, Hard and soft micromachining for BioMEMS: Review of techniques and examples of applications in microfluidics and drug delivery, Adv. Drug Deliv. Rev. 56 (2004) 145–172. doi:10.1016/j.addr.2003.09.001.
[80] H. Becker, C. Gärtner, Polymer microfabrication technologies for microfluidic systems., Anal. Bioanal. Chem. 390 (2008) 89–111. doi:10.1007/s00216-007-1692-2.
[81] C. Iliescu, H. Taylor, M. Avram, J. Miao, S. Franssila, A practical guide for the fabrication of microfluidic devices using glass and silicon, Biomicrofluidics. 6 (2012) 16505–1650516. doi:10.1063/1.3689939.
[82] Y. Cheng, X. Luo, G.F. Payne, G.W. Rubloff, Biofabrication: programmable assembly of polysaccharide hydrogels in microfluidics as biocompatible scaffolds, J. Mater. Chem. 22 (2012) 7659. doi:10.1039/c2jm16215f.
[83] X. Li, D.R. Ballerini, W. Shen, A perspective on paper-based microfluidics: Current status and future trends, Biomicrofluidics. 6 (2012). doi:10.1063/1.3687398.
[84] C.M.B. Ho, S.H. Ng, K.H.H. Li, Y. Yoon, 3D printed microfluidics for biological applications, Lab Chip. 15 (2015) 3627–3637. doi:10.1039/C5LC00685F.
[85] and H.W. Kangning Ren, Jianhua Zhou, Materials for Microfluidic Chip Fabrication, Acc. Chem. Res. 46 (2013) 2396–2406. doi:10.1021/ar300314s.
[86] C. Gärtner, S. Kirsch, B. Anton, H. Becker, Hybrid microfluidic systems – combining a polymer microfluidic toolbox with biosensors, Microfluid. BioMEMS, Med. Microsystems V. (2007) 2–5. doi:10.1117/12.715041.
[87] A.W. Martinez, S.T. Phillips, G.M. Whitesides, E. Carrilho, Diagnostics for the developing world: microfluidic paper-based analytical devices., Anal. Chem. 82 (2010) 3–10. doi:10.1021/ac9013989.
[88] D.D. Liana, B. Raguse, J.J. Gooding, E. Chow, Recent Advances in Paper-Based Sensors, Sensors. 12 (2012) 11505–11526. doi:10.3390/s120911505.
[89] A.K. Yetisen, M.S. Akram, C.R. Lowe, Paper-based microfluidic point-of-care diagnostic devices., Lab Chip. 13 (2013) 2210–2251. doi:10.1039/c3lc50169h.
[90] Y. Xia, J. Si, Z. Li, Fabrication techniques for microfluidic paper-based analytical devices and their applications for biological testing: A review, Biosens. Bioelectron. 77 (2016) 774–789. doi:10.1016/j.bios.2015.10.032.
[91] T. Naito, M. Nakamura, N. Kaji, T. Kubo, Y. Baba, K. Otsuka, Three-Dimensional Fabrication for Microfluidics by Conventional Techniques and Equipment Used in Mass Production, Micromachines. 7 (2016) 82. doi:10.3390/mi7050082.
[92] A. Ben Azouz, S. Murphy, S. Karazi, M. Vázquez, D. Brabazon, Fast Fabrication Process of Microfluidic Devices Based on Cyclic Olefin Copolymer, Mater. Manuf. Process. 29

(2014) 93–99. doi:10.1080/10426914.2013.811739.
[93] P. Kim, K.W. Kwon, M.C. Park, S.H. Lee, S.M. Kim, Soft Lithography for Microfluidics : a Review, Biochip J. 2 (2008) 1–11. http://s-space.snu.ac.kr/handle/10371/9558.
[94] U.M. Attia, S. Marson, J.R. Alcock, Micro - injection moulding of polymer microfluidic devices, 7 (2015) 1–58.
[95] G. Perozziello, F. Bundgaard, O. Geschke, Fluidic interconnections for microfluidic systems: A new integrated fluidic interconnection allowing plug'n'play functionality, Sensors Actuators B Chem. 130 (2008) 947–953. doi:10.1016/j.snb.2007.11.011.
[96] A.E. Kirby, A.R. Wheeler, Microfluidic origami: a new device format for in-line reaction monitoring by nanoelectrospray ionization mass spectrometry, Lab Chip. 13 (2013) 2533–2540. doi:10.1039/c3lc41431k.
[97] G. Perozziello, P. Candeloro, A. De Grazia, F. Esposito, M. Allione, M.L. Coluccio, R. Tallerico, I. Valpapuram, L. Tirinato, G. Das, A. Giugni, B. Torre, P. Veltri, U. Kruhne, G. Della Valle, E. Di Fabrizio, Microfluidic device for continuous single cells analysis via Raman spectroscopy enhanced by integrated plasmonic nanodimers, Opt. Express. 24 (2016) A180. doi:10.1364/OE.24.00A180.
[98] H. Kimura, T. Ikeda, H. Nakayama, Y. Sakai, T. Fujii, An On-Chip Small Intestine–Liver Model for Pharmacokinetic Studies, J. Lab. Autom. 20 (2015) 265–273. doi:10.1177/2211068214557812.
[99] Y. Zheng, W. Dai, H. Wu, A screw-actuated pneumatic valve for portable , disposable microfluidics, Lab Chip. 9 (2009) 469–472. doi:10.1039/b811526e.
[100] W. Gu, H. Chen, Y. Tung, J.-C. Meiners, S. Takayama, Multiplexed hydraulic valve actuation using ionic liquid filled soft channels and Braille displays, Appl. Phys. Lett. 90 (2007) 33505. doi:10.1063/1.2431771.
[101] H. Madadi, J. Casals-Terré, M. Mohammadi, Self-driven filter-based blood plasma separator microfluidic chip for point-of-care testing, Biofabrication. 7 (2015) 25007. doi:10.1088/1758-5090/7/2/025007.
[102] F. Sassa, K. Morimoto, W. Satoh, H. Suzuki, Electrochemical techniques for microfluidic applications, Electrophoresis. 29 (2008) 1787–1800. doi:10.1002/elps.200700581.
[103] C.Y. Lim, A.E. Lim, Y.C. Lam, pH Change in Electroosmotic Flow Hysteresis, Anal. Chem. (2017). doi:10.1021/acs.analchem.7b02219.
[104] A. Liau, R. Kamik, A. Majumdar, J.H.D. Cate, Mixing crowded biological solutions in milliseconds, Anal. Chem. 77 (2005) 7618–7625. doi:10.1021/ac050827h.
[105] C.-Y. Lee, C.-L. Chang, Y.-N. Wang, L.-M. Fu, Microfluidic Mixing: A Review, Int. J. Mol. Sci. 12 (2011) 3263–3287. doi:10.3390/ijms12053263.
[106] X. Niu, F. Gielen, J.B. Edel, A.J. deMello, A microdroplet dilutor for high-throughput screening, Nat. Chem. 3 (2011) 437–442. doi:10.1038/nchem.1046.
[107] H.S. Rho, A.T. Hanke, M. Ottens, H. Gardeniers, Mapping of Enzyme Kinetics on a Microfluidic Device, PLoS One. 11 (2016) e0153437. doi:10.1371/journal.pone.0153437.
[108] S.L. Stott, C.-H.C.-H. Hsu, D.I. Tsukrov, M. Yu, D.T. Miyamoto, B.A. Waltman, S.M. Rothenberg, A.M. Shah, M.E. Smas, G.K. Korir, F.P. Floyd, A.J. Gilman, J.B. Lord, D. Winokur, S. Springer, D. Irimia, S. Nagrath, L. V Sequist, R.J. Lee, K.J. Isselbacher, S. Maheswaran, D.A. Haber, M. Toner, Isolation of circulating tumor cells using a microvortex-generating herringbone-chip, October. 107 (2010) 18392–7. doi:10.1073/pnas.1012539107/-/DCSupplemental.www.pnas.org/cgi/doi/10.1073/pnas.1012539107.
[109] W. Jing, W. Zhao, S. Liu, L. Li, C.-T. Tsai, X. Fan, W. Wu, J. Li, X. Yang, G. Sui, Microfluidic Device for Efficient Airborne Bacteria Capture and Enrichment, Anal. Chem. 85 (2013) 5255–5262. doi:10.1021/ac400590c.
[110] I. Pereiro, A. Bendali, S. Tabnaoui, L. Alexandre, J. Srbova, Z. Bilkova, S. Deegan, L.

Joshi, J.-L. Viovy, L. Malaquin, B. Dupuy, S. Descroix, A new microfluidic approach for the one-step capture, amplification and label-free quantification of bacteria from raw samples, Chem. Sci. 8 (2017) 1329–1336. doi:10.1039/C6SC03880H.

[111] A. Sarkar, H.W. Hou, A.E. Mahan, J. Han, G. Alter, Multiplexed Affinity-Based Separation of Proteins and Cells Using Inertial Microfluidics, Sci. Rep. 6 (2016) 23589. doi:10.1038/srep23589.

[112] E. Stern, A. Vacic, N.K. Rajan, J.M. Criscione, J. Park, B.R. Ilic, D.J. Mooney, M.A. Reed, T.M. Fahmy, Label-free biomarker detection from whole blood, Nat. Nanotechnol. 5 (2010) 138–142. doi:10.1038/nnano.2009.353.

[113] C.-L. Chang, W. Huang, S.I. Jalal, B.-D. Chan, A. Mahmood, S. Shahda, B.H. O'Neil, D.E. Matei, C.A. Savran, Circulating tumor cell detection using a parallel flow micro-aperture chip system, Lab Chip. 15 (2015) 1677–1688. doi:10.1039/C5LC00100E.

[114] K.J. Shaw, E.M. Hughes, C.E. Dyer, J. Greenman, S.J. Haswell, Integrated RNA extraction and RT-PCR for semi-quantitative gene expression studies on a microfluidic device, Lab. Investig. 93 (2013) 961–966. doi:10.1038/labinvest.2013.76.

[115] M. Park, H.D. Ha, Y.T. Kim, J.H. Jung, S.H. Kim, D.H. Kim, T.S. Seo, Combination of a Sample Pretreatment Microfluidic Device with a Photoluminescent Graphene Oxide Quantum Dot Sensor for Trace Lead Detection, Anal. Chem. 87 (2015) 10969–10975. doi:10.1021/acs.analchem.5b02907.

[116] X. Niu, M. Zhang, S. Peng, W. Wen, P. Sheng, Real-time detection, control, and sorting of microfluidic droplets, Biomicrofluidics. 1 (2007). doi:10.1063/1.2795392.

[117] A.R. Abate, K. Ahn, A.C. Rowat, C. Baret, M. Marquez, A.M. Klibanov, A.D. Grif, D.A. Weitz, G.A.L. Aga, Ultrahigh-throughput screening in drop-based microfluidics for directed evolution, Proc. Natl. Acad. Sci. 107 (2010) 6550–6550. doi:10.1073/pnas.1002891107.

[118] D. Frenzel, C.A. Merten, Microfluidic train station: highly robust and multiplexable sorting of droplets on electric rails, Lab Chip. 17 (2017) 1024–1030. doi:10.1039/C6LC01544A.

[119] D.R. Link, E. Grasland-Mongrain, A. Duri, F. Sarrazin, Z. Cheng, G. Cristobal, M. Marquez, D.A. Weitz, Electric control of droplets in microfluidic devices, Angew. Chemie - Int. Ed. 45 (2006) 2556–2560. doi:10.1002/anie.200503540.

[120] X. Wang, S. Chen, M. Kong, Z. Wang, K.D. Costa, A. Li, Lab on a Chip Enhanced cell sorting and manipulation with combined optical tweezer and microfluidic chip technologies, Lab Chip. 11 (2011) 3656–3662. doi:10.1039/c1lc20653b.

[121] A.R. Abate, J.J. Agresti, D.A. Weitz, Microfluidic sorting with high-speed single-layer membrane valves, Appl. Phys. Lett. 96 (2010). doi:10.1063/1.3431281.

[122] Z. Wang, J. Zhe, Recent advances in particle and droplet manipulation for lab-on-a-chip devices based on surface acoustic waves, Lab Chip. 11 (2011) 1280–1285. doi:10.1039/c0lc00527d.

[123] C.-H. Hsu, D. Di Carlo, C. Chen, D. Irimia, M. Toner, Microvortex for focusing, guiding and sorting of particles, Lab Chip. 8 (2008) 2128. doi:10.1039/b813434k.

[124] Z.T.F. Yu, K.M. Aw Yong, J. Fu, Microfluidic blood cell sorting: Now and beyond, Small. 10 (2014) 1687–1703. doi:10.1002/smll.201302907.

[125] Y. Schaerli, R.C. Wootton, T. Robinson, V. Stein, C. Dunsby, M. a a Neil, P.M.W. French, A.J. DeMello, C. Abell, F. Hollfelder, Continuous-Flow Polymerase Chain Reaction of Single-Copy DNA in Microfluidic Microdroplets, Anal. Chem. 81 (2009) 302–306. doi:10.1021/ac802038c.

[126] Z. Yu, S. Lu, Y. Huang, Microfluidic Whole Genome Amplification Device for Single Cell Sequencing, Anal. Chem. 86 (2014) 9386–9390. doi:10.1021/ac5032176.

[127] I.K. Dimov, J.L. Garcia-Cordero, J. O'Grady, C.R. Poulsen, C. Viguier, L. Kent, P. Daly,

B. Lincoln, M. Maher, R. O'Kennedy, T.J. Smith, A.J. Ricco, L.P. Lee, Integrated microfluidic tmRNA purification and real-time NASBA device for molecular diagnostics, Lab Chip. 8 (2008) 2071. doi:10.1039/b812515e.
[128] A.B. Theberge, E. Mayot, A. El Harrak, F. Kleinschmidt, W.T.S. Huck, A.D. Griffiths, Microfluidic platform for combinatorial synthesis in picolitre droplets, Lab Chip. 12 (2012) 1320. doi:10.1039/c2lc21019c.
[129] P. Mary, A.R. Abate, J.J. Agresti, D.A. Weitz, Controlling droplet incubation using close-packed plug flow, Biomicrofluidics. 5 (2011) 1–6. doi:10.1063/1.3576934.
[130] A.J. de Mello, N. Beard, Dealing with "real" samples: sample pre-treatment in microfluidic systems, Lab Chip. 3 (2003) 11N–20N. doi:10.1039/B301019H.
[131] X. Chen, D.F. Cui, Microfluidic devices for sample pretreatment and applications, Microsyst. Technol. 15 (2009) 667–676. doi:10.1007/s00542-009-0783-8.
[132] Y. Huang, E.L. Mather, J.L. Bell, M. Madou, MEMS-based sample preparation for molecular diagnostics, Anal. Bioanal. Chem. 372 (2002) 49–65. doi:10.1007/s00216-001-1191-9.
[133] D. Hess, A. Rane, A.J. Demello, S. Stavrakis, High-throughput, quantitative enzyme kinetic analysis in microdroplets using stroboscopic epifluorescence imaging, Anal. Chem. 87 (2015) 4965–4972. doi:10.1021/acs.analchem.5b00766.
[134] L.X. Quang, C. Lim, G.H. Seong, J. Choo, K.J. Do, S.-K. Yoo, A portable surface-enhanced Raman scattering sensor integrated with a lab-on-a-chip for field analysis, Lab Chip. 8 (2008) 2214. doi:10.1039/b808835g.
[135] B. Ungerböck, A. Pohar, T. Mayr, I. Plazl, Online oxygen measurements inside a microreactor with modeling of transport phenomena, Microfluid. Nanofluidics. 14 (2013) 565–574. doi:10.1007/s10404-012-1074-8.
[136] G. Hu, D. Li, Multiscale phenomena in microfluidics and nanofluidics, Chem. Eng. Sci. 62 (2007) 3443–3454. doi:10.1016/j.ces.2006.11.058.
[137] Z.G. Mills, W. Mao, A. Alexeev, Mesoscale modeling: solving complex flows in biology and biotechnology, Trends Biotechnol. 31 (2013) 1–9. doi:10.1016/j.tibtech.2013.05.001.
[138] J. Luecha, A. Hsiao, S. Brodsky, G.L. Liu, J.L. Kokini, Green microfluidic devices made of corn proteins., Lab Chip. 11 (2011) 3419–25. doi:10.1039/c1lc20726a.
[139] C.A. Mills, M. Navarro, E. Engel, E. Martinez, M.P. Ginebra, J. Planell, A. Errachid, J. Samitier, Transparent micro- and nanopatterned poly(lactic acid) for biomedical applications, J. Biomed. Mater. Res. - Part A. 76 (2006) 781–787. doi:10.1002/jbm.a.30539.
[140] E. Corradini, P.S. Curti, A.B. Meniqueti, A.F. Martins, A.F. Rubira, E.C. Muniz, Recent advances in food-packing, pharmaceutical and biomedical applications of zein and zein-based materials, Int. J. Mol. Sci. 15 (2014) 22438–22470. doi:10.3390/ijms151222438.
[141] P.G. Gezer, A. Hsiao, J.L. Kokini, G.L. Liu, Simultaneous transfer of noble metals and three-dimensional micro- and nanopatterns onto zein for fabrication of nanophotonic platforms, J. Mater. Sci. 51 (2016) 1–11. doi:10.1007/s10853-015-9699-0.
[142] J.L. Kokini, G.L. Liu, A. Hsiao, J. Luecha, Microfluidic device comprising a biodegradable material and method of making such a microfluidic device, US 8956577 B2, 2015. https://www.google.com/patents/US8956577.
[143] J.W. Lawton, Zein: A history of processing and use, Cereal Chem. 79 (2002) 1–18. doi:10.1094/CCHEM.2002.79.1.1.
[144] Y. Chen, L. Zhang, G. Chen, Fabrication, modification, and application of poly(methyl methacrylate) microfluidic chips, Electrophoresis. 29 (2008) 1801–1814. doi:10.1002/elps.200700552.
[145] D. Duval, L.M. Lechuga, Breakthroughs in photonics 2012: 2012 breakthroughs in lab-on-a-chip and optical biosensors, IEEE Photonics J. 5 (2013).

doi:10.1109/JPHOT.2013.2250943.
[146] H. Lee, E. Sun, D. Ham, R. Weissleder, Chip-NMR biosensor for detection and molecular analysis of cells, Nat. Med. 14 (2008) 869–874. doi:10.1038/nm.1711.
[147] M. Bridgelal Ram, P.R. Grocott, H.C.M. Weir, Issues and challenges of involving users in medical device development, Heal. Expect. 11 (2008) 63–71. doi:10.1111/j.1369-7625.2007.00464.x.
[148] S.G.S. Shah, I. Robinson, S. AlShawi, Developing medical device technologies from users' perspectives: A theoretical framework for involving users in the development process, Int. J. Technol. Assess. Health Care. 25 (2009) 514–521. doi:10.1017/S0266462309990328.
[149] T. Martin, E. Jovanov, D. Raskovic, Issues in wearable computing for medical monitoring applications: a case study of a wearable ECG monitoring device, Fourth Int. Symp. Wearable Comput. (2000) 43–49. doi:10.1109/ISWC.2000.888463.
[150] S. Matosevic, N. Szita, F. Baganz, Fundamentals and applications of immobilized microfluidic enzymatic reactors, J. Chem. Technol. Biotechnol. 86 (2011) 325–334. doi:10.1002/jctb.2564.
[151] G.T. John, E. Heinzle, Quantitative screening method for hydrolases in microplates using pH indicators: Determination of kinetic parameters by dynamic pH monitoring, Biotechnol. Bioeng. 72 (2001) 620–627. doi:10.1002/1097-0290(20010320)72:6<620::AID-BIT1027>3.0.CO;2-W.
[152] C. Ferreira-Torres, M. Micheletti, G.J. Lye, Microscale process evaluation of recombinant biocatalyst libraries: Application to Baeyer-Villiger monooxygenase catalysed lactone synthesis, Bioprocess Biosyst. Eng. 28 (2005) 83–93. doi:10.1007/s00449-005-0422-4.
[153] M. Micheletti, G.J. Lye, Microscale bioprocess optimisation, Curr. Opin. Biotechnol. 17 (2006) 611–618. doi:10.1016/j.copbio.2006.10.006.
[154] S.D. Doig, S.C.R. Pickering, G.J. Lye, J.M. Woodley, The use of microscale processing technologies for quantification of biocatalytic Baeyer-Villiger oxidation kinetics, Biotechnol. Bioeng. 80 (2002) 42–49. doi:10.1002/bit.10344.
[155] J.Z. Baboo, J.L. Galman, G.J. Lye, J.M. Ward, H.C. Hailes, M. Micheletti, An automated microscale platform for evaluation and optimization of oxidative bioconversion processes, Biotechnol. Prog. 28 (2012) 392–405. doi:10.1002/btpr.1500.
[156] M. Samorski, G. Müller-Newen, J. Büchs, Quasi-continuous combined scattered light and fluorescence measurements: A novel measurement technique for shaken microtiter plates, Biotechnol. Bioeng. 92 (2005) 61–68. doi:10.1002/bit.20573.
[157] M. Funke, A. Buchenauer, U. Schnakenberg, W. Mokwa, S. Diederichs, A. Mertens, C. Müller, F. Kensy, J. Büchs, Microfluidic biolector-microfluidic bioprocess control in microtiter plates, Biotechnol. Bioeng. 107 (2010) 497–505. doi:10.1002/bit.22825.
[158] M. Funke, S. Diederichs, F. Kensy, C. Müller, J. Büchs, The baffled microtiter plate: Increased oxygen transfer and improved online monitoring in small scale fermentations, Biotechnol. Bioeng. 103 (2009) 1118–1128. doi:10.1002/bit.22341.
[159] W.A. Duetz, Microtiter plates as mini-bioreactors: miniaturization of fermentation methods, TRENDS Microbiol. 15 (2007) 469–475. doi:10.1016/j.tim.2007.09.004.
[160] C.Y. Lee, W.T. Wang, C.C. Liu, L.M. Fu, Passive mixers in microfluidic systems: A review, Chem. Eng. J. 288 (2016) 146–160. doi:10.1016/j.cej.2015.10.122.
[161] S. Heintz, A. Mitic, R.H. Ringborg, U. Krühne, J.M. Woodley, K. V. Gernaey, A microfluidic toolbox for the development of in-situ product removal strategies in biocatalysis, J. Flow Chem. 6 (2016) 18–26. doi:10.1556/1846.2015.00040.
[162] H. Mao, T. Yang, P.S. Cremer, Design and characterization of immobilized enzymes in microfluidic systems, Anal. Chem. 74 (2002) 379–385. doi:10.1021/ac010822u.
[163] F. Costantini, R. Tiggelaar, S. Sennato, F. Mura, S. Schlautmann, F. Bordi, H. Gardeniers, C. Manetti, Glucose level determination with a multi-enzymatic cascade

reaction in a functionalized glass chip., Analyst. 138 (2013) 5019–24. doi:10.1039/c3an00806a.
[164] S. Sun, B. Ungerböck, T. Mayr, Imaging of oxygen in microreactors and microfluidic systems, Methods Appl. Fluoresc. 3 (2015). doi:10.1088/2050-6120/3/3/034002.
[165] P. Gruber, M.P.C. Marques, N. Szita, T. Mayr, Integration and application of optical chemical sensors in microbioreactors, Lab Chip. (2017). doi:10.1039/C7LC00538E.
[166] D.G. Rackus, M.H. Shamsi, A.R. Wheeler, Electrochemistry, biosensors and microfluidics: a convergence of fields, Chem. Soc. Rev. 44 (2015) 5320–5340. doi:10.1039/C4CS00369A.
[167] X. Wang, L. Yi, N. Mukhitov, A.M. Schrell, R. Dhumpa, M.G. Roper, Microfluidics-to-mass spectrometry: A review of coupling methods and applications, J. Chromatogr. A. 1382 (2015) 98–116. doi:10.1016/j.chroma.2014.10.039.
[168] D. Issadore, Y.I. Park, H. Shao, C. Min, K. Lee, M. Liong, R. Weissleder, H. Lee, Magnetic sensing technology for molecular analyses, Lab Chip. 14 (2014) 2385–2397. doi:10.1039/C4LC00314D.
[169] A.F. Chrimes, K. Khoshmanesh, P.R. Stoddart, A. Mitchell, K. Kalantar-zadeh, Microfluidics and Raman microscopy: current applications and future challenges., Chem. Soc. Rev. 42 (2013) 5880–5906. doi:10.1039/c3cs35515b.
[170] J. Yue, J.C. Schouten, T.A. Nijhuis, Integration of Microreactors with Spectroscopic Detection for Online Reaction Monitoring and Catalyst Characterization, Ind. Eng. Chem. Res. 51 (2012) 14583–14609. doi:10.1021/ie301258j.
[171] F. Gielen, L. Van Vliet, B.T. Koprowski, S.R.A. Devenish, A Fully Unsupervised Compartment-on-Demand Platform for Precise Nanolitre Assays of Time- Dependent Steady-State Enzyme Kinetics and Inhibition, Anal. Chem. 85 (2013) 4761–4769.
[172] P. Gruber, M.P.C. Marques, P. Sulzer, R. Wohlgemuth, T. Mayr, F. Baganz, N. Szita, Real-time pH monitoring of industrially relevant enzymatic reactions in a microfluidic side-entry reactor (μSER) shows potential for pH control, Biotechnol. J. 12 (2017) 1–13. doi:10.1002/biot.201600475.
[173] S.A. Pfeiffer, S.M. Borisov, S. Nagl, In-line monitoring of pH and oxygen during enzymatic reactions in off-the-shelf all-glass microreactors using integrated luminescent microsensors, Microchim. Acta. 184 (2017) 621–626. doi:10.1007/s00604-016-2021-2.
[174] J. Ehgartner, P. Sulzer, T. Burger, A. Kasjanow, D. Bouwes, U. Krühne, I. Klimant, T. Mayr, Online analysis of oxygen inside silicon-glass microreactors with integrated optical sensors, Sensors Actuators B Chem. 228 (2016) 748–757. doi:10.1016/j.snb.2016.01.050.
[175] F.B. Myers, L.P. Lee, Innovations in optical microfluidic technologies for point-of-care diagnostics., Lab Chip. 8 (2008) 2015–2031. doi:10.1039/b812343h.
[176] S. a Pfeiffer, S. Nagl, Microfluidic platforms employing integrated fluorescent or luminescent chemical sensors: a review of methods, scope and applications, Methods Appl. Fluoresc. 3 (2015) 34003-1-16. doi:10.1088/2050-6120/3/3/034003.
[177] M. Nirschl, F. Reuter, J. Vörös, Review of Transducer Principles for Label-Free Biomolecular Interaction Analysis, Biosensors. 1 (2011) 70–92. doi:10.3390/bios1030070.
[178] H.J. Lee, A.W. Wark, R.M. Corn, Enhanced bioaffinity sensing using surface plasmons, surface enzyme reactions, nanoparticles and diffraction gratings., Analyst. 133 (2008) 596–601. doi:10.1039/b718713k.
[179] M. Li, S.K. Cushing, N. Wu, Plasmon-enhanced optical sensors: a review, Analyst. 140 (2015) 386–406. doi:10.1039/C4AN01079E.
[180] M.C. Estevez, M. Alvarez, L.M. Lechuga, Integrated optical devices for lab-on-a-chip biosensing applications, Laser Photon. Rev. 6 (2012) 463–487. doi:10.1002/lpor.201100025.
[181] H. Mukundan, A.S. Anderson, W.K. Grace, K.M. Grace, N. Hartman, J.S. Martinez, B.I. Swanson, Waveguide-based biosensors for pathogen detection, Sensors. 9 (2009) 5783–

5809. doi:10.3390/s90705783.
[182] J. Vörös, J.J. Ramsden, G. Csúcs, I. Szendro, S.M. De Paul, M. Textor, N.D. Spencer, Optical grating coupler biosensors, Biomaterials. 23 (2002) 3699–3710. doi:10.1016/S0142-9612(02)00103-5.
[183] M.A. Brusatori, Y. Tie, P.R. Van Tassel, Protein Adsorption Kinetics under an Applied Electric Field: An Optical Waveguide Lightmode Spectroscopy Study, Langmuir. 19 (2003) 5089–5097. doi:10.1021/la0269558.
[184] R. Ince, R. Narayanaswamy, Analysis of the performance of interferometry, surface plasmon resonance and luminescence as biosensors and chemosensors, Anal. Chim. Acta. 569 (2006) 1–20. doi:10.1016/j.aca.2006.03.058.
[185] K.R. Strehle, D. Cialla, P. Rösch, T. Henkel, M. Köhler, J. Popp, A reproducible surface-enhanced Raman spectroscopy approach. Online SERS measurements in a segmented microfluidic system, Anal. Chem. 79 (2007) 1542–1547. doi:10.1021/ac0615246.
[186] J. Lou, Y. Wang, L. Tong, Microfiber optical sensors: A review, Sensors (Switzerland). 14 (2014) 5823–5844. doi:10.3390/s140405823.
[187] W.K. Ridgeway, E. Seitaridou, R. Phillips, J.R. Williamson, RNA-protein binding kinetics in an automated microfluidic reactor, Nucleic Acids Res. 37 (2009) 1–11. doi:10.1093/nar/gkp733.
[188] N.M. iguel M. Pires, T. Dong, U. Hanke, N. Hoivik, Recent developments in optical detection technologies in lab-on-a-chip devices for biosensing applications, Sensors (Basel). 14 (2014) 15458–15479. doi:10.3390/s140815458.
[189] L.C. Lasave, S.M. Borisov, J. Ehgartner, T. Mayr, Quick and simple integration of optical oxygen sensors into glass-based microfluidic devices, RSC Adv. 5 (2015) 70808–70816. doi:10.1039/C5RA15591F.
[190] B. Ungerböck, S. Fellinger, P. Sulzer, T. Abel, T. Mayr, Magnetic optical sensor particles: a flexible analytical tool for microfluidic devices, Analyst. 139 (2014) 2551–2559. doi:10.1039/c4an00169a.
[191] N. Klauke, P. Monaghan, G. Sinclair, M. Padgett, J. Cooper, Characterisation of spatial and temporal changes in pH gradients in microfluidic channels using optically trapped fluorescent sensors., Lab Chip. 6 (2006) 788–793. doi:10.1039/b517237c.
[192] M.D. Brennan, M.L. Rexius-Hall, L.J. Elgass, D.T. Eddington, Oxygen control with microfluidics., Lab Chip. 14 (2014) 4305–18. doi:10.1039/c4lc00853g.
[193] L. Basabe-Desmonts, F. Benito-López, H.J.G.E. Gardeniers, R. Duwel, A. Van Den Berg, D.N. Reinhoudt, M. Crego-Calama, Fluorescent sensor array in a microfluidic chip, Anal. Bioanal. Chem. 390 (2008) 307–315. doi:10.1007/s00216-007-1720-2.
[194] A.R. Thete, G.A. Gross, J.M. Koehler, Differentiation of liquid analytes in gel films by permeability-modulated double-layer chemo-chips., Analyst. 134 (2009) 394–400. doi:10.1039/b808257j.
[195] V. Nock, R.J. Blaikie, M.M. Alkaisi, Optical Oxygen Sensors for Micro- and Nanofluidic Devices, in: S.S. K. Iniewski (Ed.), Smart Sensors Ind. Appl., Vol. 14, CRC Press, 2013: pp. 129–153.
[196] R.H.W. Lam, M. Kim, T. Thorsen, Culturing Aerobic and Anaerobic Bacteria and Mammalian Cells with a Microfluidic Differential Oxygenator, Anal. Chem. 81 (2009) 5918–5924. doi:10.1021/ac9006864.
[197] R. Wilson, A.P.F. Turner, Glucose oxidase: an ideal enzyme, Biosens. Bioelectron. 7 (1992) 165–185. doi:10.1016/0956-5663(92)87013-F.
[198] V. Leskovac, S. Trivić, G. Wohlfahrt, J. Kandrač, D. Peričin, Glucose oxidase from Aspergillus niger: The mechanism of action with molecular oxygen, quinones, and one-electron acceptors, Int. J. Biochem. Cell Biol. 37 (2005) 731–750. doi:10.1016/j.biocel.2004.10.014.

[199] S.B. Bankar, M. V Bule, R.S. Singhal, L. Ananthanarayan, Glucose oxidase--an overview., Biotechnol. Adv. 27 (2009) 489–501. doi:10.1016/j.biotechadv.2009.04.003.
[200] K. Kleppe, The effect of hydrogen peroxide on glucose oxidase from Aspergillu niger, Biochemistry. 5 (1966) 139–143.
[201] A. Cornish-Bowden, Reactions of More than One Substrate, in: Fundam. Enzym. Kinet., 4th ed., Wiley-VCH Verlag GmbH & Co. KGaA, Singapore, 2014: pp. 189–226.
[202] V. Linek, P. Beneš, J. Sinkule, O. Holeček, V. Malý, Oxidation of D -glucose in the presence of glucose oxidase and catalase, Biotechnol. Bioeng. 22 (1980) 2515–2527. doi:10.1002/bit.260221203.
[203] B.E.P. Swoboda, V. Massey, Purification and Properties of the Glucose Oxidase from Aspergillus niger, J. Biol. Chem. 240 (1965) 2209–2215.
[204] A. Cornish-Bowden, Introduction to enzyme kinetics, in: Fundam. Enzym. Kinet., 4th ed., Wiley-Blackwell, Singapore, 2014: pp. 25–75.
[205] W.P. Dijkman, G. De Gonzalo, A. Mattevi, M.W. Fraaije, Flavoprotein oxidases: Classification and applications, Appl. Microbiol. Biotechnol. 97 (2013) 5177–5188. doi:10.1007/s00253-013-4925-7.
[206] G. Senter, Studies on Enzyme Action : The Effect of â€™ Poisons â€™ on the Rate of Decomposition of Hydrogen Peroxide by Hæmase, Proc. R. Soc. London. 74 (n.d.) 201–217.
[207] A. Deisseroth, A.L. Dounce, Catalase: Physical and chemical properties, mechanism of catalysis, and physiological role, Physiol Rev. 50 (1970) 319–375. http://www.ncbi.nlm.nih.gov/entrez/query.fcgi?cmd=Retrieve&db=PubMed&dopt=Citation&list_uids=4912904.
[208] M. Yoshimoto, M. Higa, A kinetic analysis of catalytic production of oxygen in catalase-containing liposome dispersions for controlled transfer of oxygen in a bioreactor, J. Chem. Technol. Biotechnol. 89 (2014) 1388–1395. doi:10.1002/jctb.4216.
[209] H. Aebi, [13] Catalase in vitro, in: Methods Enzymol., 1984: pp. 121–126. doi:10.1016/S0076-6879(84)05016-3.
[210] J.M. Bolivar, S. Schelch, M. Pfeiffer, B. Nidetzky, Intensifying the O2-dependent heterogeneous biocatalysis: Superoxygenation of solid support from H2O2 by a catalase tailor-made for effective immobilization, J. Mol. Catal. B Enzym. 134 (2016) 302–309. doi:10.1016/j.molcatb.2016.10.017.
[211] J. Switale, P.C. Loewen, Diversity properties among catalases, Arch. Biochem. Biophys. 401 (2002) 145–154.
[212] J.H. Northrop, The Kinetics of the Decomposition of Peroxide By Catalase., J. Gen. Physiol. 7 (1925) 373–87.
[213] H.G. Schlegel, Aeration without air: Oxygen supply by hydrogen peroxide, Biotechnol. Bioeng. 19 (1977) 413–424. doi:10.1002/bit.260190311.
[214] J.R. Lakowicz, Frequency-Domain Lifetime Measurements, Princ. Fluoresc. Spectrosc. (2010) 157–204. doi:10.1016/0925-4005(96)80051-7.
[215] C.M. McGraw, G. Khalil, J.B. Callis, Comparison of Time and Frequency Domain Methods for Luminescence Lifetime Measurements †, J. Phys. Chem. C. 112 (2008) 8079–8084. doi:10.1021/jp711867u.
[216] E.R. Carraway, J.N. Demas, B.A. DeGraff, J.R. Bacon, Photophysics and photochemistry of oxygen sensors based on luminescent transition-metal complexes, Anal. Chem. 63 (1991) 337–342. doi:10.1021/ac00004a007.
[217] H. Becker, R. Klemm, R. Sewart, C. Gärtner, A Multiport Metering Valve Technology for on-Chip Valving, 16th Int. Conf. Miniaturized Syst. Chem. Life Sci. (2012) 308–310. http://www.rsc.org/images/loc/2012/pdf/M.1.8.pdf.
[218] D.P.H.M. Heuts, E.W. Van Hellemond, D.B. Janssen, M.W. Fraaije, Discovery, characterization, and kinetic analysis of an alditol oxidase from Streptomyces coelicolor,

J. Biol. Chem. 282 (2007) 20283–20291. doi:10.1074/jbc.M610849200.
[219] R.F.B. and I.W. Sizer, A Spectrophotometric Method for Measuring the Breakdown of Hydrogen Peroxide By Catalase, J. Biol. Chem. 195 (1952) 133–140.
[220] H. Lück, Catalase, in: H.-Ui. Bergmeyer (Ed.), Methods Enzym. Anal., 1st ed., Elsevier, 1965: pp. 885–888.
[221] R. Sander, Compilation of Henry's Law Constants for Inorganic and Organic Species of Potential Importance in Environmental Chemistry, in: Intergovernmental Panel on Climate Change (Ed.), Clim. Chang. 2013 - Phys. Sci. Basis, Cambridge University Press, Cambridge, 1999: pp. 1–30. doi:10.1017/CBO9781107415324.004.
[222] Z. Zhang, P. Gibson, S.B. Clark, G. Tian, P.L. Zanonato, L. Rao, Lactonization and protonation of gluconic acid: A thermodynamic and kinetic study by potentiometry, NMR and ESI-MS, J. Solution Chem. 36 (2007) 1187–1200. doi:10.1007/s10953-007-9182-x.
[223] H. Pan, Y. Xia, M. Qin, Y. Cao, W. Wang, A simple procedure to improve the surface passivation for single molecule fluorescence studies., Phys. Biol. 12 (2015) 45006. doi:10.1088/1478-3975/12/4/045006.
[224] L. Gregg, Novozymes glucose oxidase enzyme preparation GRAS, 2002.
[225] E.N. Ramsden, Chemistry of the Environment, Nelson Thornes Ltd, 1996.
[226] J. Chen, H.D. Kim, K.C. Kim, Measurement of dissolved oxygen diffusion coefficient in a microchannel using UV-LED induced fluorescence method, Microfluid. Nanofluidics. 14 (2013) 541–550. doi:10.1007/s10404-012-1072-x.
[227] V. Nock, R.J. Blaikie, Spatially resolved measurement of dissolved oxygen in multistream microfluidic devices, IEEE Sens. J. 10 (2010) 1813–1819. doi:10.1109/JSEN.2010.2049016.
[228] N.T.S. Evans, T.H. Quinton, Permeability and diffusion coefficient of oxygen in membranes for oxygen electrodes, Respir. Physiol. 35 (1978) 89–99. doi:10.1016/0034-5687(78)90044-0.
[229] Y.-A. Chen, A.D. King, H.-C. Shih, C.-C. Peng, C.-Y. Wu, W.-H. Liao, Y.-C. Tung, Generation of oxygen gradients in microfluidic devices for cell culture using spatially confined chemical reactions, Lab Chip. 11 (2011) 3626. doi:10.1039/c1lc20325h.
[230] J. Park, T. Bansal, M. Pinelis, M.M. Maharbiz, A microsystem for sensing and patterning oxidative microgradients during cell culture., Lab Chip. 6 (2006) 611–22. doi:10.1039/b516483d.
[231] R.J. Gilbert, L.M. Carleton, K.A. Dasse, P.M. Martin, R.E. Williford, B.F. Monzyk, Photocatalytic generation of dissolved oxygen and oxyhemoglobin in whole blood based on the indirect interaction of ultraviolet light with a semiconducting titanium dioxide thin film, J. Appl. Phys. 102 (2007). doi:10.1063/1.2738375.
[232] A. Subrahmanyam, T. Arokiadoss, T.P. Ramesh, Studies on the oxygenation of human blood by photocatalytic action, Artif. Organs. 31 (2007) 819–825. doi:10.1111/j.1525-1594.2007.00468.x.
[233] M. Rasponi, T. Ullah, R.J. Gilbert, G.B. Fiore, T.A. Thorsen, Realization and efficiency evaluation of a micro-photocatalytic cell prototype for real-time blood oxygenation, Med. Eng. Phys. 33 (2011) 887–892. doi:10.1016/j.medengphy.2010.10.008.
[234] C. Mccullagh, J.M.C. Robertson, D.W. Bahnemann, P.K.J. Robertson, The application of TiO₂ photocatalysis for disinfection of water contaminated with pathogenic micro-organisms: a review, Res. Chem. Intermed. 33 (2007) 359–375. doi:10.1163/156856707779238775.
[235] H. Song, Y. Wang, K. Pant, Cross-stream diffusion under pressure-driven flow in microchannels with arbitrary aspect ratios: a phase diagram study using a three-dimensional analytical model, Microfluid. Nanofluidics. 12 (2012) 265–277. doi:10.1007/s10404-011-0870-x.

[236] H.J. Bright, Q.H. Gibson, The Oxidation of 1-Deuterated Glucose by Glucose Oxidase, J. Biol. Chem. 242 (1967) 994–1003.
[237] Z. Tao, R.A. Raffel, A.K. Souid, J. Goodisman, Kinetic studies on enzyme-catalyzed reactions: Oxidation of glucose, decomposition of hydrogen peroxide and their combination, Biophys. J. 96 (2009) 2977–2988. doi:10.1016/j.bpj.2008.11.071.
[238] J.M. Halder, Naphthalene Dioxygenase from Pseudomonas sp. NCIB 9816-4: Systematic Analysis of the Active Site, Stuttgart Universität, 2017.
[239] J.L. Adrio, A.L. Demain, Microbial enzymes: tools for biotechnological processes, Biomolecules. 4 (2014) 117–139. doi:10.3390/biom4010117.
[240] S.G. Burton, D.A. Cowan, J.M. Woodley, The search for the ideal biocatalyst, Nat. Biotechnol. 20 (2002) 37–45. doi:10.1038/nbt0102-37.
[241] N. Ladkau, A. Schmid, B. Bühler, The microbial cell-functional unit for energy dependent multistep biocatalysis, Curr. Opin. Biotechnol. 30 (2014) 178–189. doi:10.1016/j.copbio.2014.06.003.
[242] P. Tufvesson, J. Lima-Ramos, M. Nordblad, J.M. Woodley, Guidelines and cost analysis for catalyst production in biocatalytic processes, Org. Process Res. Dev. 15 (2011) 266–274. doi:10.1021/op1002165.
[243] T. Ishige, K. Honda, S. Shimizu, Whole organism biocatalysis, Curr. Opin. Chem. Biol. 9 (2005) 174–180. doi:10.1016/j.cbpa.2005.02.001.
[244] J. Wachtmeister, D. Rother, Recent advances in whole cell biocatalysis techniques bridging from investigative to industrial scale, Curr. Opin. Biotechnol. 42 (2016) 169–177. doi:10.1016/j.copbio.2016.05.005.
[245] D. Kuhn, L.M. Blank, A. Schmid, B. Bühler, Systems biotechnology - Rational whole-cell biocatalyst and bioprocess design, Eng. Life Sci. 10 (2010) 384–397. doi:10.1002/elsc.201000009.
[246] C.C.C.R. De Carvalho, Enzymatic and whole cell catalysis: Finding new strategies for old processes, Biotechnol. Adv. 29 (2011) 75–83. doi:10.1016/j.biotechadv.2010.09.001.
[247] U.T. Bornscheuer, G.W. Huisman, R.J. Kazlauskas, S. Lutz, J.C. Moore, K. Robins, Engineering the third wave of biocatalysis, Nature. 485 (2012) 185–194. doi:10.1038/nature11117.
[248] A.G. Marr, Growth Rate of Escherichia coli, Microbiol. Mol. Biol. Rev. 55 (1991) 316–333.
[249] M. Martínez-Alonso, N. González-Montalbán, E. García-Fruitós, A. Villaverde, Learning about protein solubility from bacterial inclusion bodies, Microb. Cell Fact. 8 (2009) 4. doi:10.1186/1475-2859-8-4.
[250] A. Ramón, M. Señorale-Pose, M. Marín, Inclusion bodies: Not that bad..., Front. Microbiol. 5 (2014) 2010–2015. doi:10.3389/fmicb.2014.00056.
[251] S.G. Burton, Oxidizing enzymes as biocatalysts, Trends Biotechnol. 21 (2003) 543–549. doi:10.1016/j.tibtech.2003.10.006.
[252] J.B. Van Beilen, W.A. Duetz, A. Schmid, B. Witholt, Practical issues in the application of oxygenases, Trends Biotechnol. 21 (2003) 170–177. doi:10.1016/S0167-7799(03)00032-5.
[253] P.C. Cirino, F.H. Arnold, Protein engineering of oxygenases for biocatalysis, Curr. Opin. Chem. Biol. 6 (2002) 130–135. doi:10.1016/S1367-5931(02)00305-8.
[254] D.J. Ferraro, L. Gakhar, S. Ramaswamy, Rieske business: Structure-function of Rieske non-heme oxygenases, Biochem. Biophys. Res. Commun. 338 (2005) 175–190. doi:10.1016/j.bbrc.2005.08.222.
[255] S.M. Barry, G.L. Challis, Mechanism and catalytic diversity of rieske non-heme iron-dependent oxygenases, ACS Catal. 3 (2013) 2362–2370. doi:10.1021/cs400087p.
[256] C. Gally, B.M. Nestl, B. Hauer, Engineering Rieske Non-Heme Iron Oxygenases for the Asymmetric Dihydroxylation of Alkenes, Angew. Chemie - Int. Ed. 54 (2015) 12952–12956. doi:10.1002/anie.201506527.

[257] B. Kauppi, K. Lee, E. Carredano, R.E. Parales, D.T. Gibson, H. Eklund, S. Ramaswamy, Structure of an aromatic-ring-hydroxylating dioxygenase – naphthalene 1,2-dioxygenase, Structure. 6 (1998) 571–586. doi:10.1016/S0969-2126(98)00059-8.
[258] X. Cui, H.M. Yip, Q. Zhu, C. Yang, R.H.W. Lam, Microfluidic long-term differential oxygenation for bacterial growth characteristics analyses, RSC Adv. 4 (2014) 16662–16673. doi:10.1039/C4RA01577K.
[259] M. Polinkovsky, E. Gutierrez, A. Levchenko, A. Groisman, Fine temporal control of the medium gas content and acidity and on-chip generation of series of oxygen concentrations for cell cultures., Lab Chip. 9 (2009) 1073–1084. doi:10.1039/b816191g.
[260] J. Ogawa, S. Shimizu, Microbial enzymes: New industrial applications from traditional screening methods, Trends Biotechnol. 17 (1999) 13–21. doi:10.1016/S0167-7799(98)01227-X.
[261] C.M. Clouthier, J.N. Pelletier, Expanding the organic toolbox: a guide to integrating biocatalysis in synthesis, Chem. Soc. Rev. 41 (2012) 1585. doi:10.1039/c2cs15286j.
[262] M.S. Packer, D.R. Liu, Methods for the directed evolution of proteins, Nat. Rev. Genet. 16 (2015) 379–394. doi:10.1038/nrg3927.
[263] T. Van Rossum, S.W.M. Kengen, J. Van Der Oost, Reporter-based screening and selection of enzymes, FEBS J. 280 (2013) 2979–2996. doi:10.1111/febs.12281.
[264] E. Fernández-Álvaro, R. Snajdrova, H. Jochens, T. Davids, D. Böttcher, U.T. Bornscheuer, A combination of in vivo selection and cell sorting for the identification of enantioselective biocatalysts, Angew. Chemie - Int. Ed. 50 (2011) 8584–8587. doi:10.1002/anie.201102360.
[265] M.T. Reetz, M.H. Becker, A Method for High-Throughput Screening of Enantioselective Catalysts, Communications. (1999) 1758–1761.
[266] J. Guo, J. Wu, G. Siuzdak, M.G. Finn, Measurement of Enantiomeric Excess by Kinetic Resolution and Mass Spectrometry, Angew. Chemie Int. Ed. 38 (1999) 1755–1758. doi:10.1002/(SICI)1521-3773(19990614)38:12<1755::AID-ANIE1755>3.0.CO;2-Q.
[267] C. Yan, F. Parmeggiani, E.A. Jones, E. Claude, S.A. Hussain, N.J. Turner, S.L. Flitsch, P.E. Barran, Real-time screening of biocatalysts in live bacterial colonies, J. Am. Chem. Soc. 139 (2017) 1408–1411. doi:10.1021/jacs.6b12165.
[268] F. Parmeggiani, S.L. Lovelock, N.J. Weise, S.T. Ahmed, N.J. Turner, Synthesis of D- and L-Phenylalanine Derivatives by Phenylalanine Ammonia Lyases: A Multienzymatic Cascade Process, Angew. Chemie - Int. Ed. 54 (2015) 4608–4611. doi:10.1002/anie.201410670.
[269] Z.L. and F.H.A. Hyun Joo, Akira Arisawa, A high-throughput digital imaging screen for the discovery and directed evolution of oxygenases, Chem. Biol. 6 (1999) 699–706. http://biomednet.com/elecref/1074552100600699.
[270] U. Schwaneberg, C. Schmidt-Dannert, J. Schmitt, R.D. Schmid, A Continuous Spectrophotometric Assay for P450 BM-3, a Fatty Acid Hydroxylating Enzyme, and Its Mutant F87A, Anal. Biochem. 269 (1999) 359–366. doi:10.1006/abio.1999.4047.
[271] W.A. Duetz, L. Rüedi, R. Hermann, K. O'Connor, J. Büchs, B. Witholt, Methods for intense aeration, growth, storage, and replication of bacterial strains in microtiter plates, Appl. Environ. Microbiol. 66 (2000) 2641–2646. doi:10.1128/AEM.66.6.2641-2646.2000.
[272] U. Schwaneberg, C. Otey, P.C. Cirino, E. Farinas, F.. Arnold, Cost-Effective Whole-Cell Assay for Laboratory Evolution of Hydroxylases in Escherichia coli, J. Biomol. Screen. 6 (2001) 111–117.
[273] C.C.C.R. De Carvalho, M. Manuela, R. Da Fonseca, Bacterial Whole Cell Biotransformations: In Vivo Reactions Under In Vitro Conditions, Dyn. Biochem. Process Biotechnol. Mol. Biol. 1 (2007) 32–39.
[274] S.R. Quake, A.Y. Fu, C. Spence, A. Scherer, F.H. Arnold, A microfabricated fluorescence-

activated cell sorter, Nat. Biotechnol. 17 (1999) 1109–1111. doi:10.1038/15095.
[275] M. Horka, S. Sun, A. Ruszczak, P. Garstecki, T. Mayr, Lifetime of Phosphorescence from Nanoparticles Yields Accurate Measurement of Concentration of Oxygen in Microdroplets, Allowing One To Monitor the Metabolism of Bacteria, Anal. Chem. 88 (2016) 12006–12012. doi:10.1021/acs.analchem.6b03758.
[276] J.A.N. Brophy, C.A. Voigt, Principles of genetic circuit design, Nat. Methods. 11 (2014) 508–520. doi:10.1038/nmeth.2926.
[277] J.M. Choi, S.S. Han, H.S. Kim, Industrial applications of enzyme biocatalysis: Current status and future aspects, Biotechnol. Adv. 33 (2015) 1443–1454. doi:10.1016/j.biotechadv.2015.02.014.
[278] J.W. Whittaker, A.M. Orville, J.D. Lipscomb, [14] Protocatechuate 3,4-dioxygenase from Brevibacterium fuscum, in: Methods Enzymol., 1990: pp. 82–88. doi:10.1016/0076-6879(90)88016-4.
[279] K. Lee, D.T. Gibson, Stereospecific dihydroxylation of the styrene vinyl group by purified naphthalene dioxygenase from Pseudomonas sp. strain NCIB 9816-4, J. Bacteriol. 178 (1996) 3353–3356.
[280] Y. Jouanneau, C. Meyer, J. Jakoncic, V. Stojanoff, J. Gaillard, Characterization of a naphthalene dioxygenase endowed with an exceptionally broad substrate specificity toward polycyclic aromatic hydrocarbons, Biochemistry. 45 (2006) 12380–12391. doi:10.1021/bi0611311.
[281] R.E. Parales, J. V. Parales, D.T. Gibson, Aspartate 205 in the catalytic domain of naphthalene dioxygenase is essential for activity, J. Bacteriol. 181 (1999) 1831–1837.
[282] K. Rachinskiy, M. Kunze, C. Graf, H. Schultze, M. Boy, J. B??chs, Extension and application of the “enzyme test bench” for oxygen consuming enzyme reactions, Biotechnol. Bioeng. 111 (2014) 244–253. doi:10.1002/bit.25020.
[283] A. Berry, T.C. Dodge, M. Pepsin, W. Weyler, Application of metabolic engineering to improve both the production and use of biotech indigo, J Ind Microbiol Biotechnol. 28 (2002) 127–133. doi:10.1038/sj/jim/7000228.
[284] I.P. Petrounia, F.H. Arnold, Designed evolution of enzymatic properties, Curr. Opin. Biotechnol. 11 (2000) 325–330. doi:10.1016/S0958-1669(00)00107-5.
[285] A.H. Badran, D.R. Liu, In vivo continuous directed evolution, Curr. Opin. Chem. Biol. 24 (2015) 1–10. doi:10.1016/j.cbpa.2014.09.040.
[286] I. Cherny, P. Greisen, Y. Ashani, S.D. Khare, G. Oberdorfer, H. Leader, D. Baker, D.S. Tawfik, Engineering V-Type Nerve Agents Detoxifying Enzymes Using Computationally Focused Libraries, ACS Chem. Biol. 8 (2013) 2394–2403. doi:10.1021/cb4004892.
[287] D. Röthlisberger, O. Khersonsky, A.M. Wollacott, L. Jiang, J. DeChancie, J. Betker, J.L. Gallaher, E.A. Althoff, A. Zanghellini, O. Dym, S. Albeck, K.N. Houk, D.S. Tawfik, D. Baker, Kemp elimination catalysts by computational enzyme design, Nature. 453 (2008) 190–195. doi:10.1038/nature06879.
[288] R.E. Parales, S.M. Resnick, C.L. Yu, D.R. Boyd, N.D. Sharma, D.T. Gibson, Regioselectivity and enantioselectivity of naphthalene dioxygenase during arene cis-dihydroxylation: Control by Phenylalanine 352 in the alfa subunit, J. Bacteriol. 182 (2000) 5495–5504. doi:10.1128/JB.182.19.5495-5504.2000.
[289] B.D. Ensley, B.J. Ratzkin, T.D. Osslund, M.J. Simon, L.P. Wackett, D.T. Gibson, Expression of Naphthalene Oxidation Genes in Escherichia coli Results in the Biosynthesis of Indigo, Sci. New Ser. 222 (1983) 167–169. doi:10.1002/9780470114735.hawley00624.
[290] H. Pathak, D. Madamwar, Biosynthesis of indigo dye by newly isolated naphthalene-degrading strain pseudomonas sp. HOB1 and its application in dyeing cotton fabric, Appl. Biochem. Biotechnol. 160 (2010) 1616–1626. doi:10.1007/s12010-009-8638-4.

[291] J.M. Bergada, J. Watton, S. Kumar, Pressure, Flow, Force, and Torque Between the Barrel and Port Plate in an Axial Piston Pump, J. Dyn. Syst. Meas. Control. 130 (2008) 11011. doi:10.1115/1.2807183.
[292] S. Wang, The Analysis of Cavitation Problems in the Axial Piston Pump, J. Fluids Eng. 132 (2010) 74502. doi:10.1115/1.4002058.
[293] O. Frey, S. Talaei, P.D. van der Wal, M. Koudelka-Hep, N.F. de Rooij, Continuous-flow multi-analyte biosensor cartridge with controllable linear response range., Lab Chip. 10 (2010) 2226–2234. doi:10.1039/c004851h.
[294] J. Wu, M. Gu, Microfluidic sensing: state of the art fabrication and detection techniques, J. Biomed. Opt. 16 (2011) 80901. doi:10.1117/1.3607430.
[295] D. Grieshaber, R. MacKenzie, J. Vörös, E. Reimhult, Electrochemical Biosensors - Sensor Principles and Architectures, Sensors. 8 (2008) 1400–1458. doi:10.3390/s8031400.
[296] J.P. Hart, A. Crew, E. Crouch, K.C. Honeychurch, R.M. Pemberton, Some Recent Designs and Developments of Screen-Printed Carbon Electrochemical Sensors/Biosensors for Biomedical, Environmental, and Industrial Analyses, Anal. Lett. 37 (2004) 789–830. doi:10.1081/AL-120030682.
[297] A.F.D. Cruz, N. Norena, A. Kaushik, S. Bhansali, A low-cost miniaturized potentiostat for point-of-care diagnosis, Biosens. Bioelectron. 62 (2014) 249–254. doi:10.1016/j.bios.2014.06.053.
[298] E. Ghodsevali, S. Morneau-Gamache, J. Mathault, H. Landari, É. Boisselier, M. Boukadoum, B. Gosselin, A. Miled, Miniaturized FDDA and CMOS Based Potentiostat for Bio-Applications, Sensors. 17 (2017) 810. doi:10.3390/s17040810.
[299] U. Guth, W. Vonau, J. Zosel, Recent developments in electrochemical sensor application and technology—a review, Meas. Sci. Technol. 20 (2009) 42002. doi:10.1088/0957-0233/20/4/042002.
[300] P. He, J. Davies, G. Greenway, S.J. Haswell, Measurement of acetylcholinesterase inhibition using bienzymes immobilized monolith micro-reactor with integrated electrochemical detection., Anal. Chim. Acta. 659 (2010) 9–14. doi:10.1016/j.aca.2009.11.052.
[301] J.G. Alves Brito-Neto, J.A. Fracassi Da Silva, L. Blanes, C.L. Do Lago, Understanding capacitively coupled contactless conductivity detection in capillary and microchip electrophoresis. Part 1. Fundamentals, Electroanalysis. 17 (2005) 1198–1206. doi:10.1002/elan.200503237.
[302] A. Arvinte, A.M. Sesay, V. Virtanen, C. Bala, Evaluation of meldola blue-carbon nanotube-sol-gel composite for electrochemical NADH sensors and their application for lactate dehydrogenase-based biosensors, Electroanalysis. 20 (2008) 2355–2362. doi:10.1002/elan.200804332.
[303] I. Grabowska, M. Sajnoga, M. Juchniewicz, M. Chudy, A. Dybko, Z. Brzozka, Microfluidic system with electrochemical and optical detection, Microelectron. Eng. 84 (2007) 1741–1743. doi:10.1016/j.mee.2007.01.248.
[304] X. Kang, G. Cheng, S. Dong, A novel electrochemical SPR biosensor, Electrochem. Commun. 3 (2001) 489–493. doi:10.1016/S1388-2481(01)00170-9.
[305] K.A. Marx, Quartz crystal microbalance: A useful tool for studying thin polymer films and complex biomolecular systems at the solution-surface interface, Biomacromolecules. 4 (2003) 1099–1120. doi:10.1021/bm020116i.
[306] W.B. Zimmerman, Electrochemical microfluidics, Chem. Eng. Sci. 66 (2011) 1412–1425. doi:10.1016/j.ces.2010.03.057.
[307] C. Chen, Q. Xie, D. Yang, H. Xiao, Y. Fu, Y. Tan, S. Yao, Recent advances in electrochemical glucose biosensors: a review, RSC Adv. 3 (2013) 4473. doi:10.1039/c2ra22351a.

[308] A. Heller, B. Feldman, Electrochemical Glucose Sensors and Their Applications in Diabetes Management, Chem. Rev. 108 (2008) 2482–2505. doi:10.1021/cr068069y.
[309] J. Wang, Electrochemical Glucose Biosensors, Chem. Rev. 108 (2008) 814–825. doi:10.1021/cr068123a.
[310] A.A. Karyakin, E.E. Karyakina, L. Gorton, On the mechanism of H2O2 reduction at Prussian Blue modified electrodes, Electrochem. Commun. 1 (1999) 78–82. doi:10.1016/S1388-2481(99)00010-7.
[311] A.A. Karyakin, Prussian blue and its analogues: Electrochemistry and analytical applications, Electroanalysis. 13 (2001) 813–819. doi:10.1002/1521-4109(200106)13:10<813::AID-ELAN813>3.0.CO;2-Z.
[312] F. Ricci, A. Amine, G. Palleschi, D. Moscone, Prussian Blue based screen printed biosensors with improved characteristics of long-term lifetime and pH stability, Biosens. Bioelectron. 18 (2003) 165–174. doi:10.1016/S0956-5663(02)00169-0.
[313] E. Thrush, O. Levi, L.J. Cook, J. Deich, A. Kurtz, S.J. Smith, W.E. Moerner, J.S. Harris, Monolithically integrated semiconductor fluorescence sensor for microfluidic applications, Sensors Actuators, B Chem. 105 (2005) 393–399. doi:10.1016/j.snb.2004.06.028.
[314] S. Billat, K. Kliche, R. Gronmaier, P. Nommensen, J. Auber, F. Hedrich, R. Zengerle, Monolithic integration of micro-channel on disposable flow sensors for medical applications, TRANSDUCERS EUROSENSORS '07 - 4th Int. Conf. Solid-State Sensors, Actuators Microsystems. 146 (2007) 29–32. doi:10.1109/SENSOR.2007.4300064.
[315] C. Ricciardi, G. Canavese, R. Castagna, I. Ferrante, A. Ricci, S.L. Marasso, L. Napione, F. Bussolino, Integration of microfluidic and cantilever technology for biosensing application in liquid environment, Biosens. Bioelectron. 26 (2010) 1565–1570. doi:10.1016/j.bios.2010.07.114.
[316] M. Hashimoto, S. Upadhyay, H. Suzuki, Dependence of the response of an amperometric biosensor formed in a micro flow channel on structural and conditional parameters, Biosens. Bioelectron. 21 (2006) 2224–2231. doi:10.1016/j.bios.2005.11.009.
[317] P.K. Yuen, Embedding objects during 3D printing to add new functionalities, Biomicrofluidics. 10 (2016). doi:10.1063/1.4958909.
[318] F. Lamberti, C. Luni, A. Zambon, P. Andrea Serra, M. Giomo, N. Elvassore, Flow biosensing and sampling in indirect electrochemical detection, Biomicrofluidics. 6 (2012) 1–13. doi:10.1063/1.4705368.
[319] J.L. Erkal, A. Selimovic, B.C. Gross, S.Y. Lockwood, E. Walton, L., S. McNamara, R.S. Martin, and D.M. Spence, 3D Printed Microfluidic Devices with Integrated Versatile and Reusable Electrodes, Lab Chip. 14 (2014) 2023–2032. doi:10.1039/c4lc00171k.3D.
[320] J.W. Park, B. Vahidi, A.M. Taylor, S.W. Rhee, N.L. Jeon, Microfluidic culture platform for neuroscience research., Nat. Protoc. 1 (2006) 2128–36. doi:10.1038/nprot.2006.316.
[321] U.Y. Schaff, M.M.Q. Xing, K.K. Lin, N. Pan, N.L. Jeon, S.I. Simon, Vascular mimetics based on microfluidics for imaging the leukocyte-endothelial inflammatory response, Lab Chip. 7 (2007) 448. doi:10.1039/b617915k.
[322] E. Wilhelm, C. Neumann, T. Duttenhofer, L. Pires, B.E. Rapp, Connecting microfluidic chips using a chemically inert, reversible, multichannel chip-to-world-interface., Lab Chip. 13 (2013) 4343–51. doi:10.1039/c3lc50861g.
[323] B.E. Rapp, B. Schickling, J. Prokop, V. Piotter, M. Rapp, K. Länge, Design and integration of a generic disposable array-compatible sensor housing into an integrated disposable indirect microfluidic flow injection analysis system, Biomed. Microdevices. 13 (2011) 909–922. doi:10.1007/s10544-011-9560-4.
[324] J. Yang, J.H. Yu, J. Rudi Strickler, W.J. Chang, S. Gunasekaran, Nickel nanoparticle-chitosan-reduced graphene oxide-modified screen-printed electrodes for enzyme-free

glucose sensing in portable microfluidic devices, Biosens. Bioelectron. 47 (2013) 530–538. doi:10.1016/j.bios.2013.03.051.
[325] E. Tkachenko, E. Gutierrez, M.H. Ginsberg, A. Groisman, An easy to assemble microfluidic perfusion device with a magnetic clamp., Lab Chip. 9 (2009) 1085–1095. doi:10.1039/b812184b.
[326] A.M. Gonçalves, A.Q. Pedro, F.M. Santos, L.M. Martins, C.J. Maia, J.A. Queiroz, L.A. Passarinha, Trends in protein-based biosensor assemblies for drug screening and pharmaceutical kinetic studies, Molecules. 19 (2014) 12461–12485. doi:10.3390/molecules190812461.
[327] M.A. Alonso-Lomillo, O. Domínguez-Renedo, M.J. Arcos-Martínez, Screen-printed biosensors in microbiology; A review, Talanta. 82 (2010) 1629–1636. doi:10.1016/j.talanta.2010.08.033.
[328] L.D. Mello, L.T. Kubota, Review of the use of biosensors as analytical tools in the food and drink industries, Food Chem. 77 (2002) 237–256. doi:10.1016/S0308-8146(02)00104-8.
[329] A.P.F. Turner, I. Karube, G.S. Wilson, Biosensors Fundamentals and Applications, Oxford University Press, Walton Street, Oxford OX2 6DP Oxford, New York, 1989. doi:10.1017/CBO9781107415324.004.
[330] S. Borgmann, A. Schulte, S. Neugebauer, W. Schuhmann, Amperometric biosensors, in: R.C. Alkire, D.M. Kolb, J. Lipkowski (Eds.), Adv. Electrochem. Sci. Eng. Bioelectrochemistry, Wiley-VCH Verlag GmbH & Co. KGaA, Weinheim, 2012: pp. 50–54. doi:10.1016/S0958-1669(96)80094-2.
[331] I.R.G. Ogilvie, V.J. Sieben, C.F. a Floquet, R. Zmijan, M.C. Mowlem, H. Morgan, Solvent processing of PMMA and COC chips for bonding devices with optical quality surfaces, 14th Int. Conf. Miniaturized Syst. Chem. Life Sci. (2010) 1244–1246. doi:10.1088/0960-1317/20/6/065016.
[332] M. Mahosenaho, F. Caprio, L. Micheli, A.M. Sesay, G. Palleschi, V. Virtanen, A disposable biosensor for the determination of alpha-amylase in human saliva, Microchim. Acta. 170 (2010) 243–249. doi:10.1007/s00604-010-0360-y.
[333] W. Jeon, C.B. Shin, Design and simulation of passive mixing in microfluidic systems with geometric variations, Chem. Eng. J. 152 (2009) 575–582. doi:10.1016/j.cej.2009.05.035.
[334] A.A.S. Bhagat, E.T.K. Peterson, I. Papautsky, A passive planar micromixer with obstructions for mixing at low Reynolds numbers, J. Micromechanics Microengineering. 17 (2007) 1017–1024. doi:10.1088/0960-1317/17/5/023.
[335] C.-C. Hong, J.-W. Choi, C.H. Ahn, A novel in-plane passive microfluidic mixer with modified Tesla structures, Lab Chip. 4 (2004) 109–113. doi:10.1039/B305892A.
[336] Y. Wang, Z. Li, J. Wang, J. Li, Y. Lin, Graphene and graphene oxide: Biofunctionalization and applications in biotechnology, Trends Biotechnol. 29 (2011) 205–212. doi:10.1016/j.tibtech.2011.01.008.
[337] D. Chen, H. Feng, J. Li, Graphene Oxide: Preparation, Functionalization, and Electrochemical Applications, Chem. Rev. 112 (2012) 6027–6053. doi:10.1021/cr300115g.
[338] D.C. Demirjian, F. Morís-Varas, C.S. Cassidy, Enzymes from extremophiles, Curr. Opin. Chem. Biol. 5 (2001) 144–151. doi:10.1016/S1367-5931(00)00183-6.
[339] M. Ahnoff, L.H. Cazares, K. Sköld, Thermal inactivation of enzymes and pathogens in biosamples for MS analysis, Bioanalysis. 7 (2015) 1885–1899. doi:10.4155/bio.15.122.
[340] S.-G. Jeong, O.-D. Baik, D.-H. Kang, Evaluation of radio-frequency heating in controling Salmonella enterica in raw shelled almonds, Int. J. Food Microbiol. 254 (2017) 54–61. doi:10.1016/j.ijfoodmicro.2017.04.007.
[341] H. Jaeger, A. Janositz, D. Knorr, The Maillard reaction and its control during food processing. The potential of emerging technologies, Pathol. Biol. 58 (2010) 207–213.

doi:10.1016/j.patbio.2009.09.016.
[342] X. Michalet, S. Weiss, M. Jager, Single-molecule fluorescence studies of protein folding and conformational dynamics, Chem. Rev. 106 (2006) 1785–1813. doi:10.1021/cr0404343.
[343] C.M. Dobson, Protein folding and misfolding, Nature. 426 (2003) 884–890. doi:10.1038/nature02261.
[344] E.P. e Melo, Estabilidade de Proteínas, in: J.M.S. Cabral, M.R. Aires-Barros, M. Gama (Eds.), Eng. Enzimática, 1st ed., Lidel - edições técnicas, lda, 2003: pp. 67–90.
[345] V. V. Mozhaev, K. Martinek, Inactivation and reactivation of proteins (enzymes), Enzyme Microb. Technol. 4 (1982) 299–309. doi:10.1016/0141-0229(82)90050-3.
[346] P. V. Iyer, L. Ananthanarayan, Enzyme stability and stabilization-Aqueous and non-aqueous environment, Process Biochem. 43 (2008) 1019–1032. doi:10.1016/j.procbio.2008.06.004.
[347] C. Tsou, Inactivation precedes overall molecular conformation changes during enzyme denaturation, Biochim. Biophys. Acta. 1253 (1995) 151–162. doi:0167-4838/95.
[348] E. V. Kuzmenkina, C.D. Heyes, G.U. Nienhaus, Single-molecule Forster resonance energy transfer study of protein dynamics under denaturing conditions, Proc. Natl. Acad. Sci. 102 (2005) 15471–15476. doi:10.1073/pnas.0507728102.
[349] A. Kumar, P. Venkatesu, Overview of the Stability of alpha-Chymotrypsin in Different Solvent Media, Chem. Rev. 112 (2012) 4283–4307. doi:10.1021/cr2003773.
[350] B.A. Shirley, Protein Stability and Folding - Theory and Practice, Humana Press, Totowa, New Jersey, 1995.
[351] C.C. You, M. De, G. Han, V.M. Rotello, Tunable inhibition and denaturation of alfa-chymotrypsin with amino acid-functionalized gold nanoparticles, J. Am. Chem. Soc. 127 (2005) 12873–12881. doi:10.1021/ja0512881.
[352] T. Koudelakova, R. Chaloupkova, J. Brezovsky, Z. Prokop, E. Sebestova, M. Hesseler, M. Khabiri, M. Plevaka, D. Kulik, I. Kuta Smatanova, P. Rezacova, R. Ettrich, U.T. Bornscheuer, J. Damborsky, Engineering enzyme stability and resistance to an organic cosolvent by modification of residues in the access tunnel, Angew. Chemie - Int. Ed. 52 (2013) 1959–1963. doi:10.1002/anie.201206708.
[353] P. Attri, E.H. Choi, Influence of Reactive Oxygen Species on the Enzyme Stability and Activity in the Presence of Ionic Liquids, PLoS One. 8 (2013). doi:10.1371/journal.pone.0075096.
[354] E. Longo, R. Hussain, G. Siligardi, Application of circular dichroism and magnetic circular dichroism for assessing biopharmaceuticals formulations photo-stability and small ligands binding properties, Int. J. Pharm. 480 (2015) 84–91. doi:10.1016/j.ijpharm.2015.01.026.
[355] S. Kelly, N. Price, The Use of Circular Dichroism in the Investigation of Protein Structure and Function, Curr. Protein Pept. Sci. 1 (2000) 349–384. doi:10.2174/1389203003381315.
[356] P. Venkatesu, M.J. Lee, H.M. Lin, Thermodynamic characterization of the osmolyte effect on protein stability and the effect of GdnHCl on the protein denatured state, J. Phys. Chem. B. 111 (2007) 9045–9056. doi:10.1021/jp0701901.
[357] R.M. Daniel, M.E. Peterson, M.J. Danson, N.C. Price, S.M. Kelly, C.R. Monk, C.S. Weinberg, M.L. Oudshoorn, C.K. Lee, The molecular basis of the effect of temperature on enzyme activity, Biochem. J. 425 (2010) 353–360. doi:10.1042/BJ20091254.
[358] R. Lumry, H. Eyring, Conformation Changes of Proteins, J. Phys. Chem. 58 (1954) 110–120. doi:10.1021/j150512a005.
[359] M. Polakovič, P. Vrábel, Analysis of the mechanism and kinetics of thermal inactivation of enzymes: Critical assessment of isothermal inactivation experiments, Process Biochem. 31 (1996) 787–800. doi:10.1016/S0032-9592(96)00026-X.
[360] R. Eisenthal, M.E. Peterson, R.M. Daniel, M.J. Danson, The thermal behaviour of enzyme

activity: implications for biotechnology, Trends Biotechnol. 24 (2006) 289–292. doi:10.1016/j.tibtech.2006.05.004.
[361] Ciarán Ó Fágáin, Understanding and increasing protein stability, Biochim. Biophys. Acta (BBA)/Protein Struct. Mol. 1252 (1995) 1–14. doi:10.1016/0167-4838(95)00133-F.
[362] T.J. Ahern, A.M. Klibanov, Analysis of Processes Causing Thermal Inactivation of Enzymes, in: D. Glick (Ed.), Methods Biochem. Anal., John Wiley & Sons, Inc., 1988: pp. 91–127. doi:10.1002/9780470110546.
[363] M.E. Peterson, R.M. Daniel, M.J. Danson, Ro. Eisenthal, The dependence of enzyme activity on temperature: determination and validation of parameters, Biochem. J. 402 (2007) 331–337. doi:10.1042/BJ20061143.
[364] N.G. Chen, K. Gregory, Y. Sun, V. Golovlev, Transient model of thermal deactivation of enzymes, Biochim. Biophys. Acta - Proteins Proteomics. 1814 (2011) 1318–1324. doi:10.1016/j.bbapap.2011.06.010.
[365] V.K. Tyagi, S.L. Lo, Microwave irradiation: A sustainable way for sludge treatment and resource recovery, Renew. Sustain. Energy Rev. 18 (2013) 288–305. doi:10.1016/j.rser.2012.10.032.
[366] K. Kultima, K. Sköld, M. Borén, Biomarkers of disease and post-mortem changes - Heat stabilization, a necessary tool for measurement of protein regulation, J. Proteomics. 75 (2011) 145–159. doi:10.1016/j.jprot.2011.06.009.
[367] A. Siddharta, S. Pfaender, A. Malassa, J. Doerrbecker, Anggakusuma, M. Engelmann, B. Nugraha, J. Steinmann, D. Todt, F.W.R. Vondran, P. Mateu-Gelabert, C. Goffinet, E. Steinmann, Inactivation of HCV and HIV by microwave: a novel approach for prevention of virus transmission among people who inject drugs, Sci. Rep. 6 (2016) 36619. doi:10.1038/srep36619.
[368] S.C. Ojha, S. Chankhamhaengdecha, S. Singhakaew, P. Ounjai, T. Janvilisri, Inactivation of Clostridium difficile spores by microwave irradiation, Anaerobe. 38 (2016) 14–20. doi:10.1016/j.anaerobe.2015.10.015.
[369] F.-G. Chizoba Ekezie, D.-W. Sun, Z. Han, J.-H. Cheng, Microwave-assisted food processing technologies for enhancing product quality and process efficiency: A review of recent developments, Trends Food Sci. Technol. 67 (2017) 58–69. doi:10.1016/j.tifs.2017.05.014.
[370] P. Piyasena, C. Dussault, T. Koutchma, H.S. Ramaswamy, G.B. Awuah, Radio Frequency Heating of Foods: Principles, Applications and Related Properties—A Review, Crit. Rev. Food Sci. Nutr. 43 (2003) 587–606. doi:10.1080/10408690390251129.
[371] K.S. Varghese, M.C. Pandey, K. Radhakrishna, A.S. Bawa, Technology, applications and modelling of ohmic heating: a review, J. Food Sci. Technol. 51 (2012) 2304–2317. doi:10.1007/s13197-012-0710-3.
[372] K. Krishnamurthy, H.K. Khurana, J. Soojin, J. Irudayaraj, A. Demirci, Infrared Heating in Food Processing: An Overview, Compr. Rev. Food Sci. Food Saf. 7 (2008) 2–13. doi:10.1111/j.1541-4337.2007.00024.x.
[373] J.W. Ha, D.H. Kang, Enhanced inactivation of food-borne pathogens in ready-to-eat sliced ham by near-infrared heating combined with UV-C irradiation and mechanism of the synergistic bactericidal action, Appl. Environ. Microbiol. 81 (2015) 2–8. doi:10.1128/AEM.01862-14.
[374] A.A.P. de Alwis, P.J. Fryer, Operability of the ohmic heating process: Electrical conductivity effects, J. Food Eng. 15 (1992) 21–48. doi:10.1016/0260-8774(92)90038-8.
[375] A. Jakób, J. Bryjak, H. Wójtowicz, V. Illeová, J. Annus, M. Polakovič, Inactivation kinetics of food enzymes during ohmic heating, Food Chem. 123 (2010) 369–376. doi:10.1016/j.foodchem.2010.04.047.
[376] V. Miralles, A. Huerre, F. Malloggi, M.-C. Jullien, A Review of Heating and Temperature

Control in Microfluidic Systems: Techniques and Applications, 2013. doi:10.3390/diagnostics3010033.
[377] T. Yamamoto, T. Fujii, T. Nojima, PDMS–glass hybrid microreactor array with embedded temperature control device. Application to cell-free protein synthesis, Lab Chip. 2 (2002) 197–202. doi:10.1039/B205010B.
[378] M.G. Roper, C.J. Easley, J.P. Landers, Advances in polymerase chain reaction on microfluidic chips, Anal. Chem. 77 (2005) 3887–3893. doi:10.1021/ac050756m.
[379] V.N. Hoang, G. V. Kaigala, A. Atrazhev, L.M. Pilarski, C.J. Backhouse, Strategies for enhancing the speed and integration of microchip genetic amplification, Electrophoresis. 29 (2008) 4684–4694. doi:10.1002/elps.200800351.
[380] G. Wang, H.-P. Ho, Q. Chen, A.K.-L. Yang, H.-C. Kwok, S.-Y. Wu, S.-K. Kong, Y.-W. Kwan, X. Zhang, A lab-in-a-droplet bioassay strategy for centrifugal microfluidics with density difference pumping, power to disc and bidirectional flow control, Lab Chip. 13 (2013) 3698. doi:10.1039/c3lc50545f.
[381] E.A. Oblath, W.H. Henley, J.P. Alarie, J.M. Ramsey, A microfluidic chip integrating DNA extraction and real-time PCR for the detection of bacteria in saliva, Lab Chip. 13 (2013) 1325. doi:10.1039/c3lc40961a.
[382] G. V. Kaigala, J. Jiang, C.J. Backhouse, H.J. Marquez, System design and modeling of a time-varying, nonlinear temperature controller for microfluidics, IEEE Trans. Control Syst. Technol. 18 (2010) 521–530. doi:10.1109/TCST.2009.2015937.
[383] G. Velve Casquillas, C. Fu, M. Le Berre, J. Cramer, S. Meance, A. Plecis, D. Baigl, J.-J. Greffet, Y. Chen, M. Piel, P.T. Tran, Fast microfluidic temperature control for high resolution live cell imaging, Lab Chip. 11 (2011) 484–489. doi:10.1039/C0LC00222D.
[384] M. Colombo, I. Peretto, Chemistry strategies in early drug discovery: an overview of recent trends, Drug Discov. Today. 13 (2008) 677–684. doi:10.1016/j.drudis.2008.03.007.
[385] J.J. Shah, J. Geist, M. Gaitan, Microwave-induced adjustable nonlinear temperature gradients in microfluidic devices, J. Micromechanics Microengineering. 20 (2010) 105025. doi:10.1088/0960-1317/20/10/105025.
[386] M.S. Boybay, A. Jiao, T. Glawdel, C.L. Ren, Microwave sensing and heating of individual droplets in microfluidic devices, Lab Chip. 13 (2013) 3840–3846. doi:10.1039/c3lc50418b.
[387] B.C. Giordano, J. Ferrance, S. Swedberg, A.F.R. Hühmer, J.P. Landers, Polymerase Chain Reaction in Polymeric Microchips: DNA Amplification in Less Than 240 Seconds, Anal. Biochem. 291 (2001) 124–132. doi:10.1006/abio.2000.4974.
[388] Y. Yu, B. Li, C. a Baker, X. Zhang, M.G. Roper, Quantitative polymerase chain reaction using infrared heating on a microfluidic chip, Anal Chem. 84 (2012) 2825–2829. doi:10.1021/ac203307h.
[389] M. Subramanian, A. Miaskowski, G. Pearce, J. Dobson, A coil system for real-time magnetic fluid hyperthermia microscopy studies, Int. J. Hyperth. 32 (2016) 112–120. doi:10.3109/02656736.2015.1104732.
[390] F. Gazeau, M. Lévy, C. Wilhelm, Optimizing magnetic nanoparticle design for nanothermotherapy, Nanomedicine. 3 (2008) 831–844. doi:10.2217/17435889.3.6.831.
[391] S. Singh, K.C. Barick, D. Bahadur, Inactivation of bacterial pathogens under magnetic hyperthermia using Fe 3 O 4 – ZnO nanocomposite, Powder Technol. 269 (2015) 513–519. doi:10.1016/j.powtec.2014.09.032.
[392] A. Ilovitsh, P. Polak, Z. Zalevsky, O. Shefi, Selective inactivation of enzymes conjugated to nanoparticles using tuned laser illumination, Cytom. Part A. (2016). doi:10.1002/cyto.a.23005.
[393] C. Zhang, J. Xu, W. Ma, W. Zheng, PCR microfluidic devices for DNA amplification, Biotechnol. Adv. 24 (2006) 243–284. doi:10.1016/j.biotechadv.2005.10.002.
[394] G. Maltezos, M. Johnston, A. Scherer, Thermal management in microfluidics using micro-

Peltier junctions, Appl. Phys. Lett. 87 (2005) 1–3. doi:10.1063/1.2089174.
[395] S. Placzek, I. Schomburg, A. Chang, L. Jeske, M. Ulbrich, J. Tillack, D. Schomburg, BRENDA in 2017: new perspectives and new tools in BRENDA, Nucleic Acids Res. 45 (2017) D380–D388. doi:10.1093/nar/gkw952.
[396] Y.Y. Yan, Recent Advances in Computational Simulation of Macro-, Meso-, and Micro-Scale Biomimetics Related Fluid Flow Problems, J. Bionic Eng. 4 (2007) 97–107. doi:10.1016/S1672-6529(07)60021-3.
[397] A.B. Thrane, Lars, W. Paul, Bakker, Brameshuber, B. Cazacliu, L. Ferrara, D. Feys, M. Geiker, A. Gram, S.M. , Steffen Grünewald, N. Roquet, S.U. NicolasRoussel, Surendra Shah, Nathan Tregger, and J.E.W. Frederick Van Waarde, Computational Fluid Dynamics, in: N. Roussel, A. Gram (Eds.), Simul. Fresh Concr. Flow, Springer, 2014: pp. 25–63. doi:10.1007/978-94-017-8884-7.
[398] D.L. Brown, R. Cortez, M.L. Minion, Accurate Projection Methods for the Incompressible Navier–Stokes Equations, J. Comput. Phys. 168 (2001) 464–499. doi:10.1006/jcph.2001.6715.
[399] G.M. Mala, D. Li, J.D. Dale, Heat transfer and fluid flow in microchannels, Int. J. Heat Mass Transf. 40 (1997) 3079–3088. doi:10.1016/S0017-9310(96)00356-0.
[400] P.D.D. Schomburg, BRENDA - The Comprehensive Enzyme Information System, Tech. Univ. Braunschweig, BRICS, Dep. Bioinforma. Biochem. Rebenring 56 38106 Braunschweig, Ger. (n.d.). www.brenda-enzymes.org.
[401] R. Fernandez-Lafuente, Stabilization of multimeric enzymes: Strategies to prevent subunit dissociation, Enzyme Microb. Technol. 45 (2009) 405–418. doi:10.1016/j.enzmictec.2009.08.009.
[402] M.D. Gouda, S.A. Singh, A.G.A. Rao, M.S. Thakur, N.G. Karanth, Thermal inactivation of glucose oxidase: Mechanism and stabilization using additives, J. Biol. Chem. 278 (2003) 24324–24333. doi:10.1074/jbc.M208711200.
[403] G. Zoldák, A. Zubrik, A. Musatov, M. Stupák, E. Sedlák, Irreversible thermal denaturation of glucose oxidase from Aspergillus niger is the transition to the denatured state with residual structure, J. Biol. Chem. 279 (2004) 47601–47609. doi:10.1074/jbc.M406883200.
[404] I.W. Sizer, Temperature activation and inactivation of the crystalline catalase-hydrogen peroxide system, J. Biol. Chem. (1944) 461–473.
[405] H.C. Eyster, Effect of Temperature on Catalase Activity, Ohio J. Sci. 50 (1950) 273–277. http://hdl.handle.net/1811/3787.
[406] M. Bartoszek, M. Kściuczyk, Study of the temperature influence on catalase using spin labelling method, J. Mol. Struct. 744–747 (2005) 733–736. doi:10.1016/j.molstruc.2004.11.080.
[407] I. V Sochava, T. V Belopolskaya, O.I. Smirnova, Dsc Study of Reversible and Irreversible Thermal Denaturation of Concentrated Globular Protein Solutions, Biophys. Chem. 22 (1985) 323–336. http://www.sciencedirect.com/science/article/B6TFB-44FDPS6-HC/2/f713d865e32bb76544ee795515fd7aee.
[408] Y.-F. Maa, C.C. Hsu, Protein denaturation by combined effect of shear and air-liquid interface, Biotechnol. Bioeng. 54 (1997) 503–512. doi:10.1002/(SICI)1097-0290(19970620)54:6<503::AID-BIT1>3.0.CO;2-N.
[409] Y.F. Yano, Kinetics of protein unfolding at interfaces, J. Phys. Condens. Matter. 24 (2012) 503101. doi:10.1088/0953-8984/24/50/503101.
[410] T.J.A. and A.M. Klibanov, The Mechanism of Irreversible Enzyme Inactivation at 100° C, Sci. New Ser. 228 (1985) 1280–1284.

Process and Systems Engineering Centre (PROSYS)
Department of Chemical and Biochemical Engineering
Technical University of Denmark
Søltofts Plads, Building 229
DK - 2800 Kgs. Lyngby
Denmark

Phone: +45 45 25 28 00
Web: www.kt.dtu.dk/forskning/prosys